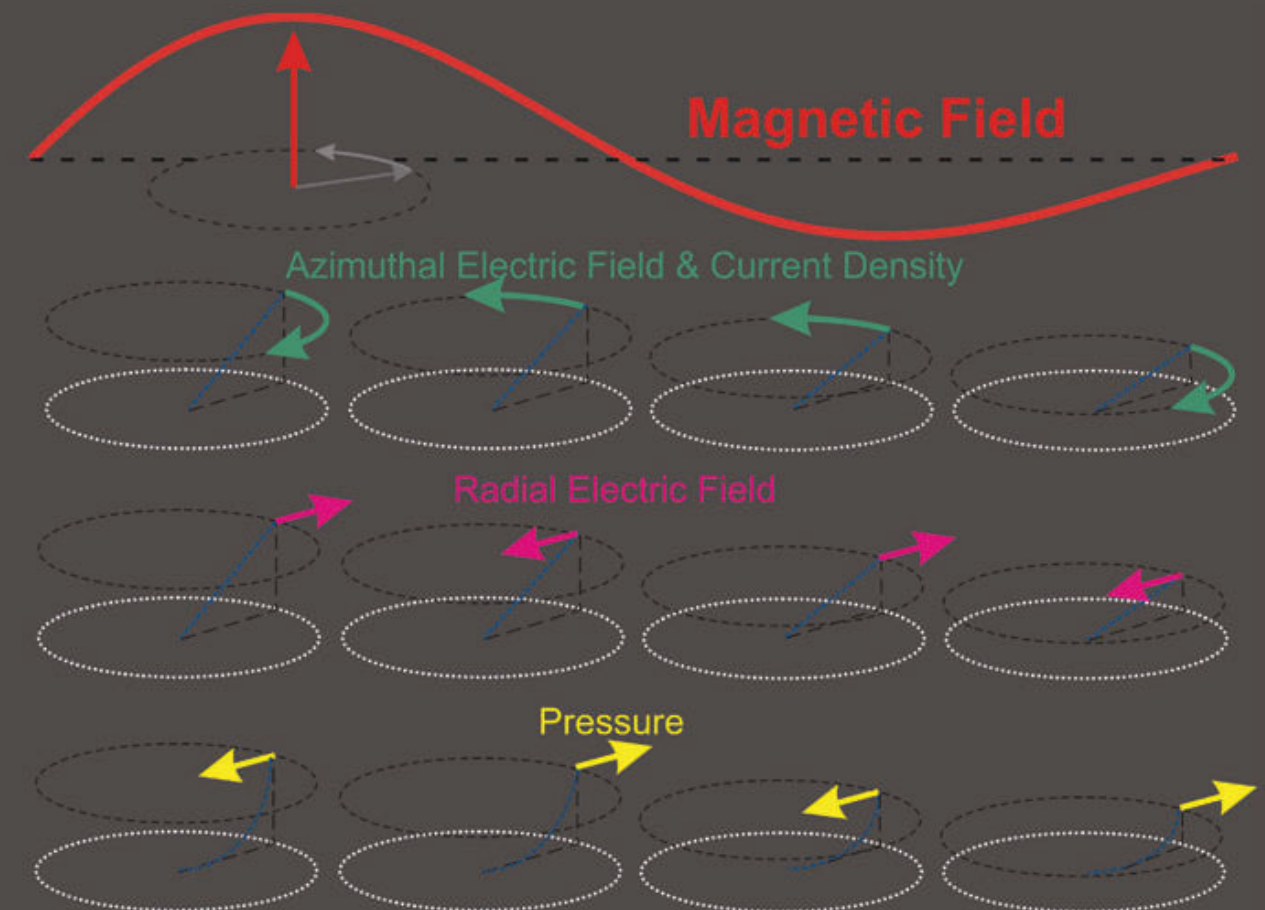


# Hysteresis in Optical Megagauss Spectroscopy

An analysis



# Hysteresis in Optical Megagauss Spectroscopy

An analysis

## DISSERTATION

zur Erlangung des akademischen Grades  
doctor rerum naturalium  
(Dr. rer. nat.)  
im Fach Physik

eingereicht an der  
Mathematisch-Naturwissenschaftlichen Fakultät I  
der Humboldt-Universität zu Berlin

von  
Dipl.-Phys. Stefan Hansel  
geboren am 09.03.1976 in Berlin

Präsident der Humboldt-Universität zu Berlin:  
Prof. Dr. Christoph Markschies

Dekan der Mathematisch-Naturwissenschaftlichen Fakultät I:  
Prof. Thomas Buckhout, PhD

Gutachter:

- (1) Prof. Dr. Michael von Ortenberg
- (2) Prof. Dr. Recardo Manzke
- (3) Prof. Junichiro Kono, PhD

Tag der mündlichen Prüfung: 19. Juli 2006

### **Bibliografische Information Der Deutschen Bibliothek**

Die Deutsche Bibliothek verzeichnet diese Publikation in der Deutschen Nationalbibliografie; detaillierte bibliografische Daten sind im Internet über <http://dnb.ddb.de> abrufbar.

1. Aufl. - Göttingen : Cuvillier, 2006

Zugl.: Berlin, Univ., Diss., 2006

ISBN 3-86727-014-7

© CUVILLIER VERLAG, Göttingen 2006

Nonnenstieg 8, 37075 Göttingen

Telefon: 0551-54724-0

Telefax: 0551-54724-21

[www.cuvillier.de](http://www.cuvillier.de)

Alle Rechte vorbehalten. Ohne ausdrückliche Genehmigung des Verlages ist es nicht gestattet, das Buch oder Teile daraus auf fotomechanischem Weg (Fotokopie, Mikrokopie) zu vervielfältigen.

1. Auflage, 2006

Gedruckt auf säurefreiem Papier

ISBN 3-86727-014-7

# Contents

<b>Introduction</b>	<b>1</b>
<b>1 Motivation</b>	<b>3</b>
1.1 General Features	3
1.2 InAs/AlSb Single-Quantum Well	3
1.3 Quasi Bulk HgSe	6
1.4 Quasi Bulk HgTe	7
1.5 Bulk InSb	8
1.6 Conclusions	9
<b>2 Conductors in Transient Magnetic Fields</b>	<b>11</b>
2.1 Cyclotron Resonance	12
2.1.1 Quantum Mechanics	16
2.2 Eddy Currents	18
2.2.1 Eddy Currents in a Circular Thin Disc	18
2.2.2 The Diffusion Approximation	22
2.2.3 Skin Depth and Diffusion Time	24
2.2.4 Solution of the Diffusion Equation	26
2.2.5 The Eddy Current Density	30
2.2.6 Induced Temperature	32
2.2.7 Mechanical Forces on and within the Sample	34
2.2.8 Summary of Eddy Current Effects	37
<b>3 Magnetic Field Generation</b>	<b>39</b>
3.1 General Remarks on Magnetic Field Generation	39
3.2 The Single Turn Coil Technique	41
3.3 Setup & Performance of the STC-Megagauss Generator	43
3.4 Nondestructive Operation of the STC	45
3.5 Measurement of the Magnetic Field Intensity	48
<b>4 Cyclotron Resonance Setup</b>	<b>51</b>
4.1 Parameters for Experiments in STCs	51
4.2 Radiation Sources	52
4.3 Detector System	53
4.4 Low Temperatures	54
4.5 Data Management	56

---

<b>5</b>	<b>Indium Antimonide</b>	<b>63</b>
5.1	An Infrared Transmission Experiment . . . . .	63
5.2	Steady Field Transport . . . . .	67
5.3	Eddy Current Spectroscopy . . . . .	71
5.3.1	The Lattice Temperature . . . . .	78
5.3.2	Mechanical Pressure . . . . .	80
5.3.3	The Radial Electric Field . . . . .	82
5.4	Measurements with the Cyclotron Resonance Setup . . . . .	86
5.4.1	Temperature Dependence . . . . .	86
5.4.2	Wavelength Dependence . . . . .	91
5.5	Undoped Indium Antimonide . . . . .	95
5.5.1	Type I hysteresis? . . . . .	96
5.5.2	CO-Laser Measurements . . . . .	97
5.5.3	Comparison With Previous Measurements . . . . .	99
<b>6</b>	<b>Mercury Based Compounds</b>	<b>101</b>
6.1	Mercury Selenide . . . . .	101
6.2	Mercury Telluride . . . . .	103
6.3	Mercury Cadmium Telluride (MCT) . . . . .	106
6.3.1	Epitaxial MCT . . . . .	107
6.3.2	Bulk MCT . . . . .	110
	<b>Summary</b>	<b>113</b>
	<b>Deutsche Zusammenfassung</b>	<b>115</b>
	<b>Bibliography</b>	<b>117</b>
	<b>List of Publications</b>	<b>125</b>

# Introduction

The cyclotron resonance is a very traditional tool in semiconductor physics for determining carrier effective masses. Materials with high effective masses, low mobility or high carrier concentration require high energies for the observation of cyclotron resonance. Therefore, Mid Infra-Red radiation energies are used in combination with very high magnetic fields.

The highest magnetic fields on a laboratory scale can only be generated at the expense of a very short pulse time of order  $\mu s$ . Whereas the field magnitude effects on semiconductors are well investigated, the transient character of the field generation has been assumed to be of minor influence.

Analytical methods developed for steady magnets with comparably low fields have been used in pulsed fields accordingly. In pulsed, sinusoidal fields it is possible to measure optical resonances in rising and falling field in one experiment. Intuitively one would expect identical behavior in this case. With improved experimental resolution and the resulting possibility of fully using available data on rising and falling field sides of a pulse the respective spectra showed discrepancies between each other.

In the last few years, it became apparent that observable cyclotron resonance spectra are not independent of the magnetic field generation process, that means, they depend on the sweep rate or pulse duration.

A spin hysteresis of the conduction band electrons of narrow gap semiconductors has been observed in transient magnetic fields [1–5]. The results could be readily explained with a spin lattice relaxation time of the conduction band electrons of order  $1 \mu s$ . In this case the time dependence of the magnetic field enabled the detection of population dynamics for the spin split cyclotron resonances of electrons.

Recently, other hysteretic phenomena on the cyclotron resonances of electrons have been observed that could not be explained by a spin hysteresis, but showed a dependence rather on the field derivative than its temporal structure [6, 7]. Moreover, even well known materials, such as InSb, exhibited completely unexpected hysteretic behavior in transient magnetic fields. No previously known resonance was involved in the hysteresis, but a completely new phenomenon. This leads to the conclusion that the interaction of the transient magnetic field generation with a conducting sample is not negligible and must be systematically examined.

Although this problem has been known for many years, the influence of eddy currents and electric fields as induced by the transient character of the magnetic field pulse has been treated only by crude approximations. It was also incomplete regarding the effects connected with that such as a rise in temperature, a screened magnetic field and an exertion of pressure onto the conductor.

The goal of this thesis is a fundamental expanding of the understanding of the effect of transient magnetic fields and semi-conducting samples with the focus on the implications

for cyclotron resonance measurements, that is for magneto-transmission experiments. The magnitude and quality of eddy current related effects will be rigorously derived in unprecedented complexity. The experimental focus will be upon hysteretic phenomena in InSb that are analyzed with respect to the theoretical findings.

This thesis is divided into 6 chapters.

The first chapter summarizes hysteretic phenomena in cyclotron resonance experiments in single turn coils as have been reported prior to and at an early stage of this work. An analysis will be performed to draw conclusions upon the experimental requirements for the investigation of similar effects.

The second chapter will review the theory of cyclotron resonance and illuminate what sample properties can be deduced from experimental spectra. A large part of this chapter will deal with the interaction of a conducting sample with a transient magnetic field, that is a field with pulse durations of order  $\mu s$ . The effects of induced electric fields and eddy currents will be derived.

Chapters three and four are dedicated to the experimental setup and focus upon the required modifications imposed by the considerations in chapter one and two. Chapter three will focus upon the magnetic field generation, chapter four upon the optical setup for measurements of cyclotron resonance.

Chapter five is dealing with a hysteretic phenomenon that has not been previously reported in InSb. It will be shown how the transient magnetic field character interacts with the infrared relative transmission spectra of InSb. For this purpose various experimental techniques beyond the cyclotron resonance setup in a transient field will be used and extended. The influence of eddy currents on the spectra will be quantitatively determined and it will be demonstrated that a radial, HALL-like electrical field is built up inside the sample due to the transient magnetic field and causes the above mentioned hysteretic phenomena in InSb that have not been understood previously.

Chapter six will briefly report and investigate sweep rate dependent hysteretic phenomena on mercury based compounds. Measurements depending on the macroscopic sample dimensions will show that the size of the sample radius affects the observed spectra and macroscopic phenomena such as eddy currents become effective.

Finally a summary will be presented.

# Chapter 1

## Motivation

As of present day magnetic fields in the 100 T, or *Megagauss*, range and above can only be generated in a laboratory with various methods on a very short timescale of order microseconds. The time dependence of the magnetic field pulse enabled the observation of various hysteretic phenomena. Methods of data evaluation and drawing conclusions developed for DC magnetic fields can neither predict nor explain any of these results.

At first, this chapter reviews previous reports on hysteretic phenomena of non-magnetic semi-conducting systems on a  $\mu s$  timescale in transient magnetic fields as found in the literature.

### 1.1 General Features

A hysteretic phenomenon can generally be defined as a retardation of an effect behind its cause. Thus, hysteresis is a property of physical systems that do not instantly follow the forces applied to them, but react slowly, or do not return completely to their original state: that is, systems whose states are not in thermodynamical equilibrium and depend on their immediate history [8].

For magnetic materials this has been subject of many studies [9]. In the present investigation, semi-conducting materials shall be focused upon that do not contain magnetic dopants or components besides of the spin.

In this work hysteresis will be understood as discrepancies in the transmission of infrared electromagnetic radiation through a semiconductor during the rising and falling magnetic field, respectively. Two fundamentally different hysteretic phenomena can be observed, firstly, a discrepancy of the time relation of the magnetic field and the optical response of the semi-conducting system, secondly, differences in the absorption strength of optical transitions.

The first phenomenon is very difficult to be determined or observed conclusively, thus previous reports deal predominantly with the latter effect.

### 1.2 InAs/AlSb Single-Quantum Well

Historically the first publications and reports on hysteresis effects observed in infrared spectroscopy of semiconductors in transient magnetic fields investigated a single quantum well of InAs/AlSb [1–3] by the Megagauss Laboratory of the ISSP, Tokyo, Japan.



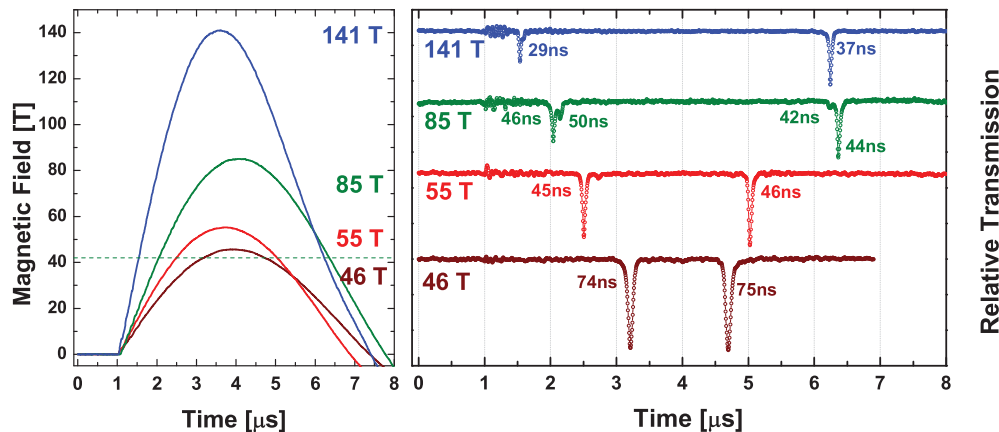


Figure 1.1: Comparison of relative transmission through samples at 16 K and  $10.59 \mu\text{m}$  at various magnetic fields with significantly different sweep rates [1–3]. It can clearly be seen that the sweep rate does have an effect on the relative population of the spin split electron level. The FWHM values of time are given at the respective resonances. The corresponding magnetic field traces are given on the left side. The horizontal line indicates the spin down resonance position.

The investigations have been carried out on samples with 15 nm InAs quantum wells in 15 nm and 20 nm barriers of AlSb with InSb like interfaces, carrier concentration was determined to be  $3 - 5 \times 10^{11} \text{ cm}^{-2}$  at 4 K and  $9 - 12 \times 10^{11} \text{ cm}^{-2}$  at 300 K and mobilities of  $26 \text{ m}^2/\text{Vs}$  and  $10 \text{ m}^2/\text{Vs}$ , respectively [3].

Using a cyclotron resonance setup with a single turn coil magnetic field generator for a wavelength of  $10.6 \mu\text{m}$  and a temperature of 16 K a dependence of the spin split cyclotron resonance on the maximum field was observed. The raw data is given in fig. 1.1 which can be transferred into the relative transmission spectrum vs. magnetic field of fig. 1.2.

While in the falling field side only the spin down state is observed, the spin up state becomes increasingly prominent in the rising field side with increasing maximum field. It is however, important to note that the total absorption intensity for spin up + spin down absorptions is conserved for all fields.

For detailed analysis of the optical traces it is important to estimate the effects of the recording equipment. There is no report on the parameters of the detector system used to obtain the data in [1–3]. For a cyclotron resonance measurement increasing the maximum field means a higher field derivative and thus a shorter time a resonance can be recorded by the detector system.

It can be clearly observed in fig. 1.1 that the resonance strength increases with decreasing maximum field, that is, increases with increasing recording time. This is a phenomenon that can occur when the resonance FWHM is short in time, shorter than the time defined by the bandwidth of the detector system. To obtain the signal from the sample the optical trace must be convolved with the response function of the detector system. It is approximately constant from DC to the detector bandwidth, but decreasing rapidly beyond that value. The FWHM time during which the resonance is recorded

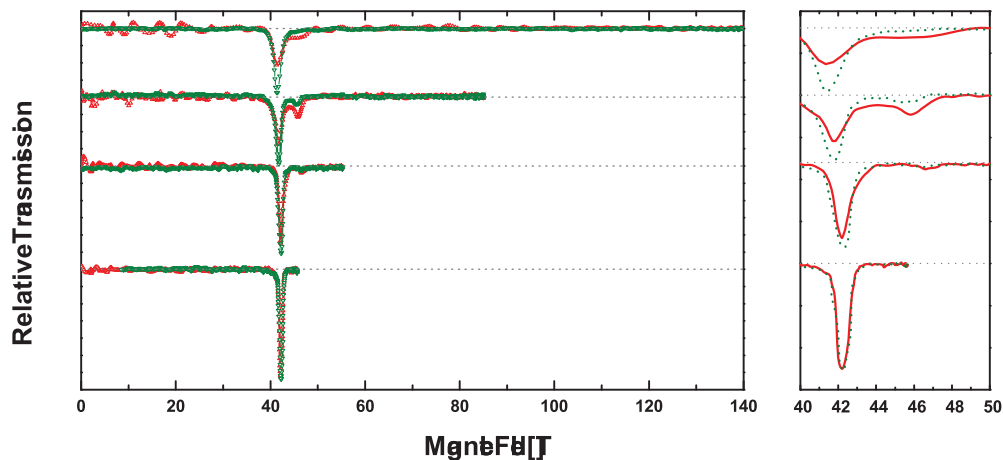


Figure 1.2: *Hysteresis in the relative transmission spectra of a InAs/AlSb single quantum well at  $10.59\ \mu\text{m}$  wavelength and 16 K Temperature. [1–3] The graph on the right shows details of the hysteresis affected spin split CR. The dashed lines are the down sweeps.*

increase from 29 ns at the fastest rising field to 74 ns at the slowest field rise. There is a time comparable to that value recorded in falling field side except for the highest field due to a much smaller value for the field derivative.

A band width of 20 MHz of the detection system could explain the trace for the highest field and the increase of resonance strength with increasing FWHM time of the resonance in all spectra. The quantitative data evaluation of these traces is questionable without detailed information on the detector system. However, the falling field resonance has approximately the same FWHM as the rising field resonance for the other fields. The response function will be similar for both resonances so that differences in relative resonance strength will be sample related. The discussion by [1–3] attributes all phenomena to the sample response to the magnetic field.

The pulse duration for all fields was  $\sim 6\ \mu\text{s}$ , much longer than the experimentally determined momentum scattering times of typically 0.1 ns at 12.5 T. Thus thermal equilibrium distributions for carriers can be expected at fields at this value, both spin split levels should be equally populated for a slowly varying field.

For a transient magnetic field the situation changes. With increasing field electrons depopulate the spin up level and relax into the spin down level. Thus the lower level will be populated by more electrons than expected from equilibrium statistics. Using a rate equation similar to equation (1.2) a spin relaxation time of  $\sim 1\ \mu\text{s}$  was obtained.

The LANDAU level wave functions are a mixture between spin up and down states, thus relaxation processes between different spin states by a electric type perturbation are possible [10]. Because of the discrete density of states, the spin flip relaxation is an energy loss process and can happen through an inelastic emission of phonons. It was found that single phonon processes are unlikely due to the LO phonon energy of 29.5 meV which is larger than the ZEEMAN energy and scattering by single acoustic phonons cannot satisfy energy and momentum conservation at the same time. Yet, it was shown that multi-phonon scattering can bypass these processes and account for the long relaxation

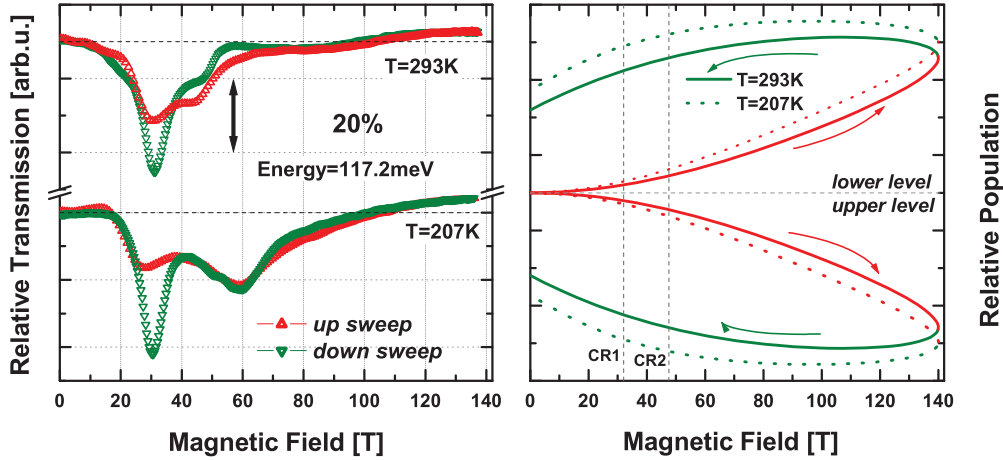


Figure 1.3: *Left: the relative transmission of infrared radiation of 117.2 meV through a HgSe sample at room temperature and 207K in a magnetic field of up to 140 T. The population changes for the spin split electron cyclotron resonance can clearly be observed [4, 5]. Right: The non-equilibrium distribution for the upper and lower spin-state of the spin split cyclotron transition.*

times [2, 3, 11].

Non-equilibrium populations of electron spins created by a transient magnetic field can be probed by CR for characteristic times of 0.1- few  $\mu s$ . The authors of [3] suggest that InSb-related 2DEGs should be the most promising candidates for the observation of that effect as the g-factor is large, therefore a large ZEEMAN splitting results in long spin flip relaxation time.

The observations could only be made for the higher carrier concentration sample and have been obscured by other effects for the lower concentration sample [3].

### 1.3 Quasi Bulk HgSe

A pronounced hysteresis of the population of the magnetic field dependent electronic energy levels in a quasi bulk sample of  $2 \mu m$  MBE grown HgSe has been reported on several occasions [4, 5]. The phenomenon affecting the spin split electron cyclotron resonance was observed at elevated temperatures  $T \geq 207 K$  in a single turn coil generated magnetic field of  $6 \mu s$  pulse length and 140 T magnitude.

The data of [4, 5] are shown in figure 1.3. The relative transmission spectra of the up and down sweep have identical resonance positions but the respective intensity of absorption is higher in the down sweep for the spin down resonance at cost of the intensity of the spin up resonance line. The total absorption intensity  $I_{tot} = I(\uparrow) + I(\downarrow)$  is conserved in up and down sweep. Earlier reports of a similar observation (section 1.2) have tentatively been explained by a delayed population adjustment of the energy levels involved due to the finite spin-lattice relaxation time in pulsed transient magnetic fields.

Applying a two level system for spin states equally populated at zero magnetic field the relative population was simulated. The non-equilibrium distribution functions  $f_1(t)$

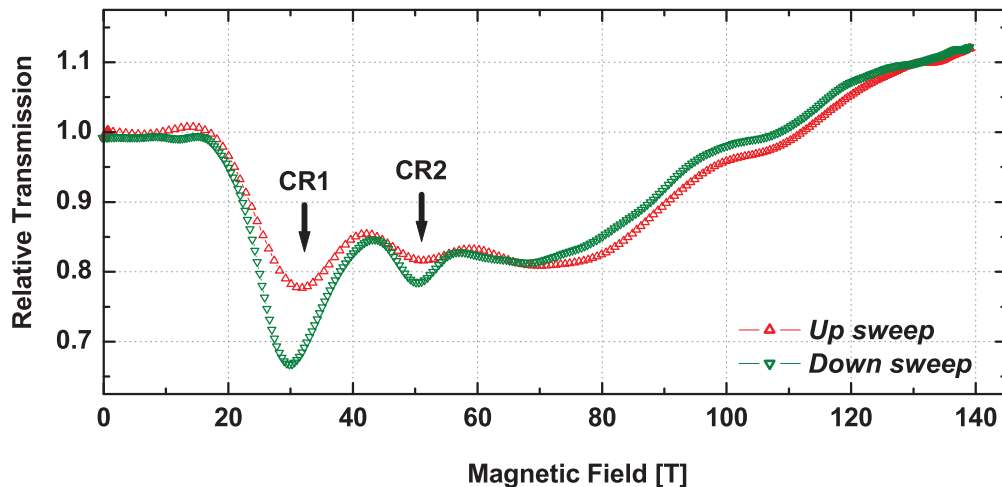


Figure 1.4: The relative transmission of infrared radiation of 117.2 meV through HgTe at room temperature in magnetic fields up to 140 T. The population changes for the spin split electron cyclotron resonance can clearly be observed [6, 7].

and  $f_2(t)$  for the two magnetic field dependent energy levels  $E_1(B(t))$  and  $E_2(B(t))$  can be characterized starting with the equilibrium distributions  $f_{oi/2}(t)$  of the Boltzmann type

$$f_{oi}(t) = \frac{e^{-E_i(B(t))/kT}}{e^{-E_1(B(t))/kT} + e^{-E_2(B(t))/kT}} \quad (1.1)$$

with  $i=1,2$ . The non-equilibrium distribution functions  $f_i(t)$  then obey the equation

$$\frac{df_i(t)}{dt} = -\frac{f_i(t) - f_{oi}(t)}{\tau} \quad (1.2)$$

assuming that the relaxation time  $\tau$  is equal for both levels.

Considering the time dependence of the magnetic field pulse and combining it with a  $\vec{k} \cdot \vec{p}$  calculation of the energy levels involved the non-equilibrium distribution functions have been simulated. The result is given in figure 1.3. A spin lattice relaxation time  $\tau = 1.2\mu s$  is in complete agreement with the experimental findings.

The actual physical mechanism responsible for this spin lattice relaxation has not been deduced [4,5]. For higher carrier concentration samples the effect was not observed. [12]

## 1.4 Quasi Bulk HgTe

Being similar to HgSe in most important electronic properties a study of HgTe was performed and compared with the results of HgSe [6,7]. The most important experimental finding is reproduced in figure 1.4. The sample was  $2\mu m$  MBE grown quasi bulk HgTe. A change in the absorption strength in up and down sweep could be detected, yet the increase in the absorption strength of the spin up resonance was not on cost of the magnitude of the spin down resonance, the total absorption intensity is not conserved

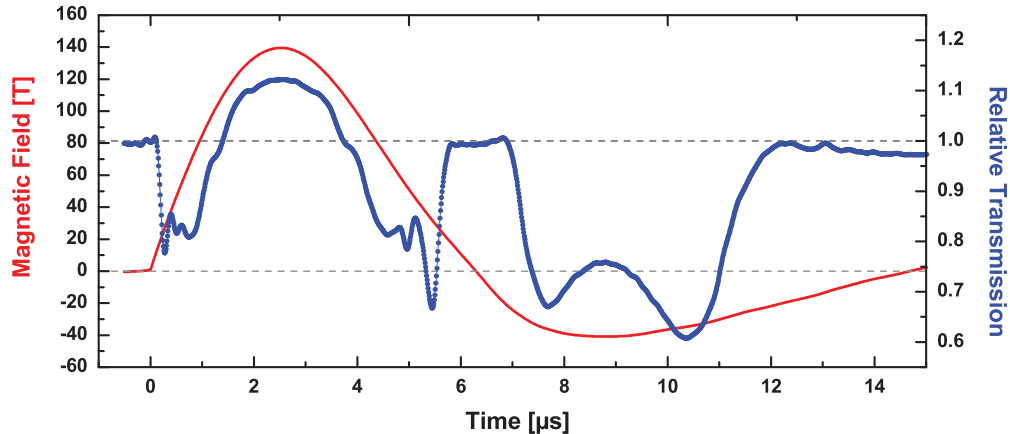


Figure 1.5: The relative transmission and magnetic field trace for HgTe at  $10.59 \mu\text{m}$  and room temperature. It is clearly seen that the resonance strength continues to increase after the first zero crossing. Moreover, the FWHM of the resonances are larger than  $100 \text{ ns}$  for all resonances.

during up and down sweep. Tentatively, this suggests two competing physical processes or a completely different one.

Moreover, a further increase in absorption strength was observed even after the zero crossing when the resonance field was met in opposite field direction as depicted in fig. 1.5. This could be observed for various temperatures in the range from 6 K to 300 K and was found to be sweep rate dependent [6, 7].

Temperature dependent studies have been carried out to deduce a set of high field parameters for the  $\mathbf{k} \cdot \mathbf{p}$  - model but the respective spectra have not contributed to further insights on relaxation phenomena [6, 7].

However, the data were insufficient for detailed analysis and conclusions regarding exact derivation of relaxation times and physical mechanisms.

## 1.5 Bulk InSb

At the beginning of this study, a new and very remarkable observation was made in the infrared transmission of bulk InSb samples. The experimental data have been reported at several occasions, e.g. [13]. An example optical trace is given in fig. 1.6.

There is a transmission drop at very low fields that can be observed only *after* zero crossings of the magnetic field while there is no feature at the respective position before the zero crossing. The magnitude of the drop is proportional to the absolute value of the field derivative. The authenticity of the spectra is given by the observation of the cyclotron resonance of electrons that is in excellent agreement with theory and literature.

The cyclotron resonance of InSb has been previously investigated in STC generated fields [14–16] as well as extensively in non-destructive pulsed magnets on a 100 ms time scale e.g. [17]. The phenomenon described here could not be observed in those publications because of the trigger noise [14], the generally poorer signal to noise ratio and

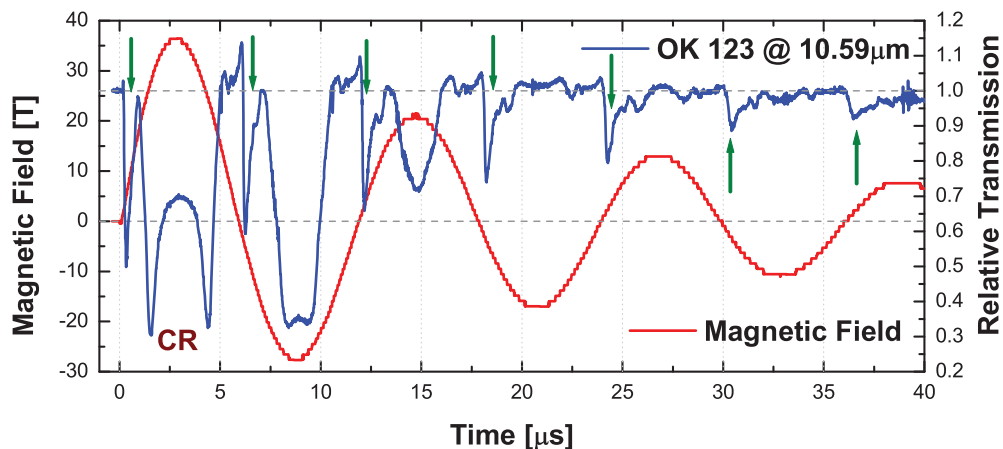


Figure 1.6: *Relative transmission of InSb, sample OK 123, at room temperature with  $\lambda = 10.59\mu\text{m}$ . The optical trace shows the electron cyclotron resonance marked CR and an additional feature after each zero crossing of the magnetic field marked by arrows. Further discussion in the text.*

slower sweep rate [15–17].

At this point it must be pointed out that for all three, InSb, HgTe and HgSe the FWHMs of all resonances are larger than 100 ns and the detector bandwidth of 60 MHz there were no contributions from the response function to the resonance strength.

## 1.6 Conclusions

Three types of hysteretic phenomena reported so far can be distinguished.

- **Type I:** (observed in InAs/AlSb SQWs and quasi bulk HgSe) A relaxation of charge carriers from one energetic level into another. That manifests itself in a characteristic spectrum. In a material showing two resonant features in the rising field trace we find the absorption intensity of one resonant feature increasing vs. the rising field trace at the expense of the other decreasing in the falling field trace while the overall integrated intensity is preserved. This process is reasonably well understood if the two resonances involved are the spin split cyclotron resonances.
- **Type II:** (observed in quasi bulk HgTe) An increase of absorption intensity in the falling field trace for resonant features without decreasing the intensity of any other resonant feature or the overall transmission. Type I and II hysteretic phenomena are modifications to well described resonant features and are explainable with variations of energy level population.
- **Type III:** (observed in bulk InSb) Additional transmission drops, possibly resonant structures, can be observed depending on the sweep rate of the magnetic field generation. These features do only occur in fields generated on a  $\mu\text{s}$ -timescale. These phenomena have no slow field or DC field analogon.

Whereas type I phenomena can be readily explained using the time dependence of the magnetic field only, the other two types cannot. A careful analysis of both, experimental equipment and theory, must be carried out with emphasis on the transient character of the magnetic field generation.

All types of hysteretic phenomena may occur as single effects or combined with each other. Types I and II are competing processes that cannot be observed on the same resonance line at the same time. That means type I phenomena may be obscured by type II.

Apart from the obvious time difference the most likely candidate for discrepancies between DC field data and transient field data are phenomena connected with the electric field or eddy currents that accompany the transient magnetic field generation. Eddy currents are known to cause a screening field, a temperature rise and mechanical forces. Those phenomena are usually estimated as a small perturbation to the DC field situation. The latter hypothesis cannot be held up, a quantitative analysis is required.

The present study is dedicated to hysteretic phenomena in transient magnetic fields. The goals are an unambiguous observation of and understanding the origin of the respective hysteresis. Therefore the following requirements must be met:

- Equipment related requirements
  - High enough signal to noise ratio as the effect of population changes can be rather small compared to the absorption in general as seen in fig. 1.2.
  - Signal fluctuations on a timescale comparable to the field pulse as well as to resonances must be avoided. This requires short term stability of the radiation source as well as a flat signal background.
  - Precise magnetic field determination.
  - Reproducible experimental conditions.
- Sample related requirements
  - For investigation of spin flip hysteresis the respective resonances must meet the general requirement for cyclotron resonance  $\omega_c \tau \gg 1$  as well as a separate detectability. The field positions of resonances must be more than half of the half width at full maximum apart.
  - Thus materials with high g-value are the most promising samples to observe spin related relaxation phenomena. This is a common feature of narrow gap semiconductors and zero gap semiconductors.
- Methodical requirements
  - All measurements of hysteresis effects require measurements with different sweep rates in addition to varying temperature and wavelength as routinely performed. If possible the time between the resonances should be varied by at least a factor of two if equipment supports it.
  - The resonance separation can be enhanced by increasing the energy or frequency of the radiation, thus decreasing the wavelength.
  - The effects of eddy currents must be deduced theoretically and measured if possible. Their influence on the transmission spectra must be estimated.

## Chapter 2

# Conductors in Transient Magnetic Fields

The interaction of electromagnetic waves as well as external magnetic fields with matter are described by MAXWELL's equations (2.1). They relate the magnetic field strength  $\vec{\mathbf{H}}$ , the magnetic flux density or magnetic induction  $\vec{\mathbf{B}}$ , the electric displacement  $\vec{\mathbf{D}}$  and the electric field strength  $\vec{\mathbf{E}}$  with the free current density  $\vec{\mathbf{j}}$  and the volume density of free electric charges  $\rho_e$ :

$$\begin{aligned}\vec{\nabla}_{\vec{\mathbf{r}}} \times \vec{\mathbf{E}} &= -\frac{\partial}{\partial t} \vec{\mathbf{B}} \\ \vec{\nabla}_{\vec{\mathbf{r}}} \cdot \vec{\mathbf{D}} &= \rho_e \\ \vec{\nabla}_{\vec{\mathbf{r}}} \times \vec{\mathbf{H}} &= \frac{\partial}{\partial t} \vec{\mathbf{D}} + \vec{\mathbf{j}} \\ \vec{\nabla}_{\vec{\mathbf{r}}} \cdot \vec{\mathbf{B}} &= 0.\end{aligned}\tag{2.1}$$

$\vec{\mathbf{j}}$  and  $\rho$  can be considered sources determining the electromagnetic fields  $\vec{\mathbf{H}}$ ,  $\vec{\mathbf{B}}$ ,  $\vec{\mathbf{E}}$  and  $\vec{\mathbf{D}}$ . They are related by the charge or current conservation equation

$$\vec{\nabla}_{\vec{\mathbf{r}}} \cdot \vec{\mathbf{j}} + \frac{\partial}{\partial t} \rho_e = 0.\tag{2.2}$$

These equations represent a system of linear differential equations of first order in space and time. For such a system a FOURIER basis of the form

$$\vec{\mathbf{A}}(\omega, \vec{\mathbf{k}}, \vec{\mathbf{r}}, t) = \vec{\mathbf{A}}(\omega, \vec{\mathbf{k}}) \mathbf{e}^{i(\vec{\mathbf{k}}\vec{\mathbf{r}} - \omega t)}\tag{2.3}$$

for all  $\omega$  and  $\vec{\mathbf{k}}$  form a complete set of basis functions. All future considerations can be limited to these components.

MAXWELL' equations (2.1) can be described in terms of monochromatic plane waves:

$$\begin{aligned}\vec{\mathbf{k}} \times \vec{\mathbf{E}}(\omega, \vec{\mathbf{k}}) &= -\omega \vec{\mathbf{B}}(\omega, \vec{\mathbf{k}}) \\ \vec{\mathbf{k}} \cdot \vec{\mathbf{D}}(\omega, \vec{\mathbf{k}}) &= \rho_e(\omega, \vec{\mathbf{k}}) \\ \vec{\mathbf{k}} \times \vec{\mathbf{H}}(\omega, \vec{\mathbf{k}}) &= \omega \vec{\mathbf{D}}(\omega, \vec{\mathbf{k}}) + \vec{\mathbf{j}}(\omega, \vec{\mathbf{k}}) \\ \vec{\mathbf{k}} \cdot \vec{\mathbf{B}}(\omega, \vec{\mathbf{k}}) &= 0.\end{aligned}\tag{2.4}$$



The constitutive equations (2.5 - 2.7) are required to a general solution. That is OHM's Law (2.5) and two material relations (2.6-2.7):

$$\vec{\mathbf{j}}(\omega, \vec{\mathbf{k}}) = \vec{\sigma}(\omega, \vec{\mathbf{k}})\vec{\mathbf{E}}(\omega, \vec{\mathbf{k}}) \quad (2.5)$$

$$\vec{\mathbf{B}}(\omega, \vec{\mathbf{k}}) = \vec{\mu}(\omega, \vec{\mathbf{k}})\vec{\mathbf{H}}(\omega, \vec{\mathbf{k}}) \quad (2.6)$$

$$\vec{\mathbf{D}}(\omega, \vec{\mathbf{k}}) = \vec{\varepsilon}(\omega, \vec{\mathbf{k}})\vec{\mathbf{E}}(\omega, \vec{\mathbf{k}}), \quad (2.7)$$

where the tensor functions  $\vec{\sigma}(\omega, \vec{\mathbf{k}})$ ,  $\vec{\mu}(\omega, \vec{\mathbf{k}})$  and  $\vec{\varepsilon}(\omega, \vec{\mathbf{k}})$  are general functions of  $\omega$  and  $\vec{\mathbf{k}}$ . We must emphasize that OHM's law (2.5) is only valid for constant temperature and the absolute value of the conductivity tensor, a proportionality factor  $\sigma = |\vec{\sigma}|$  between current density  $\vec{\mathbf{j}}$  and electric field  $\vec{\mathbf{E}}$  may itself be strongly dependent on the electric field magnitude,  $\sigma = \sigma(|\vec{\mathbf{E}}|)$ . In the following considerations we will deal with a linear approximation of OHM's Law as given in (2.5), that is a small absolute value of electric field unless stated otherwise.

In linear response approximation linearized material equations for the electromagnetic fields  $\vec{\mathbf{E}}$ ,  $\vec{\mathbf{D}}$ ,  $\vec{\mathbf{H}}$  and  $\vec{\mathbf{B}}$  follow:

$$\begin{aligned} \vec{\mathbf{D}}(\omega, \vec{\mathbf{k}}) = \varepsilon_0\vec{\mathbf{E}}(\omega, \vec{\mathbf{k}}) + \vec{\mathbf{P}}(\omega, \vec{\mathbf{k}}) &= \varepsilon_0\vec{\varepsilon}_r(\omega, \vec{\mathbf{k}})\vec{\mathbf{E}}(\omega, \vec{\mathbf{k}}) \\ \vec{\mathbf{B}}(\omega, \vec{\mathbf{k}}) = \mu_0 [\vec{\mathbf{H}}(\omega, \vec{\mathbf{k}}) + \vec{\mathbf{M}}(\omega, \vec{\mathbf{k}})] &= \mu_0\vec{\mu}_r(\omega, \vec{\mathbf{k}})\vec{\mathbf{H}}(\omega, \vec{\mathbf{k}}) \\ \vec{\mathbf{j}}(\omega, \vec{\mathbf{k}}) &= \vec{\sigma}(\omega, \vec{\mathbf{k}})\vec{\mathbf{E}}(\omega, \vec{\mathbf{k}}). \end{aligned} \quad (2.8)$$

$\vec{\mathbf{P}}$  and  $\vec{\mathbf{M}}$  are the material dependent polarization and magnetization fields, respectively. For non-magnetic materials we find  $\vec{\mu}_R(\omega, \vec{\mathbf{k}}) = \vec{\mathbf{1}}$ .

In the following sections we will discuss two components of an experiment, one, the interaction of infrared light with matter to deduce the resonance properties of a semi-conductor, two, the interaction of the transient magnetic field with the conductor. The two cases are substantially different in the magnitude of the relevant field strengths and, most importantly, their time scales of the interaction process.

## 2.1 Cyclotron Resonance

The interaction of light with the semi-conducting material can be deduced if we consider any material as a neutral composition of charge in vacuum  $\vec{\varepsilon}_R(\omega, \vec{\mathbf{k}}) = \vec{\mathbf{1}}$ . We obtain

$$\vec{\mathbf{k}} \times (\vec{\mathbf{k}} \times \vec{\mathbf{E}}(\omega, \vec{\mathbf{k}})) + \varepsilon_0\mu_0\omega^2\varepsilon_{lat}\vec{\mathbf{E}}(\omega, \vec{\mathbf{k}}) + \mathbf{i}\mu_0\omega\vec{\mathbf{j}}(\omega, \vec{\mathbf{k}}) = 0. \quad (2.9)$$

as an effective wave equation. Any dielectric response is characterized by the suitable contribution to the current  $\vec{\mathbf{j}}(\omega, \vec{\mathbf{k}})$  of the oscillating charges in the vacuum. Often it proves to be advantageous to split the response of the charge carriers into an explicit part under consideration and a remaining part defining an effective displacement current:

$$\vec{\mathbf{j}}(\omega, \vec{\mathbf{k}}) = \vec{\mathbf{j}}_{\text{global}}(\omega, \vec{\mathbf{k}}) + \vec{\mathbf{j}}_{\text{explicit}}(\omega, \vec{\mathbf{k}}) \quad (2.10)$$

so that

$$\begin{aligned} \vec{\varepsilon}(\omega, \vec{\mathbf{k}}) &= \mathbf{i}\frac{\sigma_{\text{global}}(\omega, \vec{\mathbf{k}})}{\varepsilon_0\omega} + \mathbf{i}\frac{\sigma_{\text{explicit}}(\omega, \vec{\mathbf{k}})}{\varepsilon_0\omega} \\ &= \varepsilon_{lat}(\omega, \vec{\mathbf{k}}) + \mathbf{i}\frac{\sigma_{\text{explicit}}(\omega, \vec{\mathbf{k}})}{\varepsilon_0\omega} \end{aligned} \quad (2.11)$$

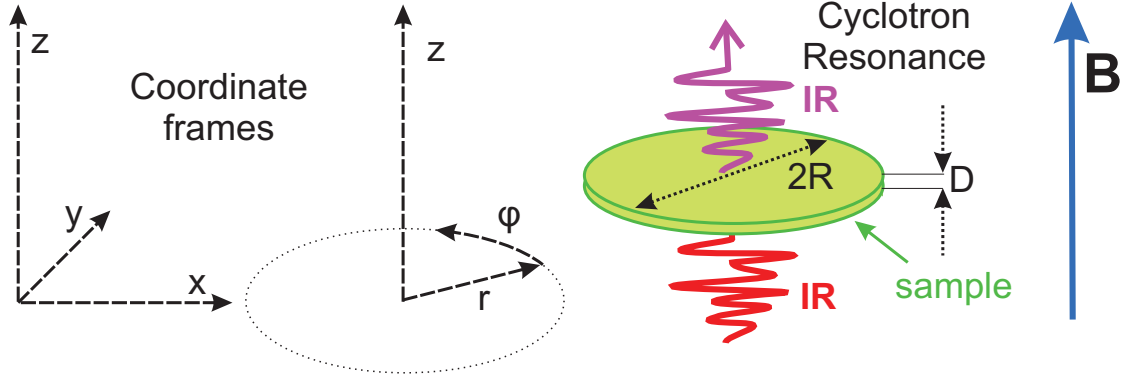


Figure 2.1: Schematic arrangement of coordinate frames (left) and sample (right) in reference to the external magnetic field  $\vec{\mathbf{B}}$ . This will be applied to all sections to follow, especially section 2.2.

Thus, an effective dielectric displacement  $\vec{\mathbf{D}}_{\text{total}}(\omega, \vec{\mathbf{k}})$  can be defined:

$$\vec{\mathbf{D}}_{\text{total}}(\omega, \vec{\mathbf{k}}) = \vec{\mathbf{D}}_{\text{effective}}(\omega, \vec{\mathbf{k}}) + \mathbf{i} \frac{\vec{\mathbf{j}}_{\text{explicit}}(\omega, \vec{\mathbf{k}})}{\omega} = \varepsilon_0 \vec{\varepsilon}_r(\omega, \vec{\mathbf{k}}) \vec{\mathbf{E}}(\omega, \vec{\mathbf{k}}). \quad (2.12)$$

Conceptual that means, that part of the dielectric response of the charge carriers in the material has been combined with the response of the vacuum thus defining an effective background medium.

With (2.11) and (2.9) we yield a set of linear homogeneous equations for the components  $E_x$ ,  $E_y$  and  $E_z$  of the electric field vector  $\vec{\mathbf{E}}(\omega, \vec{\mathbf{k}})$  for a Cartesian coordinate system:

$$\begin{pmatrix} -k_y^2 - k_z^2 + k_0^2 \varepsilon_{xx} & k_x k_y + k_0^2 \varepsilon_{xy} & k_x k_z + k_0^2 \varepsilon_{xz} \\ k_x k_y + k_0^2 \varepsilon_{yx} & -k_x^2 - k_z^2 + k_0^2 \varepsilon_{yy} & k_y k_x + k_0^2 \varepsilon_{yz} \\ k_x k_z + k_0^2 \varepsilon_{zx} & k_y k_x + k_0^2 \varepsilon_{zy} & -k_x^2 - k_y^2 + k_0^2 \varepsilon_{zz} \end{pmatrix} \begin{pmatrix} E_x \\ E_y \\ E_z \end{pmatrix} = 0, \quad (2.13)$$

with  $k_0 = \frac{\omega}{c}$  as the vacuum wave vector and all components  $\varepsilon_{ij}$  and  $E_i$  being functions of  $(\omega, \vec{\mathbf{k}})$  for  $i, j = x, y, z$ .

For a medium with rotational symmetry with respect to the magnetic field  $\vec{\mathbf{B}} = B_0 \vec{\mathbf{e}}_z$  in FARADAY-geometry,  $\vec{\mathbf{k}} \parallel \vec{\mathbf{B}} \parallel \vec{\mathbf{e}}_z$ , the dielectric tensor acquires the extended gyrotropic form for a gyrotropic medium ( $\varepsilon_{xx} = \varepsilon_{yy} \neq \varepsilon_{zz}$ ):

$$\varepsilon_{gyro} = \begin{pmatrix} \varepsilon_{xx}(\omega, \vec{\mathbf{k}}) & \varepsilon_{xy}(\omega, \vec{\mathbf{k}}) & 0 \\ -\varepsilon_{xy}(\omega, \vec{\mathbf{k}}) & \varepsilon_{yy}(\omega, \vec{\mathbf{k}}) & 0 \\ 0 & 0 & \varepsilon_{zz}(\omega, \vec{\mathbf{k}}) \end{pmatrix}. \quad (2.14)$$

A schematic drawing of the coordinate frames and geometry of the cyclotron resonance measurements with respect to the external magnetic field is given in fig. 2.1.

Solving (2.13) requires the evaluation of the secular equation to deduce EIGENvalues and EIGENvectors. For a cubic crystal in FARADAY configuration we obtain in a local approximation  $\vec{\varepsilon}(\omega, \vec{\mathbf{k}}) = \vec{\varepsilon}(\omega, \vec{\mathbf{k}} = 0)$  a biquadratic polynomial with solutions:

$$\begin{aligned}\vec{\mathbf{k}}_{\pm} &= \vec{\mathbf{k}}_0 \sqrt{\varepsilon_{xx} \pm i\varepsilon_{xy}} \\ \vec{\mathbf{E}}_{\pm}(\omega, \vec{\mathbf{k}}) &= \frac{E_0}{\sqrt{2}} (\vec{\mathbf{e}}_x \pm i\vec{\mathbf{e}}_y) e^{i(k_{\pm}z - \omega t)}.\end{aligned}\quad (2.15)$$

The EIGENvectors are left and right circularly polarized normal modes, whose unperturbed propagation is preferred under the given conditions. They are referred to as *cyclotron resonance active* and *cyclotron resonance inactive* modes.

From the scalar complex propagation constants (2.16) the complex index of refraction and the optical constants can be written:

$$k_{\pm} = k_0 N_{\pm} = k_0(n_{\pm} + i\kappa_{\pm}) = \alpha_{\pm} + i\beta_{\pm}, \quad (2.16)$$

Here  $\alpha$  determines the effective wavelength in the medium via  $\alpha = \frac{2\pi}{\lambda}$  and the phase velocity  $v_{\text{phase}} = \omega/\alpha$ ;  $\beta$  the attenuation of intensity of the radiation by the medium and is therefore called the attenuation length or skin depth  $\delta = \frac{1}{\beta}$  [18].

In real experiments the requirement of a free infinite medium can not be met, however, the aforementioned considerations do apply to uniform media individually. The effects of finite size and boundaries must be taken into account. For adjacent regions of different media, the integral formulation of MAXWELL's equations yields continuous transitions for the normal components of  $\vec{\mathbf{D}}$  and  $\vec{\mathbf{B}}$  and accordingly for tangential components of  $\vec{\mathbf{E}}$  and  $\vec{\mathbf{H}}$  at the boundary. With  $\vec{\mathbf{e}}_n$  as the normal vector on the boundary surface we obtain:

$$\begin{aligned}\vec{\mathbf{D}}_1 \vec{\mathbf{e}}_n &= \vec{\mathbf{D}}_2 \vec{\mathbf{e}}_n \\ \vec{\mathbf{B}}_1 \vec{\mathbf{e}}_n &= \vec{\mathbf{B}}_2 \vec{\mathbf{e}}_n \\ \vec{\mathbf{E}}_1 \times \vec{\mathbf{e}}_n &= \vec{\mathbf{E}}_2 \times \vec{\mathbf{e}}_n \\ \vec{\mathbf{H}}_1 \times \vec{\mathbf{e}}_n &= \vec{\mathbf{H}}_2 \times \vec{\mathbf{e}}_n.\end{aligned}\quad (2.17)$$

From these conditions reflection and transmission coefficients can be deduced.

Since the LORENTZ force scales with  $\frac{v}{c}$  compared to the electrical force we can neglect the magnetic field component of radiation. Therefore the magnetic field will be considered as an external magnetic field  $\vec{\mathbf{B}}_0$  solely. An electron in a harmonic electromagnetic field  $\vec{\mathbf{E}}(t)$  and a homogeneous magnetic field  $\vec{\mathbf{B}}_0$  follows the classical equation of motion:

$$m^* \frac{d}{dt} \vec{\mathbf{v}} + \frac{m^*}{\tau} \vec{\mathbf{v}} = -e(\vec{\mathbf{v}} \times \vec{\mathbf{B}}_0 + \vec{\mathbf{E}}_0 e^{i(k \cdot r - \omega t)}). \quad (2.18)$$

$m^*$  is the effective mass,  $\vec{\mathbf{v}}$  the carrier velocity,  $e$  the elementary charge and  $\tau$  the relaxation time. The resulting dielectric displacement is defined by local effects, spatial variations of  $\vec{\mathbf{E}}$  are neglected. The Ansatz  $\vec{\mathbf{v}} = \vec{\mathbf{v}}_0 e^{-i\omega t}$  solves (2.18):

$$\left(\frac{1}{\tau} - i\omega\right) \vec{\mathbf{v}}_0 = \frac{e}{m} (\vec{\mathbf{v}}_0 \times \vec{\mathbf{B}}_0 + \vec{\mathbf{E}}_0), \quad (2.19)$$

The current density is described by  $\vec{\mathbf{j}} = -ne\vec{\mathbf{v}} = \sigma\vec{\mathbf{E}}$ . With  $\vec{\mathbf{B}}_0 \parallel \vec{\mathbf{e}}_z$  the magnetoconductivity tensor is given as:

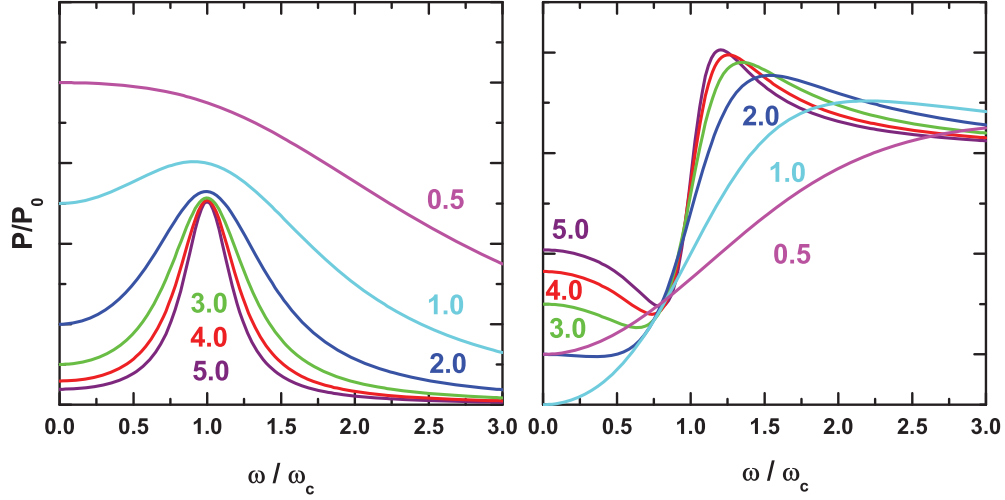


Figure 2.2: Left: Imaginary part of complex refractive index equivalent to absorption line shapes for  $\omega\tau = 0.5, 1.0, 2.0, 3.0, 4.0$  and  $5.0$ . Right: The corresponding real part of complex refractive index.

$$\sigma = \begin{pmatrix} \sigma_{xx} & \sigma_{xy} & 0 \\ -\sigma_{yx} & \sigma_{yy} & 0 \\ 0 & 0 & \sigma_{zz} \end{pmatrix} = \varepsilon_{lat}\varepsilon_0\omega_p^2 \begin{pmatrix} \frac{\mathbf{i}\omega\tau}{\omega^2 - \omega_c^2} & \frac{\omega_c}{\omega^2 - \omega_c^2} & 0 \\ \frac{-\omega_c}{\omega^2 - \omega_c^2} & \frac{\mathbf{i}\omega\tau}{\omega^2 - \omega_c^2} & 0 \\ 0 & 0 & \frac{\mathbf{i}}{\omega\tau} \end{pmatrix}, \quad (2.20)$$

with the plasma frequency  $\omega_p^2 = \frac{ne^2}{m\varepsilon_0\varepsilon_{lat}}$ , the cyclotron frequency  $\omega_c = \frac{eB_0}{m}$  and  $\omega\tau = \omega + \frac{\mathbf{i}}{\tau}$ . In the DC case  $\omega = 0$  non-diagonal terms describe the classical HALL effect, in the dynamic case the FARADAY rotation. Further analysis of absorption processes can be performed with the use of the normal modes  $\sigma_{\pm}$ :

$$\sigma_{\pm} = \sigma_{xx} \pm \mathbf{i}\sigma_{xy} = \varepsilon_{lat}\varepsilon_0\omega_p^2 \frac{1}{\gamma - \mathbf{i}(\omega \mp \omega_c)} \quad (2.21)$$

The power absorbed per unit volume for linear polarization is given by [19]

$$\begin{aligned} P &= \frac{1}{2}\Re(J_x E_x) = P_+ + P_- = \frac{1}{2} \frac{ne^2\tau}{m^*} E_x^2 \Re \left[ \frac{1 - \mathbf{i}\omega\tau}{(1 - \mathbf{i}\omega\tau)^2 + \omega_c^2\tau^2} \right] \\ &= \frac{1}{4}\sigma_0 E_x^2 \left[ \frac{1}{(\omega - \omega_c)^2\tau^2 + 1} + \frac{1}{(\omega + \omega_c)^2\tau^2 + 1} \right] \end{aligned} \quad (2.22)$$

with  $\sigma_0 = ne^2\tau/m^*$ , the DC conductivity of a semiconductor with carrier concentration  $n$ . The line shapes for various parameters  $\omega_c\tau$  are given in figure 2.2. The resonance is clearly observed for  $\omega_c\tau \gg 1$ . The line width of the cyclotron resonance is related to the scattering lifetime and the integrated absorption intensity of a CR line is related to the density of carriers participating in CR. [20]. If the observed line shape is well fitted by a LORENTZian, the absorption and reflection are small we can compare it to

$$\frac{T(\omega, B)}{T(\omega, 0)} = 1 - A(\omega, B) = 1 - \frac{1}{2} \frac{Dne^2\tau}{c\epsilon_0\epsilon_{\text{lat}}^{1/2}m^*} \frac{1}{(\omega - \omega_c)^2\tau^2 + 1} \quad (2.23)$$

when  $D$  is the sample thickness and  $c$  the speed of light. This represents a resonance Full Width at Half Maximum (FWHM) of  $2/\tau$ .

### 2.1.1 Quantum Mechanics

Quantum-mechanically the macroscopic observable, the current density  $\vec{\mathbf{j}}$  and the corresponding perturbation, the electric field  $\vec{\mathbf{E}}$ , are given by

$$\langle \vec{\mathbf{j}} \rangle = Tr\{\vec{\mathbf{j}}\rho(\mathcal{H}, \vec{\mathbf{E}})\} \quad (2.24)$$

where  $\rho$  is the density operator of the system perturbed by the electric field  $\vec{\mathbf{E}}$  and  $\mathcal{H}$  is the unperturbed HAMILTONIAN of the system.  $Tr$  denotes the many particle trace.

The density operator formalism and OHM's law (2.5) are linked via KUBO's formula in *linear response theory* [21] by:

$$\sigma_{\mu\nu}(\omega) = \frac{1}{V} \int_0^\infty dt e^{-\mathbf{i}\omega t} \int_0^{1/kT} d\lambda \langle j_\nu(-\mathbf{i}\hbar\lambda)j_\mu(t) \rangle_0. \quad (2.25)$$

here  $V$  denotes the normalized volume of the crystal,  $kT$  the thermal energy at temperature  $T$ ,  $j_\nu(t)$  the  $\nu$ th component of the current density operator at a time  $t$  in the HEISENBERG picture and  $\langle j_\nu(-\mathbf{i}\hbar\lambda)j_\mu(t) \rangle_0$  the thermodynamical expectation value of the unperturbed system.

And we find

$$\sigma_{\mu\nu}(\omega) = F_{\mu\nu} + \frac{\mathbf{i}}{\pi} \int_{-\infty}^\infty d\omega' \frac{F_{\mu\nu}(\omega')}{\omega' - \omega} \quad (2.26)$$

$$F_{\mu\nu}(\omega) = \frac{\pi\hbar}{V} \int_{-\infty}^\infty dE \frac{f(E) - f(E + \hbar\omega)}{\hbar\omega} tr(\delta(E - \mathcal{H} - \mathcal{U})j_\nu\delta(E - \mathcal{H} - \mathcal{U} + \hbar\omega)j_\mu) \quad (2.27)$$

The KRAMERS KRONIG relation (2.26) derives the real and imaginary parts of the complex conductivity from a single function, the response function  $F_{\mu\nu}$  and refers to general mathematical properties and does not contain physical information, but causality.  $tr$  is the single particle trace and  $f$  the FERMI - DIRAC distribution function,  $\mathcal{U}$  is the scattering potential. The response function  $F_{\mu\nu}$  as given in (2.27) relates the conductivity to transitions between single particles of a microscopic system.

Equation (2.27) contains physical information on

- The spectral densities of initial and final states separated by the applied excitation energy  $\hbar\omega$  which represents energy conservation with the density of states defined as  $D(E) = Tr\{\delta(E - \mathcal{H})\}$ .
- The relative occupation of initial and final states characterized by the appropriate FERMI functions  $f(E)$  and  $f(E + \hbar\omega)$
- The transition amplitudes  $j_\nu$  and  $j_\mu$  specifying the quantum mechanical coupling

However, two quantities are left to be determined, the unperturbed HAMILTONIAN  $\mathcal{H}$ , implicitly defining  $j_\nu = -e \frac{\partial}{\partial t} x_\nu = -\frac{ie}{\hbar} [\mathcal{H}, x_\nu]$ , and the scattering potential  $\mathcal{U}$ .

The matrix elements of the  $\delta$ -distribution can be decomposed into a part that is diagonal with respect to the EIGENfunctions of  $\mathcal{H}$  and a non-diagonal part. According to damping theory [22–24] the diagonal part can be replaced by an appropriate spectral function  $\mathcal{S}(E)$  in lowest order approximation described by a LORENTZIAN function:

$$\{\delta(\mathcal{H} + \mathcal{U} - E)\}_{dg} = \mathcal{S}(E) = \frac{\Gamma/\pi}{(\mathcal{H} + \Delta - E)^2 + \Gamma^2} \quad (2.28)$$

The non diagonal terms depend explicitly on scattering matrix elements with mostly negligible influence on cyclotron resonance. Thus  $\Delta$  and  $\Gamma$  are determined as a function of the impurity potential  $\mathcal{U}$ . The level broadening  $\Gamma$  of the LORENTZIAN is roughly proportional to the density of states  $\Gamma(E) \sim D(E)$  whereas the displacement  $\Delta$  represents the repulsion by quantum parts from other parts of the density of states:

$$\Delta(E) \sim \int_{-\infty}^{\infty} dE' \frac{D(E')}{E - E'} \quad (2.29)$$

However, a more general consideration [21,22] derives  $\Gamma$  and  $\Delta$  from effects related to multi-scattering processes described by the complex self energy  $\Sigma_n(E) = \Delta_n(E) + i\Gamma_n(E)$ . In the present study, the LORENTZIAN line shape is sufficient for approximation.

Magneto-optical transitions between oscillator EIGENstates  $|\Psi\rangle$  caused by an external perturbation  $\mathcal{H}_{pert} = \mathcal{H}_\omega e^{i\omega t}$  are given by the matrix elements of the one electron current operator  $\vec{j}_\nu = -e\vec{v}_\nu = -\frac{e}{m}\vec{\pi}_\nu$ , producing selection rules. Introducing creation and annihilation operators for the momentum operator  $\vec{\pi}$  in LANDAU gauge we obtain:

$$\pi_x = -i\sqrt{\frac{\hbar e B_o}{2}} (a - a^\dagger); \quad \pi_y = -i\sqrt{\frac{\hbar e B_o}{2}} (a + a^\dagger); \quad \pi_z = \hbar k_z \quad (2.30)$$

Combinations of initial and final states need to be evaluated to derive possible transitions. With the harmonic oscillator EIGENfunctions  $\phi_N$  the following relations hold true:

$$a\phi_N = \sqrt{N}\phi_{N-1}; \quad a^\dagger\phi_N = \sqrt{N+1}\phi_{N+1}; \quad a^\dagger a\phi_N = N\phi_N \quad (2.31)$$

Still the HAMILTONIAN and thus the energy levels remain to be calculated with methods of energy band structure calculation [25,26].

## 2.2 Eddy Currents

According to MAXWELL's equations (2.1) a transient magnetic field with high derivative vs. time causes a much higher electric field and consequently a much high current density than a DC or slowly varying field. Currents induced in a conductor by an external magnetic field are referred to as eddy currents.

Eddy current effects are magnetic diffusion processes that can easily be determined for two cases, a purely axial field penetration into the sample and a purely radial penetration. The purely axial penetration is given for a thin disc with thickness  $D$  much smaller than the sample radius  $R$  much smaller than the penetration depth  $\delta$  of the magnetic field. In this case the magnetic field can be assumed to be constant over the sample volume and be calculated straightforwardly. This case will be discussed in the first part of this section with examples to estimate the order of magnitude of the effects.

A purely radial field penetration is given for a cylindrical rod with infinite length along the axis parallel to the magnetic field axis. This assumption ignores edge effects and variations of the external magnetic field magnitude along the axis. We will deal with this problem in the sections that follow the first.

However, neither case will be realized in actual experimental setup due to the idealized character therefore all calculations must be considered qualitative.

### 2.2.1 Eddy Currents in a Circular Thin Disc

For a magnetic field  $\vec{\mathbf{B}}$  applied normal to a sample area  $\vec{\mathbf{f}}$  with contour  $\vec{\mathbf{s}}$  we find the induced electric field  $\vec{\mathbf{E}}$  using

$$\oint \vec{\mathbf{E}} d\vec{\mathbf{s}} = - \int \frac{\partial}{\partial t} \vec{\mathbf{B}} d\vec{\mathbf{f}} \quad . \quad (2.32)$$

If the external magnetic field is applied perpendicular to the surface of the sample  $B_{\text{ext}} = (0, 0, (B_{\text{ext}})_z)$  we find in cylindrical coordinates  $(r, \varphi, z)$ :

$$\oint (E_\varphi r d\varphi) = 2\pi r E_\varphi(r) = -\pi r^2 \frac{\partial}{\partial t} (B_{\text{ext}})_z \quad , \quad (2.33)$$

if the magnetic field is uniform over the area  $\vec{\mathbf{f}}$  under discussion. Therefore

$$\vec{\mathbf{E}} = E_\varphi(r) \vec{\mathbf{e}}_\varphi \quad , \quad E_\varphi(r) = -\frac{r}{2} \frac{\partial}{\partial t} (B_{\text{ext}})_z \quad . \quad (2.34)$$

The magnetic field derivative induces primarily an azimuthal electric field. Its magnitude can be estimated for an example field with a maximum sweep rate of 0.1T/ns and a sample radius of 1 mm we obtain an azimuthal electric field of 50 kV/m, that is 500 V/cm. This value depends only on geometry of the sample and the sweep rate, but is independent of material under investigation, it has the same magnitude and orientation for metallic, insulating or semi-conducting samples. An illustration of the time dependence is given in fig. 2.3 for a transient magnetic field normal to the sample surface with initial field slope of  $\approx 70 T/\mu s$ . For a sinusoidal magnetic field the azimuthal electric field acquires a cosine behavior, that is it is extremal at the zero crossings of the magnetic field and zero at the magnetic field extrema. The geometrical dependence is shown in fig. 2.12.

At the given electric field magnitude the linear relationship  $\vec{\mathbf{j}} = \vec{\sigma} \vec{\mathbf{E}}$  is no longer valid. The conductivity tensor is dependent on the absolute electric field value and the current

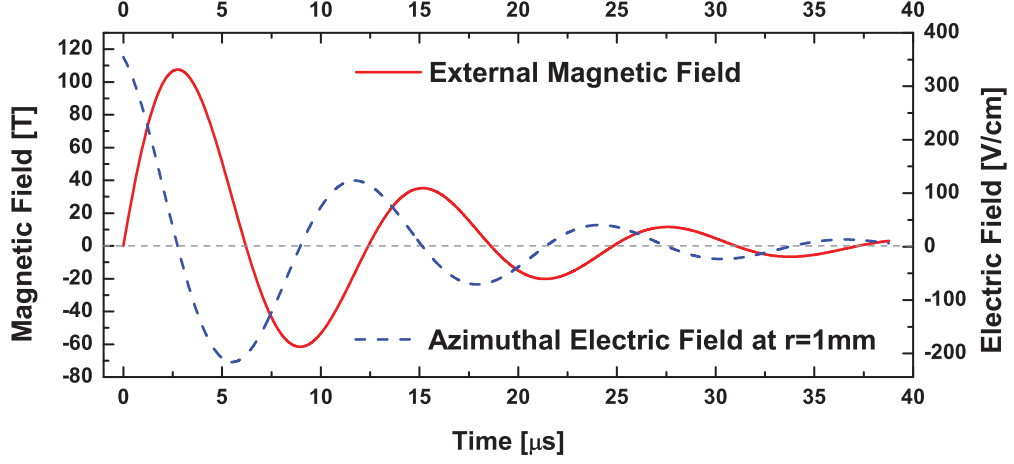


Figure 2.3: The azimuthal electric field (dashed, right scale) for a damped sinusoidal magnetic field (solid, left scale) at  $r = 1 \text{ mm}$  with an oscillation period of  $t = 12 \mu\text{s}$ .

density dependence on magnetic field must be determined using an expansion in terms of  $|\vec{\mathbf{E}}|$ . We will continue the derivation of processes involving eddy currents with a linear approximation, treating the conductivity tensor additionally as a function of electric field  $\vec{\sigma} = \vec{\sigma}(\vec{\mathbf{E}})$ .

In linear approximation we find the conductivity dependent on frequency  $\omega$  and wave vector  $\vec{\mathbf{k}}$  and the current density is given as:

$$\vec{\mathbf{j}}(\omega, \vec{\mathbf{k}}) = \vec{\sigma}(\omega, \vec{\mathbf{k}})\vec{\mathbf{E}}(\omega, \vec{\mathbf{k}}) \quad (2.35)$$

To obtain space and time dependent quantities we use the FOURIER theorem and obtain e.g.

$$\vec{\mathbf{E}}(\vec{\mathbf{r}}, t) = \int \int \vec{\mathbf{E}}(\omega, \vec{\mathbf{k}}) e^{i(\vec{\mathbf{k}}\vec{\mathbf{r}} - \omega t)} d\omega d^3\vec{\mathbf{k}}. \quad (2.36)$$

We are discussing a magnetic field with angular frequency  $\omega \ll \omega_c$  for and wave vectors  $|\vec{\mathbf{k}}| \ll \lambda = \hbar^2/eB$ . That is with a wavelength that is large in comparison to the magnetic length  $\lambda$ . Thus we have  $\omega \approx 0$ ,  $|\vec{\mathbf{k}}| \approx 0$  and find the current density  $\vec{\mathbf{j}}^1$  using OHM's law with the conductivity tensor for cylindrical coordinates  $(\vec{\mathbf{e}}_r, \vec{\mathbf{e}}_\varphi, \vec{\mathbf{e}}_z)$  in the extended gyrotropic form for free carriers

$$\begin{aligned} \vec{\mathbf{j}} = \vec{\sigma} \vec{\mathbf{E}} &= \frac{\sigma_0}{1+(\omega_c\tau)^2} \begin{pmatrix} 1 & \omega_c\tau & 0 \\ -\omega_c\tau & 1 & 0 \\ 0 & 0 & 1+(\omega_c\tau)^2 \end{pmatrix} \begin{pmatrix} E_r \\ E_\varphi \\ E_z \end{pmatrix} \\ &= \frac{\sigma_0}{1+(\omega_c\tau)^2} [\omega_c\tau E_\varphi \vec{\mathbf{e}}_r + E_\varphi \vec{\mathbf{e}}_\varphi] \end{aligned} \quad (2.37)$$

Here  $\tau$  is the momentum relaxation time,  $\omega_c = eB/m^*$  is the cyclotron frequency for any given magnetic field magnitude  $B$  and effective mass of carriers  $m^*$  with elementary charge  $e$ ,  $\sigma_0 = ne^2\tau/m^*$  where  $n$  is the free carrier concentration.

<sup>1</sup>in the literature we find the 3D current density  $\vec{\mathbf{j}}$  treated as a surface current density  $\vec{\mathbf{i}}$  with  $\vec{\mathbf{i}} = D\vec{\mathbf{j}}$  reducing the problem to two dimensions [27]



The conductivity may be dependent on the external magnetic field magnitude  $B$  as  $\sigma_0 = \sigma_0(B) = n(B) e \mu(B) = n(B) e^2 \tau(B) / m^*$ . Experiments show that the conductivity  $\sigma_0$  depends on  $B$ , the carrier concentration  $n$  does not, therefore the mobility  $\mu = \mu(B) = e \tau(B) / m^*$  is a function of magnetic field magnitude. We obtain a magnetic field dependent relaxation time  $\tau(B)$ . Additionally we must keep in mind  $\sigma_0 = \sigma_0(\vec{E})$ .

The boundary condition of zero current in radial direction,  $\vec{j}_r = 0$ , is given by the finite extension of the sample in radial direction to  $r=R$ . Therefore a HALL-Voltage is induced that compensates the current in radial direction described by equation (2.37). This effect is completely analogous to the CORBINO-disc geometry of HALL measurements [28].

We find the electric field  $\vec{E}$  given by the induction equation to yield:

$$\vec{j} = \vec{\sigma} \vec{E} = \frac{\sigma_0}{1 + (\omega_c \tau)^2} [(E_r - \omega_c \tau E_\varphi) \vec{e}_r + (\omega_c \tau E_r + E_\varphi) \vec{e}_\varphi]. \quad (2.38)$$

From  $\vec{j}_r = j_z = 0$  it follows for the steady state solution

$$\vec{j} = j_r \vec{e}_r + j_\varphi \vec{e}_\varphi + j_z \vec{e}_z = j_\varphi \vec{e}_\varphi \quad , \quad (2.39)$$

therefore

$$E_r = \omega_c \tau E_\varphi \quad \longrightarrow \quad j_\varphi \vec{e}_\varphi = \frac{\sigma_0}{1 + (\omega_c \tau)^2} [(\omega_c \tau)^2 + 1] E_\varphi \vec{e}_\varphi = \sigma_0 E_\varphi \vec{e}_\varphi \quad . \quad (2.40)$$

That means that the current density is purely azimuthal and does not experience the magneto-conductivity. The radial electric field, however, that is given by

$$E_r(r) = (\omega_c \tau) E_\varphi(r) = \mu (B_{\text{ext}})_z E_\varphi(r) = \mu (B_{\text{ext}})_z \frac{r}{2} \frac{\partial}{\partial t} (B_{\text{ext}})_z \quad (2.41)$$

is a quantity that scales to the primarily azimuthal electric field  $E_\varphi$  with the sample mobility  $\mu$  and the external magnetic field  $(B_{\text{ext}})_z$ . Thus the radial electric field depends on both the magnetic field and its derivative whereas the azimuthal electric field as well as the current density depend *only* on the field derivative. An illustration is given in fig.2.4 for very low mobilities to demonstrate the qualitative time dependence. For higher mobilities the corresponding curves are amplified by the mobility factor. The geometrical orientation is given in fig. 2.12.

For a sinusoidal field  $B_z = B_0 \sin \omega t$  we obtain:

$$E_r = \frac{\mu r}{2} B_0^2 \omega \sin \omega t \cos \omega t = \frac{\mu \omega r}{4} B_0^2 \sin(2\omega t) \quad . \quad (2.42)$$

That means, the radial electric field oscillates with the double frequency of the external magnetic field and has extrema at  $t = (n + 1/2)\pi/2\omega$  with  $n=0, 1, 2, \dots$

For an angular frequency of  $\omega = 2\pi/12.5\mu s \approx 0.5/\mu s$  the first maximum of the radial electric field occurs at  $t \approx 1\mu s$ . With  $r=1$  mm it has the magnitude

$$E_r \approx \mu \frac{0.5/\mu s \cdot 10^{-3} m \cdot B_0^2}{4} = 125 \cdot B_0^2 \cdot \mu \quad [V/m] \quad , \quad (2.43)$$

if the mobility  $\mu$  is given in  $m^2/Vs$  and  $B_0$  in T. As we are dealing with damped sinusoidal magnetic fields, the real values will be slightly smaller, but of same order of magnitude. However, we find that for mobilities of order  $1 m^2/Vs$  and magnetic fields with maximum of 100 T the radial electric field is of order 10 kV/cm.

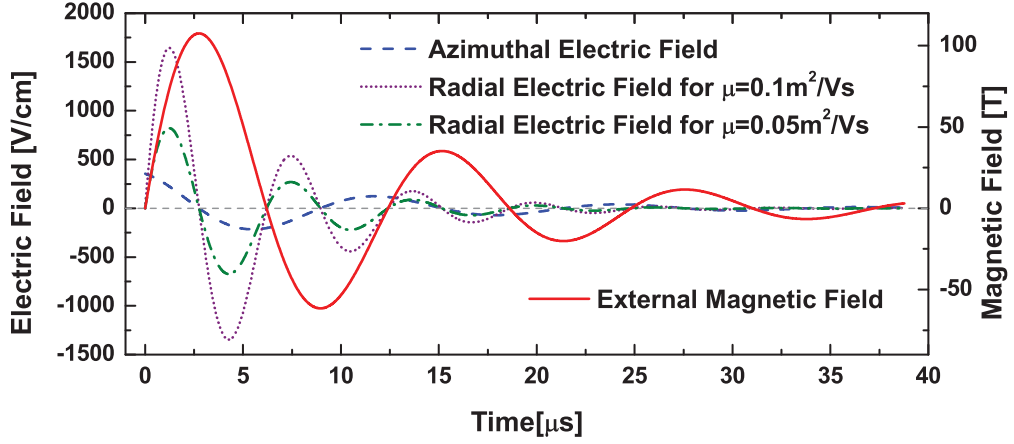


Figure 2.4: The azimuthal electric field (dashes) of the experimental situation of fig. 2.3 and the corresponding radial electric fields for mobilities  $\mu = 1000 \text{ cm}^2/\text{Vs}$  (dots) and  $\mu = 500 \text{ cm}^2/\text{Vs}$  (dash-dot). All have been calculated at  $r = 1 \text{ mm}$  and the original magnetic field (solid line, right scale).

Mobilities in excess of  $1 \text{ m}^2/\text{Vs}$  are easily encountered in present day semi-conductor materials. Therefore high electric field phenomena such as impact ionization and avalanche breakthroughs that lead to the generation of non-equilibrium charge carriers must be considered as will be done later.

The current density  $\vec{j}(\omega = 0, \vec{k} = 0)$  was found to be

$$\vec{j}(\omega = 0, \vec{k} = 0) = \sigma_0(B) E_\varphi(\omega = 0, \vec{k} = 0) \vec{e}_\varphi = \frac{\sigma_0(B) r}{2} \frac{\partial}{\partial t} (B_{\text{ext}})_z \vec{e}_\varphi \quad . \quad (2.44)$$

At  $r=1 \text{ mm}$  we obtain a current density of

$$\vec{j}(\omega = 0, \vec{k} = 0) = 5 \cdot \sigma_0(B) \cdot \frac{\partial}{\partial t} (B_{\text{ext}})_z \quad [\text{A}/\text{cm}^2] \quad (2.45)$$

for a field slope given in  $T/\mu\text{s}$  and  $\sigma_0(B)$  in  $\Omega^{-1}\text{cm}^{-1}$ . For e.g. an initial field slope of  $100T/\mu\text{s}$  and a conductivity of  $\sigma_0(B=0) = 2000\Omega^{-1}\text{cm}^{-1}$  we find a current density of  $10^6 \text{ A}/\text{cm}^2$ .

The eddy current density will itself induce a magnetic field into the conductive system. The sample location in the field axis favors  $\vec{r}_{\text{ref}} = (r = 0, r_\varphi = 0, z = 0)$  as the reference point for a calculation using the law of BIOT-SAVART. Assuming any current distribution in  $z$ -direction to be negligible, the correction term can be calculated by

$$\begin{aligned} \vec{B}_c = \mu_0 \vec{H}_c &= \frac{\mu_0}{4\pi} \int_V \frac{\vec{j} \times \vec{r}}{r^3} dV \\ &= \frac{\mu_0}{4\pi} \int_0^R r dr \int_0^{2\pi} d\varphi \int_0^D dz \left[ -\frac{\sigma_0(B)}{2} r \frac{d}{dt} B_{\text{out}} \right] \vec{e}_\varphi \times \frac{\vec{r}}{r^3} \end{aligned}$$

$$= -\sigma_0(B)\mu_0\frac{DR}{4}\frac{d}{dt}\mathbf{B}_{\text{ext}}\vec{e}_z. \quad D \ll R \ll \delta \quad (2.46)$$

Here  $D$  denotes the thickness of the conductive layer and  $R$  the sample radius. The effective magnetic field  $\vec{\mathbf{B}}_{\text{eff}}$  is thus given by

$$\vec{\mathbf{B}}_{\text{eff}} = \vec{\mathbf{B}}_{\text{ext}} - \sigma_0(B)\mu_0\frac{DR}{4}\frac{d}{dt}\vec{\mathbf{B}}_{\text{ext}}. \quad D \ll R \ll \delta \quad (2.47)$$

The conductivity  $\sigma_0$  is not required to be constant in time but only spatially uniform. Independently of the majority carrier type the magnetic field correction will always be opposite to the external magnetic field.

It is useful to calculate approximate values for the correction factor  $c$  in order to estimate its order of magnitude. A sample with conductivity  $\sigma_0(B) = 2 \times 10^5 \Omega^{-1} m^{-1}$  and typical dimensions of  $R = 1 \text{ mm}$  and  $D = 0.5 \text{ mm}$  yields a correction factor  $c = 0.03 \mu s$ , that is at a sweep rate of  $0.1 T / ns$  a magnetic field of correction of  $3 \text{ T}$  for each field direction which, in turn means, that resonance fields of up and down sweeps are different by twice that value.

For epitaxial samples with typical thicknesses of the conducting layers of order  $\mu m$  to  $nm$  the field correction factor  $c$  is smaller than  $0.1 \text{ ns}$  and can be neglected. In bulk samples of thickness of order few  $100 \mu m$  however, the field correction has a non negligible value yet it remains to be determined whether or not the thin disc approximation is still valid.

### 2.2.2 The Diffusion Approximation

This section will deal with the diffusion problem for a cylindrical sample with radius  $R$  and infinite length of a material with conductivity  $\sigma_0$  and relative permeability of  $\vec{\mu}_R = \vec{1}$  for an axial magnetic field applied perpendicular to the  $(r, \varphi)$ -plane,  $\vec{\mathbf{H}} = (0, 0, H_z)$ .

The conductivity tensor and the inverse conductivity tensor are then given by<sup>2</sup>:

$$\vec{\sigma}(B) = \frac{\sigma_0}{1 + (\omega_c \tau)^2} \begin{pmatrix} 1 & \omega_c \tau & 0 \\ -\omega_c \tau & 1 & 0 \\ 0 & 0 & 1 + (\omega_c \tau)^2 \end{pmatrix} \longrightarrow \vec{\sigma}^{-1}(B) = \frac{1}{\sigma_0} \begin{pmatrix} 1 & -\omega_c \tau & 0 \\ \omega_c \tau & 1 & 0 \\ 0 & 0 & 1 \end{pmatrix} \quad (2.48)$$

where  $\omega_c \tau = eB\tau(B)/m^*$  is an explicit function of magnetic field.

The MAXWELL equations

$$\vec{\nabla} \times \vec{\mathbf{E}} = -\mu_0 \frac{\partial}{\partial t} \vec{\mathbf{H}} \quad (2.49)$$

$$\vec{\nabla} \times \vec{\mathbf{H}} = \vec{\mathbf{j}} + \frac{\partial}{\partial t} \vec{\mathbf{D}} \quad (2.50)$$

will be used to derive the diffusion equation with the displacement currents set to zero. This can be assumed as displacement currents are not relevant at frequencies much lower than the infrared. As the field oscillates with  $\approx 10 \text{ kHz}$  this condition is met, negligible displacements of charges will occur. The current density is given by OHM's law:

<sup>2</sup>The conductivity tensor has the same form for cylindrical coordinates and Cartesian coordinates.

$$\vec{\mathbf{j}} = \vec{\sigma} \vec{\mathbf{E}} \quad \longrightarrow \quad \vec{\mathbf{E}} = \vec{\sigma}^{-1} \vec{\mathbf{j}} = \vec{\sigma}^{-1} [\vec{\nabla} \times \vec{\mathbf{H}}] \quad (2.51)$$

thus it is possible to yield the diffusion equation for  $\vec{\mathbf{H}}$  caused by eddy currents

$$\vec{\nabla} \times \left( \vec{\sigma}^{-1} [\vec{\nabla} \times \vec{\mathbf{H}}] \right) = -\mu_0 \frac{\partial}{\partial t} \vec{\mathbf{H}} \quad (2.52)$$

The problem is solved in  $\vec{\mathbf{H}}$  because of the convenient form of the boundary condition for the main tangential component of  $\vec{\mathbf{H}}$ . It can be similarly be solved for the magnetic induction  $\vec{\mathbf{B}}$ , the vector potential  $\vec{\mathbf{A}}$  or the current density  $\vec{\mathbf{j}}$ . E.g., the eddy current density  $\vec{\mathbf{j}}$  can be derived by equation  $\vec{\nabla} \times \vec{\mathbf{H}} = \vec{\mathbf{j}}$ .

In Cartesian coordinates the operator  $\vec{\nabla}$  is given by

$$\vec{\nabla} = \vec{\mathbf{e}}_x \frac{\partial}{\partial x} + \vec{\mathbf{e}}_y \frac{\partial}{\partial y} + \vec{\mathbf{e}}_z \frac{\partial}{\partial z} \quad (2.53)$$

with  $\vec{\mathbf{H}} = (H_x, H_y, H_z)$  it is

$$\vec{\nabla} \times \vec{\mathbf{H}} = \vec{\mathbf{e}}_x \left( \frac{\partial}{\partial y} H_z - \frac{\partial}{\partial z} H_y \right) + \vec{\mathbf{e}}_y \left( \frac{\partial}{\partial z} H_x - \frac{\partial}{\partial x} H_z \right) + \vec{\mathbf{e}}_z \left( \frac{\partial}{\partial x} H_y - \frac{\partial}{\partial y} H_x \right) \quad (2.54)$$

and consequently

$$\frac{1}{\sigma_0} \begin{pmatrix} 1 & -\omega_c \tau & 0 \\ \omega_c \tau & 1 & 0 \\ 0 & 0 & 1 \end{pmatrix} [\vec{\nabla} \times \vec{\mathbf{H}}] = \frac{1}{\sigma_0} \begin{pmatrix} \vec{\mathbf{e}}_x \left\{ \frac{\partial}{\partial y} H_z - \frac{\partial}{\partial z} H_y - \omega_c \tau \left[ \frac{\partial}{\partial z} H_x - \frac{\partial}{\partial x} H_z \right] \right\} \\ + \vec{\mathbf{e}}_y \left\{ \omega_c \tau \left[ \frac{\partial}{\partial y} H_z - \frac{\partial}{\partial z} H_y \right] + \frac{\partial}{\partial z} H_x - \frac{\partial}{\partial x} H_z \right\} \\ + \vec{\mathbf{e}}_z \left\{ \frac{\partial}{\partial x} H_y - \frac{\partial}{\partial y} H_x \right\} \end{pmatrix} \quad (2.55)$$

The left part of the diffusion equation (2.51) is then given by

$$\begin{aligned} & \vec{\nabla} \times \left( \vec{\sigma}^{-1} [\vec{\nabla} \times \vec{\mathbf{H}}] \right) \\ &= 1/\sigma_0 \vec{\mathbf{e}}_x \left[ \frac{\partial}{\partial y} \left\{ \frac{\partial}{\partial x} H_y - \frac{\partial}{\partial y} H_x \right\} - \frac{\partial}{\partial z} \left\{ \omega_c \tau \left[ \frac{\partial}{\partial y} H_z - \frac{\partial}{\partial z} H_y \right] + \frac{\partial}{\partial z} H_x - \frac{\partial}{\partial x} H_z \right\} \right] \\ &+ 1/\sigma_0 \vec{\mathbf{e}}_y \left[ \frac{\partial}{\partial z} \left\{ \frac{\partial}{\partial y} H_z - \frac{\partial}{\partial z} H_y - \omega_c \tau \left[ \frac{\partial}{\partial z} H_x - \frac{\partial}{\partial x} H_z \right] \right\} - \frac{\partial}{\partial x} \left\{ \frac{\partial}{\partial x} H_y - \frac{\partial}{\partial y} H_x \right\} \right] \\ &+ 1/\sigma_0 \vec{\mathbf{e}}_z \left[ \frac{\partial}{\partial x} \left\{ \omega_c \tau \left[ \frac{\partial}{\partial y} H_z - \frac{\partial}{\partial z} H_y \right] + \frac{\partial}{\partial z} H_x - \frac{\partial}{\partial x} H_z \right\} \right] \\ &+ 1/\sigma_0 \vec{\mathbf{e}}_z \left[ \frac{\partial}{\partial y} \left\{ \frac{\partial}{\partial y} H_z - \frac{\partial}{\partial z} H_y - \omega_c \tau \left[ \frac{\partial}{\partial z} H_x - \frac{\partial}{\partial x} H_z \right] \right\} \right] \end{aligned} \quad (2.56)$$

With  $\vec{\mathbf{H}} = (H_x, H_y, H_z) = (0, 0, H_z)$  and

$$\vec{\nabla} \times \left( \vec{\sigma}^{-1} [\vec{\nabla} \times \vec{\mathbf{H}}] \right) = -\mu_0 \frac{\partial}{\partial t} \vec{\mathbf{H}} \quad (2.57)$$

we yield

$$\begin{aligned} 1/\sigma_0 \vec{\mathbf{e}}_x \left\{ -\omega_c \tau \frac{\partial^2}{\partial z \partial y} H_z + \frac{\partial^2}{\partial z \partial x} H_z \right\} &= -\mu_0 \frac{\partial}{\partial t} H_x = 0 \\ 1/\sigma_0 \vec{\mathbf{e}}_y \left\{ \omega_c \tau \frac{\partial^2}{\partial z \partial y} H_z + \frac{\partial^2}{\partial z \partial x} H_z \right\} &= -\mu_0 \frac{\partial}{\partial t} H_y = 0 \\ 1/\sigma_0 \vec{\mathbf{e}}_z \left\{ -\frac{\partial^2}{\partial x^2} H_z - \frac{\partial^2}{\partial y^2} H_z \right\} &= -\mu_0 \frac{\partial}{\partial t} H_z \quad . \end{aligned} \quad (2.58)$$

Therefore

$$\omega_c \tau \frac{\partial^2}{\partial z \partial y} H_z = \frac{\partial^2}{\partial z \partial x} H_z \quad , \quad -\omega_c \tau \frac{\partial^2}{\partial z \partial y} H_z = \frac{\partial^2}{\partial z \partial x} H_z \quad . \quad (2.59)$$

From the x and y component we find

$$\frac{\partial}{\partial x} \left\{ \frac{\partial}{\partial x} \frac{\partial}{\partial z} H_z \right\} = \omega_c \tau \frac{\partial^3}{\partial x \partial y \partial z} H_z \quad , \quad \frac{\partial}{\partial y} \left\{ \frac{\partial}{\partial y} \frac{\partial}{\partial z} H_z \right\} = -\omega_c \tau \frac{\partial^3}{\partial x \partial y \partial z} H_z \quad (2.60)$$

which can be transformed into

$$\frac{\partial}{\partial z} \left\{ \frac{\partial^2}{\partial x^2} H_z + \frac{\partial^2}{\partial y^2} H_z \right\} = 0 \quad \longleftrightarrow \quad \frac{\partial}{\partial z} \sigma_0 \mu_0 \frac{\partial}{\partial t} H_z = 0 \quad (2.61)$$

The axial field and its derivative must be constant with respect to the axis direction. This is given for a slab with infinite extension parallel to the field axis.

We obtain

$$\sigma_0 \mu_0 \frac{\partial}{\partial t} \vec{\mathbf{H}} = \left\{ \frac{\partial^2}{\partial x^2} + \frac{\partial^2}{\partial y^2} \right\} \vec{\mathbf{H}} = \Delta \vec{\mathbf{H}} \quad (2.62)$$

Here  $\Delta$  is the two dimensional, in-plane LAPLACE-operator. Equation (2.62) corresponds to the diffusion equation that would have been directly obtained for a conductivity tensor without non-diagonal terms.

### 2.2.3 Skin Depth and Diffusion Time

Equation (2.62) can be written in dimensionless form by introducing a characteristic time  $t_0$  (e.g. duration of the field pulse), the conductor dimension  $l_0$ , and field amplitude  $H_0$  such that  $H^* = H/H_0$ ,  $t^* = t/t_0$ ,  $l^* = l/l_0$ ,  $\Delta^* = \Delta/l_0^2$ :

$$\Delta^* H^* = \frac{l_0^2 \sigma \mu}{t_0} \frac{\partial}{\partial t^*} H^* \quad (2.63)$$

We can define a few characteristic quantities that will be useful in the further calculation process [27], the characteristic penetration depth  $s_0$  down to which the magnetic field is still appreciable

$$s_0 \cong l_0 = \sqrt{\frac{t_0}{\sigma_0 \mu_0}} \quad , \quad (2.64)$$

the diffusion time scale on which the field decays away or penetrates the sample

$$\tau_d = l_0^2 \sigma_0 \mu_0 \quad , \quad (2.65)$$

with the formal diffusion velocity

$$v_d = l_0 / \tau_d = \sigma_0 \mu_0 / l_0 \quad . \quad (2.66)$$

In this calculation we will use the skin depth which we shall define as the depth at which the surface magnetic field has decreased to a value  $1/e$ . For any given time dependence of the magnetic field the skin depth is fixed. For a harmonic sinusoidal

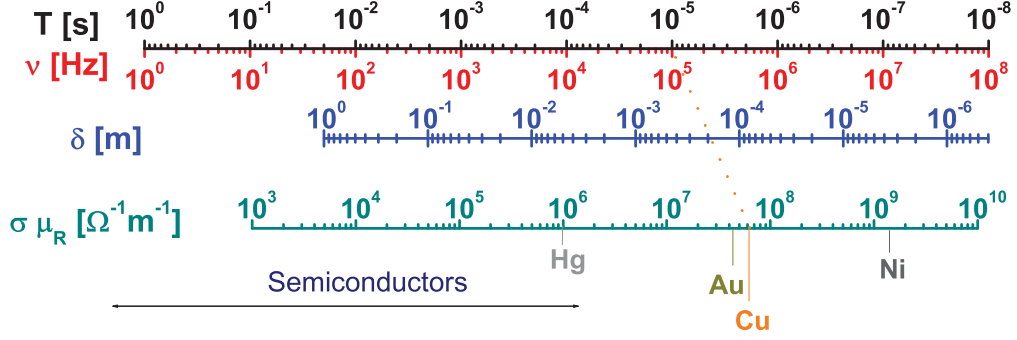


Figure 2.5: Nomograph giving the harmonic skin depth  $\delta$  as a function of frequency  $\nu = 1/T$  of a sinusoidal field and conductivity times relative permeability  $\sigma_0 \cdot \mu_R$  for relevant metal [27, 29] materials and semiconductors.

oscillating field with angular frequency  $\omega = 2\pi\nu = 2\pi/T$  we can choose the characteristic time to be  $t_0 = T/\pi$  we find the harmonic skin depth  $\delta$  to be:

$$\delta = \sqrt{\frac{2}{\omega\mu_0\sigma_0}} = \frac{1}{\sqrt{\pi\nu\mu_0\sigma_0}} = \sqrt{\frac{T}{\pi\mu_0\sigma_0}}. \quad (2.67)$$

The skin depth can be more accurately derived by analyzing the penetration into a conducting half space with MAXWELL's equations [27] that would yield an equation of the form:

$$H_z(z, t) = H_0 e^{-z/\delta} \sin\left(\omega t - \frac{z}{\delta}\right) - \frac{2H_0}{\sqrt{\pi}} \int_0^{\xi} \sin\left(\frac{2\pi t}{T} - \frac{z^2}{2\delta^2\xi'^2}\right) e^{-\xi'^2} d\xi' \quad (2.68)$$

for the retarded variable  $\xi = z/\sqrt{4\sigma_0\mu_0 t}$ .

The skin depth for any given conductivity can be derived using fig. 2.5. For any experiment in single-turn coils in this thesis we have an angular frequency of  $\omega = 2\pi/T \approx 2\pi/12 \mu s$  and find

$$\delta = \sqrt{\frac{T}{\pi\mu_0\sigma_0}} = \sqrt{\frac{30}{\pi^2\sigma_0}} = \sqrt{3.04/\sigma_0} \quad [m] \quad (2.69)$$

if  $\sigma_0$  is given in  $\Omega^{-1}m^{-1}$ . Consequently we determine

$$\begin{aligned} \delta = 1.00 \text{ cm} &\longrightarrow \sigma_0 \approx 300 \Omega^{-1}cm^{-1} & \sigma_0 = 10^2 \Omega^{-1}cm^{-1} &\longrightarrow \delta \approx 17.4 \text{ mm} \\ \delta = 0.50 \text{ cm} &\longrightarrow \sigma_0 \approx 1200 \Omega^{-1}cm^{-1} & \sigma_0 = 10^3 \Omega^{-1}cm^{-1} &\longrightarrow \delta \approx 5.5 \text{ mm} \\ \delta = 0.25 \text{ cm} &\longrightarrow \sigma_0 \approx 4800 \Omega^{-1}cm^{-1} & \sigma_0 = 10^4 \Omega^{-1}cm^{-1} &\longrightarrow \delta \approx 1.7 \text{ mm} \\ \delta = 0.10 \text{ cm} &\longrightarrow \sigma_0 \approx 30000 \Omega^{-1}cm^{-1} & \sigma_0 = 10^5 \Omega^{-1}cm^{-1} &\longrightarrow \delta \approx 0.6 \text{ mm} \end{aligned} \quad (2.70)$$

A spatially uniform field distribution inside the sample requires all sample dimensions to be well below the skin depth of the sample. Whereas for the sample thickness this

may be easily fulfilled for the thin disc, the sample radius is a critical parameter in that case too.

The condition  $R \ll \delta$  is fulfilled for e.g.  $10R = \delta$  at the present sample geometry of  $R = 1\text{mm}$  or  $R = 0.5\text{mm}$  for samples with a conductivity of  $300\Omega^{-1}\text{cm}^{-1}$  or  $1200\Omega^{-1}\text{cm}^{-1}$ , respectively. At higher conductivities of samples the thin disc approximation is no longer valid, a radial or / and an axial dependence of the diffused magnetic field and consequences thereof must be considered.

#### 2.2.4 Solution of the Diffusion Equation

Equation (2.62) is most conveniently solved in cylindrical coordinates  $(r, \varphi, z)$  that represent the symmetry of the experimental situation. It then transforms into (2.71).

$$\frac{1}{r} \frac{\partial}{\partial r} H_z + \frac{\partial^2}{\partial r^2} H_z + \frac{\partial^2}{\partial \varphi^2} H_z - \sigma_0 \mu_0 \frac{\partial}{\partial t} H_z = 0 \quad . \quad (2.71)$$

with the rotational symmetry of our field configuration we find:  $\frac{\partial^2}{\partial \varphi^2} H_z = 0$ .

To solve this problem initial and boundary conditions for an external field are required:

$$\begin{aligned} H_z(r, t) &= 0 & 0 \leq r, & \quad t \leq 0 \\ |H_z(0, t)| &< \infty & -\infty < t < \infty & \\ H_z(R, t) &= (H_{\text{ext}})_z(R, t) & t \geq 0 & \end{aligned} \quad (2.72)$$

At this point the actual character of the external magnetic field is required. For the experimental situation of this thesis we deal with damped sinusoidal fields of the form

$$(H_{\text{ext}})_z(r, t) = H_0 \mathbf{e}^{\mathbf{i}(\omega t + \phi) - \alpha t} = H_0 \mathbf{e}^{\mathbf{i}([\omega + \mathbf{i}\alpha]t + \phi)} \quad r \geq R, t \geq 0 \quad (2.73)$$

with a phase  $\phi = -\pi/2$ . We rewrite the time dependent part as  $\mathbf{i}([\omega + \mathbf{i}\alpha]t) = \mathbf{i}[\omega(1 + \mathbf{i}\alpha/\omega)]$  and solve

$$\frac{d}{dt} H_z = \mathbf{i}\omega(1 + \mathbf{i}\alpha/\omega)\sigma_0\mu_0 H_z \quad (2.74)$$

to obtain a BESSEL-KELVIN differential equation of order zero:

$$r^2 \frac{d^2}{dr^2} H_z + r \frac{d}{dr} H_z - \mathbf{i}\omega(1 + \mathbf{i}\alpha/\omega)\sigma_0\mu_0 r^2 H_z = 0 \quad . \quad (2.75)$$

The conductivity  $\sigma_0$  contains a dependence on the external magnetic field  $\sigma_0 = \sigma_0(H_z)$ . In the further process of calculation the influence of this dependence must be assumed small to be able to solve (2.75). The magnetic field dependence of the conductivity will be ignored for deducing the relevant properties. In the final result however, we will treat  $\sigma_0$  as a function of external magnetic field.

The steady state solution at  $t > 0$  to the above equation is found to be<sup>3</sup>

$$H_z(r) = C_1 J_0 \left( -\sqrt{-\mathbf{i}\omega(1 + \mathbf{i}\alpha/\omega)\sigma_0\mu_0} r \right) + C_2 Y_0 \left( -\sqrt{-\mathbf{i}\omega(1 + \mathbf{i}\alpha/\omega)\sigma_0\mu_0} r \right) \quad (2.76)$$

<sup>3</sup>transient effects have been neglected and the oscillatory behavior of the field can be described well by a damped harmonic Ansatz

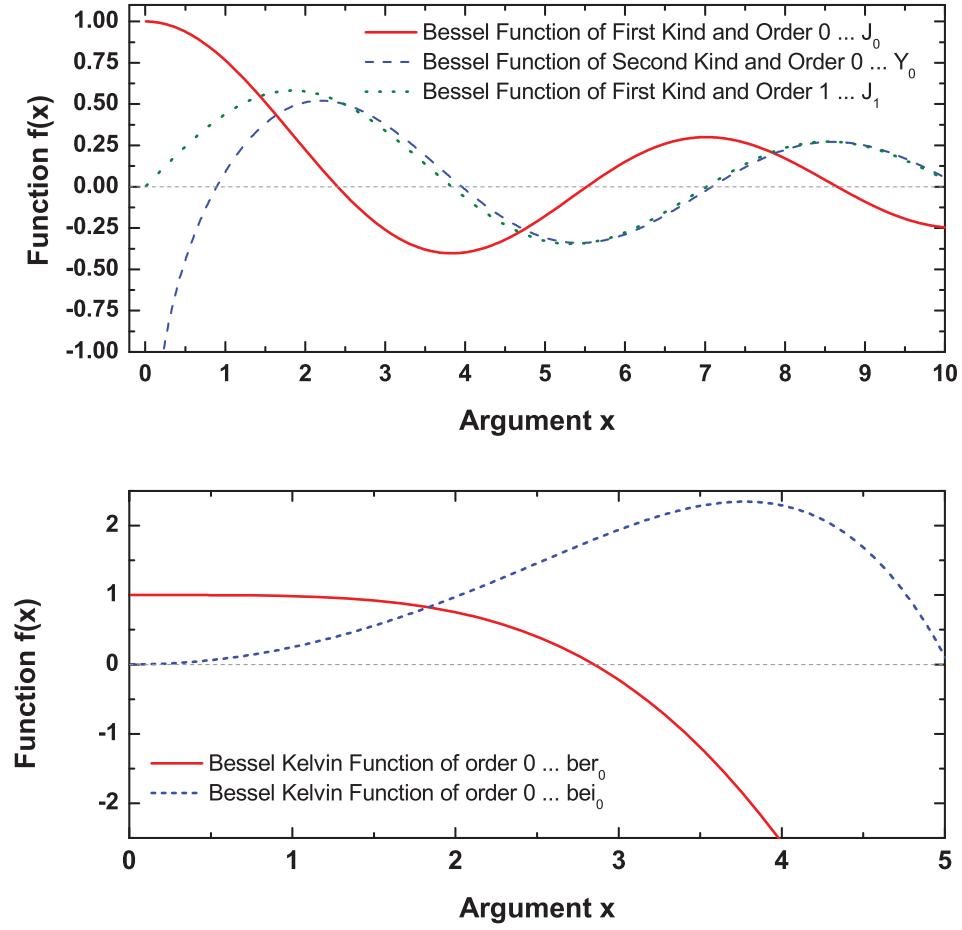


Figure 2.6: Cylindrical functions relevant to the diffusion problem. Top: BESSEL Functions of first and second kind for real arguments. Bottom: BESSEL-KELVIN functions  $ber$  and  $bei$  of order zero.

where  $J_0$  and  $Y_0$  are the BESSEL functions of the first and second kind of order zero, respectively. The functions are illustrated in fig. 2.6 for real arguments. The constants  $C_{1/2}$  are given by boundary conditions.  $Y_0$  is divergent at  $r = 0$  but  $H_z(r = 0)$  must be finite therefore  $C_2 = 0$ . The term  $\sqrt{-i\omega(1 + i\alpha/\omega)\sigma_0\mu_0}$  corresponds to  $\sqrt{-i} \sqrt{(1 + i\alpha/\omega)}\sqrt{2}/\delta$ , when delta is the harmonic skin depth (2.67).

With the boundary condition

$$H_z(R, t) = C_1 J_0(-\sqrt{-2i(1 + i\alpha/\omega)R/\delta}) = (H_{\text{ext}})_z(R, t) = H_0 e^{i(\omega(1+i\alpha/\omega)t+\phi)} \quad (2.77)$$

we find using  $J_0(-z) = J_0(z)$

$$C_1 = \frac{H_0 e^{i(\omega(1+i\alpha/\omega)t+\phi)}}{J_0(\sqrt{-i} \sqrt{(1 + i\alpha/\omega)}R\sqrt{2}/\delta)} \quad (2.78)$$

and thus the solution for the magnetic field in our sample



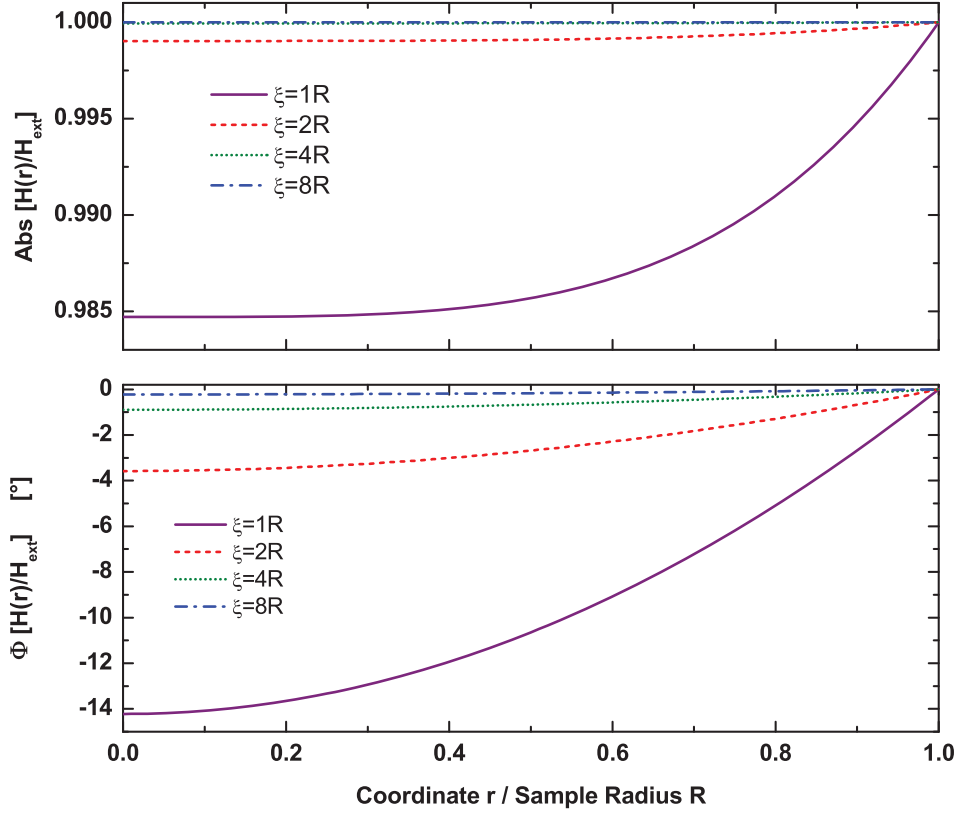


Figure 2.7: Distribution of the magnetic field inside the sample for skin depth to radius ratios  $\xi/R = \delta/\sqrt{2}R = 1$  (solid line), 2 (dashed line), 4 (dotted line) and 8 (dash-dotted line). Top: absolute value of  $H(r)/H_{ext}$ , bottom: phase of  $H(r)/H_{ext}$ . At  $r=R$  the external magnetic field value is acquired and the imaginary part vanishes.

$$H_z(r, t) = \frac{J_0(\sqrt{-i}\sqrt{(1+i\alpha/\omega)}r\sqrt{2}/\delta)}{J_0(\sqrt{-i}\sqrt{(1+i\alpha/\omega)}R\sqrt{2}/\delta)} H_0 e^{i(\omega(1+i\alpha/\omega)t+\phi)} \quad 0 \leq r \leq R \quad . \quad (2.79)$$

The solution of equation (2.75) can equivalently be expressed in terms of the BESSEL-KELVIN functions  $\text{ber}$  and  $\text{bei}$ , or modified BESSEL functions  $I_\nu$  [30,31]

$$J_\nu(z \cdot e^{i3\pi/4}) = \text{ber}_\nu(z) + i \text{bei}_\nu(z) = e^{i\nu\pi/2} I_\nu(z e^{i\pi/4}) \quad . \quad (2.80)$$

that are shown in the bottom part of fig. 2.6. The BESSEL KELVIN functions have the advantage of having exclusively real arguments and values for  $\alpha = 0$ .

The argument of the  $J_0$  represents a dimensionless phase factor times  $r/\delta$  and  $R/\delta$ , respectively. The magnetic field inside the sample is a complex quantity with a real part smaller than the externally applied field. It does have a phase shift versus the external field caused by a non-vanishing imaginary part.

The radial field distribution is given in fig. 2.7 for the ratios of skin depth to sample radius  $\delta/\sqrt{2}R = 1, 2, 4, 8$  and  $\alpha = 0$  we use the abbreviation  $\xi = \delta/\sqrt{2}$ . It can be

seen that the absolute value of magnetic field at the center of the sample is only few percent smaller than at the edge even for  $\sqrt{2}R = \delta$  and approaching the value for  $r=R$  very rapidly when the skin depth exceeds the sample dimension. The absolute values at  $\delta/\sqrt{2}R = 4$  and  $\delta/\sqrt{2}R = 8$  cannot be distinguished from each other and are both coincident with  $f(r)=1$  on this scale.

It is important to note that inside the sample the magnetic field is in general phase shifted versus the external magnetic field. This phase shift grows for  $\sqrt{2}R \rightarrow \delta$ . The phase shift is introduced by the compensating field caused by eddy currents. It works against the driving external field and resembles a screening effect. The consequence of this behavior is a time delay of the actual magnetic field inside the sample versus the external magnetic field. As  $\mu_0$  is a constant and  $\omega$  nearly a constant in the given experimental situation, the conductivity is the parameter that determines the skin depth. Therefore a linear decrease of the skin depth  $\sqrt{2}R \rightarrow \delta$  represents a quadratic increase in conductivity.

For  $R \ll \delta$  we can use the expansion of  $J_\nu$  [30]

$$J_\nu(z) = \left(\frac{1}{2}z\right)^\nu \sum_{k=0}^{\infty} \frac{\left(-\frac{1}{4}z^2\right)^k}{k! \Gamma(\nu + k + 1)} \quad \longrightarrow \quad \begin{aligned} J_0(z) &\approx 1 - \frac{1}{4}z^2 + \frac{1}{32}z^4 + \dots \\ J_1(z) &\approx \frac{1}{2}z - \frac{1}{16}z^3 + \dots \end{aligned} \quad (2.81)$$

to yield for  $0 \leq r \leq R \ll \delta$  and  $\alpha = 0$

$$\begin{aligned} H_z(r, t) &= \frac{J_0(\sqrt{-i}r\sqrt{2}/\delta)}{J_0(\sqrt{-i}R\sqrt{2}/\delta)} H_0 e^{i(\omega t + \phi)} \\ &\approx \frac{1+i r^2/2\delta^2}{1+i R^2/2\delta^2} H_0 e^{i(\omega t + \phi)} \\ &\approx H_0 e^{i(\omega t + \phi)} - i \frac{R^2-r^2}{2\delta^2} H_0 e^{i(\omega t + \phi)} \\ &= H_0 e^{i(\omega t + \phi)} - \frac{R^2-r^2}{2\delta^2} H_0 e^{i(\omega t + \phi) + i\pi/2} \\ &= H_0 e^{i(\omega t + \phi)} - i \frac{R^2-r^2}{4} \omega \mu_0 \sigma_0 H_0 e^{i(\omega t + \phi)} \\ &= H_0 e^{i(\omega t + \phi)} - \frac{R^2-r^2}{4} \sigma_0 \mu_0 \frac{\partial}{\partial t} (H_{\text{ext}})_z \end{aligned} \quad (2.82)$$

and therefore

$$B_z(r, t) = \mu_0 H_z(r, t) = (B_{\text{ext}})_z(t) - \frac{R^2-r^2}{4} \sigma_0 \mu_0 \frac{\partial}{\partial t} (B_{\text{ext}})_z(t) \quad . \quad (2.83)$$

The same result is obtained for an expansion of (2.79) with  $\alpha \neq 0$  and the modified condition  $R \ll \left| \sqrt{(1 + i\alpha/\omega)} \delta \right|$ . In this case the term  $\sqrt{(1 + i\alpha/\omega)}$  introduces an extra phase shift that is canceled when the magnetic induction is expressed depending on its derivative whereas the absolute value is preserved within  $< 10^{-4}$ . If the modified condition does not hold true, the effect of the factor  $\sqrt{(1 + i\alpha/\omega)}$  on the absolute value of the magnetic induction is not negligible.

The magnetic induction inside the sample is smaller than the external magnetic induction for all  $r$  and minimal at  $r=0$ , where the phase shift is maximal. Contrary to the thin disc case (2.47) the magnetic induction is dependent on  $r$  and can only be approximated over the sample area. The screening of the magnetic induction by a field depending on the external field derivative can be observed with magnetization equipment as will be shown later.

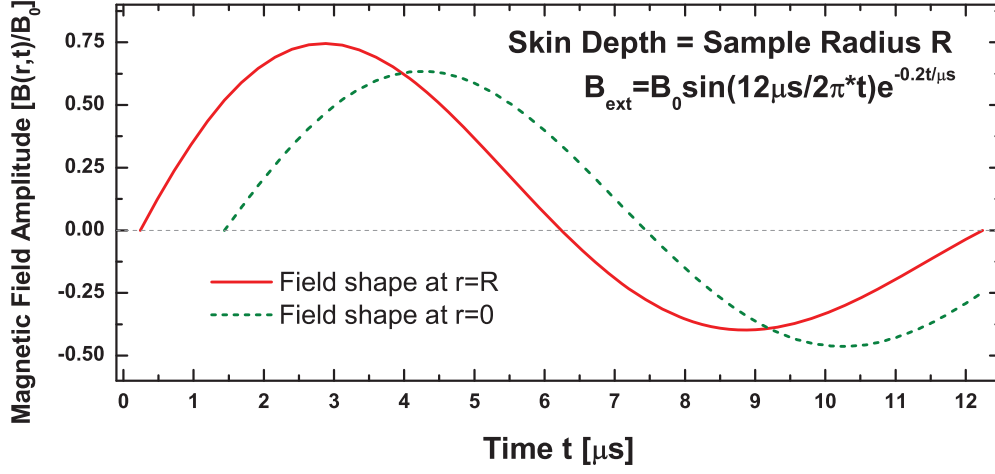


Figure 2.8: Relative magnetic field calculated for  $R=\delta$  at the edge ( $r=R$ , solid line) and center of sample ( $r=0$ , dashed line). It is clearly seen that the field inside the sample is smaller than the external field and shifted to later times in its structure.

An illustration is shown in fig. 2.8 for the case of  $R=\delta$  determined with (2.79) with parameters  $\omega = 2\pi/12\mu s$  and  $\alpha = 0.1/\mu s$ . In this limit the magnetic field at  $r=0$  is delayed by 1.5 microseconds versus the external field and the magnitude has dropped to 83% for the maximum of field, but is exceeding the absolute value at the minimum of field. For samples with  $R \ll \delta$ , therefore much lower conductivity  $\sigma_0$  the lag and the decay of the magnetic field are much smaller but still appreciable as will be shown in the experimental part of this thesis.

### 2.2.5 The Eddy Current Density

The current density  $\vec{j}$  is given by equation  $\vec{\nabla} \times \vec{H} = \vec{j}$ . As the magnetic field has a  $\varphi$ -independent  $z$ -component and no  $r$ - or  $\varphi$ -components the equation to be solved reduces to:

$$\vec{j} = \vec{\nabla} \times \vec{H} = -\frac{\partial}{\partial r} H_z(r) \vec{e}_\varphi = -\frac{\partial}{\partial r} \left[ \frac{J_0(\sqrt{-i}\sqrt{(1+i\alpha/\omega)} r\sqrt{2}/\delta)}{J_0(\sqrt{-i}\sqrt{(1+i\alpha/\omega)} R\sqrt{2}/\delta)} H_0 e^{i(\omega t + \phi)} \right] \vec{e}_\varphi \quad (2.84)$$

that can be obtained with a recurrence relation for BESSEL function derivatives [30]

$$J'_\nu(z) = -J_{\nu+1}(z) + \frac{\nu}{z} J_\nu(z) \quad (2.85)$$

and therefore

$$\begin{aligned}
\vec{\mathbf{j}} &= -\frac{\partial}{\partial r} \left[ \frac{J_0(\sqrt{-\mathbf{i}}\sqrt{(1+\mathbf{i}\alpha/\omega)}r\sqrt{2}/\delta)}{J_0(\sqrt{-\mathbf{i}}\sqrt{(1+\mathbf{i}\alpha/\omega)}R\sqrt{2}/\delta)} H_0 \mathbf{e}^{\mathbf{i}(\omega t+\phi)} \right] \vec{\mathbf{e}}_\varphi \\
&= -\sqrt{-2\mathbf{i}}\sqrt{(1+\mathbf{i}\alpha/\omega)}/\delta \frac{J_1(\sqrt{-\mathbf{i}}\sqrt{(1+\mathbf{i}\alpha/\omega)}r\sqrt{2}/\delta)}{J_0(\sqrt{-\mathbf{i}}\sqrt{(1+\mathbf{i}\alpha/\omega)}R\sqrt{2}/\delta)} H_0 \mathbf{e}^{\mathbf{i}(\omega t+\phi)} \vec{\mathbf{e}}_\varphi \\
&= -\delta^{-1} \mathbf{F}(r) \cdot H(t) \vec{\mathbf{e}}_\varphi
\end{aligned} \tag{2.86}$$

where  $\mathbf{F}$  is a scalar function with complex values. The current density is purely azimuthal.

This result can be rewritten into a form depending on the time derivative of  $\vec{\mathbf{B}}$

$$j_\varphi(r, t) = \left[ \frac{\delta\sigma_0}{2\sqrt{(1+\mathbf{i}\alpha/\omega)}} \frac{J_1(\sqrt{-\mathbf{i}}\sqrt{(1+\mathbf{i}\alpha/\omega)}r\sqrt{2}/\delta)}{J_0(\sqrt{-\mathbf{i}}\sqrt{(1+\mathbf{i}\alpha/\omega)}R\sqrt{2}/\delta)} \mathbf{e}^{-\mathbf{i}\pi/4} \right] \frac{\partial}{\partial t} B_{\text{ext}}(t) \quad . \tag{2.87}$$

The radial behavior of  $\mathbf{F}$  is given in fig. 2.9 for different ratios of skin depth vs. sample radius at  $\alpha = 0$ . The current density is shifted vs. the magnetic field by  $\approx \pi/2$ . That means the current density can likely be expressed in terms of the field derivative. The absolute value of  $\mathbf{F}(r)$  shows a linear dependence on  $r$  for all depicted ratios of skin depth to radius. That is qualitatively similar to previously found result for a magnetic field that is spatially constant with respect to the sample volume.

The bottom layer of fig. 2.9 shows the difference between the phases of magnetic field and current density. It can be seen that for  $4\sqrt{2}R < \delta$  the phase shift  $\Delta\Phi = \Phi(\vec{\mathbf{j}}) - \Phi(\vec{\mathbf{B}})$  is nearly constant over the sample dimension and  $\Delta\Phi = \pi/2$ . This holds true for  $\alpha \neq 0$  as well.

Using (2.81) we find for  $0 \leq r \leq R \ll \delta$

$$\begin{aligned}
j_\varphi &= \sqrt{(-2\mathbf{i})^2}(1+\mathbf{i}\alpha/\omega) \frac{r}{2\delta^2} H_0 \mathbf{e}^{\mathbf{i}(\omega(1+\mathbf{i}\alpha/\omega)t+\phi)} \\
&= \frac{\mathbf{i}r\omega\mu_0\sigma_0}{2} (1+\mathbf{i}\alpha/\omega) H_0 \mathbf{e}^{\mathbf{i}(\omega(1+\mathbf{i}\alpha/\omega)t+\phi)} = \frac{r\sigma_0}{2} \frac{\partial}{\partial t} B_{\text{ext}}.
\end{aligned} \tag{2.88}$$

This result is identical to the previously found one for a thin disc (2.44). The corresponding electric field  $\vec{\mathbf{E}}$  is given by

$$\begin{aligned}
\vec{\mathbf{E}} &= \begin{pmatrix} E_r \\ E_\varphi \\ E_z \end{pmatrix} = \vec{\sigma}^{-1} \vec{\mathbf{j}} \quad ; \quad \vec{\mathbf{j}} = \vec{\mathbf{j}}(\vec{\mathbf{H}}_z(r, t)) \\
&= \sqrt{-2\mathbf{i}}\sqrt{(1+\mathbf{i}\alpha/\omega)} \frac{\sigma_0}{\delta} \frac{J_1(\sqrt{-\mathbf{i}}\sqrt{(1+\mathbf{i}\alpha/\omega)}r\sqrt{2}/\delta)}{J_0(\sqrt{-\mathbf{i}}\sqrt{(1+\mathbf{i}\alpha/\omega)}R\sqrt{2}/\delta)} H_0 \mathbf{e}^{\mathbf{i}(\omega t+\phi)} \begin{pmatrix} -\omega_c\tau \\ 1 \\ 0 \end{pmatrix} \frac{\partial}{\partial t} B_{\text{ext}} \\
&= \left[ \frac{\delta\sigma_0}{2\sqrt{(1+\mathbf{i}\alpha/\omega)}} \frac{J_1(\sqrt{-\mathbf{i}}\sqrt{(1+\mathbf{i}\alpha/\omega)}r\sqrt{2}/\delta)}{J_0(\sqrt{-\mathbf{i}}\sqrt{(1+\mathbf{i}\alpha/\omega)}R\sqrt{2}/\delta)} \mathbf{e}^{-\mathbf{i}\pi/4} \right] \begin{pmatrix} -\omega_c\tau \\ 1 \\ 0 \end{pmatrix} \frac{\partial}{\partial t} B_{\text{ext}}
\end{aligned} \tag{2.89}$$

which corresponds to

$$\vec{\mathbf{E}} = \frac{r}{2} \begin{pmatrix} -\omega_c\tau \\ 1 \\ 0 \end{pmatrix} \frac{\partial}{\partial t} B_{\text{ext}} \tag{2.90}$$

for  $0 \leq r \leq R \ll \delta$ . Again we find a radial electric field that scales with  $\omega_c \tau$  to the azimuthal field. For  $0 \leq r \leq R \ll \delta$  the thin disc approximation and the slab with infinite extension in the field axis direction produce similar eddy current density and respective electric fields. The major difference reflecting the penetration of the magnetic field in an axial way (thin disc) or radial way (slab) is found in the correction to the magnetic field.

## 2.2.6 Induced Temperature

A current carrying conductor with non vanishing resistivity experiences dissipation of energy in form of heat. The adiabatic heating of the crystal lattice can be determined by the relation of JOULE and electric energy:

$$\int_0^{\Delta t} \vec{\mathbf{j}} \cdot \vec{\mathbf{E}} dt = \int_{T_i}^{T_f} \rho_m c_p(T) dT, \quad T_i < T_f \quad (2.91)$$

where  $\rho_m$  is the mass density of the sample material,  $c_p$  its specific heat and  $T_{i/f}$  the initial and final temperatures, respectively. Using the complex quantities and denotation the left part is transformed into

$$\begin{aligned} \int_0^{\Delta t} \Re(\vec{\mathbf{j}}) \cdot \Re(\vec{\mathbf{E}}) dt &= \int_0^{\Delta t} \frac{\sigma_0}{\delta^2} \Re(\mathbf{F}(r) \vec{\mathbf{H}}(r))^2 dt \\ &= \int_0^{\Delta t} \frac{\sigma_0}{\delta^2} H_0^2 (\Re[\mathbf{F}(r)] \sin(\omega t) + \Im[\mathbf{F}(r)] \cos(\omega t))^2 e^{-2\alpha t} dt \\ &= \int_0^{\Delta t} \frac{\sigma_0}{\delta^2} H_0^2 \left( \Re[\mathbf{F}(r)]^2 \sin^2(\omega t) + \Im[\mathbf{F}(r)]^2 \cos^2(\omega t) \right. \\ &\quad \left. + 2 \sin(\omega t) \cos(\omega t) \Re[\mathbf{F}(r)] \cdot \Im[\mathbf{F}(r)] \right) e^{-2\alpha t} dt \end{aligned} \quad (2.92)$$

$\Re(f)$  denotes the real part of a quantity  $f$ ,  $\Im(f)$  the imaginary part. With  $\Re[\mathbf{F}(r)] \ll \Im[\mathbf{F}(r)]$  for  $4\sqrt{2}R < \delta$  we find the  $\cos^2(\omega t)$  term to be the dominant one for the determination of the heating. For larger values of  $R$  the full expression must be evaluated.

Typical values for the temperature increase in single-turn coils themselves are of order 1000 K. [32–34] In the generation process an extremely high current density is driving a magnetic field in a metallic conductor such as copper. Due to the much smaller conductivity and hence eddy current density of semi-conducting samples investigated in this thesis effects of heating can be expected to be significantly smaller than that value. As electronic properties of semi-conductors are highly temperature dependent small changes of temperature may have substantial effects, too. To deduce this behavior in a general way, one must solve a system of differential equations yet, for a reasonable approximation it may be considered as follows.

Assuming a small temperature change to occur in the investigated semi-conducting system, the heat capacity and mass density can be considered as constant during the experiment. [33] For a thin disc or a slab with  $R \ll \delta$  we can find the lattice temperature increase  $\Delta T$  with equation (2.44):

$$\Delta T(r) = \frac{1}{\rho_m c_p} \frac{r^2}{16} \int_0^{\Delta t} \sigma_0 \left( \frac{d}{dt} \vec{\mathbf{B}}_{\text{ext}} \right)^2 dt. \quad (2.93)$$

This expression can only be evaluated if the time dependence of the conductivity  $\sigma_0$  is known. The time dependence of the conductivity will be given by its dependence on

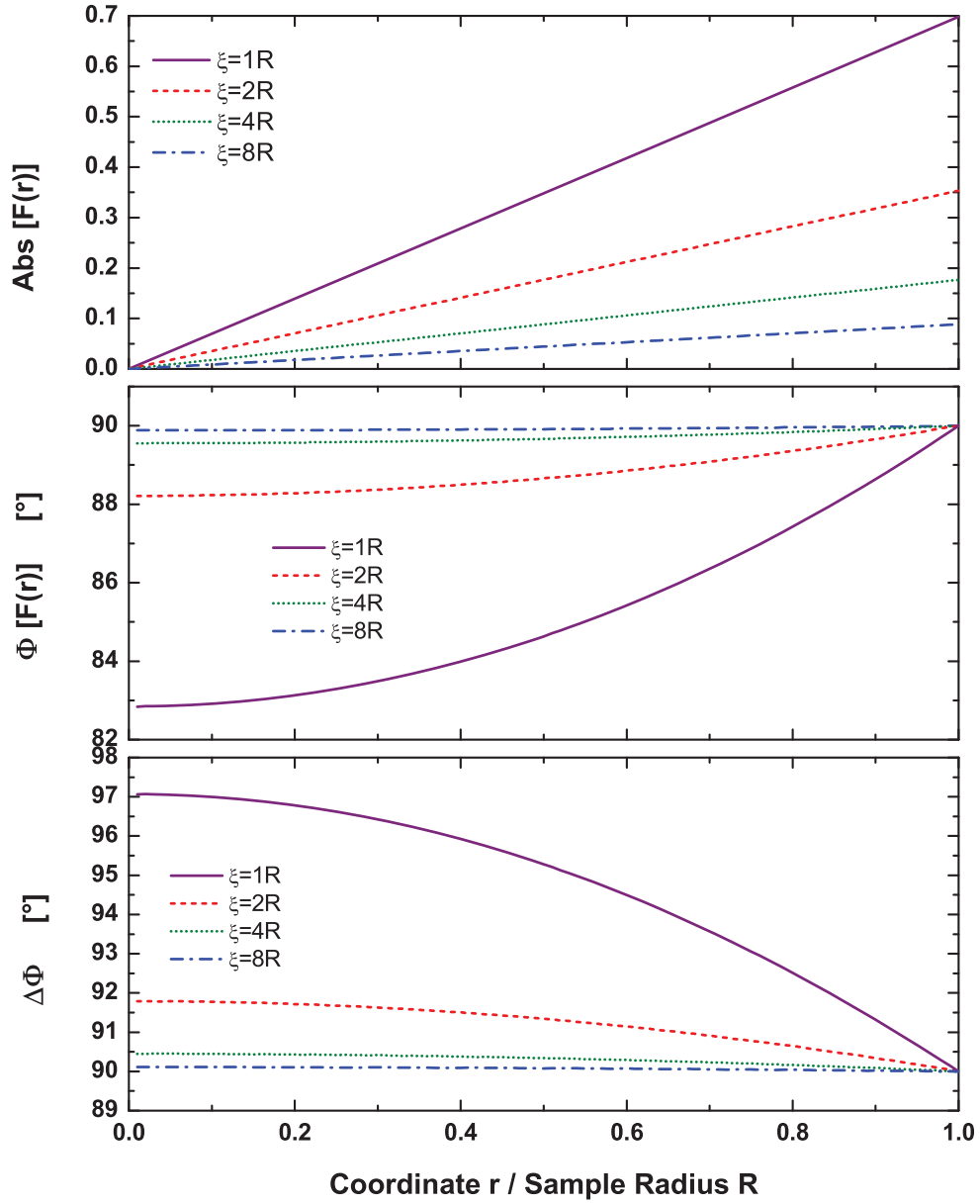


Figure 2.9: Radial dependence of the current density for the ratios of skin depth to sample radius  $\xi/R = \delta/\sqrt{2}R = 1$  (solid line), 2 (dashed line), 4 (dotted line) and 8 (dash-dotted line). Top: Absolute value of  $\mathbf{F}(r)$ , middle: phase of  $\mathbf{F}(r)$ , bottom: Phase difference of current density and magnetic field  $\Delta\Phi = \Phi(\vec{\mathbf{j}}) - \Phi(\vec{\mathbf{B}})$  It is clearly seen that for  $R \ll \delta$  we find a phase shift of  $\Delta\Phi = \pi/2$ .

magnetic field and the time dependence thereof. The lattice temperature increase can in this case easily be calculated numerically.

The magnitude of lattice temperature as given by the aforementioned formulae is

depending quadratically on  $r$ . There is a temperature gradient within the sample, thermal diffusion processes must be considered. Moreover, temperature dependent quantities such as the carrier concentration and conductivity must be treated as temperature dependent. The temperature rise is an integral and therefore cumulative process which is still ambient when its cause is gone. Furthermore the heat deposition continues to rise during a pulse that is, the temperature in the falling side of the field is in general higher than it was on the rising field side. An illustration of  $\int dt(dB/dt)^2$  is given in fig. 2.10 for typical magnetic fields.

It is not possible to directly determine the temperature during a pulse. We can measure the temperature of the heat sink to which the sample is attached before and after the pulse. For cyclotron resonance measurements in STCs an increase in temperature during the pulse can indirectly manifest itself in several ways.

- (1) The line-width will increase with a factor dependent on  $k_B T$  due to the level broadening.
- (2) The population  $f$  of energy levels  $E$  will change with increased temperatures following Boltzmann statistics

$$f(E) \propto e^{-E/k_B T} \quad (2.94)$$

That is with higher temperature there are more carriers excited into the relevant energy levels. The number of carriers involved in a resonance is proportional to the integrated area of the absorption peak in the small absorption approximation. With higher temperature resonances can be found to be broader and/or stronger.

- (3) The band structure is subject to modifications. The parameters required to calculate the band structure such as lattice constant and band gap are temperature dependent. This may shift the cyclotron resonance position. However, for a detectable shift of CR position of about 1 T temperature increases of order 50 K are required. For narrow gap semi-conductors such as InSb that have a strongly temperature dependent energy gap comparable to the radiation energies used, a temperature increase may affect the overall absorption.

The above considerations refer to the lattice temperature. The charge carriers experience an acceleration by the ambient electric field, making them hot carriers. The electron temperature can be significantly higher than the lattice temperature with impacts on point (2).

Point (2) may provide an explanation for type II hysteresis effects observed in e.g. HgTe. Whether or not a temperature increase is the cause for the absorption increase in the down sweeps can be checked with a sample diameter dependent measurement.

### 2.2.7 Mechanical Forces on and within the Sample

A conducting system experiences a local force whenever a current is applied perpendicular to the magnetic field. The force  $\vec{F}$  for a given sample volume  $V$  is given by:

$$d\vec{F} = \vec{f} dV = [\vec{j} \times \vec{B}] dV = [\Re(\vec{j}) \times \Re(\vec{B})] dV \quad (2.95)$$

The free carriers experience a LORENTZ force by the magnetic field. They are therefore shifted out of the equilibrium positions with the lattice. This causes an electrostatic

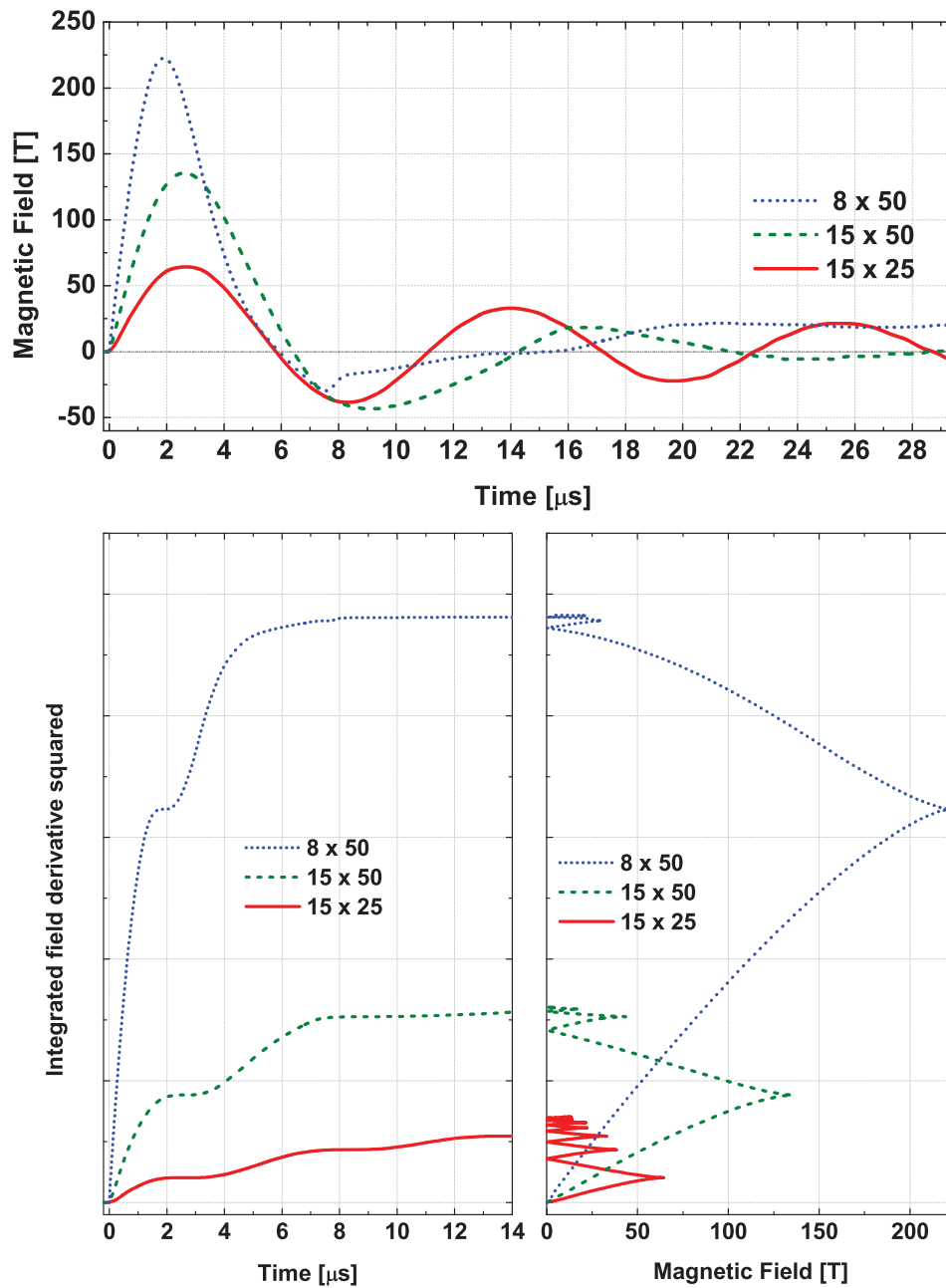


Figure 2.10: Top: Magnetic field traces for several fields that can be generated by single turn coils, dots - very high semi-destructive field, dashes - standard semi-destructive field, solid line - maximum nondestructive field. Bottom, left: Qualitative temperature increase caused by eddy currents for an assumed constant conductivity vs. time for the magnetic fields given in top frame, numbers indicate the coil diameter in mm times the charging voltage in kV, right: the similar dependence vs. magnetic field.



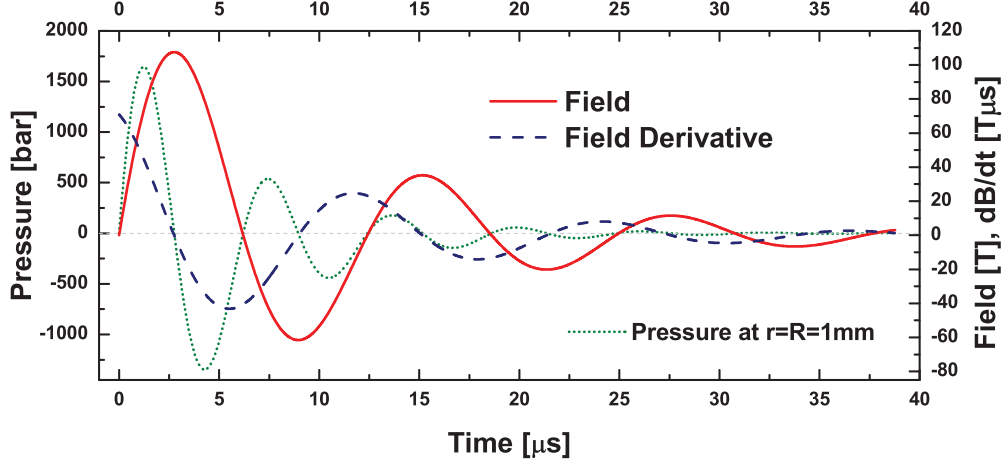


Figure 2.11: Pressure distribution for the previously used field and a sample with radius  $R=1\text{mm}$  and constant conductivity  $\sigma_0 = 2000 \Omega^{-1}\text{cm}^{-1}$ .

displacement and charge separation. The resulting electric field is caused by the displacement and acts upon the lattice only.

For  $0 \leq r \leq R \ll \delta$  we find this force as

$$d\vec{F} = -\frac{\sigma_0 r}{2} \left( \frac{d}{dt} B \right) B \overbrace{[\vec{e}_\varphi \times \vec{e}_z]}^{\vec{e}_r} dV \quad . \quad (2.96)$$

A more familiar quantity is the pressure  $\vec{p}$  that is caused by the force density  $\vec{f}$ .

$$\begin{aligned} d\vec{p} = \vec{f} dr = [\vec{j} \times \vec{B}] dr &= -\frac{\sigma_0 r}{2} \left( \frac{d}{dt} B \right) B dr \vec{e}_r \\ \vec{p}(r) &= -\frac{\sigma_0 r^2}{4} \left( \frac{d}{dt} B \right) B \vec{e}_r \end{aligned} \quad (2.97)$$

Please note that the pressure generated in a sample changes direction with up and down sweeps as well as with field polarity. That means that regardless of majority carrier type there is compressive pressure in the radial direction whenever  $\frac{d}{dt} B$  and  $B$  have the same sign. That is at the beginning of the pulse and after each zero crossing of  $B$ . This effect was used in *magneto-forming* experiments [12, 35]. However, in the down sweeps, the pressure is of expansive, that is tensile, nature. Figure 2.12 shows this.

For a sample with radius  $R=1\text{mm}$  and conductivity  $\sigma_0 = 2000 \Omega^{-1}\text{cm}^{-1}$  the pressure during a pulse exceeds 10 kbars at a sweep rate of  $140\text{T}/\mu\text{s}$  and a field of 140 T. For a sinusoidal field  $B = B_0 \sin \omega t$  the pressure is proportional to  $\sin 2\omega t$  and the maximum value occurs at  $t = \pi/8\omega$ . An illustration is given in fig. 2.11.

The discussion of this section is given for semi-conductor thin discs. The formulae show complete analogy to the situation of metallic cylindrical implosion that is widely used in high energy physics [27]. The principle is also used for the magnetic compression

of metal cylinders. The deformation of metallic tubes is characterized by a minimum pressure which is necessary to overcome the structural strength of the conductor.

It is difficult to find values of the ultimate strength for semi-conducting materials in the literature. Yet, it seems that the pressure caused by eddy currents is smaller than this value, yet of the same order of magnitude. Thus deformations can be considered to be elastic. There has been no evidence for permanent deformations in most samples. For high conductivity epitaxial and thin film samples of HgSe:Fe [36] or GaAs there have been, however, observations of cracks and ruptures that may have been caused by the mechanical forces in the samples at interfaces of the conducting layer and the nonconducting substrate, no other source of destruction was found [12, 35, 36].

The pressure is an instant local effect as opposed to the temperature accumulation. However, in mechanics a deformation can also occur when a sample is repeatedly exposed to pressure below its ultimate strength. From the experimental point of view this means that one has to analyze, how reproducible experimental conditions for a sample are.

It is important to consider how a radial pressure distribution can affect the cyclotron resonance spectra or the experimental situation in general. Dependences of the energy band structure and cyclotron resonance on uniform hydrostatic pressure along an axis can be found in the literature. The modification of energy band structure can be calculated using the deformation potentials of the material. This is, however, for a static case with same magnitude of pressure over the sample volume.

There are other effects caused by mechanical pressure on semi-conducting samples too. A well known example is the piezoelectric effect [26].

### 2.2.8 Summary of Eddy Current Effects

We have found that eddy currents are a relevant process in transient magneto-spectroscopy. The physical quantities of interest are for  $0 \leq r \leq R \ll \delta$

- the induced electric fields

$$\vec{\mathbf{E}}(r, t) = \frac{r}{2} \frac{d}{dt} B(t) \vec{\mathbf{e}}_\varphi + \omega_c \tau \frac{r}{2} \frac{d}{dt} B(t) \vec{\mathbf{e}}_r \quad , \quad (2.98)$$

- the induced current density

$$\vec{\mathbf{j}}(r, t) = \frac{\sigma_0 r}{2} \frac{d}{dt} B(t) \vec{\mathbf{e}}_\varphi \quad , \quad (2.99)$$

- the magnetic field correction for a thin disc  $D \ll R$

$$\vec{\mathbf{B}}_c(t) = -\sigma_0 \mu_0 \frac{DR}{4} \frac{d}{dt} B_{\text{ext}}(t) \vec{\mathbf{e}}_z \quad , \quad (2.100)$$

- the temperature rise

$$\Delta T(r, t) = \frac{1}{\rho_m c_p} \frac{r^2}{16} \int_0^t \sigma_0 \left( \frac{d}{dt} B(t) \right)^2 dt' \quad (2.101)$$

- and the pressure distribution

$$\vec{\mathbf{p}}(r, t) = -\frac{\sigma_0 r^2}{4} \left( \frac{d}{dt} B(t) \right) B(t) \vec{\mathbf{e}}_r \quad . \quad (2.102)$$

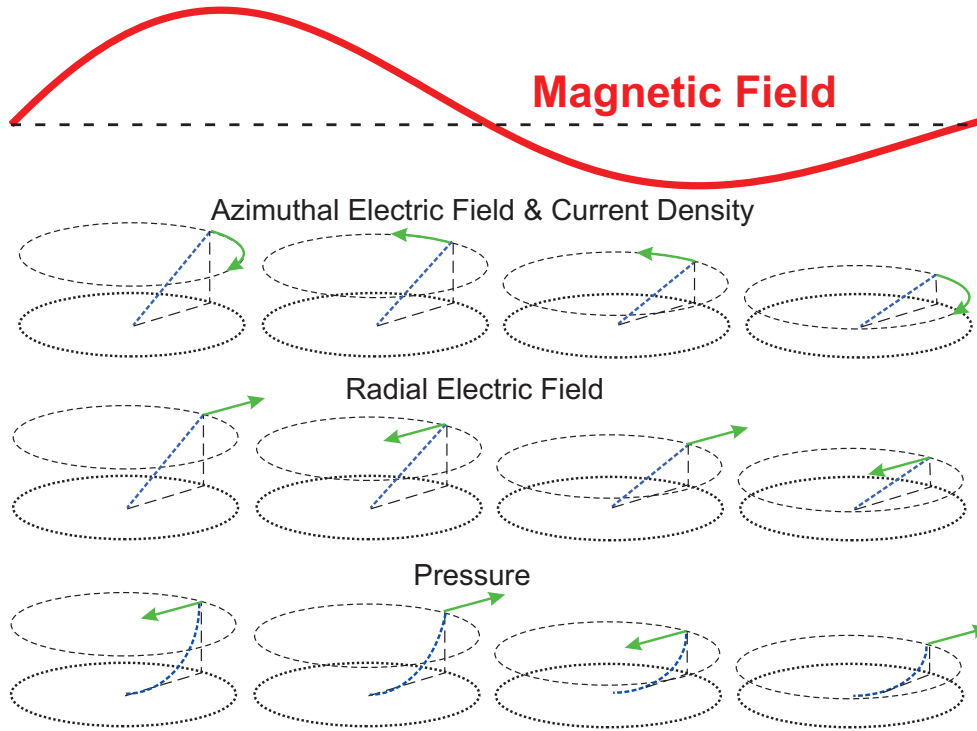


Figure 2.12: Schematic drawing of the spatial dependence over the thin disc area of the vectorial eddy current related phenomena for an arbitrary damped sinusoidal magnetic field with a time dependence as given in the top trace. The field must be applied perpendicular to the sample extension, that is in z-direction. Top to bottom: azimuthal electric field, radial electric field and pressure. Arrows indicate orientation, dashed lines originating in sample center the linear or quadratic dependence on  $r$ . The upper circles of each part are guides to the eye only. Their vertical displacement vs. the sample indicates the relative magnitude of the effects.

All quantities depend on the macroscopic parameter  $r$ , the radius position within the sample. This constitutes the criterion with which eddy current effects can be reliably distinguished from intrinsic effects of the investigated materials.  $\vec{E}_\varphi$  is the most easily determined quantity as it depends on the sweep rate and  $r$  only. The temperature distribution depends on  $r$  but is a scalar, while the other properties are vectors.  $\vec{E}_r$  is radial and azimuthal,  $\vec{j}$  is purely azimuthal,  $\vec{B}_c$  is axial in the thin disc case and additionally dependent of  $r$  in the infinite rod approximation (2.83) and  $\vec{p}$  is radial.

The phenomena described here are not specific to magnetic fields generated by single turn coils but will occur in other pulsed magnetic fields accordingly. In case of non-sinusoidal fields the diffusion equation requires a different set of characteristic parameters depending on the the actual field shape. E.g. for an exponential field rise  $B(t) = B_0 e^{\alpha t}$  we obtain a skin depth of  $\delta = \sqrt{1/\alpha\sigma_0\mu_0}$  and a solution for the magnetic field of

$$B(r, t) = \frac{J_0(i r/\delta)}{J_0(i R/\delta)} B_0 e^{\alpha t} \quad (2.103)$$

for  $0 \leq r \leq R$ .

## Chapter 3

# Magnetic Field Generation

This chapter is describing the magnetic field generator. After a short excursion to magnet and pulsed magnet application in general, the major focus will be on the MEGAGAUSS GENERATOR OF THE MEGAGAUSS LABORATORY OF THE HUMBOLDT-UNIVERSITÄT ZU BERLIN.

### 3.1 General Remarks on Magnetic Field Generation

Strong magnetic fields can be generated in several ways. The most straightforward magnet design uses superconducting coils. These magnets are usually immersed in liquid helium. The field maximum is basically determined by the breakdown field of superconductivity of the respective material used. At present the maximum field achieved by using high  $T_c$  superconductors is 23.4 T [37]. The long time availability of these magnetic fields is primarily determined by the continuous supply of liquid Helium and the properties of the superconductor.

Beyond 20 T a reliable steady magnetic field can be produced by a BITTER- or Helix-type magnet, a high-power water-cooled resistive magnet. The major difficulty at these types of magnets is given by the resistive heating of a current carrying conductor. The heating of a conducting wire can be estimated from the action or current integral [27].

$$J = \int_0^{\Delta t} j^2 dt' = \int_{Q_i}^{Q_f} \sigma dQ = \int_{T_i}^{T_f} \sigma \rho_m c_p(T) dT, \quad T_i < T_f \quad (3.1)$$

where  $j$  is the current density,  $\Delta t$  the duration of current application,  $\sigma$  the conductivity,  $Q$  the deposited heat given by  $Q = c_p \rho_m T$  with the specific heat  $c_p$ , the mass density  $\rho_m$  and the temperature  $T$ .  $i$  and  $f$  denote initial and final states. This integral is formed with the driving current as the parameter. It is different from the temperature integral of eddy currents (2.91) by the factor  $\sigma$  that transforms the electric field into a current density.

Currently, the maximum field of a BITTER type magnet is 33 T [37]. However, it can be combined with a superconducting magnet to obtain higher fields of up to 45 T [37]. Steady resistive magnets require large installations, power supplies and are, after all, limited to comparatively low fields.

An elegant way of circumnavigating these requirements that cannot be met by many laboratories is the application of pulsed magnets. A resistive conductor is exposed to a

Table 3.1: Maximum fields and characteristic timescales of magnets currently used in solid state physics

Type Of Magnet	Field	Pulse Duration
<b>Steady</b>	45 T	$\approx$ days
superconducting Magnet [37]	23.4 T	
BITTER Magnet [37]	33 T	
Hybrid Magnet [37]	45 T	
<b>Pulsed, nondestructive</b>		2 ms .. 2.6 s
capacitor discharge [39]	76 T	few ms
capacitor discharge [40]	80.8 T	7 ms
flywheel discharge [41]	60 T	100 ms
	30 T	2.6 s
<b>Pulsed, semidestructive</b>		
Single Turn Coils [32]	300 T	5 $\mu$ s
<b>Pulsed, destructive</b>		20..100 $\mu$ s
electromagnetic flux compression [42]	620 T	
explosive driven flux compression [43]	2,800 T	
experimentally usable explosive flux compression [43]	$\approx$ 1,200 T	

current and high electrical power for a much shorter period of time than steady magnets, typically ms or  $\mu$ s. This avoids continuous cooling as the coil heats up adiabatically during the pulse [38] and will be given enough time to cool down in between experiments.

The principal limitation to nondestructive pulsed magnetic field generation is the magnetic stress  $p = B^2/2\mu_0$  exerted onto the conductor. The limit of nondestructive magnets is given by the strength of the materials used, this will be less than 100 T in principle as the magnetic pressure at 100 T is  $40 t/cm^2$ . An estimate of the theoretical maximum field  $B_S$  can be derived from the ultimate tensile strength  $\sigma_{\max}$  for free standing windings by [44]:

$$B_s = \sqrt{2\mu_0} \sqrt{\sigma_{\max}} \sqrt{\ln \alpha} \quad (3.2)$$

where  $\alpha$  is the ratio of outer to inner diameters. Using equation (3.1) a scaling law for pulse duration for a given peak field  $B_p$  can be obtained:

$$\begin{aligned} \Delta t &= \xi J(T_i, T_f) G_j \frac{a^2}{B_p^2} \quad , \quad W_p = \frac{1}{2} L I_p^2 = G_w a^3 B_p^2 \\ \rightarrow \quad \Delta t &= \xi J(T_i, T_f) G_j G_W^{-2/3} W_p^{2/3} B_p^{-10/3} \end{aligned} \quad (3.3)$$

where  $J$  is a weighted average of the action integral for the materials used in the winding,  $a$  is the radius of the bore,  $W_p$  is the magnetic energy at peak field,  $G_J$  and  $G_W$  are factors depending on the geometry and  $\xi$  is a factor depending on the pulse shape which is 1 for a plateau, 2 for a sine wave and 3 for a linear ramp [44].

Thus for a given energy higher fields can only be achieved by a smaller bore and / or shorter pulse duration. Currently pulsed fields of almost 80T are available for user

operation [39], with 80.8 T being the highest nondestructive recorded field [40]. The 60 T user magnet at NHMFL can be operated with various pulse shapes up to 100 ms at 60 T [45], 2.6 s at 30 T [41], but has suffered a major failure and breakdown in 2000. With the short duration of pulses a quick delivery of the available energy of typically MJ becomes essential. The most widely used method is a capacitor bank discharge. To enhance lifetime of the capacitors storing large energies, crowbar installations prevent the charge reversal in these banks after discharge. Therefore a pulsed field will usually have only one field direction in one half sinusoidal type pulse. Alternatively to capacitor discharges, the use of a flywheel generator allows the shaping of the pulse to a flat top [41].

At present day, significant efforts aim at the completion of non-destructive 100 T user magnets [46, 47]. There is, however, the alternative approach to take advantage of inertial confinement and perform the experiments during the short time scale before the coil disintegrates [38]. There are two methods used at present to generate field in excess of 100 T, one, the semi-destructive SINGLE-TURN-COIL (STC) technique [32] preserving sample and equipment while the coil will be destroyed and two, the destructive flux compression technique, where all parts connected with the magnetic field are destroyed.

The flux compression technique is currently used for investigations in solid state science. Compressing a magnetic flux captured in a liner kinetic energy can be converted into magnetic energy. This method works on a timescale of tens of  $\mu\text{s}$  although the essential field increase of several hundred Tesla occurs at the end of the pulse in a time period of about  $2 \mu\text{s}$  only. The implosion speed of up to several km/s determines the field magnitude [38].

Two different compression techniques can be used for experiments, the electromagnetic flux compression (EMFC) [38], yielding fields up to 622 T at ISSP [48] and the explosive driven flux compression technique (EDFC) [43] that provides fields of up to 1,200 T for experimental use and a record field of 2,800 T at VNIIEF [43].

The flux compression technique is accompanied by a massive generation of shock waves that will practically inevitably destroy sample, magnetic field generators and surrounding equipment in the explosive drive case. The turnaround phenomenon, the magnetic pressure of a compressed liner flux becoming larger than the compressive forces thus creating an expanding motion away from the center has been theoretically deduced and experimentally observed in very short timescales [43, 49, 50]. However, the STC technique is currently the only reliable technique in the low Megagauss (1 MG = 100 T) range that preserves sample and equipment and provides up and down sweeps as required for the detection of any dynamics.

The pulse duration and maximum fields for various types of magnets are given in table 3.1.

## 3.2 The Single Turn Coil Technique

The STC technique is a straightforward method to generate Megagauss magnetic fields by discharging a capacitor bank directly into a coil that explodes radially outwards in the process, however not harming the enclosed experimentally usable volume. Therefore the term *semi-destructive technique* was coined. The rise time of the discharge must be fast enough to allow the peak field to be reached before the coil is substantially expanded. The low inductance met by using STCs, must be accompanied by extremely low inductance of capacitor bank and high voltage to supply the required power in very short time [38].

Table 3.2: Comparison of time relevant parameters for various coils and magnets. First part refers to STCs at Berlin, coil denotes a measure of diameter, the coil length is equal to it's diameter, wall thickness 3 mm. The maximum sweep rate and time delays between magnetic fields 50 T and 100 T between up and down sweeps are given.

Coil mm	$L_{coil}$ nH	$B_{max}$ @ 55 kV T	$t_R$ $\mu s$	$dB/dt_{max}$ $T/\mu s$	$\Delta t$ @ 50T $\mu s$	$\Delta t$ @ 100T $\mu s$
5	3.3	300	1.3	400	3.11	2.40
7	4.7	261	1.55	300	3.49	2.72
8	5.3	253	1.65	280	3.62	2.82
10	6.7	214	2.0	180	3.90	2.99
12	8.0	188	2.3	150	4.00	2.95
15	10.0	154	2.5	100	3.98	2.52
20	13.3	114	2.7	80	3.81	1.63
Reinforced						
15	10.0	65 @ 25kV	2.5	78	2.45	-
15	10.0	43 @ 17kV	2.5	25	-	-
Other pulsed magnets						
ARMS		78	$10^4$		$10^4$	-
EMFC		1000	40	$\approx 1500$	-	-
EDFC		2800	17	$\approx 500$	-	-

Much of the research on the properties of STCs has been carried out on solid massive metal blocks with a bore and a feed gap [51–55] whereas solid state applications use almost exclusively a light-weight type [32,38]. In the latter type, a small light-weight coil is formed out of thin sheets of metallic conductors, typically copper of few mm thickness. The confinement in light-weight STCs is purely inertial [56–58]. Although achieved field magnitudes do not show much difference between the massive and lightweight coils, the former type is more easily manufactured whilst the latter type seems to be less destructive to any sample or part of equipment exposed to the magnetic field itself. This being a characteristic of lightweight STCs, experiments can be carried out repeatedly with the same samples and similar or varied experimental conditions.

Currently, STC installations are operated for solid state physics application at ISSP, Tokyo / Kashiwa [48,50,59,60] and Berlin [32], that produced a great variety of results [61,62]. Investigations on the characteristics of the STC are carried out at Loughborough [49] and St. Petersburg [63]. Recently, an installation at Los Alamos NHMFL has become operational for user application [64]. As of present day, the maximum usable field in STCs of 311 T at 5 mm coil diameter has been achieved using the equipment at Berlin [65]. A similar result was obtained at ISSP, at a smaller diameter of 3 mm with no experimental application option [50,62]<sup>1</sup>. Experiments beyond 250T involve a significantly higher risk of sample destruction (close to 100%) after the pulse due to collateral effects not directly

<sup>1</sup>A comparable experiment at Berlin with 3mm diameter coil yielded a maximum field of 331 T as depicted in fig. 3.2. This has been carried out after the submission of this thesis, yet prior to the Disputation and Publication and is given for a more complete picture. Magnetic fields in excess of these values have been reported but not reproduced [55,62].

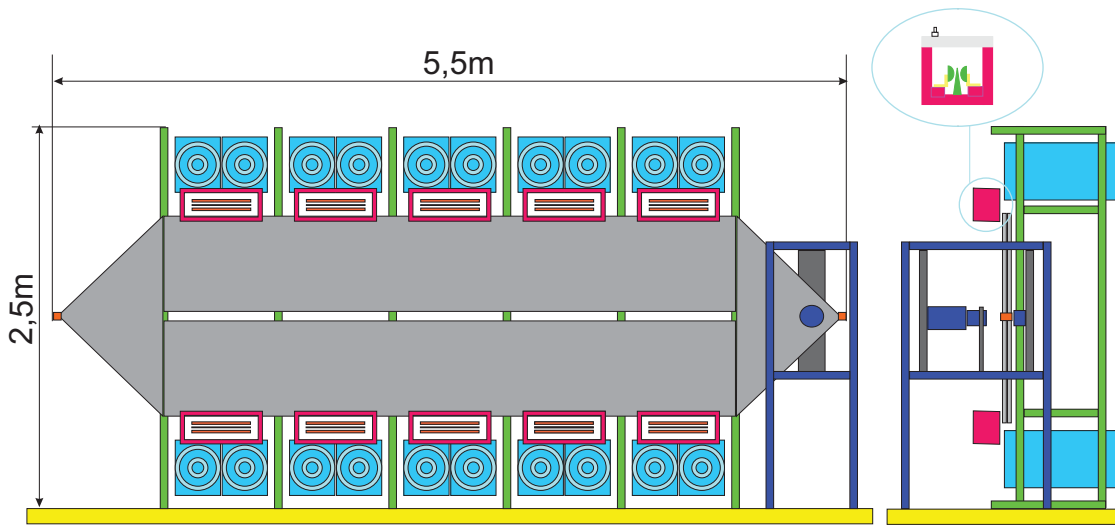


Figure 3.1: True to scale drawing of the arrangement of the capacitor bank in the Berlin STC Megagauss magnetic field generator. A detail of the rail gap switch is given. Developed from [22].

related to the magnetic field [32,62].

Principles of the construction of the installation in Berlin have been subject of various studies [9,22,32,65,66]. Therefore, the consideration in this report will not be as extensive as in the aforementioned references. Emphasis will be put on characteristic features and new ways of applying the generator with subtle modifications and improvements in construction and usage. A general extensive discussion of the STC technique can be found in the literature [29,32,38,56,62].

### 3.3 Setup & Performance of the STC-Megagauss Generator

The Berlin Megagauss generator was designed to produce a 240 T field in a vertical bore of 10mm. Thus bath cryostats can be used in addition to flow type cryostats (see 4.4). The yield strength of copper allows nondestructive fields of up to 20 T. At higher fields, the coil expansion is only delayed by mechanical inertia and the containment of magnetic flux must be supported by short rise times. Limiting the radial expansion to 10% at 200 T yields a rise time requirement of  $2.4 \mu\text{s}$ , the most important technical boundary condition [32].

All electrical parameters as a current of 2.6 MA at 200 T are fixed by the rise time. A minimized inductance of 20 nH with reasonable margins for resistive losses in a system with capacitive energy storage, upper limits of 200 kJ and  $115 \mu\text{F}$  for energy and capacitance follow. Thus the Berlin generator is composed of 20 capacitors rated at 60 kV, 40 nH and  $6 \mu\text{F}$  each, and 10 rail gap switches, nominally 20 nH and 750 kA, 1 C charge transfer limitation [32,67].

The condition of 20 nH was met in other installations by large arrangements of parallel coaxial cables. The Berlin generator uses a parallel transmission line of aluminum, the strip line, with  $2.4 \text{ nH/m}$  at a plate separation/width ratio of 1/500. The easy assembly is supported by insulating sheets of polyethylenterephthalate [68] and polyimid [32,69].

Precise control of the ignition at high voltage as well as perfect synchronization of the



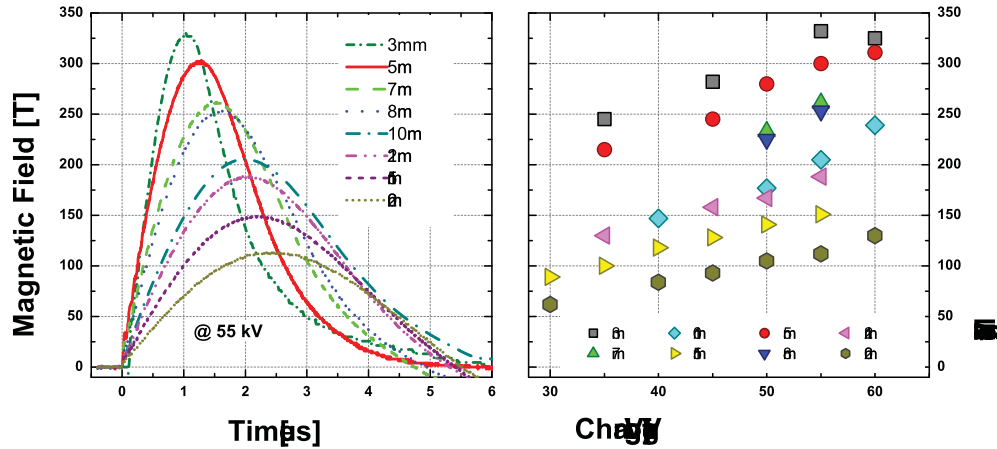


Figure 3.2: Left: Fields of coils with different diameters vs. time at a charging voltage of 55 kV [32] and new data for 3 mm. Right: Magnetic fields that can be obtained using the STC Megagauss generator at Berlin depending on the charging voltage and coil diameter as used in this thesis.

data recording equipment is realized by a 6 channel, 0.1  $\mu\text{s}$ -10 ms delay trigger unit that controls the recording systems as well as a 50/60 kV master/slave pulse generator with 10 ns rise time, a jitter of 1 ns and separate output channels for each rail gap switch that are organized with two capacitors each in a total of ten modules to prevent disastrous accidental discharges. The modules are insulated versus high voltage, interconnected only by 100 k $\Omega$  resistances which are part of the charge and shutdown circuits.

Electromagnetic forces acting on the coil will to a smaller extend affect the strip line as well. A rigid heavy weight support was, however, found unnecessary in favor of a suspension frame with flexible shock absorbers for the aluminum plates. The coil is clamped by hydraulics to withstand the enormous mechanical stress [32].

The physical setup of the Megagauss generator with the capacitor bank is shown in fig. 3.1. The left hand side shows a side view, the right hand side a front view. The two conductor plates of the stripline center in the ten modules each consisting of two capacitors and one switch. The coil (therefore the field) is situated at the end of the triangular ends of the strip line. A detail of the rail gap switches is given in fig. 3.1. Schemes of the electrical setup are given in fig. 4.5.

The high voltage trigger-discharge operation produces tremendous electromagnetic perturbations and bears the risk of fatal accidents. Therefore an interlock secured high-frequency-proof FARADAY cage houses all high-voltage equipment [32]. As the Department of Physics of the HUMBOLDT-UNIVERSITÄT was moved to the ADLERSHOF campus in early 2003 the FARADAY cage was improved and the signal-to-noise ratio of optical experiments significantly enhanced (see chapter 4). The old cage of copper mesh was replaced by a cage made of solid plates of steel [70].

The achievable magnetic fields, sweep rates and times between up and down sweep positions are given in table 3.2 for the STC generator of Berlin and a selection of other pulsed magnets. It is clear that eddy currents at a appreciable magnitude will only occur

in STCs and flux compression methods. A example of the magnetic field pulse shapes and magnitudes that can be obtained semi-destructively is given in fig. 3.2.

### 3.4 Nondestructive Operation of the STC up to 65 T

Previous studies in STCs predominantly took advantage of the high magnetic fields generated. In this study, the transient character of the pulse is of priority interest. Reinforcing the STC promises a transient magnetic field with several field reversals and small damping constant. Similarly, developing recoverable, reusable coils going along with the generation of comparatively low magnetic fields has been suggested in early investigations on STCs [52, 56, 57].

Reports on nondestructive operation of massive STCs [52] categorize nondestructive experiments into three categories: unstable (2-3 discharges), metastable (5-10) and stable (>20). The reported fields for copper are 65 T, 45-55 T and 40-50 T, respectively, in a 1 cm bore, with ranges depending on coil geometry.

Nowadays, the idea of a nondestructive use of a STC generator by a simple steel reinforcement has already been established in Japan to find the optimum setup before the actual experiment. A simple steel reinforcement was used in fields of a few Tesla up to ten times [62, 71]. A further stimulus was introduced by the proposed study of magnetization experiments that required a high  $dB/dt$  rather than a high magnetic field itself [72].

Thick walled coils manufactured by pressing heavy metal rings, e.g. from stainless steel, on to the outside of lightweight coils have been investigated [57]. The so called "jacketed" coils were used for tests of equipment before the actual experiments. Fields of 50 T have been produced up to 10 times with small readjustments after each shot.

However, the loss in the field to current ratio was larger than the modest gain in additional confinement [57]. The use of denser materials like tantalum supports the inertial mechanical confinement. Various studies have obtained promising results with denser metals [38], this was not part of the present investigation as an installation without significant changes to the coils themselves was required.

All supplied coils in the scope of this study were light weight coils made out of 3 mm copper at a inner diameter  $d$  to length  $w$  ratio of 1:1 and a feed flange angle  $\alpha$  of  $45^\circ$  as is shown in fig. 3.3 [32]. For the experiments with reinforcement coils of 15 mm inner diameter and length were used, as these reasonably set the ratio of experimentally usable volume to fields generated, typically 140 T at 50 kV discharges without reinforcement.

Regarding the experience with nondestructive pulsed magnets [38, 39] and nondestructive STCs [52, 57] a realistic goal was to obtain 60 T in a nondestructive way on a STC generator using a steel reinforcement on a 15 mm coil. The engineering of this project was carried out in collaboration with R. Chodziesner-Bonne [73] for design A as given in figure 3.3 and design B was developed by A. Kirste based on the results of design A.

Design A follows a straightforward approach of rigidly reinforcing the STC. Preliminary designs had shown that the feed flange must be as rigidly reinforced as the coils itself. The steel reinforcement is manufactured to match exactly onto the STC, it is even held by the single turn coil. There is also a direct contact of the copper of the coil to the steel reinforcement. This is equivalent to what has been investigated before [52, 57]. Design B has no direct contact from the coil to the reinforcement. Insulating layers of

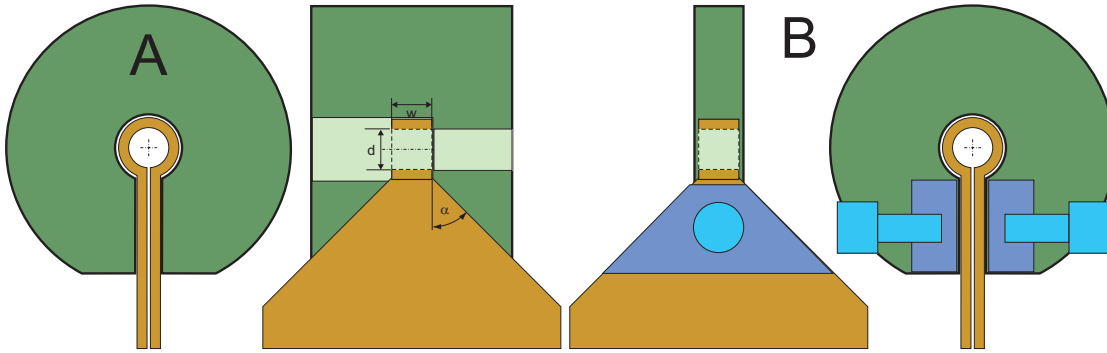


Figure 3.3: *The principle arrangement of the reinforcement on the STC. Left to right: bottom view design A, side view cut along axis design A, side view cut along axis design B, top view cut along axis for design B, explanation in the text.*

KAPTON [69] are placed between coil and reinforcement. The coil is fixed by tightening the screws using the threading of the reinforcement as depicted in figure 3.3 at the feed flange. A design corresponding to type B was also developed at Los Alamos [74].

The magnetic pressure of  $p = B^2/2\mu_0$  yields the value of  $p_{60T} \approx 14 \text{ t/cm}^2$  at the aimed maximum field of 60 T. A steel with the suitable mechanical properties of as high elastic limit and high notch impact value was chosen with the steel guide [75]. The reinforcement was accordingly manufactured out of 1.7225 or 42CrMo4 steel [73].

The reinforcement as depicted in fig. 3.3 was tested with a series of experiments aiming at both, the highest obtainable field without coil destruction and the investigation of the re-usability of the coil for succeeding experiments, respectively.

Regarding the maximum achievable field with reinforcement both designs showed the same value of  $\sim 65 \text{ T}$  with one experiment possible before the coil must be substituted. 55 T fields are easily obtained and can be reproduced up to three times without unmounting the coil. Successive fields generated are slightly smaller than the first field generated on the same coil. This is due to the coil movement that cannot be fully prevented and the coil dimensions do acquire the reinforcement inner diameters. When used with 40 T series up to ten experiments can be performed without changing the coil. All but the first experiment of a series generated approximately same field traces with similar peak fields and oscillation periods. The values do correspond to the previously reported categories [52].

However, there are differences between the two designs regarding dissipation of currents and ease of use. Design A is slightly easier to mount, yet coil exchanges / replacements are more cumbersome than with design B. The maximum field is limited by the tensile strength of the reinforcement, at the maximum field of 65 T cracks in the reinforcement as well as deformations have been found. The re-usability however, is limited by the coil. Parasitic effects caused by the heating and magnetic pressure. E.g., the magnetic saw effect [52] produces coil deformations which ultimately lead to the disruption of the coil. These effects are cumulative and limit the number of available experiments on the same coil even at comparatively low fields.

It must be noticed that with design A the charging voltage to produce 65 T is 35 kV as given in figure 3.4 compared to 25 kV for design B. The lower discharging voltage for design B to achieve similar fields holds true for all fields. Correspondingly, for the same discharging voltage fields produced by design B reinforcement are substantially higher,

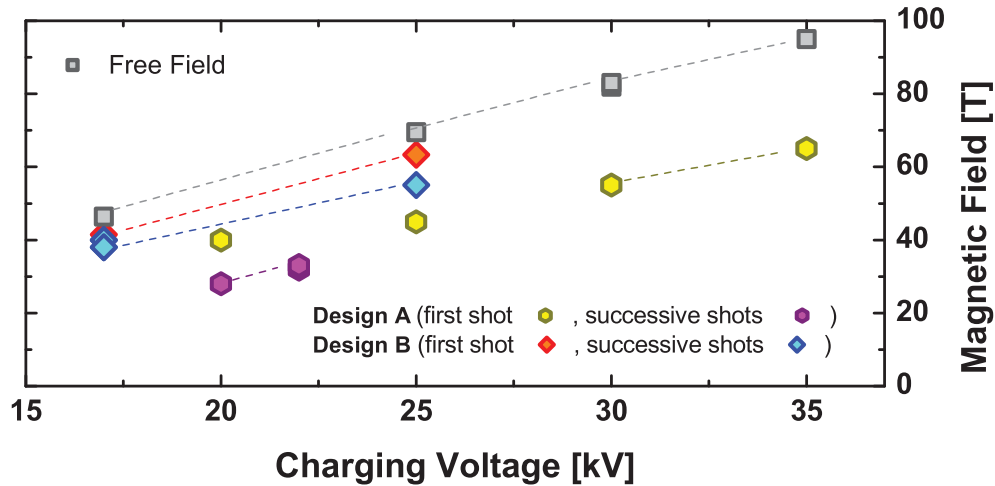


Figure 3.4: *Magnetic fields vs. charging voltages for free and reinforced coils (designs A and B). Lines are guides to the eye.*

$\sim 10\%$  smaller than field value without reinforcement as compared to  $\sim 33\%$  for design A and previous publications [52,57]. Higher fields may be obtained at an enormous expense of capacitor bank energy [55,57]. Raising the energy or discharging voltage, respectively, will reduce capacitor lifetime significantly and has therefore not been tried. A smaller discharge voltage is favoured.

The differences in achieved field between design A and B are attributed to dissipation of current into the reinforcement of design A. Moreover, a reinforcement with electrical contact to the STC generator itself forms an inductance that is larger than the one of the coil resulting in a lower field produced. The latter has been found in Los Alamos accordingly [74]. It should be pointed out that design B gives much higher field homogeneity and is therefore applicable to magnetization measurements and other experiments that require uniform fields over a larger volume [76].

An important feature of the magnetic field obtained in this non-destructive operation of the STC generator is the small damping of the oscillating magnetic field. The magnetic field has a period of  $\approx 12\ \mu\text{s}$  for a full sine. As shown in fig. 3.5 up to 4 full periods have been observed with fields larger than 10 T compared to a maximum of two full periods in semi-destructive operation. Optical traces of features in low field suggest a field oscillation for a much longer period as seen in figure 4.10. If the magnetic field is assumed to be of the following form:  $B(t) = B_0 \sin(\omega t) e^{-\alpha t}$  we can deduce the damping factor  $\alpha$  which is  $\alpha \approx 3 \dots 5 \cdot 10^4 \text{ s}^{-1}$  and thus substantially smaller than in non reinforced fields ( $\alpha > 7 \dots 50 \cdot 10^4 \text{ s}^{-1}$  with increasing field magnitude) [52].

The repetition rate of experiments was drastically increased as 15 experiments can easily be carried out in one hour as compared to the rate of one/two room temperature experiment(s) in two hours or two low temperature experiments in one day at semi-destructive operation. This constitutes one major advantage over using low charging voltage without reinforcement to perform the experiment [32], other advantages being

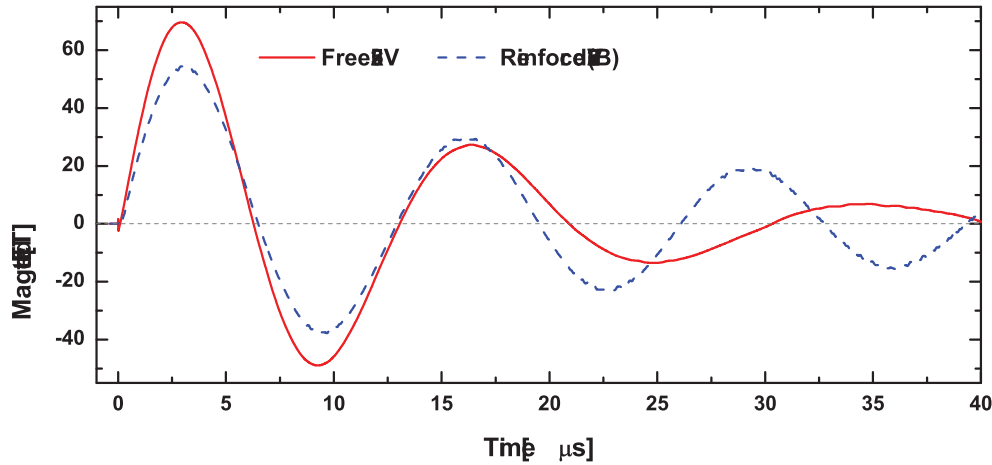


Figure 3.5: Magnetic field obtained by discharge with and without reinforcement given for design B. Please note the behavior at long times. The reinforced field is given by the dashed line.

the higher experimental volume usable and the significantly smaller coil deformations.

Hysteretic phenomena in this magnetic field range and timescale can be investigated thoroughly. The typical dependence on sweep rates can excellently be studied in that way as the sweep rate changes in small steps about one order of magnitude in one experiment for nondestructive fields, big steps for semi-destructive fields.

The field reversal every  $6 \mu\text{s}$  for a time longer than  $40 \mu\text{s}$  with a very small damping constant provides a novelty to solid state science. Although comparable magnetic field magnitudes are available with both steady and nondestructive pulsed magnets as well, usually the field sweep rate is more than three orders of magnitude slower, thus inapplicable to the study of relevant electronic processes in semiconductors with the method described here. A field reversal is seldom used in either of these methods [77] and, if used, several orders of magnitude slower.

### 3.5 Measurement of the Magnetic Field Intensity

The magnetic field is monitored by an inductive pick-up coil. The pick up coils are wound of  $80 \mu\text{m}$  KAPTON-insulated copper wire. A single loop is glued onto a tubular ceramic holder of  $2 \dots 2.5 \text{ mm}$  diameter. The voltage is proportional to the time derivative of the enclosed flux. The area of the pick up coils is determined by comparing its response to a AC signal of  $\sim 100 \text{ kHz}$  with that one of a standardized coil with precisely known area. Thus the pick up area can be determined to an accuracy of better than 1%.

Voltages of up to  $1.5 \text{ kV}$  can be induced for field slopes of  $0.1 \dots 0.2 \text{ T/ns}$ . The voltages are integrated before being digitized and stored. Thus the rail-gap-trigger noise is attenuated and gives an accurate field trace representation. The integrator is compensated for the serial resistance of the integrating capacitor [78]. However, its finite RC time constant  $\tau \approx 10^{-3} \text{ s}$  as well as its input resistance  $R_D$  and capacitance  $C_D$  cause

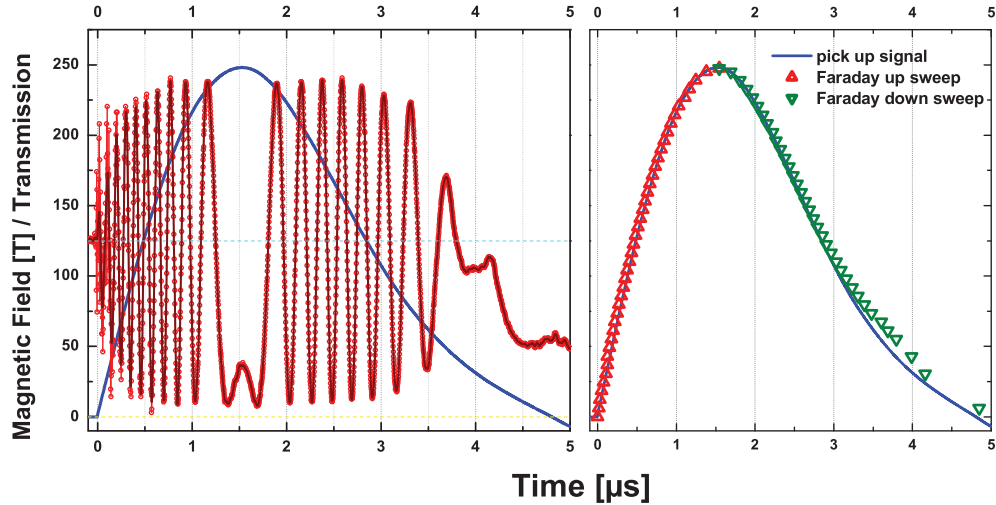


Figure 3.6: *Left: FARADAY rotation angle of CdS [22, 79]. Right: the field traces as obtained from FARADAY rotation (symbols) and integrated pick up signal (line).*

corrigible systematic errors:

$$\int^t U(t') dt' = R(C + C_D)U_{\text{ind}}(t) + (1 + R/R_D) \int^t U_{\text{int}}(t') dt' \quad (3.4)$$

where  $U$  is the input voltage that is detected,  $U_{\text{ind}}$  the voltage induced in the pick up coil and  $U_{\text{int}}$  the RC integrated voltage at the recording instrument input. [9]

A fiber optic transmission system is used to provide galvanic isolation. A digital system combines integrator, digitizer, intermediate storage, electro-optical converter in a well-shielded box inside the FARADAY cage. The 8 bit digitizer has a sampling rate of 200 MS/s, the data are stored in a 8 kByte FIFO memory. For a 200 T signal, the resolution is better than 1 T. [78] Nevertheless field values can be interpolated statistically to yield higher precisions of the field.

The field determination accuracy has been verified by using another method of field measurement [22, 79]. The FARADAY polarization rotation angle of CdS is known to be linear up to fields of 500 T for a wavelength of 632.8nm, the VERDET constant in that range is  $7.2^\circ / \text{T mm}$  [80]. Consequently it can be used to determine the magnetic field up to that value.

Using a He-Ne laser, light fibers and polished CdS samples with thickness  $1.020 \text{ mm} \pm 2 \mu\text{m}$  oriented perpendicular to the crystallographic c axis with polarizers directly attached to the sample the polarization angle could be recorded with a Si detector. Careful coverage of the setup against flash lights caused by the explosion of the coil is required to prevent overdriving of the detector.

Figure 3.6 gives the trace and the magnetic field calculated from original data of [22, 79]. Within experimental uncertainty the two traces are coincident, both independently yielding maximum field values of 247.5 T. However, experimental errors are 2 % for both methods.

A more careful analysis reveals that the magnetic field traces deviate from each other in the first 250 ns, that can be easily attributed to the ambient trigger noise, and at the zero crossing. The latter one shows no clear polarization on the FARADAY measurements probably caused by stray light from the coil disintegration. Peak fields are correctly reproduced, deviations between both methods occur at small field values.

The determination of the point in time at which the magnetic field is crossing zero is very difficult. Using the pick up coil method and a digitizer it depends significantly on the resolution of the digitized voltage. Generally the accuracy is no better than one digitizing unit, that is approximately  $2 \dots 4 T$  for measurements at high fields. This introduces an uncertainty of zero field position of about  $20 \dots 40 ns$  for the temporal position of zero-field when we assume a very large  $dB/dt$  of  $100 T/\mu s$ . For lower sweep rates the uncertainty in the timing of zero field is much larger. It is also increasing with number of zero crossing due to the damping character of the pulse.

To improve the resolution at low fields the pick-up area must be increased. That means, only low fields can be measured due to high voltages induced at high fields. When the pick-up area is reasonably increased, e.g. quadrupled, the uncertainty of zero field can be reduced to about 0.5 T. However, the time point of zero field can be fixed within 25 ns accuracy only at  $dB/dt$  of  $20 T/\mu s$ .

Other methods of determining the zero field position are HALL-probes, that cannot be used in transient magnetic fields due to the electric current they carry, or very sensitive FARADAY rotation probe, a crystal with very large VERDET-constant and large extension along the axis of magnetic field. In this case it becomes questionable if the magnetic field distribution is homogeneous over the crystal volume. Both methods have the advantage of a linear dependence on magnetic field of HALL voltage or FARADAY rotation angle, respectively, but the disadvantage of inapplicability in STC-generated fields.

## Chapter 4

# Cyclotron Resonance Setup

Cyclotron resonance experiments are among the most powerful tools in solid state science. Beside the obvious possibility of accurately determining band masses they can be used to investigate scattering mechanisms, impurity and exciton energy structures, interactions between carriers and phonons or carriers and carriers, respectively [11].

The free electron cyclotron energy corresponding to the separation of LANDAU levels  $\hbar \frac{eB}{m}$  as well as the ZEEMAN term of spin splitting  $g\mu_B B$  have nearly the same value. At 100 T this energy corresponds to 11.58 meV or 134K in terms of  $k_B T$ . Thus the extension to higher fields allows investigations at elevated temperatures compared to smaller fields.

Moreover, the necessary condition to observe the resonance  $\omega_c \tau = \mu B \gg 1$  can at high B even be fulfilled for low mobility samples, whose properties can not be directly determined by lower field methods. However, to observe the cyclotron resonance at very high magnetic fields high laser energies  $\hbar\omega$  are required according to the resonance condition  $\omega = \omega_c$ .

### 4.1 Parameters for Experiments in STCs

The experimental setup of the MEGAGAUSS GENERATOR results in several conditions for the equipment that can be used in an experiment. Major efforts aim at the protection of the devices from the strong electromagnetic pulse due to the magnetic field generation and the explosion related mechanical implications.

Therefore all magnetic field related equipment will be placed inside a FARADAY cage whereas all optical equipment such as radiation sources and detectors are placed outside of it. A straightforward requirement of this condition is the application of high power radiation source in combination with the sensitive detector system.

As the magnetic field will be transient during the experiment, any laser will be operated in *continuous wave* mode. With its high optical power, a heating of the samples by the laser must be avoided. The solution is the installation of a mechanical gate in the optical path before the sample. Furthermore high conductivity materials will experience high induced voltages. This is used for the inductive pick up probes for magnetic field monitoring, yet is not desirable for investigated materials as eddy currents will cause stress and heating up.

Another important condition to all experiments carried out in STCs is the limited amount of available space. Typically, in a 15 mm coil the available experimental volume will be about  $2.5 \text{ cm}^3$ . Thus the integration of magnetic field recording system, low



Table 4.1: *Parameters of the radiation sources and detector used. The specifications vital to the experimental setup are summarized in figure 4.2*

Laser:	Apollo 550 A	Edinburgh Instruments PL 3
Lasing gas:	CO <sub>2</sub>	CO
Operating temperature:	10°C	-10°C
Output wavelength:	9 - 11 μm	5.2 - 5.9 μm
Number of usable wavelengths:	> 50	> 20 (60 [82])
Peak Output:	30 W @ 10.59 μm	2.25 W @ μm [82]
Mode:	TEM <sub>00</sub>	TEM <sub>00</sub>
Beam diameter:	6 mm	8 mm
Detector:	MCT10PV-0025	Electro Optical Systems Inc.
Peak sensitivity wavelength		10.6 μm
3 dB cut off wavelength		11.7 μm
3 dB cut off frequency		100 MHz
Preamplifier 3 dB cut off frequency		80 MHz
Active area		0.25 × 0.25 mm <sup>2</sup>

temperature system and cyclotron resonance optical path must be arranged in very little space.

## 4.2 Radiation Sources

In the scope of this study a CO<sub>2</sub> Laser [81] has been used for wavelengths 9 - 11 μm (131 - 114 meV). The relevant parameters are given in table 4.1. Moreover, a CO Laser [82] for wavelength 5.2 - 6 μm (238 - 203 meV) has been installed. Both lasers are operated in the continuous wave mode. The CO<sub>2</sub> has more than 50 output wavelengths and a maximum peak power of > 25 W.

The CO Laser has > 50 lasing wavelengths and a maximum single mode power of 2.25 W [82]. Though all wavelengths radiation could be detected at the laser output coupler with the detector used for CR, atmospheric absorption as well as mode beating reduces the number of usable wavelengths to about 20, yet covering the full range. It has not been tried to isolate the optical beam from ambient air to provide less absorption. The relative output powers and atmospheric spectral profile in the relevant energy range are given in figure 4.2

Both lasers have shown no detectable power output fluctuations during ~ 0.5 ms thus providing sufficient short-time stability to perform experiments with the STC setup.

The installation of a vertical bore system requires the use of mirrors to guide the beam. As the direction has to be changed at least twice from the horizontal laser to vertical through the setup to horizontal to the detector, the optical path becomes much longer compared to the STC systems with horizontal setups in Tokyo or Los Alamos. The total length of about 9 m requires several focusing optics.

The optical path is given in figure 4.1. Focal mirrors with  $f = 340$  cm and  $f = 200$  cm and plane mirrors are used to focus radiation onto the sample and detector. The spatial beam profile is GAUSSIAN and the optics have been chosen accordingly [78]. The resulting

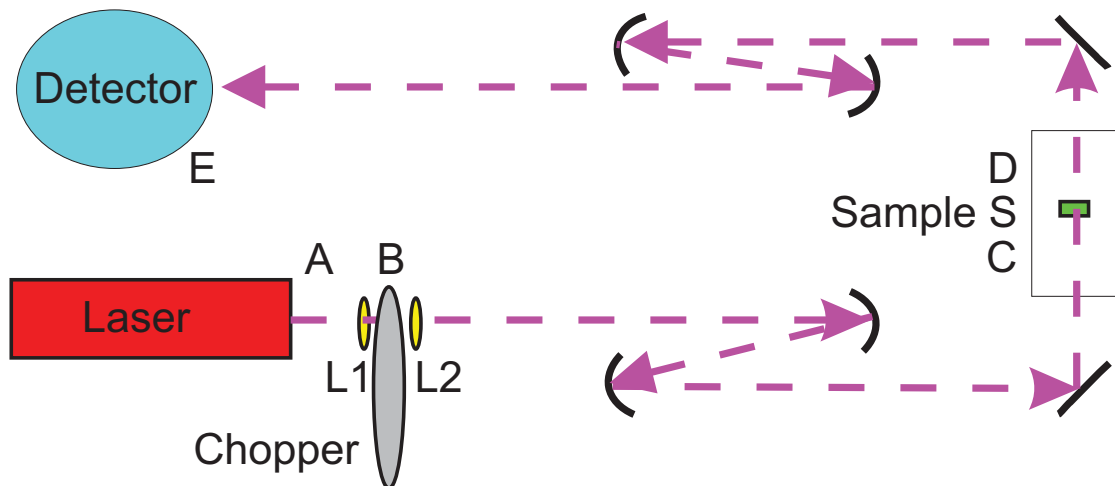


Figure 4.1: Schematic optical path for infrared radiation in the STC setup. Positions of relevance for alignment are given with capital letters. Apart from the obvious points A, B, S & E, points C and D mark the bottom and top of sample holding equipment.

Table 4.2: Beam Diameters in the optical path as marked in figure 4.1

Position:	Laser A	Chopper B	Bottom C	Sample S	Top D	Detector E
Beam waist CO <sub>2</sub> :	6 mm	< 0.3 mm	2.7 mm	< 0.9 mm	2.7 mm	< 1 mm
Beam waist CO:	8 mm	< 0.3 mm	2.5 mm	< 0.9 mm	2.5 mm	< 1 mm

beam waists are given in table 4.2.

The chopper runs at a frequency of 18 Hz and opens gate for 250  $\mu$ s, thus giving a dark to light ratio of over 200:1 or, at a Laser output power of 1 to 25 W, an average power on the sample of < 5 mW (CO) to < 100 mW (CO<sub>2</sub>). Measurements of laser power in the optical path showed a strong decrease in power for CO<sub>2</sub> so that the real power on the sample is at least one order of magnitude smaller. The reasons for this drop are probably atmospheric absorption or beam divergence losses. The AR coated ZnSe lenses L1 / L2 with a focal length of 50 mm create a focus spot much smaller than the chopper gate to provide rectangular temporal shape pulse with flat top and focus the beam after the chopper onto the sample focusing mirrors.

### 4.3 Detector System

The applied radiation sources require an appropriate detection system. Thus a HgCdTe (MCT) detector is used with an energy gap matched to detect radiation of wavelengths smaller than 12  $\mu$ m. Additional parameters are given in table 4.1. The spectral response is given in fig. 4.2 in vacuum (smooth curve) and in ambient air with two different water vapor concentrations. The bandwidth of 60 MHz enables the data to be taken with a maximum resolution of 17 ns, corresponding to  $\approx 0.5 \dots 2$  T resolution in magnetic fields generated by STCs depending on sweep rate.

The detector and its preamplifier are housed in a metallic box outside the magnetic

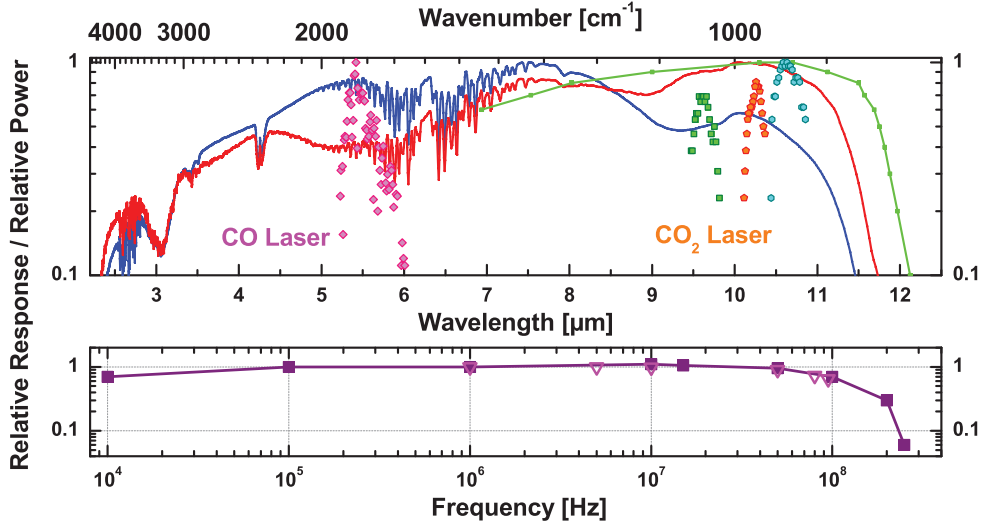


Figure 4.2: *Top: Spectral response of the MCT detector according to manufacturer and measured in ambient air by FOURIER transform infrared spectroscopy. Output powers normalized to the maximum intensity of each laser for available lines are given for comparison as dots. 9 – 11 μm : CO<sub>2</sub> Laser; 5 – 6 μm : CO Laser. Bottom: Frequency response of the detector (squares, from [83]) and preamplifier (triangles, measured).*

field generator's FARADAY cage. The use of a triply coaxial BNC cable to transfer the data to two transient recorders HP [84] with 8 bit @ 1 GS/s and RTD [85] with 10 bit @ 200 MS/s screens the trigger noise on the up sweep data. Combined with the improved FARADAY cage of the new building the trigger noise is attenuated to the order of magnitude of the bit-noise of the digitizers. The principal arrangement is depicted in fig. 4.5. The arrows mark information flows during an experiment. The transmission data recording equipment including cables from the detector to the transient recorders is fully electrically screened. The sampling rates of the transient recorders are higher than the bandwidth of the detector (RTD 1.5 times, HP 8 times higher) thus giving a satisfactory data resolution. Though positions of resonances are limited by the resolution of the digital voltage converter of the magnetic field recorder, the optical traces are monitored with higher accuracy in line width.

#### 4.4 Low Temperatures

The ability to vary temperature over a wide range from room temperature to cryogenic temperatures is one of the most efficient methods of gaining insight on sample properties. Thus a cryostat system was used to vary temperature during measurements from  $\approx 6$  K to 300 K. In a transient magnetic field all parts of an experimental setup must be produced out of non-conductive materials to avoid compression caused by eddy currents [22]. The materials of choice for the flow type cryostat used are epoxy, glass or paper.

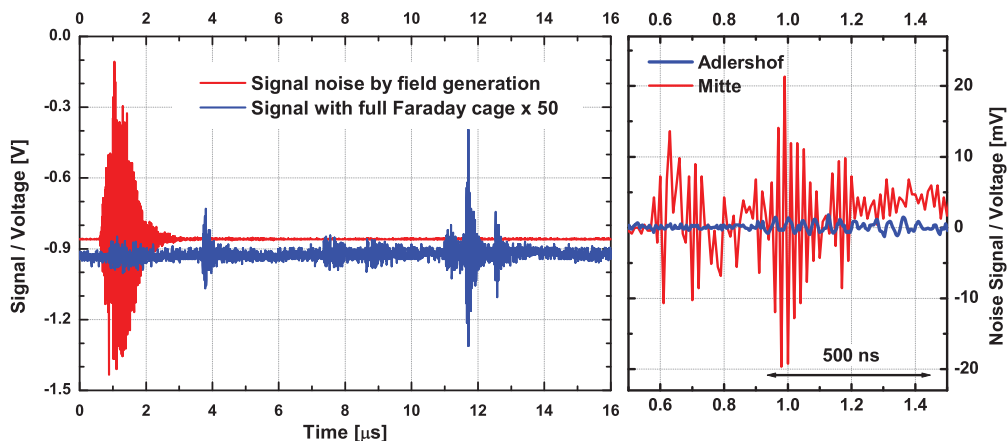


Figure 4.3: *Screening by the FARADAY cage. Data from the ADLERSHOF installation (left) showing the screening power. The signal curve with completely screened equipment has been amplified by a factor of 50. Right side shows the improvement in attenuation by the solid cage of ADLERSHOF, installed in 2003 without amplification of any of the curves.*

The cryostat used consists of three different concentric non-conductive tubes. The innermost tube is made of glass and houses the sample holding device with the thermocouple and pick-up coil. The tube with 5 mm inner and 7 mm outer diameters is filled with Helium as an exchange gas. This ensures the temperature transfer from the liquid Helium or Nitrogen surrounding the glass tube. Components of air such as Nitrogen and water vapor freeze out at temperatures above the targeted one and therefore the ambient air is evacuated and replaced by gaseous Helium. Evacuating the space around the sample provides optically better experiments, yet was frequently found to destroy sample and cryostat due to electric discharges.

The outer perimeter for the cryogenic liquid(s) is realized by an epoxy tube that is made low-temperature tight and connected to steel tubes at 7 cm distance from magnetic field by epoxy glue, Stycast 1266 [87]. The outer vacuum is kept by a glass fiber tube that is sealed with silicon-rubber tube and compressive fittings, respectively. This proves sufficient for the required thermally insulating vacuum of order  $10^{-4}$  mbar. The full cryogenic setup is depicted in figure 4.6.

The temperature was monitored using a CHROMEL / CuFe (0.15%) thermocouple [88] placed inside the cryostat at the sample position. A thermocouple made of this material is less precise as e.g. CHROMEL - Au, yet mechanically significantly more stable. The thermo-voltage is referenced to 77 K, filtered and amplified, transformed to an optical signal and transmitted to the thermo-interface where it is digitized and converted into a temperature value [78].

At present day there is no method of accurately determining the temperature of the sample during the magnetic field pulse. The method used gives the temperature of the heat bath connected to the sample at the start of the experiment. Controlling the surrounding pressure at the Helium transfer is the temperature adjusting method.

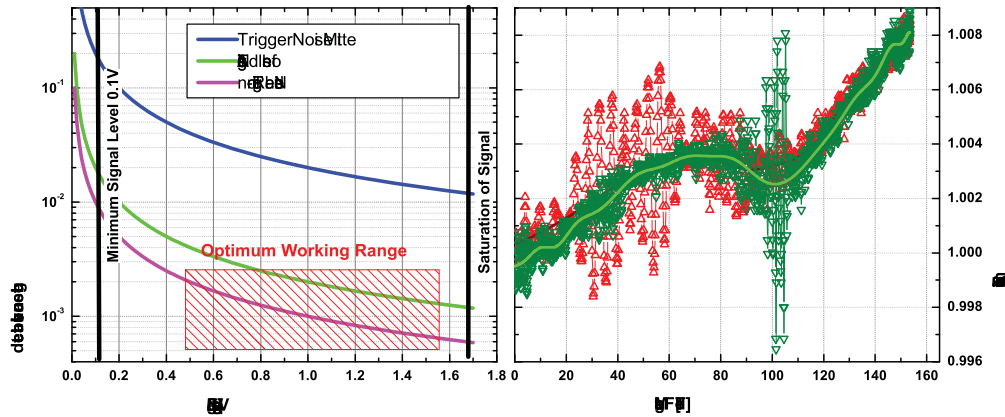


Figure 4.4: *Left: detectable resolution of any spectral feature in the CR setup of Adlershof. Right: the smallest detected resonance using the present equipment is of 0.2% absorption of 10.59  $\mu\text{m}$  radiation in a MQW sample of InGaAs/GaAs/InGaAs [86].*

However, due to the measurement principle there is an uncertainty in the actual sample temperature of order 2 K.

Summarizing the low temperature equipment used in this thesis we find the following:

- Room temperature measurements with CR are possible up to a 5 mm coil, thus a maximum of 311 T is accessible.
- The cryostat for 15 mm coil enables transmission experiments in a temperature range from 6 - 300 K. The  $^4\text{He}$  consumption is approximately 1 l per experiment, that can be performed up to a maximum field of 150 T.
- Special designs deviating from the standard cryostat, e.g. cooling from the outside directly on the glass tube without vacuum or protective gadgets, can be used to produce lower temperatures at higher fields or smaller coil diameters, respectively. [66]

## 4.5 Data Management

The use of several different recording mechanisms, field generation devices and safety switches requires elaborate coordination. The timing and steering of the experiment are realized by a 6-channel delay unit [22, 66, 78]. The warm up of the ADC precedes the chopper gate, the magnetic field generation, the magnetic field recording and the two optical recorders that are handled as given in figure 4.7. The most important characteristic of the timing is the precisely timed generation of the magnetic field and recording of all signals in the maximum of the laser pulse generated by the chopper. The present setup deviates from previous publications [22, 66] in the flat shape of the laser pulse that was realized by using the two lenses as shown in figure 4.1.

An experiment provides a magnetic field trace, two two-channel RTD traces of the optical signal with the high speed sampling rate of 100 MSa/s, and three channel record-

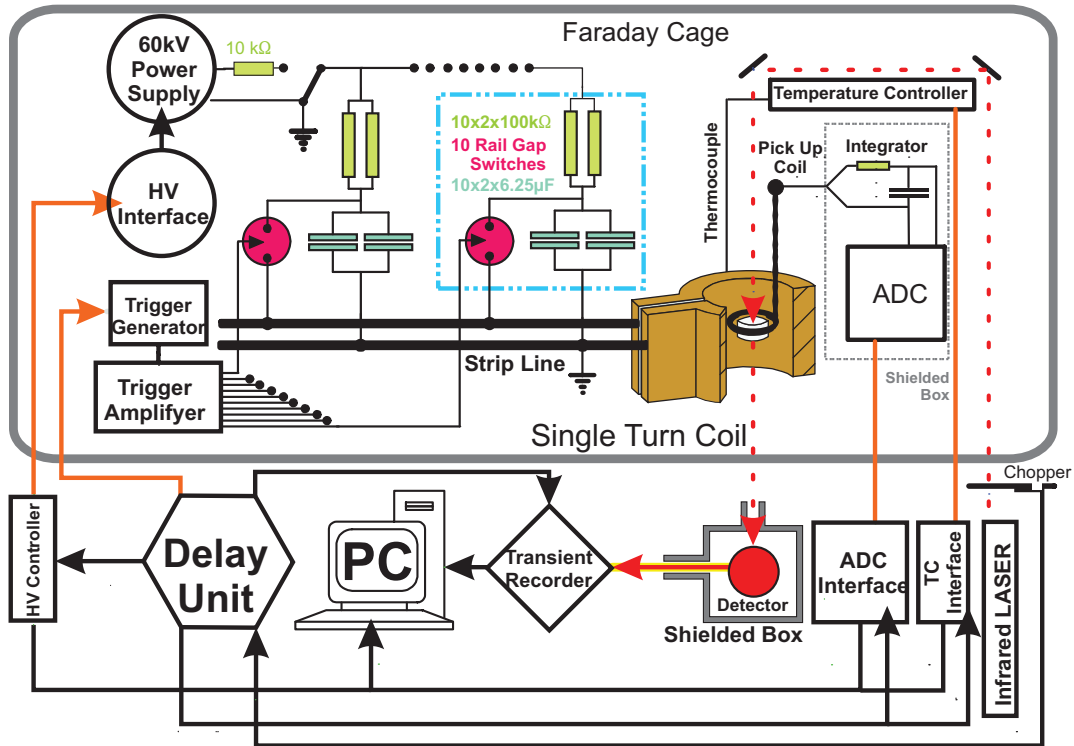


Figure 4.5: Schematic setup of a cyclotron resonance experiment using the STC Mega-gauss generator. Developed from previous publications. [66, 78]

ing of the optical trace by the HP with 500 MSa/s. All channels of both types of transient recorders are used with different sensitivities and / or offsets to provide the maximum information as well as best resolution in each shot. The RTD provides additional information with a 2 MSa/s over the full optical pulse. Thus information can be obtained at times before or after the magnetic field too.

The physical information is best obtained from the relation of the optical data with the magnetic field. Hence both traces must be related to each other by a processing routine. Though this is a straightforward routine, there are a few points that require attention.

The magnetic field trace will be smoothed in all cases as the resolution of 8-bit will cause steps in the field trace as well as jumps due to bit noise of the ADC. This is fully justified by the smooth pulse shape without artifacts that could cause similar features.

The different sampling rates of the field recording and the optical traces must be adjusted to obtain an appropriate spectrum. This means for the RTD that only one in two data points of the magnetic field trace will be used, whereas for the HP the sufficiently smooth magnetic field trace will be linearly interpolated to provide the appropriate values. It was confirmed that the sampling intervals of all the different recording systems were the same within the accuracy of the measuring period and sample intervals.

However, the most crucial aspect of relating the trace to each other is the time delay of the events in different curves. All of the recording devices (RTD, HP, ADC) have a set time they record before the magnetic field is generated. This purely equipment related delay time must be determined and should be highly reproducible. E.g. the optical trace

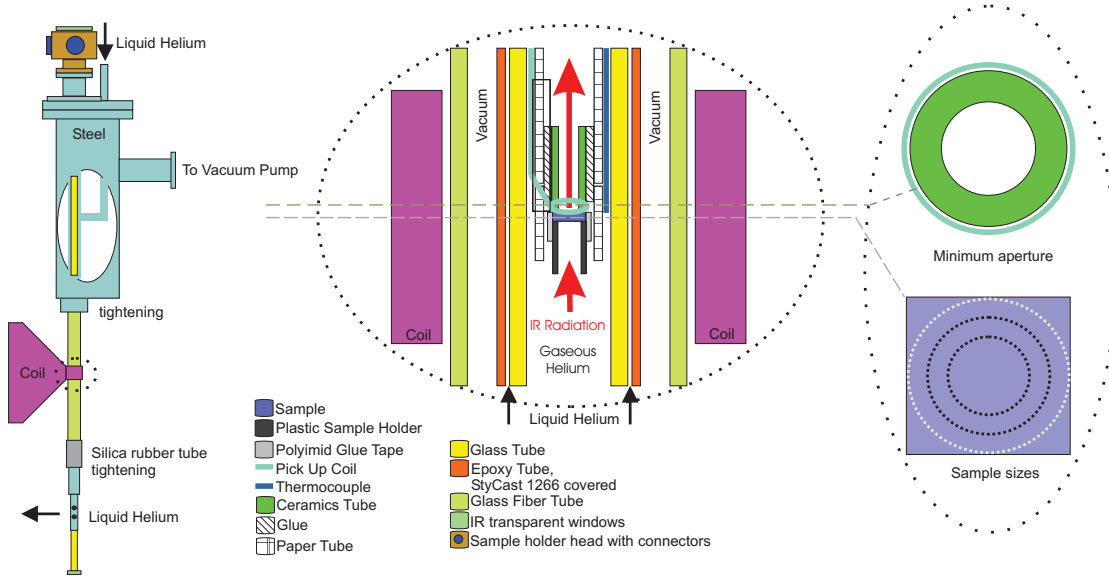


Figure 4.6: True to scale drawing of the flow type cryostat set-up for a 15 mm coil. For a smaller cryostat, e.g. 12 mm only the diameters of the outermost glass fiber tube and the coil are changed. Left: overall set-up, side view, center: arrangement of setup at place of sample, side view cut along axis, right: minimum aperture and pick up coil given for size comparison with sample sized at cross cuts as indicated by dashed lines.

signals have a delay to the magnetic field trace given by the impedance of the cable necessary to transfer the signal from the detector to the recorders.

To obtain a correct value for the delay including unknown sources of delay, extensive testing during this study with a strong signal at the point of the field generation, the noise with open cage, confirmed the set time for each recorder channel. The timing for each channel was reproducible within few ns. The time difference between different channels however was constant.

From the starting point of the trigger noise we find reproducibly within one sampling interval

- The high resolution RTD sampling starts for each RTD channel after  $t_0 = 256.16 \mu s$ . The noise signal can be found at slightly different times  $t_{ij}$  for each channel with  $\Delta t_{ij}$  in reference to  $t_0$ .
  - RTD #1, channel #1:  $t_{11} = 258.55 \mu s \rightarrow \Delta t_{11} = 2.39 \mu s$
  - RTD #1, channel #2:  $t_{22} = 258.56 \mu s \rightarrow \Delta t_{12} = 2.40 \mu s$
  - RTD #2, channel #1:  $t_{21} = 258.57 \mu s \rightarrow \Delta t_{21} = 2.41 \mu s$
  - RTD #2, channel #2:  $t_{22} = 258.59 \mu s \rightarrow \Delta t_{22} = 2.43 \mu s$
- The HP shows the noise signal at
  - channel #1:  $t_1 = 562 ns$
  - channel #2:  $t_2 = 570 ns$
  - channel #3:  $t_3 = 578 ns$

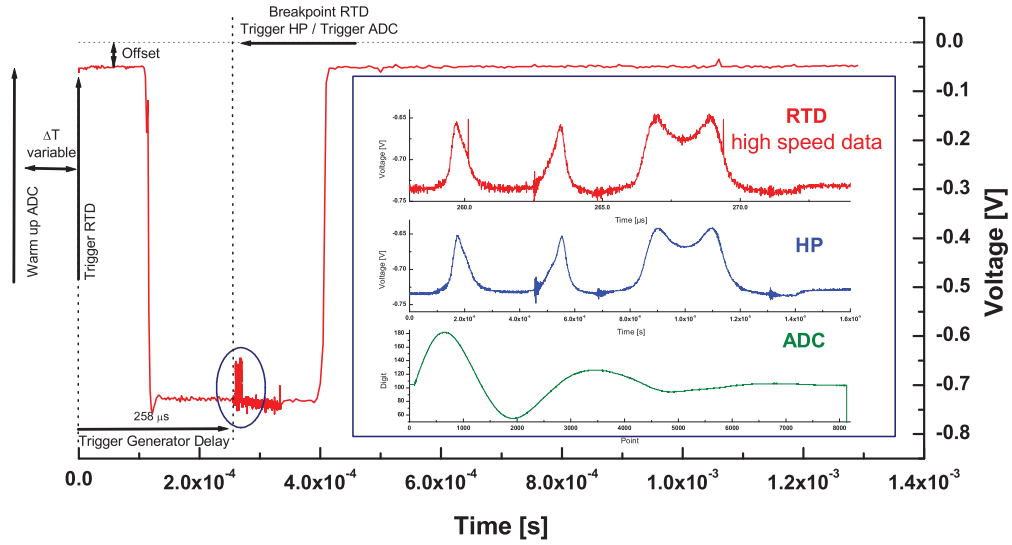


Figure 4.7: Raw data obtained of a typical experiment. The large layer shows the total record of the optical pulse. The warm up, trigger and breakpoints times are marked. The insets show the data to be evaluated, the high speed RTD data, the HP data and the ADC recording. Please note that all data are given in raw form.

- The ADC shows the trigger noise in this case starting at  $t_{ADC} = 445 \text{ ns}$ .
- The time difference between the magnetic field trace and the optical recorders results in a shift of traces vs each other that is dependent on the recorder and channel. It was found to be constant within one sampling base unit of 10 ns for RTD to ADC relation, 5 ns for HP to ADC relation.

Each experiment will be evaluated with respect to this timing. Moreover, as was shown in chapter 1, there is another, non equipment related component in each experiment, the magnetic field correction, that is proportional to the field derivative and must be subtracted from the magnetic field to obtain appropriate traces. However, the field derivative is determined numerically.

Please note that the actual time shift in terms of data points is depending on the smoothing algorithm used to obtain the magnetic field as well as optical traces. This must be included in the considerations and tested for each algorithm individually. It was found to be a shift of several data points in addition to the determined timing. The numerical smoothing causes a time-shift that becomes smaller with better resolution of the magnetic field trace. A maximum smoothing related shift of  $\Delta t_{\text{smoothing}} = 80 \text{ ns}$  was found.

With this considerations the traces have no uncertainty regarding the timing with respect to each other larger than one sampling point. This constitutes a major difference to previous measurements in Berlin as well as elsewhere [12, 35].

The full process of data processing is given schematically in figure 4.8.

The data processing routine as described till this point provides the magnetic field



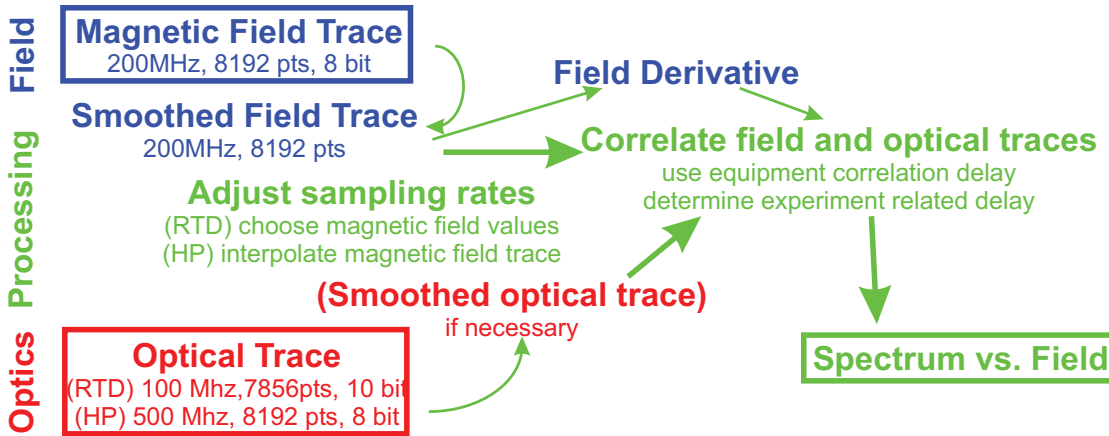


Figure 4.8: Scheme of the data evaluation process, initial and final information are framed. Explanation in the text.

and optical traces on a shared timescale with equivalent starting points. Now it is easy to obtain an optical trace vs. the magnetic field, yet for practical reasons, especially in the scope of this study, it is useful to split the trace into different sections. The first, further called the *up sweep* and denoted "A" in figure 4.9 is the trace from the start of magnetic field till its maximum, the second part, *down sweep* or "B", the trace from the maximum to the first zero magnetic field. "C" maybe referred to as *second up sweep* as it represents the trace from first zero to the next extremum (minimum) of field, "D" traces to the second zero crossing of the magnetic field.

In this study, the raw traces of up sweeps will be symbolized by  $\Delta$ , down sweeps by  $\nabla$ . Smoothed optical traces will be plotted over the symbols if the trace requires smoothing. All experimental traces given in this thesis have been reproducible.

The bit resolution of the ADC causes an uncertainty of the magnetic field zero position of one digit. Within this uncertainty of  $\Delta_0 \approx 0.5 - 2.5 T$  that is depending on the field resolution, hence the pick-up area, all resonance positions are shifted. Trace "A" is shifted to higher fields, trace "B" to lower fields by that value. This effect is a systematic error that has been corrected in fig. 4.9 assuming that cyclotron resonances occur coincident in up and down sweeps. This assumption is justified if the cyclotron resonance position is not subject to a hysteresis effect. However, hysteresis effects in an arbitrary resonance position in up and down sweeps can only be reliably observed, if they exceed the value of  $2\Delta_0$ .

The optical trace depicted in fig. 4.9 shows a type III hysteretic phenomenon as described in chapter 1. Moreover, down sweep trace is shifted to higher transmission than the up sweep trace but has resonant structures at similar magnetic field positions. The sample, OK 123, was bulk InSb. This demonstrates the usefulness of the excellent signal-to-noise ratio and the improved setup. Even in well known materials, new phenomena can be observed.

This phenomenon encourages further investigations in non-destructive fields. It will turn out that the feature is reproducible and similar observations can be found in other materials as well. A trace of MCT with a band gap comparable to InSb is given in fig. 4.10. As the resonances seem to be very much dependent on the sweep rate, the great advantage of using nondestructive fields is obvious.

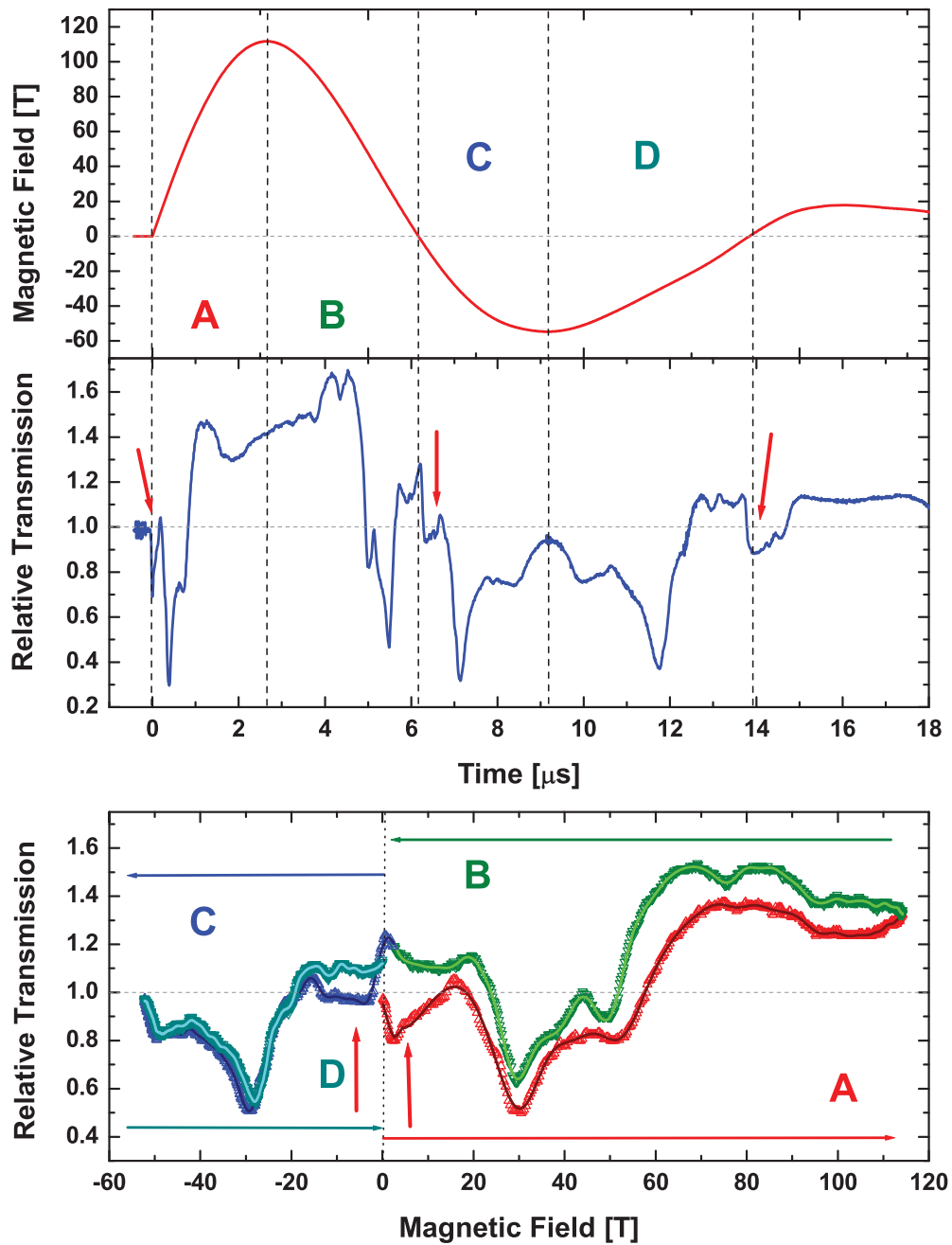


Figure 4.9: Final data processed with magnetic field / optical trace for the experimentally determined timing. Sections A, B, C and D mark the up-, down-, 2nd down and up sweeps respectively. The experimental traces are for an experiment of InSb in a coil of  $15 \times 15 \times 3 \text{ mm}$  at room temperature and  $\lambda = 9.67 \mu\text{m}$ . Please note the transmission drop at low field marked by the arrows.

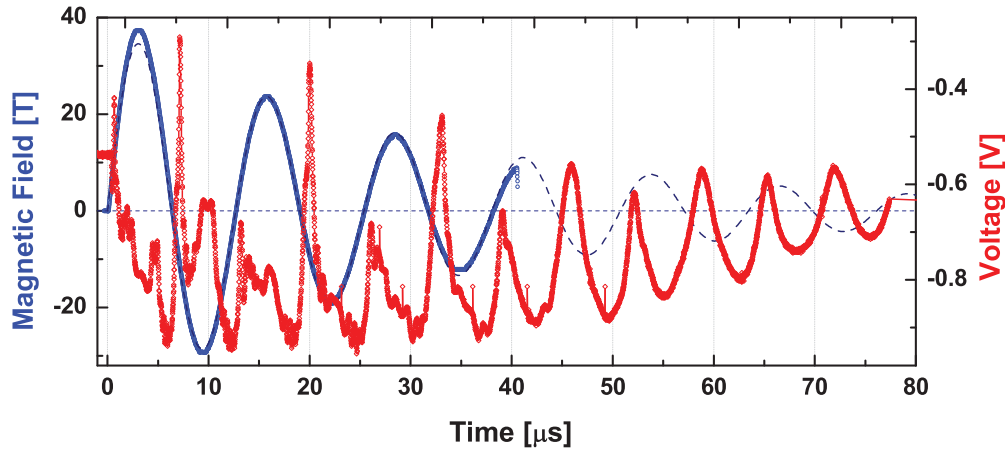


Figure 4.10: *Field and optical traces of an MCT sample at  $10.6\ \mu\text{m}$  and  $166\ \text{K}$ . The response to the field can be tracked to times even after the field recording stops and must be interpolated (dashed line). Here asymmetries are clearly detected and can be analyzed thus demonstrating the big advantage of nondestructive field generation.*

Summarizing the setup we can state the following improvements from previous works on the Berlin STC CR setup:

- The improved FARADAY cage and screening results in a better data resolution. The up sweep can now fully be included in analysis. The minimum detectable resonance is now at 0.2% (before 0.5% [79]).
- The data processing is based on precise knowledge of the timing of the setup. The uncertainties introduced by an inaccurate timing have been reduced to 1 sampling base unit.
- The uncertainty of zero field and the resulting shift in magnetic field position of up and down sweep of order one digit of the ADC can be determined and corrected.
- Nondestructive fields have become available as a tool for routine operation with advantages in the low field range as seen in figure 4.10.
- A radiation source in a matching wavelength range has been installed for routine operation (CO-Laser).
- The pulse shape is now flat within 3 digits of the optical recorders. That has been achieved by using ZnSe lenses to focus the beam. This allows a more reliable interpretation of differences in transmission intensity between up and down sweeps.

## Chapter 5

# Indium Antimonide

In this chapter we will investigate the origin and behavior of the type III hysteresis phenomenon that was found in InSb at very low fields as described in chapter 1 and the last chapter.

At first, the discussion will be focused upon the sample OK 123 because of the availability of a large wafer of this ingot. It was possible to make samples suited for various types of experiments out of different parts of this wafer. It is now assumed that the physical processes under investigation are uniform over the wafer and results obtained with one sample and one method apply equivalently to other sample pieces investigated with other methods. As the type III hysteresis effects was observed at elevated temperatures such as room temperature in the intrinsic conductivity range a non-uniform distribution of impurities within the wafer is negligible. For cyclotron resonance measurements there was no detectable difference in the spectra for three different pieces with similar proportions indicating sufficient uniformity of the wafer.

OK 123 is a wafer of CZOCHRALSKI-grown bulk InSb. It has been intentionally doped with Germanium to compensate the intrinsic electron concentration. It was designed to be used as an detector for mid-infrared radiation and is p-type at low temperatures. The hole concentration at 77K is  $p \approx 5 \times 10^{12} \text{ cm}^{-3}$ , the mobility  $\mu \approx 4.5 \times 10^3 \text{ Vs/cm}^2$  and the conductivity  $\sigma_0 = 4 \times 10^{-3} \Omega^{-1} \text{ cm}^{-1}$  [89]. The orientation is (211).

It should be emphasized that the material is p-type at low temperatures only. A temperature dependent HALL-measurement showed a change in sign of the HALL-voltage at a temperature of 150 K, below which the voltage was positive, above that value negative. This and measurements of the conductivity indicate that above 150 K the sample is intrinsically conducting with the fundamental contribution to conduction deriving from thermally excited electrons due to their higher mobility in comparison to holes.

### 5.1 An Infrared Transmission Experiment

We will start with a careful analysis of the infrared transmission trace reported in chapter 1. We used a sample of length by width by height  $2 \times 2 \times 0.5 \text{ mm}^3$  that can be well approximated by a cylindrical sample with radius 1.15 mm and 0.5 mm height. The experiment was carried out at room temperature at a wavelength of  $\lambda = 10.59 \mu\text{m}$  which corresponds to a radiation energy of 117 meV. That is well below the energy gap of InSb at room temperature of about 170-180 meV [25,90,91].

The acquired data is shown in dependence of time in fig. 5.1. The vertical lines

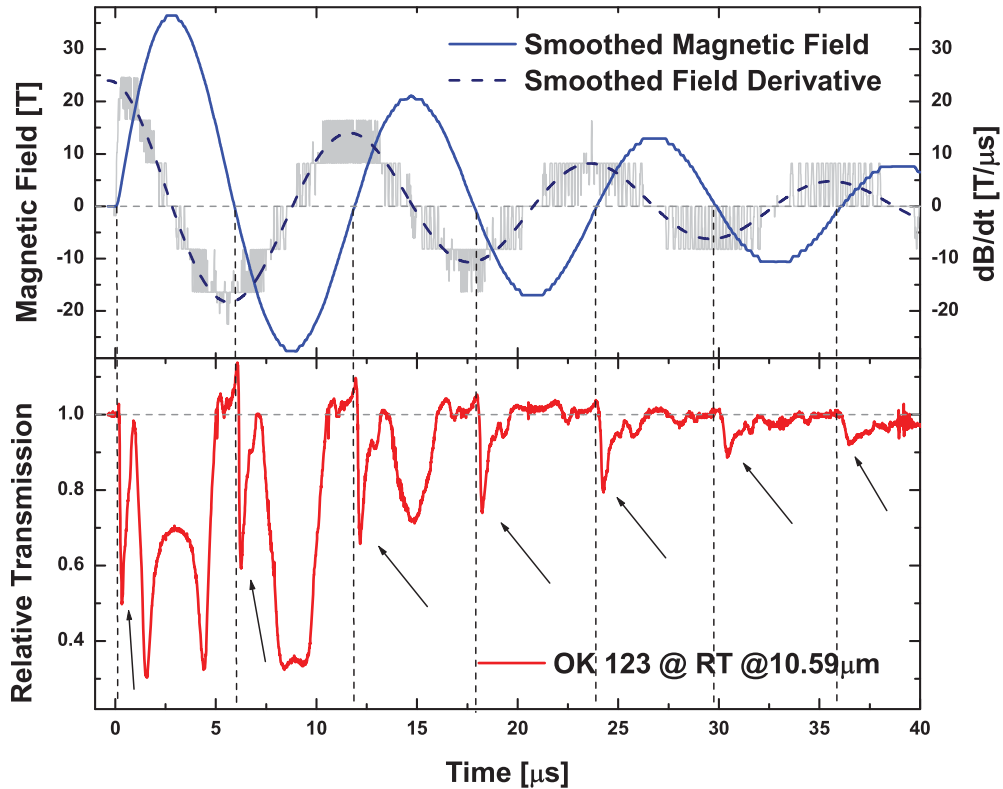


Figure 5.1: Initial field and optical traces vs. time of an infrared transmission experiment on OK 123. Explanation in the text.

represent the zero field position. It is clearly seen that the type III hysteresis indicated by arrows occurs shortly after the seven zero crossings of the magnetic field at  $t \approx 0, 6, 12, 18, 24, 30$  and  $36 \mu s$  but can not be observed before. The initial field rise is taken as zero crossing 1. The relative transmission drop of the phenomenon changes from  $\approx 51\%$  at the first up sweep to  $\approx 8\%$  at the seventh. The time difference between each occurrence of the transmission drop is nearly constant  $6 \mu s$ . It does not change by factor of 5. This suggests that the *time difference* between different sweeps is *not* a critical parameter, the origin of the transmission drop is not a relaxation phenomenon as in type I hysteresis.

A quantity that changes by a factor of 5 during this experiment is the absolute value of the magnetic field derivative. The magnetic field trace has been numerically smoothed. The dashed line gives a field derivative trace that has been calculated from a fitted field dependence on time. A numerical processing of the original field data yielded a trace with poor resolution as can be seen in the step like trace that is the original field derivative as processed numerically. This is caused by the digitizing process of the magnetic field acquisition. We will use the calculated curve for analysis to minimize uncertainty and avoid steps in the field derivative of  $8 T/\mu s$  within which we cannot distinguish its values.

Using the calculated curve we find the field derivative to decrease from  $\approx 25 T/\mu s$  at the start of experiment and thus the first observation of the transmission drop to  $\approx 5 T/\mu s$  at  $36 \mu s$  and the seventh observation of the transmission drop.

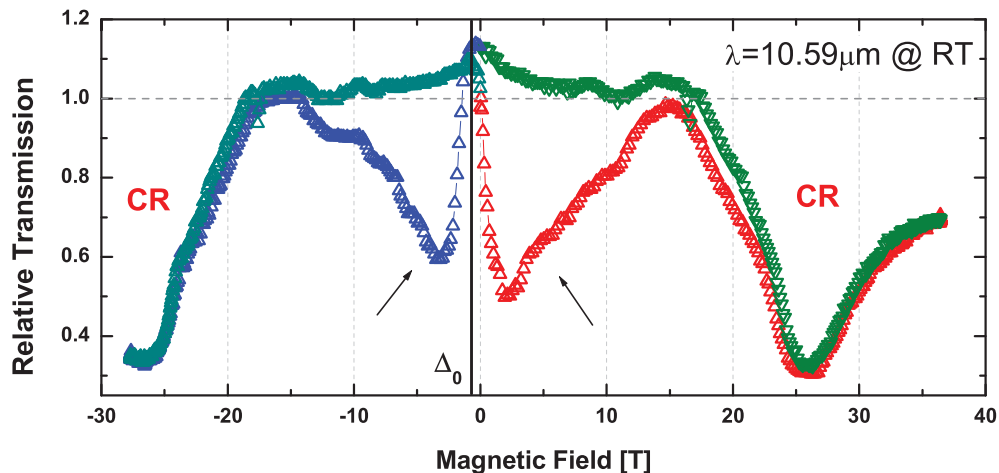


Figure 5.2: Infrared transmission vs. external magnetic field of OK 123. Explanation in the text.

Now we will process a transmission trace in dependence of the magnetic field to analyze the development of the transmission drop regarding its position in magnetic field. The resulting trace is given in fig. 5.2 for the first two up and down sweeps. The transmission drop is indicated by arrows, the electron cyclotron resonance is marked by "CR".

It must be pointed out that the resolution of the magnetic field in this case is about 1T per bit so that there is an uncertainty of zero field of about 1T. The cyclotron resonance position is  $(25.6 \pm 0.5) T$  in the first half sine,  $(26.8 \pm 0.5) T$  in the second. However, if we assume that the electron cyclotron resonance position is independent of field orientation and occurs at the same magnetic field value in the first and second half sine we can determine a zero field offset  $\Delta_0 = -0.6 T$  with the resulting magnetic field  $B = B - \Delta_0$  in the evaluation process. The value  $\Delta_0$  is indicated by the solid vertical line in fig. 5.2. The resulting electron cyclotron resonance position at  $(26.2 \pm 0.5) T$  is in excellent agreement with previously reported values [14–16].

If we refer all data to the value of  $\Delta_0 = -0.6 T$  we find that the maximum of the type III transmission drop occurs at  $|B| = (2.7 \pm 0.5) T$  in both up sweeps. This holds true at the other zero crossings too with an increasing uncertainty due to the digitized signal of the magnetic field trace. The *position* of the type III transmission drop in magnetic field *does not* change with time nor field orientation nor field derivative within experimental error.

Moreover, the shape of the transmission drop vs. the magnetic field does not change for each observation, only its magnitude. There is a maximum at  $|B| \approx (2.7 \pm 0.5) T$  and a sharp rise from zero field to that value and a less sharp decay after it. The magnitude of the transmission drop seems to be dependent on the field derivative. The magnitude of the transmission drop maximum  $T_m$  is given in fig. 5.3 in reference to the absolute value of the field derivative  $B_d$  for each observation of it. A linear fit of  $T_m$  to  $B_d$  yields a nearly proportional relation of  $T_m = (0.003 \pm 0.018) + (23 \pm 1) \times 10^{-3} B_d [T/\mu s]$  within

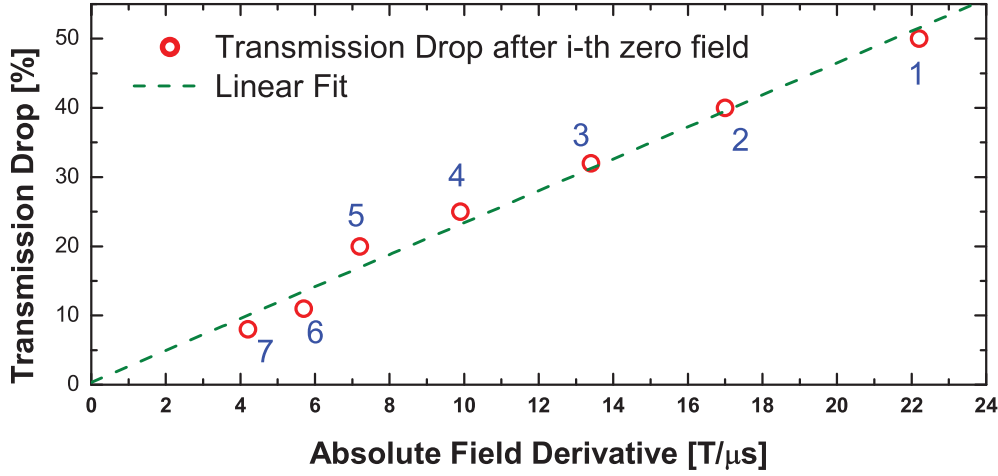


Figure 5.3: Dependence of the transmission drop on the absolute value of field derivative. The data points are given as circles with numbers corresponding to  $i$ , the number of occurrence in the optical trace. The time for  $i=1$  is  $\approx 0.15\mu s$ , for  $i=7 \approx 36.5\mu s$ . Error bars are smaller than the symbol size.

a probability of 99% at one standard deviation.

The value of the fit relation is valid for this one experiment only, at higher sweep rates of destructive experiments the transmission drop was found to be proportional to  $B_d$  but with a smaller proportionality factor.

To find further evidence for a dependence on sweep rate we have carried out an experiment in a slowly varying DC field with a sweep rate that is by a factor of  $10^9$  smaller. We have performed infrared transmission measurements in steady magnets using the same radiation source and detector as in the STC setup. After a gate the radiation was transmitted onto the sample and onto the detector by means of fiber optics [92]. The fibers are made of polycrystalline KBr. The fiber at the bottom of the magnet has been shaped as a U-turn with a radius of about 3 mm. The sample sizes were considerably larger than in STC setups, rectangular shapes with about  $5 \times 5 \text{ mm}^2$ . The thickness of samples, however, was the same as in the STCs as was the area where light was shone onto the sample. The signal was amplified and detected using the lock-in technique.

The magnet used was a superconducting magnet from OXFORD INSTRUMENTS. This magnet is capable of generating a maximum field 12.1 T when used at 4.2 K. The coil consists of filaments of  $NbTi$  and  $Nb_3Sn$  with a bore of 52 mm. It is possible to achieve 14.5 T with further cooling but that was not carried out as we are interested in the low field range. The sweep rate chosen was 12.1 T/8 min. The polarity of the field was not changed, yet traces for up and down sweep do not deviate from each other, just by a field independent offset that is caused by long time fluctuations of laser intensity.

The resulting trace of a down sweep is given in fig. 5.4. It has the best available signal to noise ratio of all recorded traces. For OK 123 there is no transmission drop in low field at all, a small change in transmission at higher fields is due to long time fluctuations of laser intensity that occur on a timescale of minutes. The signal to noise ratio is in

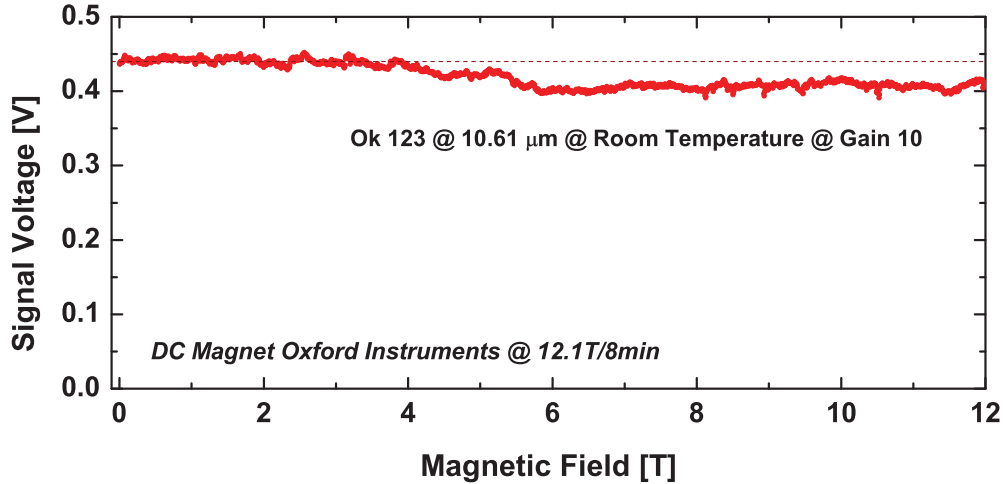


Figure 5.4: Infrared transmission through InSb sample OK 123 in a steady magnet that was swept at a rate of 12.1 T/8 min and  $\lambda = 10.61\mu\text{m}$  at room temperature.

general much poorer than in the STC equipment. This is caused by the several orders of magnitude smaller transmission through the fiber optical setup compared to the STC free space setup. The reason of the poorer transmission through the fiber system are the input and output coupling.

However, there is *no* indication at all that there is a resonance or transmission drop at fields up to 5 T at all in the DC trace. This trace is a clear indication that an effect of the magnetic field *magnitude* is *not* the origin of the transmission drop, but the transient character of the field generation in STCs. This trace and the findings reported above are a very clear indication that processes depending *linearly* on the *field derivative* are the cause for the type III hysteresis in OK 123.

As we have shown, processes that depend linearly on the field derivative are the electric field and the eddy current density. However, the transmission drop occurs only after zero crossings of the magnetic field which points to an eddy current related phenomenon with an asymmetry to zero field. This would involve the temperature rise, the pressure distribution and the radial electric field. We must determine the magnitude of these values.

## 5.2 Steady Field Transport

The starting point for any eddy current discussion is the measurement of the conductivity  $\sigma_0(B)$  with appropriate methods. Using a HALL-bar sample the conductivity was determined in a steady magnet with a lock-in technique. The results of the measurements are the transversal and HALL-resistances  $R_{xx}$  and  $R_{xy}$ . Transversal refers to the direction parallel to the applied current perpendicular to the external magnetic field, HALL to the direction perpendicular to current and field. A schematic drawing is given in fig. 5.5. The magnetic field dependent resistances are depicted in fig. 5.6 for room temperature.



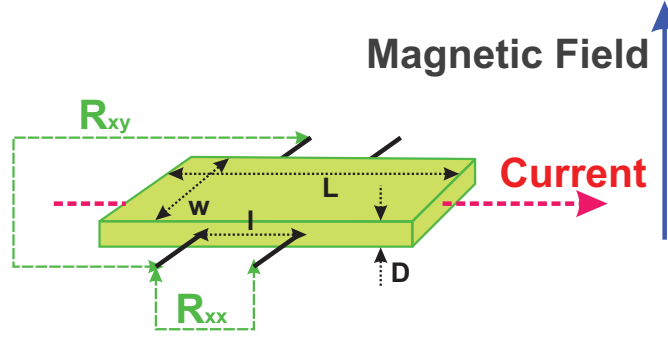


Figure 5.5: Schematic drawing of the HALLbar geometry with indicated resistances and measures with respect to the external field.

Assuming one dominant type of charge carriers at room temperature, the HALL resistance  $R_{xy}$  is given as

$$R_{xy}(B) = \pm \frac{1}{ne} \frac{B}{D} \quad (5.1)$$

when  $n$  is the carrier concentration,  $e$  the elementary charge,  $B$  the magnetic field magnitude and  $D$  the sample thickness [19]. The HALL resistance is positive for holes and negative for electrons. From the linear dependence of  $R_{xy}$  on  $B$  as seen in fig. 5.6 we can conclude that there is a constant electron concentration over this magnetic field range. With the sample thickness of  $D = (1.18 \pm 0.02) \text{ mm}$  and the elementary charge of  $e = 1.602 \times 10^{19} \text{ C}$  we obtain an electron concentration of  $n = (2.0 \pm 0.1) \times 10^{16} \text{ cm}^{-3}$ .

The conductivity can be deduced from the transversal and HALL resistivities  $\rho_{xx} = R_{xx} \times l / (D * w)$  and  $\rho_{xy} = R_{xy} / D$  where  $l$  is the length of the sample conductor between the two contacts used to measure the voltage, hence the resistance,  $w$  is the width of the sample as depicted in fig. 5.5. In the given investigation we had  $w = (1.96 \pm 0.02) \text{ mm}$  and  $l = (1.80 \pm 0.05) \text{ mm}$  with the total length of the sample  $L = (6.00 \pm 0.05) \text{ mm}$ .

The conductivity can be determined using

$$\sigma_{xx} = \frac{\rho_{xx}}{\rho_{xx}^2 + \rho_{xy}^2} \quad , \quad \sigma_{xy} = -\frac{\rho_{xy}}{\rho_{xx}^2 + \rho_{xy}^2} \quad , \quad \sigma_0 = \rho_{xx}^{-1} \quad . \quad (5.2)$$

The conductivity  $\sigma_0$  is relevant to all formulae for eddy currents. It is equivalent to the transversal conductivity for a vanishing magnetic field but has a substantially different dependence on magnetic field as depicted in fig. 5.7.

We find the conductivity  $\sigma_0$  to decrease from  $(173 \pm 10) \Omega^{-1} \text{ cm}^{-1}$  at zero field to  $(75 \pm 6) \Omega^{-1} \text{ cm}^{-1}$  at 1.5 T and  $\approx 4.5 \Omega^{-1} \text{ cm}^{-1}$  at 10 T. The conductivity is proportional to mobility, elementary charge and electron concentration  $\sigma_0 = ne\mu$ . The mobility of holes is two orders of magnitude smaller and therefore holes do not substantially contribute to  $\sigma_0$ . From the HALL-effect we know that the electron concentration does not change in this magnetic field range, therefore it must be a mobility effect that causes the decrease of conductivity with increasing field. Consequently we determine the electron mobility decrease from  $\approx 5.5 \times 10^4 \text{ cm}^2/\text{Vs}$  at zero field to  $\approx 2.5 \times 10^4 \text{ cm}^2/\text{Vs}$  at 1.5 T and  $\approx 1.5 \times 10^3 \text{ cm}^2/\text{Vs}$  at 10 T.

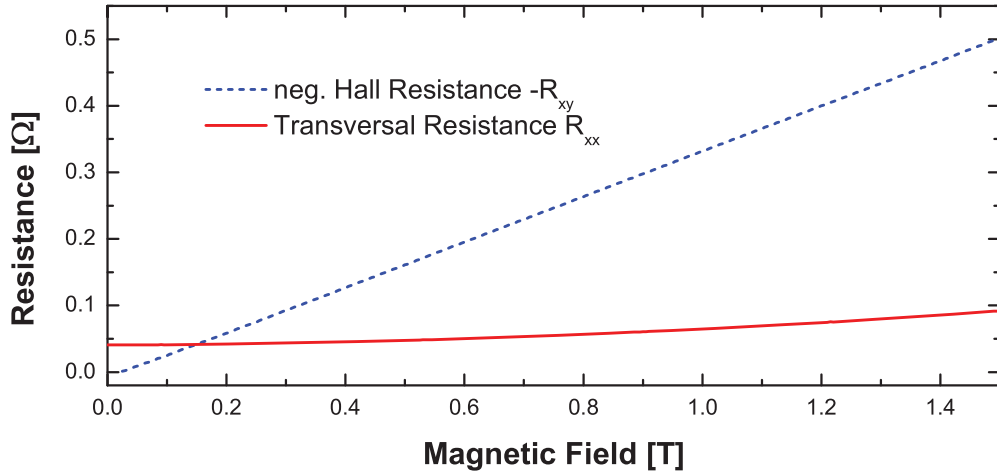


Figure 5.6: Steady field transport parameters at room temperature of sample OK 123. The HALL resistance has been inverted  $R_{xy} \rightarrow -R_{xy}$  in this graph.

The transversal conductivity on the other hand drops from  $(173 \pm 10) \Omega^{-1} \text{cm}^{-1}$  at zero field to  $\approx 6 \Omega^{-1} \text{cm}^{-1}$  at 1.5T. This shows the importance of distinguishing the conductivity  $\sigma_0$  from  $\sigma_{xx}$ , especially at high magnetic fields.

The values for conductivity at zero field as well as the mobility are in excellent agreement with available data in the literature for InSb in the intrinsic conductivity range at room temperature of  $\sigma_0 \approx 200 \Omega^{-1} \text{cm}^{-1}$  and  $\mu \approx 7.7 \times 10^4 \text{ cm}^2/\text{Vs}$  [90,91].

The temperature dependence of resistance and conductivity  $\sigma_0$  is depicted in fig. 5.8. It can be clearly seen that the intrinsic conductivity range is found at temperatures higher than 150 K. This is in excellent agreement with the change of sign in the HALL-voltage from positive to negative at this temperature value as has been observed in this series of measurements but not shown here.

When considering InSb in transient magnetic fields we must analyze the influence of the high induced voltage on the conductivity. In InSb the breakdown field is of the same order of magnitude as the electric field on the sample generated by the transient magnetic field. Phenomena such as impact ionization, avalanche ionizations and, if the two are non-negligible, related phenomena such as free carrier absorption must be considered. This also means that OHM's law breaks down, the current density is no longer proportional to the electric field. Nevertheless for this thesis we will use the term conductivity for the factor  $\sigma_0$  having in mind that it is not necessarily equal to the DC conductivity and not independent of the electric field magnitude.

In the literature we can find empirical formulae to describe the generation of carriers when undoped InSb is subject to a high electric field of order 30-300 V/cm at room temperature [93]. Although the measurement methods used in this reference applied an electric field of comparable magnitude to the present situation, it was applied for a smaller period of time, typically 250 ns.

The authors of [93] have combined available data [94,95] with data obtained by the HALL-resistance and light modulation techniques with a  $\text{CO}_2$ -Laser to yield a relation

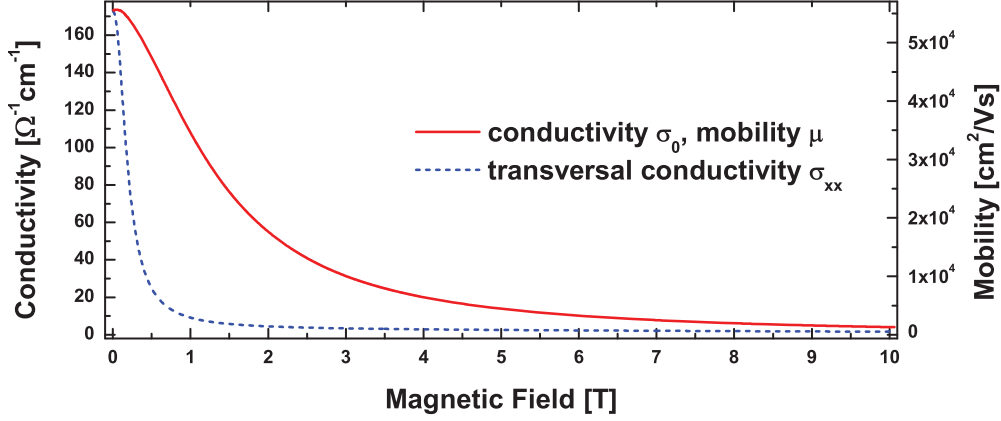


Figure 5.7: Conductivity  $\sigma_0$  and electron mobility  $\mu$  of InSb OK 123 at room temperature obtained with steady magnet. The transversal conductivity  $\sigma_{xx}$  is given for comparison.

between electric field and carrier concentration. It is pointed out that the absorption coefficient of the infrared radiation is the most sensitive probe to changes induced by an electric field as low as 30 V/cm. According to [93] the transparency of a sample is reduced due to free carrier absorption on excess electrons and holes.

However, they found a formula for the generation rate  $g(E)$  representing a steady state in which carrier generation and AUGER-recombination are in equilibrium

$$g(E) = 126E^2 e^{E/160} s^{-1} \quad (5.3)$$

when the absolute value of the electric field  $E$  is given in V/cm. Here the exponential factor describes the avalanche ionization at fields exceeding 160 V/cm whereas the first term describes the impact ionization. The steady state is acquired at timescales smaller than  $10^{-7} s$  [93]. The authors of [93] use a lifetime of hot carriers  $\tau_i = 5.7 \times 10^{-8} s$  to derive the generation rate. The change  $\Delta K$  of absorption coefficient  $K$  with the electric field is proportional to the change of carrier concentration [93] and both quantities are depicted in fig. 5.9. The dependence is described by

$$\Delta K/K = 126 \times E^2 e^{E/160} \times 5.7 \times 10^{-8} \quad (5.4)$$

It is seen that the absorption coefficient of  $K = (10.0 \pm 0.3) cm^{-1}$  at  $\lambda = 10.59 \mu m$  is changing by  $\approx 1\%$  at 30 V/cm and  $\approx 100\%$  at 200 V/cm. That means that a transmission drop at 200 V/cm will be about 50%.

The carrier concentration  $n$  is given by

$$n(E, t) = n_0 e^{g(E)} = n_0 \times e^{126E^2 e^{E/160} s^{-1} \cdot t} \quad (5.5)$$

Assuming an electric field present for about  $t = 1 \mu s$  we find that the carrier concentration is doubled for a field of approximately 60 V/cm. For the azimuthal electric field this may be well realized for high field experiments at the sample position  $r=R$  but cannot explain the observation of the type III hysteresis in nondestructive fields with azimuthal electric fields at zero magnetic field as low as 20 V/cm. At sweep rates of

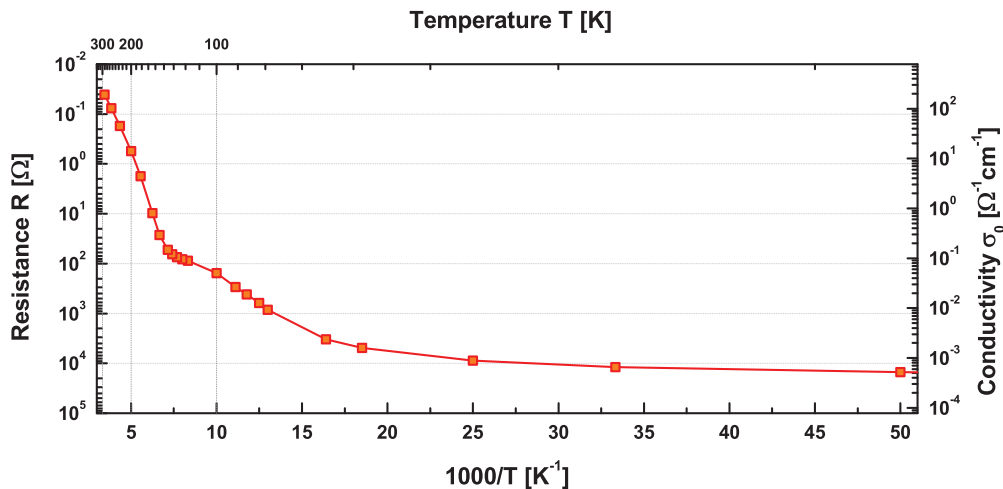


Figure 5.8: Arrhenius plot of the DC conductivity at zero magnetic field of sample OK 123 as a function of inverse temperature. The transition from p-type conduction to n-type intrinsic conduction occurs at a temperature of about 150 K or  $6.7 \text{ K}^{-1}$  in this plot depending on  $1000/T$ . This is in complete agreement with HALL-voltage findings as described in the text.

$\approx 4 T/\mu\text{s}$ , thus at  $R=1.15 \text{ mm}$   $E_\varphi = 22 \text{ V/cm}$  the hysteresis effect was still observed as was shown in the previous section.

Based on the above estimate we do not expect a substantial increase of carrier concentration in non-destructive fields due to the azimuthal electric field. The radial electric field is larger than the azimuthal electric field by a factor  $\omega_c \tau$ . That is a material dependent magnitude that can easily exceed the threshold values for avalanche breakdowns even in comparatively small samples.

Moreover, the generation of carriers at  $r=R$  is only relevant to the infrared transmission in the previously described situation in STCs if there is a mechanism that can transfer generated carriers from  $r=R$  to the center of the sample that is subject to the incident radiation. This may be provided by the radial electric field.

The conductivity, hence the mobility and  $\omega_c \tau$ , must be determined with methods in the exact same experimental situation of STC generated magnetic fields as applied for the infrared transmission experiments. The significant contribution of eddy currents have even led to a technique called *eddy current spectroscopy* in STC generated fields [96]. This contact-less method can be used to determine the behavior of conductivity in STC generated fields and will be discussed in the following section. It can however only be applied to bulk samples. For other samples such as layers and epitaxial samples, the influence of eddy currents can be evaluated with diameter dependent measurements.

### 5.3 Eddy Current Spectroscopy

In section 2.2.4 we have found that the magnetic field inside conductors is substantially different from the external magnetic field. We can use the magnetization techniques such

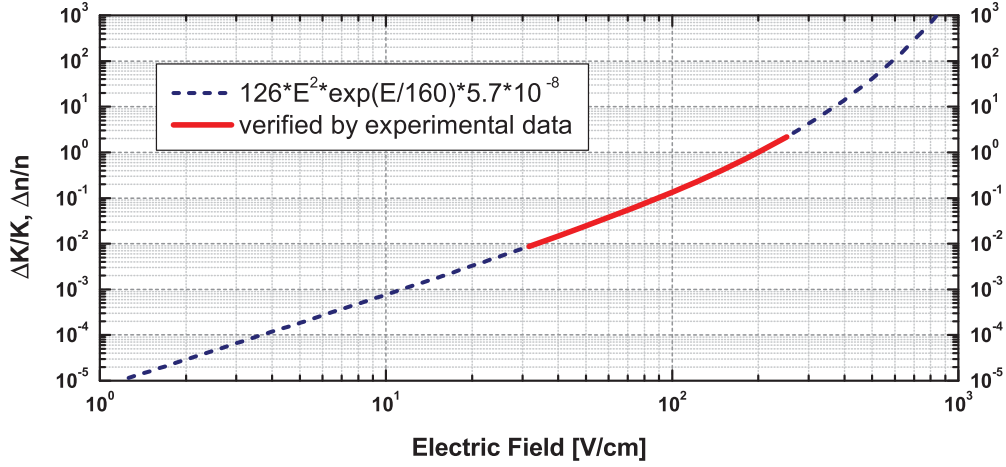


Figure 5.9: The dependence of the relative change in absorption coefficient  $K$  for  $\lambda = 10.59 \mu\text{m}$  and carrier concentration  $n$  on the electric field as determined by [93]. The dashed line gives the functional relationship that has been fit to the data in the range of 30-300 V/cm as indicated by the solid line.

as the compensated pick-up coil technique [9] to determine its behavior directly in STCs.

We are using compensated coils of the radial alternative type [9] with inner diameters of about  $1.4 \text{ mm}$  with  $W = 16$  windings of insulated copper wire of  $70 \mu\text{m}$  diameter on each coil and length  $L$  of about the same value as the inner diameters. An illustration of the compensation coils is given schematically in fig. 5.10. The area of one of the coils is about  $30 \text{ mm}^2$  with a residual, uncompensated area of order  $0.1 \text{ mm}^2$ , corresponding to a ratio of compensation of  $3 \times 10^{-3}$ . This type of compensation coils has a very good compensation and high voltage insulation strength [9].

In each of the compensated coils (1/2) we find a voltage  $U$  induced

$$U_{1/2} = \frac{d}{dt} \Phi_{1/2} = \frac{d}{dt} \int_{A_{1/2}} B_{1/2} dA \quad (5.6)$$

where  $A$  is the area perpendicular to the field and  $\Phi$  the magnetic flux in each coil. For perfectly compensated coils  $A_1 = -A_2 = A$  we obtain the resulting voltage  $U_{\text{result}}$

$$U_{\text{result}} = U_1 - U_2 = \frac{d}{dt} \int_A (B_1 - B_2) dA \quad . \quad (5.7)$$

In InSb, sample OK 123, we found a maximal conductivity at DC fields and room temperature of  $\sigma_0 \approx 175 \Omega^{-1} \text{ cm}^{-1}$ . That means that the skin depth is  $\delta \approx 1.2 \text{ cm}$ . At fields in excess of 1 T the skin depth is larger but of the same order of magnitude. The equipment supports slab like samples of diameter  $2R \approx 1.2 \text{ mm}$  so that we can use equation (2.83) for  $R \ll \delta$ .

With one coil containing the sample and the other one non-conducting, non-magnetic materials such as Helium or air, we obtain for perfectly compensated coils:

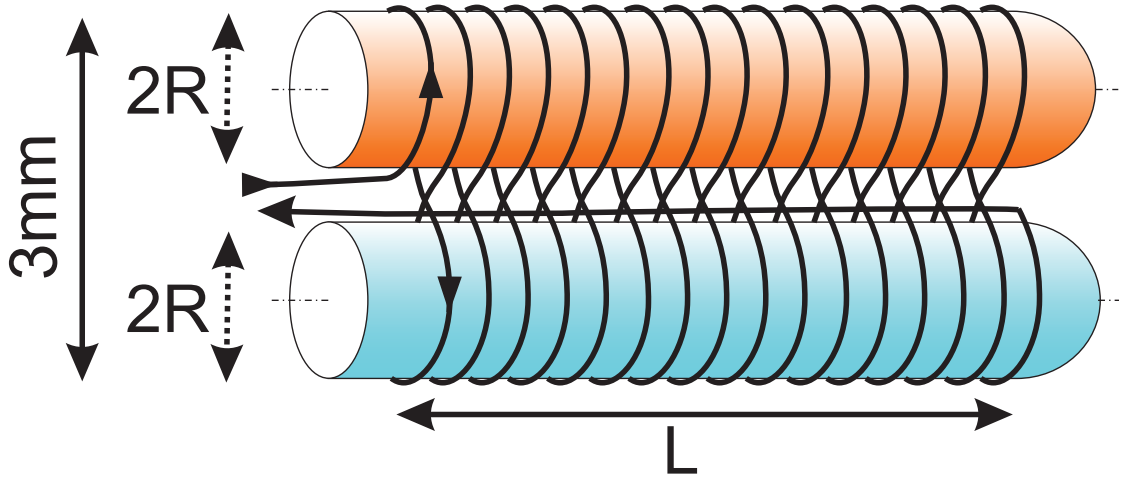


Figure 5.10: Schematic drawing of compensation coils of the radial alternative type after [9]. The drawing is not to scale. Due to the lack of gaps between the windings we find that the length of the coil  $L$  is approximately equal to the diameter of the coils  $L \approx 2R = 1.4 \text{ mm}$ .

$$U_{\text{result}} = U_1 - U_2 = \frac{d}{dt} \int_A \frac{R^2 - r^2}{4} \sigma_0 \mu_0 \frac{d}{dt} (B_{\text{ext}})_z(t) dA \quad (5.8)$$

therefore with the number of windings  $W$  and  $dA = Wrdrd\varphi$

$$\begin{aligned} U_{\text{result}} &= \frac{d}{dt} \int_0^R \int_0^{2\pi} \frac{R^2 - r^2}{4} \sigma_0 \mu_0 \frac{d}{dt} (B_{\text{ext}})_z(t) W r dr d\varphi \\ &= \frac{d}{dt} \left[ W \sigma_0 \mu_0 \frac{d}{dt} (B_{\text{ext}})_z(t) \int_0^R \int_0^{2\pi} \frac{rR^2 - r^3}{4} dr d\varphi \right] \\ &= \frac{d}{dt} \left[ \frac{\pi R^4 W \sigma_0 \mu_0}{8} \frac{d}{dt} (B_{\text{ext}})_z(t) \right] \\ &= \text{const} \cdot \frac{d}{dt} \left[ \sigma_0 \frac{d}{dt} (B_{\text{ext}})_z(t) \right] \end{aligned} \quad (5.9)$$

For real compensation coils there will be a residual area which adds a signal proportional to the induced voltage times the residual area to the signal. This is a systematic error that can easily be corrected.

For a constant conductivity we find  $\frac{d}{dt} \sigma_0$  equal to zero and the response signal being proportional to  $\frac{d^2}{dt^2} B$ . As the time dependence of conductivity is given by the time dependence of the magnetic field,  $\frac{d}{dt} \sigma_0 \frac{d}{dt} B = \left( \frac{d}{dB} \sigma_0 \frac{d}{dt} B \right) \frac{d}{dt} B$  will similarly produce a response that is symmetric with respect to the magnetic field maxima even for time dependent conductivity.

This gives a clear indication of eddy current related magnetic moments as intrinsic magnetic moments in the sample will cause a signal proportional to  $\frac{d}{dt} B$ . In other words, if the response signal points in the same direction for up and down sweeps it the response is clearly caused by eddy currents, if it points to different directions it is due to non equipment related magnetization of sample.

The magnetization equipment requires a different sample shape than cyclotron resonance measurements. A typical samples used are either a powder of grains of a size of about  $100 \mu\text{m}$  immersed in an insulating non-magnetic matrix material as in [96] or rods

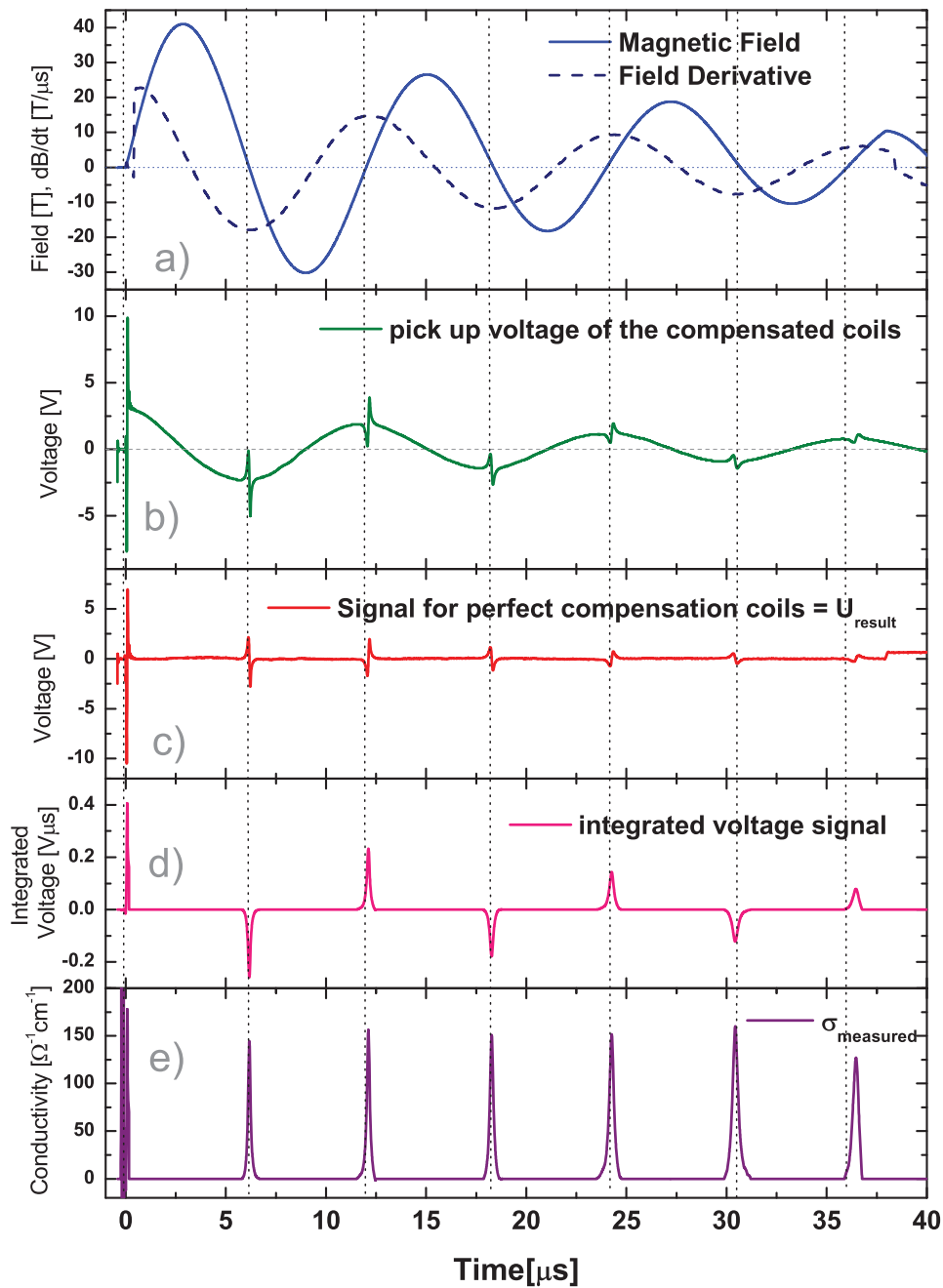


Figure 5.11: Eddy Current Spectroscopy on Sample OK 123 at room temperature. Explanations are given in the text.

of approximately 1.2 mm diameter and few mm length. In the former case the infinite rod approximation is not valid, neither is the thin disc. Therefore a geometry dependent factor must be introduced in the calculation representing edge phenomena of the field distribution. However, for a rod like sample we can well use (2.83).

The magnetic response at room temperature of a 4 mm long rod with 1.2 mm diameter of the same bulk InSb wafer as OK 123 used in optical measurements is given in fig. 5.11 b). It was obtained in a non-destructive field with a field maximum of 41 T. Trace c) shows the data corrected by subtracting a signal proportional to the field derivative as given in trace a). The proportionality factor is given by the imperfect compensation of the coil that was used. It is clearly seen that the magnetic response is strongest near the zero crossings of the magnetic field that correspond to the extrema of the field derivative. The response for up and down sweep have the same direction, therefore the magnetic response must be originating from eddy currents.

The subtracted signal is of same order of magnitude as is the eddy current related signal. Taking account of the compensation of the coils of order  $10^{-3}$  [9] we can estimate that the eddy current contribution to the magnetic field is much smaller than that value as would be expected from the radius to skin depth ratio. That means also, that the time shift for cyclotron resonance measurements in up and down sweep is smaller than can be detected with the recording equipment. Nevertheless, the eddy current related signal is detectable at timescales of  $\approx 0.5 \mu s$  much higher than the response time of the magnetization measurement system of order 25 ns [9].

For comparison it is useful to determine the conductivity from the magnetic response. For the calculation process we can use (5.8) and yield

$$U_{\text{result}} = C_M \frac{d}{dt} \left[ \sigma_0 \frac{d}{dt} B \right] \quad (5.10)$$

with  $C_M = \pi \mu_0 R^4 W / 8$  being a constant. It is practical to deduce the conductivity with

$$\int_{t_1}^{t_2} U_{\text{result}} dt' = C_M \int_{t_1}^{t_2} \frac{d}{dt} \left[ \sigma_0 \frac{d}{dt} B \right] dt' = C_M \left[ \sigma_0 \frac{d}{dt} B \right]_{t_1}^{t_2} \quad (5.11)$$

that can be solved for  $\sigma_0 \frac{d}{dt} B$ .

$$\sigma_0 \frac{d}{dt} B = \frac{8}{W \pi \mu_0 R^4} \int_0^t U_{\text{result}} dt' \quad (5.12)$$

The product of conductivity and field derivative can be obtained by integration and is given in fig. 5.11, trace d). This corresponds to the current density dependence of time. Similarly the qualitative behavior of the azimuthal electric field is given in trace a) via the field derivative. The conductivity as obtained by this analysis is depicted in trace e) of fig. 5.11. The traces of fig. 5.11 show qualitative behavior of response and conductivity in reference to the magnetic field and its derivative. The vertical lines of fig. 5.11 are given for the zero crossings of the magnetic field which, in turn correspond to the field derivative extrema.

With this contact-less measurement method it is possible to determine the conductivity  $\sigma_0$ . Using equation (5.11) and the parameters for  $C_M$  of  $R = (0.60 \pm 0.03) \text{ mm}$  the experimental value for  $dB/dt \approx 18 \text{ T} / \mu s$  at the first zero crossing we obtain an order of magnitude for the maximal conductivity from the data given in fig. 5.11 of  $\sigma_0(B = 0) \approx 160 \Omega^{-1} \text{ cm}^{-1}$ . With the uncertainty of the determination of R of about 5% we are introducing a relative error of 20% to the conductivity that was numerically



determined by eddy current spectroscopy. The uncertainties of the other quantities used are of much smaller influence to the result. The resulting value is in good agreement with the DC conductivity determined by transport methods.

The trace in the first up sweep is affected by the trigger noise of the magnetic field generation due to the position of the measurement system inside the FARADAY-cage. However, there are three remarks at this point:

- 1) The conductivity is high only near the zero crossings of the external field, yet seems to show a delay versus the latter. This is most likely due to screening effects as discussed in section 2.2.1 and the uncertainty in the determination of zero field. Comparing equations (2.83) and (5.11) we find that the field correction is given qualitatively by trace d) of fig. 5.11, that is by integrated voltage signal corresponding to a constant times conductivity and field derivative.
- 2) The conductivity is of similar magnitude for each zero crossing corresponding to the DC conductivity within few percent. The conductivity at zero field does *not* depend on the field derivative within experimental resolution.
- 3) It must be noted that we can only monitor the *change* of conductivity with time, that is magnetic field with the magnetization technique. A constant contribution of conductivity to the signal is obscured by the imperfect compensation of the coils and the bit noise of the ADC data.

It is useful to zoom in on the first zero crossing of B to analyze the conductivity at that point. The dependence of the conductivity on the external magnetic field for the first zero crossing is depicted in figure 5.12. The dependence of conductivity on the external magnetic field as obtained from DC transport measurements is given for comparison. The conductivity obtained from eddy current spectroscopy shows the same behavior as the DC conductivity and is of the same magnitude lest a few percent that are well explained within the resolution of the method.

There is *no* evidence for an increase of conductivity in single turn coils at all of order 50% as would be required by the observation of the transmission drop as discussed in section 5.1. We can conclude that the eddy current effects accompanying the magnetic field generation process do not substantially change the azimuthal conductivity. There is no detectable generation of charge carriers, the behavior corresponds to the DC case. Moreover, effects such as the temperature increase do not contribute to the conductivity in this case as will be shown in the next section.

More precisely, there is no contribution of hot electrons or charge carriers to the azimuthal current density which is responsible for the magnetization signal, that is, there are no large quantities of additional free carriers generated that can move azimuthally. There are no extra carriers compared to the DC case, or they are trapped in a bound state and have a very low mobility. According to [93,97] the electric field has no influence on the electron mobility of InSb at room temperature up to fields of 500 V/cm.

From (5.4) we can expect the conductivity at  $dB/dt = 18 T/\mu s$ , hence  $|\vec{E}_\varphi| \approx 55 V/cm$  at  $r=R=0.6$  mm to change by approximately 5%. This cannot be resolved within eddy current spectroscopy for two reasons, 1) the expected change is much smaller than the resolution of the method and 2) it is valid only for  $r=R$  and linearly decreasing with  $r$  at  $r < R$ . *The azimuthal electric field can not cause the observed transmission drop.*

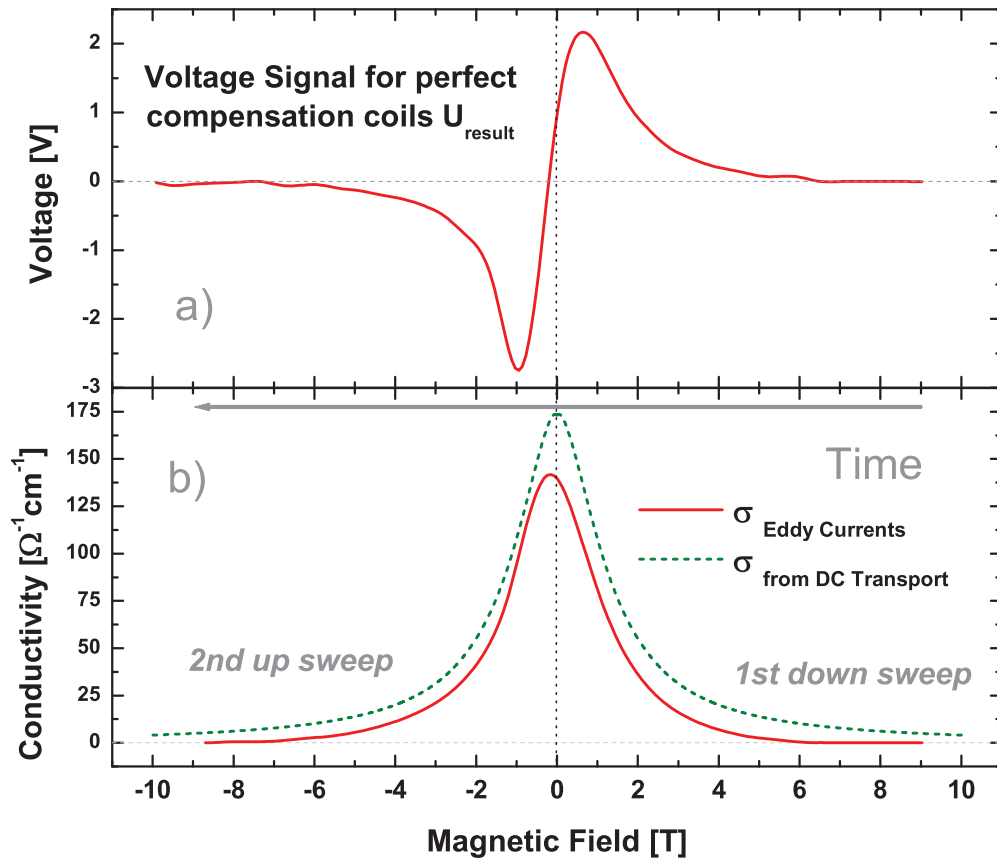


Figure 5.12: a) Voltage response of InSb sample OK 123 at the first zero crossing of  $B$  at room temperature. b) Relative conductivity as obtained from eddy current spectroscopy (solid line) and DC transport measurements (dashed line) on the same sample at room temperature. The arrow indicates the direction of time.

From fig. 5.12 it is clear that the magnetic field correction due to screening effects is only relevant for comparatively low fields. Using the estimate values for the conductivity we obtain correction fields of order 0.01 T that can well be neglected.

The peak conductivity seems to be shifted to later times from the zero value of the external field. The screening effect was not corrected for this consideration because it is smaller than the temporal resolution. The uncertainty of zero field, however, is estimated to be of order 20 ns for the first zero crossing of  $B$ , corresponding to a 0.4 T shift of the conductivity vs. magnetic field trace. Please note that with decreasing sweep rate the determination of the zero field position becomes more inaccurate, with increasing number of zero crossing the uncertainty of its position increases similarly.

It should be emphasized, however, that the result obtained by magnetization measurements at room temperature have been reproducibly obtained. The depicted data are from the trace with the best signal-to-noise ratio. In low temperature measurements at 80 K no response from the sample could be observed within the resolution of the mag-

netization equipment [9], at 200 K a qualitatively similar behavior to the one at room temperature was observed, but the response was smaller by one order of magnitude. This observation corresponds to the on order of magnitude lower conductivity 200K and several orders of magnitude lower conductivity at low temperatures of  $T < 100K$  as can be expected from DC transport.

### 5.3.1 The Lattice Temperature

With the obtained product of conductivity and field derivative (5.12) and (2.91) it is now possible to determine the actual heat deposition  $\Delta Q(r)$  in the sample lattice for a realistic conductivity dependence on the external field.

$$\Delta Q(r) = \frac{r^2}{16} \int_0^\tau \sigma_0 \left( \frac{d}{dt} \vec{B}_{ext} \right)^2 dt = \frac{r^2}{2W\pi\mu_0 R^4} \int_0^t \left( \int_0^t U_{result} dt' \right) \frac{d}{dt} \vec{B}_{ext} dt''. \quad (5.13)$$

Using equation (5.13) and (2.93) for an assumed small change of temperature the lattice temperature increase  $\Delta T$  is then given by:

$$\Delta T(r) = \frac{r^2}{2W\pi\mu_0 R^4 \rho_m c_p} \int_0^t \left( \int_0^t U_{result} dt' \right) \frac{d}{dt} \vec{B}_{ext} dt''. \quad (5.14)$$

The problem of lattice temperature increase in a the given experimental situation is given in fig. 5.13: a) The magnetic field and its derivative b) the integral of  $(dB/dt)^2$  for constant conductivity  $\sigma_0 = 2000 \Omega^{-1} cm^{-1}$  and trace of  $(dB/dt)^2$ , c) the temperature as obtained from eddy current spectroscopy with measured  $(\sigma_0 dB/dt)$  at  $r=R=0.6$  mm with literature parameters for InSb  $\rho_m = 5.77 g/cm^3$  and  $c_p = 0.2 J/gK$  [90, 91] d) An infrared transmission trace of InSb sample OK 123 is given for comparison and was obtained with a similar non-destructive field.

It is clearly seen that the action integral and the lattice temperature increase show a step like behavior in STC generated magnetic fields. The effect becomes even more pronounced at higher sweep rates. An illustration of the sweep rate dependence is given in fig. 2.10. This finding is in complete analogy to considerations obtained for the generating current in STC [32, 34] and eddy currents in metallic samples [33], yet is several orders of magnitude smaller. There are plateaus at the field extrema and more or less step function like increases at the field derivative extrema, that is at zero crossings of B. In InSb this behavior becomes more pronounced by the field dependence of the conductivity as found by eddy current spectroscopy.

From the cyclotron resonance trace that is depicted in fig. 5.13, trace d) it can be seen that the transmission drop of interest occurs coincident with extrema of conductivity and its magnitude seems to be proportional to the absolute value of the field derivative. This suggests a connection of eddy-current-related phenomena and the observed transmission drop .

However, the magnitude of the temperature accumulation at the sample edge is very small, of order 0.1 K, therefore the lattice temperature cannot contribute to the observed type III hysteresis in this case. As we have found in section 2.2.6 the heat deposition is increasing quadratically with the radius and field derivative. In an experiment with initial sweep rate  $100 T/\mu s$  and radius 1mm the temperature accumulation can be easily higher by a factor of 25 on sample OK 123. This does not account for a possibly increased

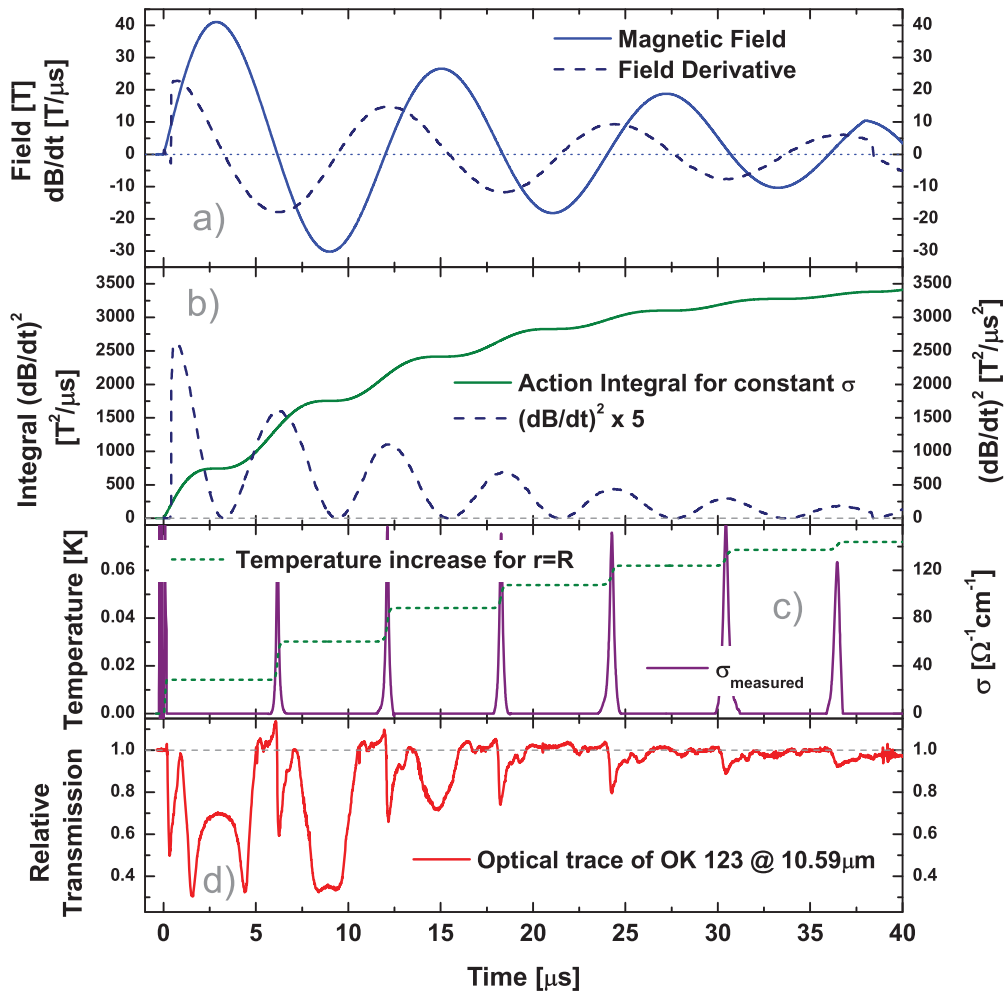


Figure 5.13: Temperature increase due to eddy currents, explanation given in the text.

conductivity caused by the even higher electric fields ambient at that field parameter that would yield an even higher temperature rise. However, even those temperature rises would have an effect that is virtually undetectable with the given equipment resolution on sample OK 123.

For cyclotron resonance measurements it is important to note that the heat generation is a cumulative process. It does not depend on the sample thickness  $D$  as long as the *thin disc* approximation  $D \ll \delta$  holds. However, the distribution of the deposited heat can depend on  $D$ .

Moreover, the temperature increase is a radially increasing phenomenon. It is highest at the sample edges and zero at its center. Thus the temperature distribution in a sample must be determined. In a crude approximation the value at half the radius can be used for the whole sample. The problem of heat flow inside the sample must also be considered.

The problems of heating by as well as a delay of the magnetic field inside the sample has been addressed by previous publications with qualitatively similar findings but much

higher magnitude due to the more than one order of magnitude larger conductivity of the respective samples that is less strongly dependent on the magnetic field: for bulk samples of HgSe:Fe temperature increases of 10 K have been observed after a single turn coil experiment by directly measuring the sample temperature before and after the pulse [12]. It is important to emphasize that the measured temperature is the temperature of the lattice that is not necessarily equal to the electron temperature during the experiment. For the same type of samples magnetic field corrections of 15 T have been found in a STC magnetic field [96]. In the same series of experiments a significant line broadening of SHUBNIKOV-DE-HAAS oscillations increasing with sweep rate was found [12] indicating a substantial temperature rise in the sample.

### 5.3.2 Mechanical Pressure

With the measured value for the conduction it is now possible to estimate the pressure in the sample caused by the magnetic field acting upon the sample. Using (5.12) and (2.98) we find:

$$p(r) = -\frac{r^2}{4} \left( \sigma_0 \frac{dB}{dt} \right) B \vec{e}_r = \frac{2r^2}{W\pi\mu_0 R^4} B \int_0^t U_{\text{result}} dt' \quad (5.15)$$

The behavior of pressure, magnetic field and its derivative are shown in fig. 5.14. A trace of the pressure was determined for InSb, sample OK 123.

As an example for illustration purposes the trace for a sample with constant conductivity  $\sigma_0 = 2000 \Omega^{-1} \text{cm}^{-1}$  shows the pressure at this field to be of order 300 bars at  $r=R=1\text{mm}$  as depicted in fig. 5.14, trace b). For InSb sample OK 123 pressures of an order less of magnitude, maximal 30 bars at  $r=R=1\text{mm}$  can be expected as seen in trace c). With these values it is possible to estimate the influence of pressure upon the band gap  $E_g$  and other parameters. Using

$$E_g = E_g(P=0) + 13.7 \times 10^{-3} P - 3.6 \times 10^{-5} P^2 (\text{eV}) \quad (5.16)$$

when P is given in kbar [90] we find the energy gap to change by  $\approx 0.4 \text{meV}$ . That is at room temperature a change of 0.2%. The influence of pressure upon the energy gaps at the L- and X- points parameters is smaller by a factor of 3. There is *no* influence of pressure on the electronic band structure of detectable magnitude in this case. The piezoelectric as well as deformation effects can be neglected.

At higher sweep rates, e.g.  $100 \text{T}/\mu\text{s}$  the absolute value of the pressure can very easily be larger by a factor of 25. The pressure should be point symmetric with respect to zero crossings of B as given by its dependence on the field times its derivative. This is not correctly reproduced in fig. 5.14 due to slightly deviating timing of both curves versus each other. Nevertheless its magnitude is estimated rather to large than too small due to this fact. However, the findings in low field derivative and field experiments suggest that the pressure is *not* a cause for the transmission drop.

Summarizing the eddy-current spectroscopy we can determine the conductivity and all related quantities quantitatively for bulk samples. In InSb, sample OK 123, we found that all properties involving the azimuthal conductivity, that is the current density, magnetic field correction, the temperature and pressure are of negligible magnitude. There is no additional contribution of the transient generation of the magnetic field to the conductivity at this scale of field and its derivative compared to DC measurements.

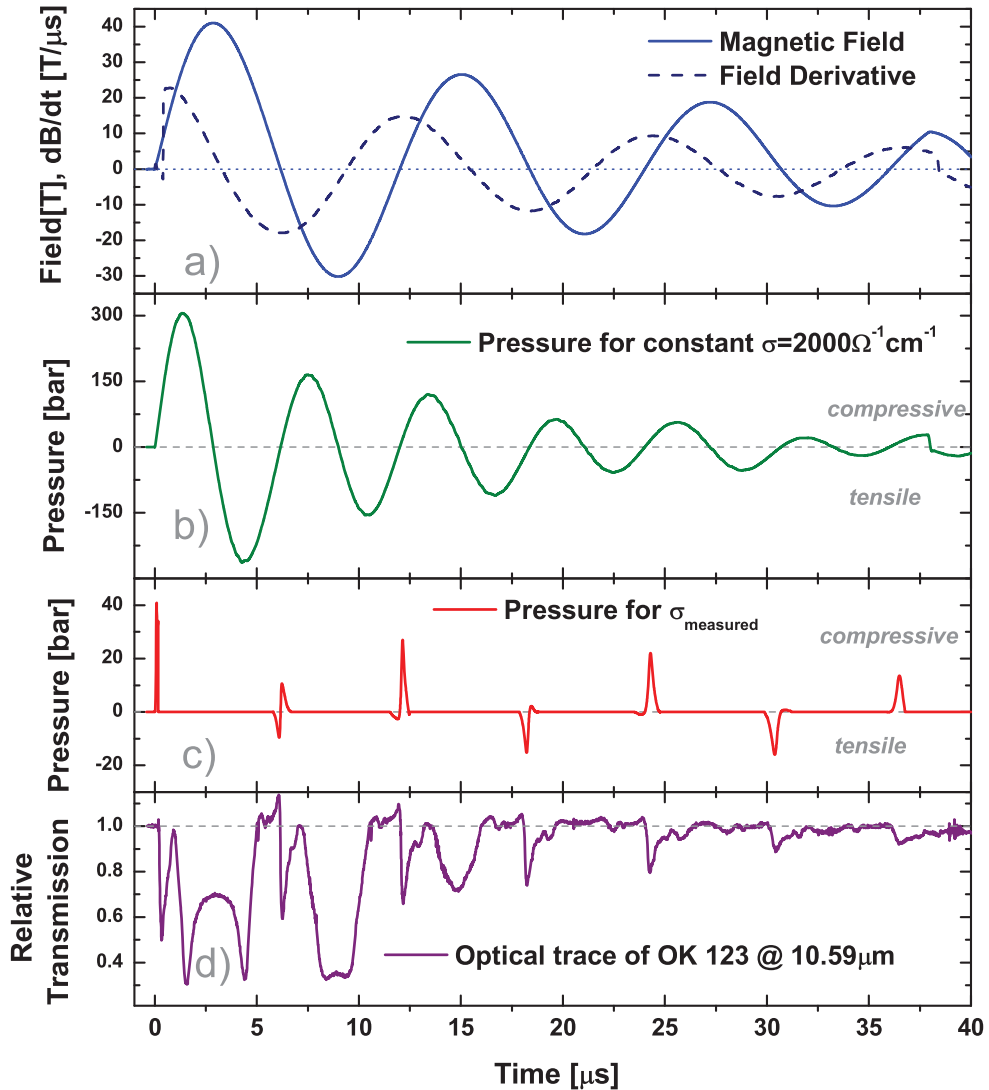


Figure 5.14: a) Magnetic field and its derivative. b) Pressure trace for a constant conductivity  $\sigma_0 = 2000\Omega^{-1}cm^{-1}$ . c) Pressure calculated for the experimental situation of InSb Ok 123 at room temperature with the experimentally determined conductivity d) Trace of a cyclotron resonance experiment with InSb OK 123 at  $10.59\mu m$  over time given for comparison.

The cause for any changes in optical transmission in the low field range can only be caused by quantities accompanying the magnetic field generation that do not depend on azimuthal conductivity. There are two possible candidates, the azimuthal electric field and the radial electric field.

An azimuthal electric field influence would be symmetric at zero crossings of  $B$  and should also be influencing the current density of azimuthal conductivity respectively. No evidence was found for such a behavior. The radial electric field is asymmetric vs. zero

crossings of B and its influence must be analyzed.

### 5.3.3 The Radial Electric Field

The radial electric field has been introduced by the boundary condition  $\vec{j}_r = 0$ , the absence of radial currents due to the finite size of the sample. It is proportional to the mobility, the magnetic field, its derivative and the coordinate r (2.41). It scales versus the azimuthal electric field with  $\mu B = \omega_c \tau$ . An illustration of the factor  $\mu B$  is given in fig. 5.15 for OK 123 as obtained from DC transport at room temperature which gives a good approximation for the situation in STCs as well. The DC data is presented because of the possibility of accurately determining the zero field position within few mT. We observe a peak at  $B \approx 1.5 T$  with value  $\omega_c \tau = \mu B \approx 3.5$ . That means, the radial electric field will be 3.5 times larger than the azimuthal electric field at 1.5 T.

High electric fields are known to change the transmission properties of semiconductors. They manifest themselves in effects such as the PÖCKELS-, KERR- and FRANZ-KELDYSH-effects [19,26]. All of them are based on the breaking of translational symmetry by an applied electric field. As a result, the wave functions of electrons and holes in the conduction and valence bands are penetrating into the fundamental band gap. Thus it is possible to absorb radiation with an energy smaller than the band gap.

However, the effects become effective at electric fields exceeding  $10^7 V/m$  and are of one percent or less magnitude even in this case [19]. With the radial electric field of about 300 V/cm we can find the potential over one lattice constant to change by  $\approx 20 \mu V$ . There is *no* appreciable modification to the fundamental band gap of InSb that could result in a transmission drop due to inter-band absorption in the given case with  $E_g \approx 170 meV$  and  $E_{laser} \approx 120 meV$ .

All of the electric field effects on the optical properties of a sample assume a spatially constant electric field. In the present situation the electric fields depend linearly on r. The above considerations can thus only be carried out at each specific r individually, being maximal at the sample edge  $r=R$ . It remains a question, what dimensions of the sample are active and can contribute to the type III hysteresis in the CR measurement, the overall sample size or the size of the focal spot of the incident radiation.

The radial electric field is balancing the LORENTZ-force acting upon the current. It creates a charge separation. Electrons or holes will be accumulating in a layer at  $r=R$ .

To determine the influence of this accumulation we must determine the charge density inside the sample. The charge density  $\rho_e$  can be deduced from MAXWELL's equations (2.1)

$$\vec{\nabla}_{\vec{r}} \vec{D} = \rho_e \quad \longrightarrow \quad \vec{\nabla}_{\vec{r}} \varepsilon_0 \varepsilon_R \vec{E} = \varepsilon_0 \varepsilon_R \frac{1}{r} \frac{\partial}{\partial r} (r E_r) = \rho_e \quad (5.17)$$

and we obtain

$$\rho_e = \varepsilon_0 \varepsilon_R \frac{1}{r} \frac{\partial}{\partial r} \left( r \frac{\mu r}{2} B \frac{\partial}{\partial t} B \right) = \varepsilon_0 \varepsilon_R \mu B \frac{\partial}{\partial t} B \quad [Cm^{-3}] \quad (5.18)$$

that is a spatially constant charge density over the sample volume. For the given experimental situation we find the field derivative at  $B = 1.5 T$  to be  $22 T/\mu s$  at the beginning of the field pulse, with  $\varepsilon_0 \varepsilon_R = 8.854 \times 10^{-12} F/m \cdot 16$  and  $kT = 25 meV$  the value of  $n_e = \rho_e/e = 7 \times 10^{10} cm^{-3}$  over the sample volume at the maximal radial electric field of  $E_r \approx 230 V/cm$  at  $r=R=0.6 mm$  whereas the azimuthal field is  $E_\varphi \approx 66 V/cm$  in this case.

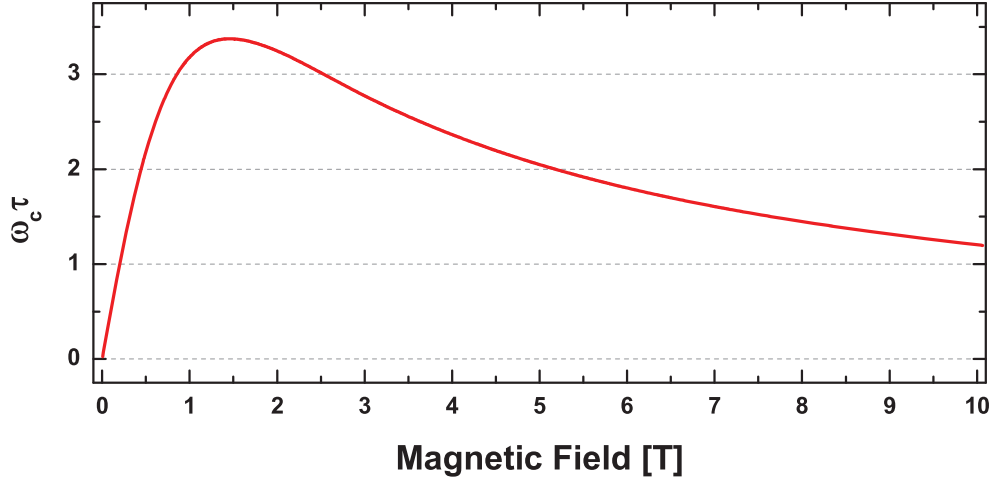


Figure 5.15:  $\mu B = \omega_c \tau$  as obtained with DC transport at room temperature.

At  $B=1.5$  T after the first zero crossing of the magnetic field we find the sweep rate to be  $18 T/\mu s$  and accordingly at  $r=R=0.6$  mm  $E_r \approx 190$  V/cm,  $E_\varphi \approx 54$  V/cm and  $n_e = \rho_e/e = 6 \times 10^{10} \text{ cm}^{-3}$ .

The extension of the accumulation layer into the sample can be determined with the DEBYE screening potential  $\Phi(r)$  and the respective screening length

$$\Phi = \text{const} \cdot \frac{e^{-\kappa r}}{r}, \quad \kappa^2 = \frac{4\pi e^2 n}{\varepsilon_0 \varepsilon_R kT} \quad (5.19)$$

when  $n$  is the intrinsic carrier concentration. The value  $\delta_D = \kappa^{-1}$  is the DEBYE screening length. At  $n = 2 \times 10^{16} \text{ cm}^{-3}$  we yield  $\delta_D \approx 10$  nm. The number of carriers in the accumulation (or depletion) layer must be equal to the number of opposite charge carriers over the sample volume. We can estimate the respective carrier concentration  $n_{\text{layer}}$  by the ratio of volumina of the sample and the layer.

$$n_e V_{\text{sample}} = n_{\text{layer}} V_{\text{layer}} \quad \longleftrightarrow \quad n_{\text{layer}} = n_e \frac{R}{2\delta_D} \quad (5.20)$$

In the given case we obtain  $n_{\text{layer}} = 2.2 \times 10^{15} \text{ cm}^{-3}$  at the beginning of field and  $n_{\text{layer}} = 1.8 \times 10^{15} \text{ cm}^{-3}$  after the first zero crossing, respectively. These values represent a  $\pm 10\%$  change of carrier concentration in the accumulation / depletion layer. The carrier concentration in the layer depends on the radial extension  $R$  of the sample, the density  $\rho_e$  does not nor does  $\delta_D$ . For larger  $R$  or sweep rates  $n_{\text{layer}}$  becomes comparable or even larger than  $n$ .

However, we find  $R/\delta_D \approx 10^5$ . The influence of such a small change of carrier concentration on such a small length scale is not detectable with eddy current spectroscopy. The densities of charges  $n_e$  and  $n_{\text{layer}}$  refer to opposite charges with respect to each other and change directions at every zero crossing *and* extremum of the magnetic field. Moreover, it is also not possible to observe any optical effects in the center of the sample caused by the charge carrier accumulation in this layer.



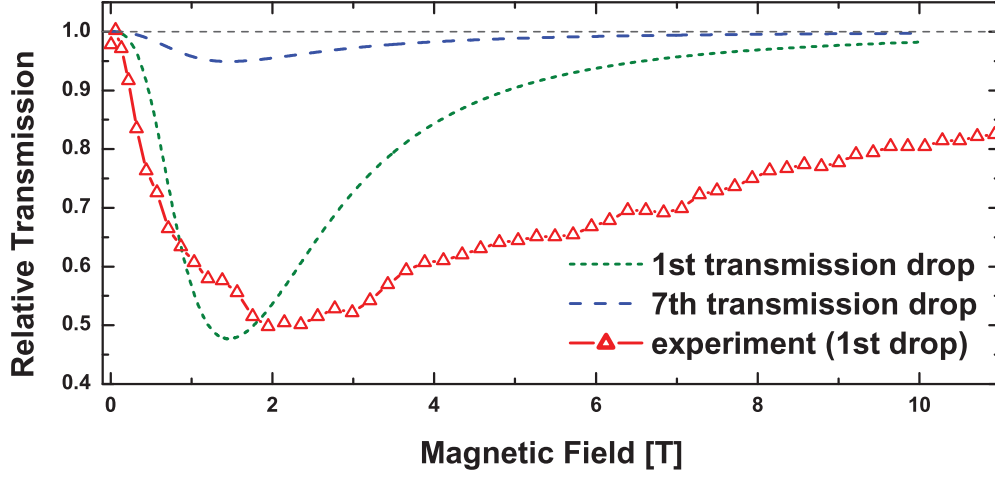


Figure 5.16: Calculated transmission drops at  $r=R=1.15$  mm for the 1st (short dashes) and 7th (long dashes) observation of the transmission drop in section 5.1. For comparison the experimental curve at the first observation of the drop (not corrected for magnetic field) is given (triangles).

The considerations above *do not* include hot carriers generated by the radial electric field that are free to move in radial direction. The change of the absorption coefficient of InSb for the exact same experimental situation, that is at  $\lambda = 10.59\mu\text{m}$  and room temperature for an applied electric field of order 30-300 V/cm has been investigated by [93]. It provides a large enough effect onto the transmission of infrared radiation. We will now find an approximation for its magnitude using the empirical relations derived in [93] given in equation (5.4). On this sample of  $R=1.15$  mm we find for the first observation of the transmission drop at  $dB/dt = 22\text{ T}/\mu\text{s}$  an azimuthal electric field of  $\approx 120\text{ V/cm}$  ambient during the first few T.

We can use the experimentally determined relation  $\omega_c(B)\tau(B)$  to calculate the change of absorption coefficient during this period with the help of (5.4) and estimate the transmission drop that can be expected. Using the value of absorption coefficient  $K = (10.0 \pm 0.3)\text{ cm}^{-1}$  at  $B=0$  the relative transmission change  $T(B)/T(0)$  can be calculated with the magnetic field dependent change of absorption coefficient  $\Delta K(B)$ :

$$T(B)/T(0) = e^{-(K+\Delta K(B))D} \quad (5.21)$$

where  $D$  is the sample thickness, in this case  $D=0.5$  mm.

The results of this calculation which is very crude are depicted in fig. 5.16. From the given infrared transmission trace it can be seen that the transmission drop magnitude dependence on sweep rate is correctly reproduced and the overall line-shape is qualitatively similar. The numerical agreement with the observed transmission drop may be coincidental. The authors of [93] attribute the increase of absorption coefficient with electric field to absorption on free carriers. However, if this is the reason for the transmission drop it must be pointed out that there is no effect of similar magnitude in the eddy current spectroscopy data.

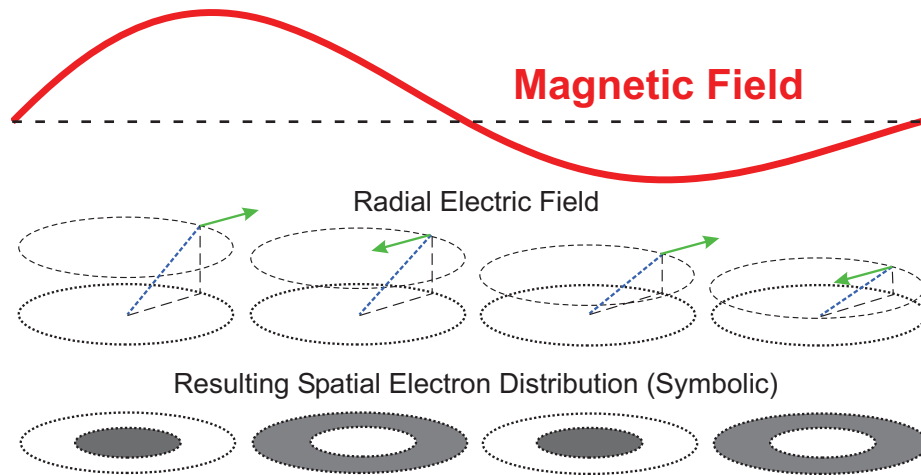


Figure 5.17: Geometrical distribution of generated electrons in an external magnetic field as given by the top trace. The middle trace shows the radial electric field spatially. The bottom trace of this drawing is symbolic only. The inner circles correspond to the sample area (larger circles) that light is focused upon and contributes to the transmission. Dark indicates high electron concentration, bright low electron concentration.

Discrepancies are the magnetic field magnitude of the transmission drop maximum and the strength of the decay. The reasons for this behavior are found in the finite time required for a steady state solution and the charge separation, that is, the transfer of electrons toward the center of sample as characterized by a finite drift velocity. The mechanism of this process cannot be assumed to be independent of magnetic field and might result in a slower decay.

The carrier generation process is cumulative, an influence which is ignored in this calculation due to the number of additional parameters that are required. The value of  $K$  can only be deduced as an integral or iterative because its magnitude depends on  $B(t)$  as  $K(t) \rightarrow K(t) + \Delta K(B(t))$ . This would result in an ever increasing transmission drop with rising magnetic field. This is contradictory to the observation and a mechanism that reduces the number of hot carriers on a similar timescale must be ambient. There is no reference for high temperature but for low temperatures it is known that the magnetic field will cool hot electrons [98–102] by reducing the electron mobility even at low field magnitudes.

The radial electric field has opposite orientation for up and down sweeps, but the same orientation after each zero crossing of the magnetic field. Correspondingly it acts upon charge carriers, that means, in up sweeps free electrons are moving into the center of sample, in down sweeps the electrons move toward the sample boundaries. That means that in up sweeps there is a large number of carriers present in the region that is subject to incident radiation and in the down sweep an approximately similar number of carriers is absent from this region. That means the transmission in up sweeps is smaller than in the down sweeps. Moreover, the transmission drop should not be observable in down sweeps. Schematically this is depicted in fig. 5.17 for the first complete oscillation of the magnetic field.

Although this is a very crude estimate of the effects of the radial electric field it provides a quantitative explanation of the type III hysteresis in InSb.

## 5.4 Measurements with the Cyclotron Resonance Setup

The infrared transmission experiments were performed on  $2^\circ$  wedged samples and roughened samples with parallel surfaces. The two showed no difference in behavior even quantitatively regarding the relative transmission drop. The overall transmission was higher for the parallel samples. Thus we can rule out optical interference of a plane parallel plate system as the cause for the transmission drop.

The sample dimensions are in this case length by width by height:  $2 \times 2 \times 0.5 \text{ mm}^3$ . This shape can be well approximated by a disc with diameter  $2.3 \text{ mm}^2$ . That means, the samples in these cyclotron resonance measurements are roughly twice as large in diameter compared to the eddy-current-spectroscopy sample. The maximum electric field at  $r=R$  is twice as large as is the respective current density, the temperature increase is larger by a factor of four as is the pressure.

We have found the eddy current effects on the magnetization measurements to be negligible and this is not changed by a factor of 2 or 4, respectively, introduced by the larger radial extension. The effect of the electric fields is not negligible when amplified by a factor of two.

We will present data obtained in nondestructive magnetic fields comparable to the ones that were used for the eddy current spectroscopy to provide comparable conditions and no additional or amplified effects to the findings. Moreover, we are interested in the low field range that can more thoroughly be studied that way and can compare the results with DC measurements.

### 5.4.1 Temperature Dependence

We have found in the preceding sections that eddy current related phenomena or the radial electric field are likely responsible for the transmission drop. The former depends on the conductivity, the latter on the mobility times the magnetic field. Both of which are parameters that do strongly depend on temperature as was shown by DC transport for conductivity and can likewise be shown for mobility, yet with a different, not necessarily monotonous dependence.

Furthermore we know, that the conductivity is not changed by the transient character of the magnetic field at room temperature and there was no indication for any large effect at lower temperatures. Temperature dependent infrared transmission experiments will thus contribute to insights on the physical effect causing the type III hysteresis.

The temperature dependence of the infrared transmission spectra is depicted in fig. 5.18 for the wavelength  $\lambda = 10.59 \mu\text{m}$  at temperatures from 24 K to room temperature. The relative transmission spectra have been shifted with respect to each other but have the same vertical scale. This holds true for further figures. The magnetic field used was nondestructive and the trace was comparable, but not exactly identical for all curves. The traces are only given to show the appearance of the transmission drop with temperature at the positions indicated by arrows. It is most pronounced and clearly asymmetric at times larger than  $12 \mu\text{s}$ . The traces of 45 K and 24 K are data obtained at a very poor signal-to-noise ratio caused by low transmission, the structures in the spectra of these temperatures can hardly be attributed to sample related phenomena.

It is clearly seen that the transmission drop at the beginning of the trace and after zero crossing of the magnetic field occurs at temperatures higher than 180 K. Simultaneously with the observation of the transmission drop, we can find the electron cyclotron

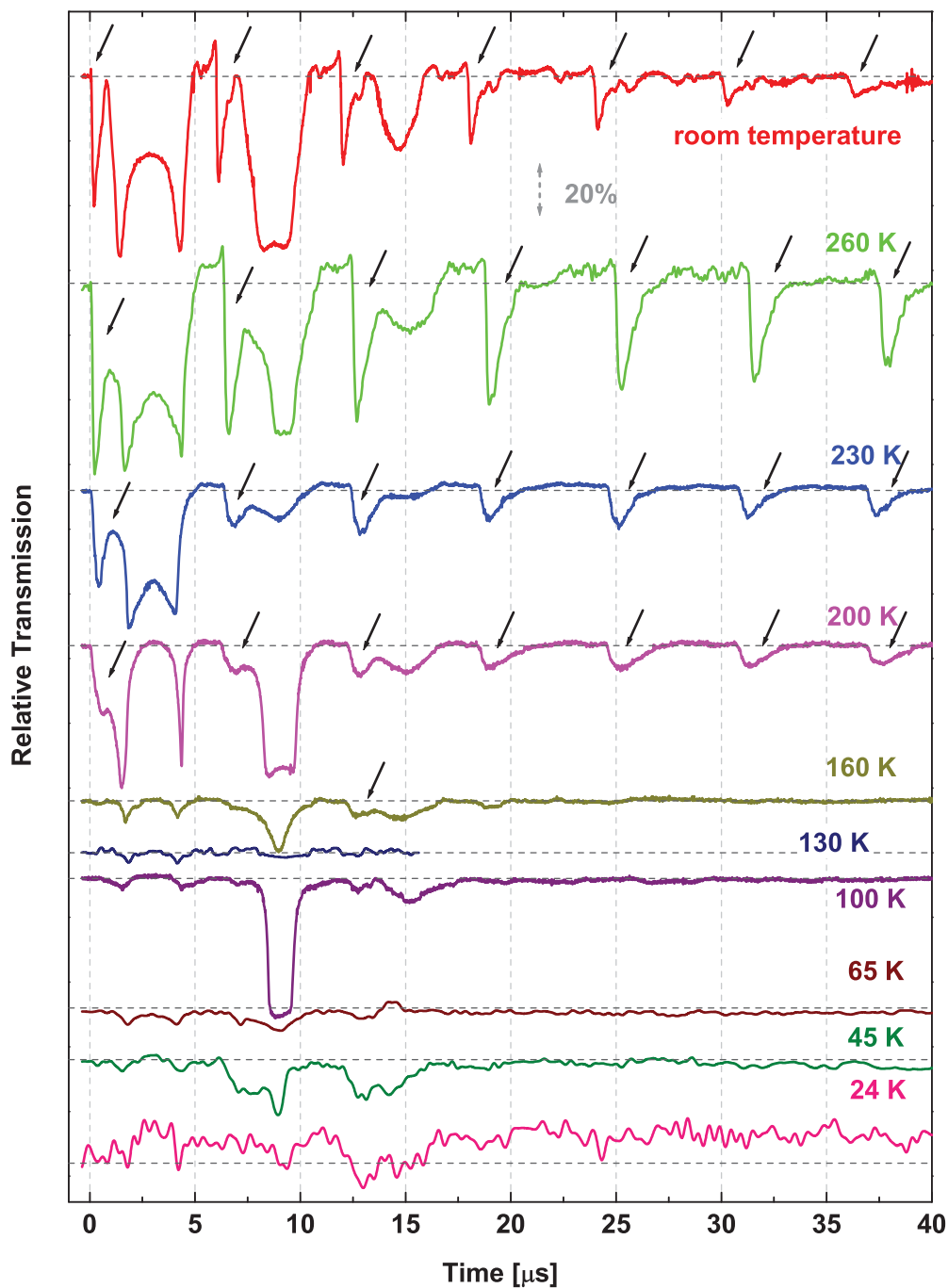


Figure 5.18: Temperature dependent spectra for sample OK 123 at  $10.59\ \mu\text{m}$  vs time. The fields used for the spectra have been non-destructive, of comparable field trace but not identical. This graph shall only illustrate the appearance of the phenomenon as indicated by the arrows.

resonance to increase in absorption strength. This points to a significantly higher number of electrons in the conduction band. Transport measurements confirmed that the onset of intrinsic conductivity can be observed at that temperature range 150-180 K. The conductivity at zero field dependence on temperature is given in fig. 5.8.

This is also in good agreement with the finding of eddy-current spectroscopy that a response is observable at 200 K, yet one order of magnitude smaller than at room temperature, and no detectable response at 80 K.

At temperatures lower than 160 K we can observe a transmission drop after  $12 \mu\text{s}$  that was reproducibly observed. These spectra show no or a very little transmission drop at the beginning of field and the first zero crossing after  $\approx 6 \mu\text{s}$ . It cannot be distinguished from the noise at the trace of 24 K. However, it indicates a cumulative process being responsible for the transmission drop in these cases as would be the excitation of carriers into the conduction band by the electric field. Another hint for that behavior is the increase of cyclotron resonance absorption at  $\approx 9 \mu\text{s}$  that is found after the first zero crossing for temperatures 160 K, 100 K, 65 K and 45 K. This behavior is even more pronounced at higher sweep rates as will be shown in section 5.4.2.

The dependence on magnetic field of the spectra is depicted in fig. 5.19 for temperatures above 150 K. We can find a dependence on temperature of the transmission drop position. The intensity increases with rising temperature and the position of the peak transmission drop is shifting from  $\approx 3 T$  at room temperature to  $\approx 12 T$  at 160 K. This behavior is typical for the formation of a bound state or an impurity band.

The electron cyclotron resonance shifts from 28 T at 160 K to 26 T at room temperature and 117 meV energy. The resonance position at room temperature is in good agreement with previous measurements of other groups in STC fields [14–16]. These measurements have been carried out on CZOCHRALSKI-grown intrinsic InSb, that was not intentionally doped. There was no report of the type three hysteresis investigated in this thesis due to much smaller sweep rate [15,16] or very noisy up sweep data [14]. The second half sine of the field has not been recorded in both publications. However, both groups of authors find a dependence on sweep rate of the cyclotron resonance line-width or an estimate of eddy-current heating of electrons, respectively. We will show data in section 5.5 for intrinsic InSb in which a type III as well as type I hysteresis could be observed.

The dependencies of the transmission drop position and the cyclotron resonance position on temperature are given in fig. 5.20 for sample OK 123. It can clearly be seen that the transmission drop has a much stronger dependence on temperature than the cyclotron resonance.

For temperatures above 180 K the resonance intensity is depending almost linearly on the absolute value of the field derivative. An illustration is given in fig. 5.21. The linear dependence on sweep rate is more clear at higher temperatures  $T > 260$  K. At  $T = 230$  K and  $T = 200$  K the linear dependence is given when the point with the highest sweep rate is ignored. It is much smaller than the dependence at 260 K and 295 K. Coincidentally the trace of 260 K and 295 K have the same slope within experimental error but the trace of 260 K is shifted by an offset of 23% at  $B_d = 0$  and does not show a proportionality.

We find the transmission drop to be larger at  $T = 260$  K than at 230 K and 295 K. The transport measurements showed that the conductivity is decreasing monotonously with falling temperature in this temperature range. This is another hint toward a quantity causing the type III hysteresis that is not depending directly on conductivity. A possible candidate is the radial electric field that depends on mobility that is increased at 260 K

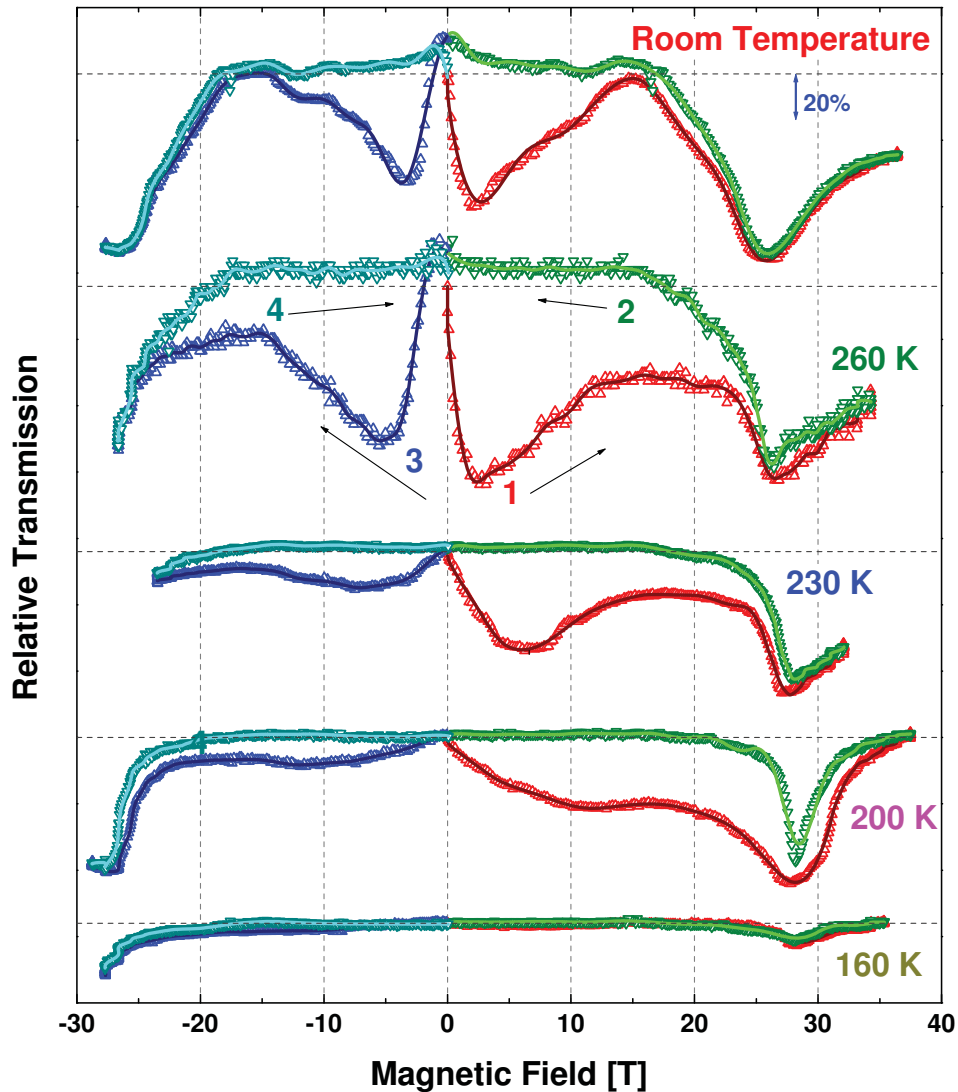


Figure 5.19: Traces of fig. 5.18 vs. magnetic field at  $\lambda = 10.59 \mu\text{m}$ . It is clearly seen that the hysteretic resonance is located at  $\approx 3 \text{ T}$  at room temperature and moves gradually toward  $12 \text{ T}$  as the temperature is decreased to  $200 \text{ K}$ . Moreover, the resonance becomes more pronounced with rising temperature. It is also shown that the resonance is shifted to higher fields for negative fields. The traces have not been corrected for magnetic field. Lower traces are up sweeps, the sequence of sweeps is indicated by numbers at the trace of  $260 \text{ K}$ .

with respect to  $295 \text{ K}$  and  $230 \text{ K}$  and magnetic field only but does not depend on the carrier concentration. Another possibility is a very complex dependence on a larger number of parameters.

The observation of the phenomenon at temperatures that have been determined to show intrinsic conductivity and not for lower temperatures indicates that highly mobile free carriers, that is electrons in the conduction band, are required to observe the

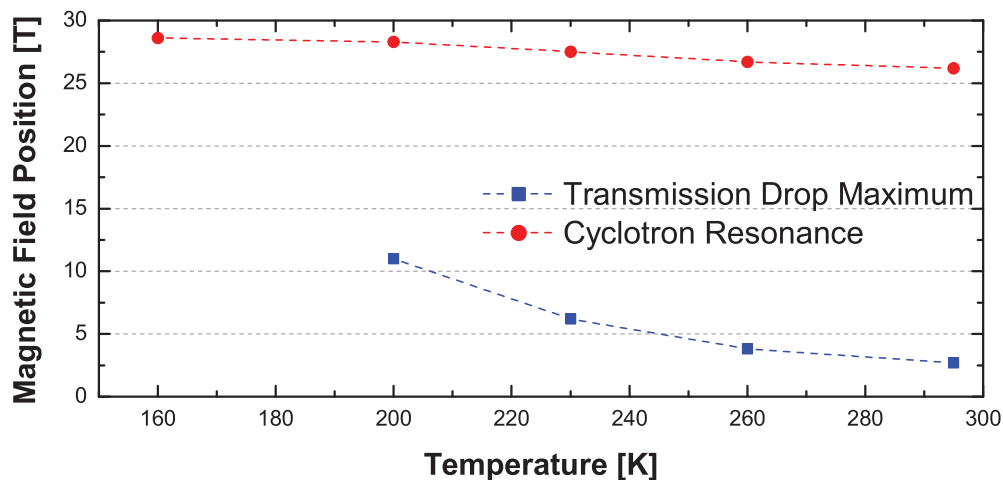


Figure 5.20: Dependence of the positions in magnetic field of the cyclotron resonance and transmission drop maximum on temperature. Lines are guides to the eye. The uncertainty of position is approximately the symbol size ( $\pm 0.5 T$ ).

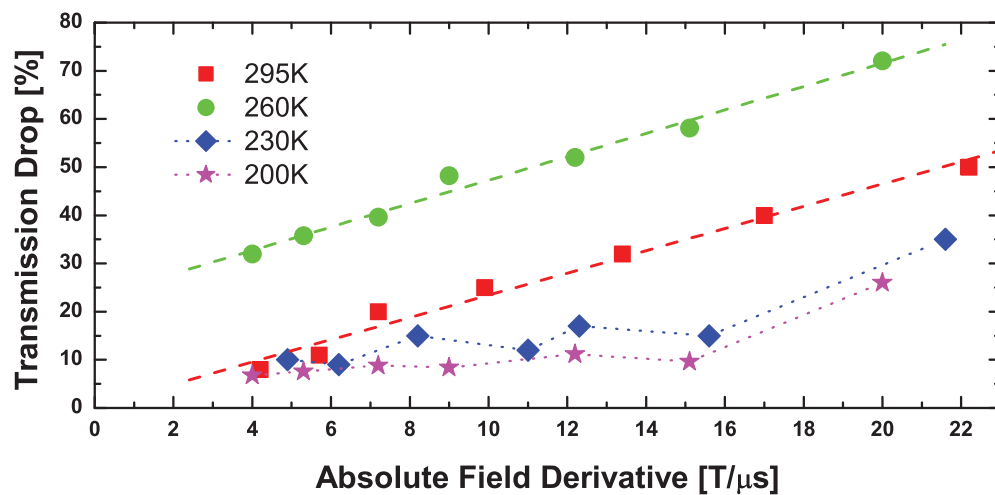


Figure 5.21: Dependence of absorption intensity on the absolute value of field derivative for temperatures 295 K (squares), 260 K (circles), 230 K (diamonds) and 200 K (stars). For  $T > 250 K$  the lines represent linear fits, for  $T < 250 K$  the lines are guides to the eye.

transmission drop. These electrons, however, do not contribute to the eddy currents.

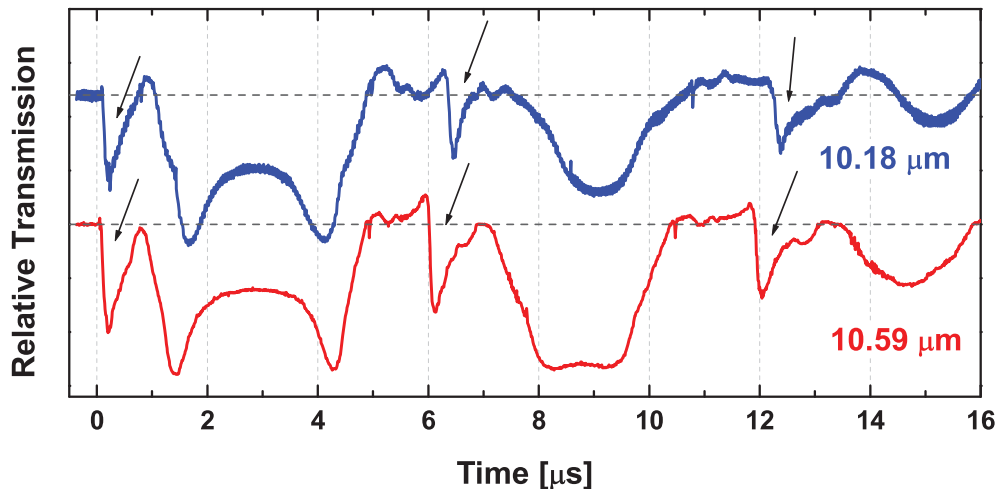


Figure 5.22: Traces of OK 123 at wavelengths  $10.59 \mu\text{m}$  and  $10.18 \mu\text{m}$  at room temperature and a non-destructive field of comparable magnitude. The type III phenomenon can be seen in both traces as indicated by the arrows.

#### 5.4.2 Wavelength Dependence

To understand the phenomenon in more detail we have carried out measurements with different wavelengths, that is, different energies of radiation. It was revealed that the type III hysteresis occurs at all  $\text{CO}_2$  Lasing energies. A trace versus time is given in fig. 5.22. It can be clearly seen that the hysteresis occurs in the two depicted traces at wavelengths  $10.59 \mu\text{m}$  and  $10.18 \mu\text{m}$  in room temperature experiments with nondestructive coils and field magnitudes and sweep rates comparable to the situation in the eddy current spectroscopy. The slightly deviating time dependence trace of  $\lambda = 10.18 \mu\text{m}$  was obtained with a multiply used reinforcement that resulted in a larger diameter of the coil and hence a lower angular frequency  $\omega$ .

The variation of laser energy in this case is  $117 \text{ meV}$  ( $10.59 \mu\text{m}$ ) to  $122 \text{ meV}$  ( $10.18 \mu\text{m}$ ). For more detailed analysis the position of the resonance in magnetic field must be determined. This is depicted in fig. 5.23. The absolute value of the transmission drop is strongly dependent on the optical conditions, e.g. the laser mode. However, the structure is reproducible at various wavelengths. The shape of the transmission drop seems to be reproducible at all wavelength. The transmission drop maximum shifts from  $(2.7 \pm 0.5) T$  at  $10.59 \mu\text{m}$  to  $(3.0 \pm 0.5) T$  at  $10.18 \mu\text{m}$ . The cyclotron resonance on the other hand shifts from  $26.2 T \rightarrow 27.5 T$  which is in excellent agreement with previous publications [14–16].

We have found in section 5.1 that the position of the transmission drop is not changed by changing the sweep rate. With higher sweep rates, as will be shown soon, the transmission drop position occurs at  $(3.2 \pm 0.9) T$  with a similar line shape at  $9.64 \mu\text{m}$ . In this case the same piece of the wafer OK 123 was used as in the nondestructive traces at  $10.59 \mu\text{m}$  and  $10.18 \mu\text{m}$ . This indicates a rather small dependence on wavelength, the transmission drop is found to be shifting within experimental error only and by less than



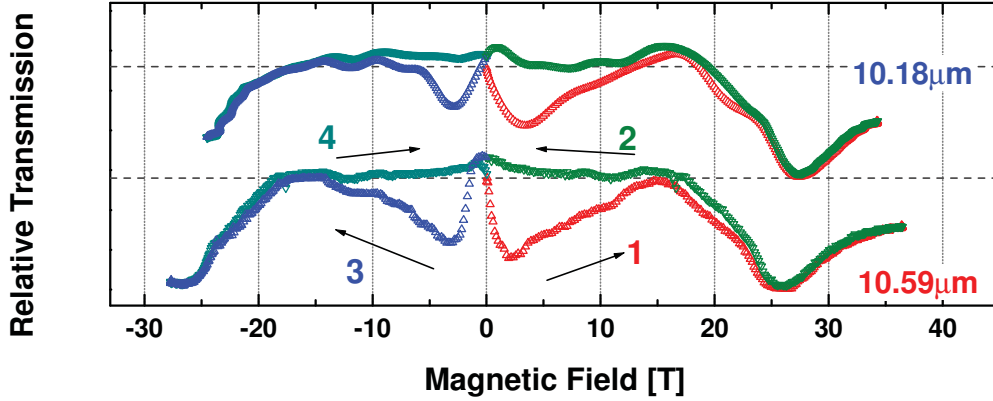


Figure 5.23: Traces of OK 123 at wavelengths  $10.59 \mu\text{m}$  and  $10.18 \mu\text{m}$  at room temperature. The type III phenomenon is clearly seen in both traces. Lower traces are up sweeps.

the electron cyclotron resonance.

This is indicating that the transmission drop is not a resonant phenomenon but rather a change of the optical properties of the material. It is depending on the direction of the field derivative. As was discussed before, the only property that is clearly asymmetric and of non-negligible magnitude is the radial electric field.

The temperature dependence of the transmission drop at wavelengths  $\neq 10.59 \mu\text{m}$  was found to be qualitatively similar to the one at  $10.59 \mu\text{m}$ . The transmission drop occurs at temperatures higher than 180 K and shifts to higher fields with decreasing temperature. A linear dependence on magnetic field derivative could be observed at temperatures higher than 200 K.

To illustrate the temperature dependence we will show the infrared transmission traces in a medium field range with maximal field magnitude of 110 T at a wavelength of  $9.64 \mu\text{m}$ . The resulting transmission traces versus time are depicted in fig. 5.24. It must be pointed out that at this maximum field value the sweep rate at zero field and hence at the transmission drop position in magnetic field is substantially higher than in the nondestructive case. As shown in fig. 5.24 the field derivative exceeds  $80 \text{ T}/\mu\text{s}$  at the beginning of field and  $40 \text{ T}/\mu\text{s}$  at the first zero crossing. That means, the influence of eddy current related phenomena is larger by a factor of four or two respectively, if we assume a linear dependence. For phenomena such as impact ionization and avalanche breakthroughs the dependence will be highly non-linear.

As seen in fig. 5.24, indicated by arrows, in this experimental situation the transmission drop occurs right after the beginning of field and after each zero crossing for temperatures above 150 K too. It is, however, very weak at 165 K. Moreover, there is an increase of intensity in the electron cyclotron resonance after the first zero crossing at temperatures  $T=133 \text{ K}$ ,  $100 \text{ K}$  and  $5 \text{ K}$  marked with "!". This finding is in complete analogy to the rise of cyclotron resonance as observed for nondestructive fields at  $10.59 \mu\text{m}$  at  $T < 165 \text{ K}$  in section 5.4.1.

This is a clear indication for the generation of electrons, or rather their excitation into

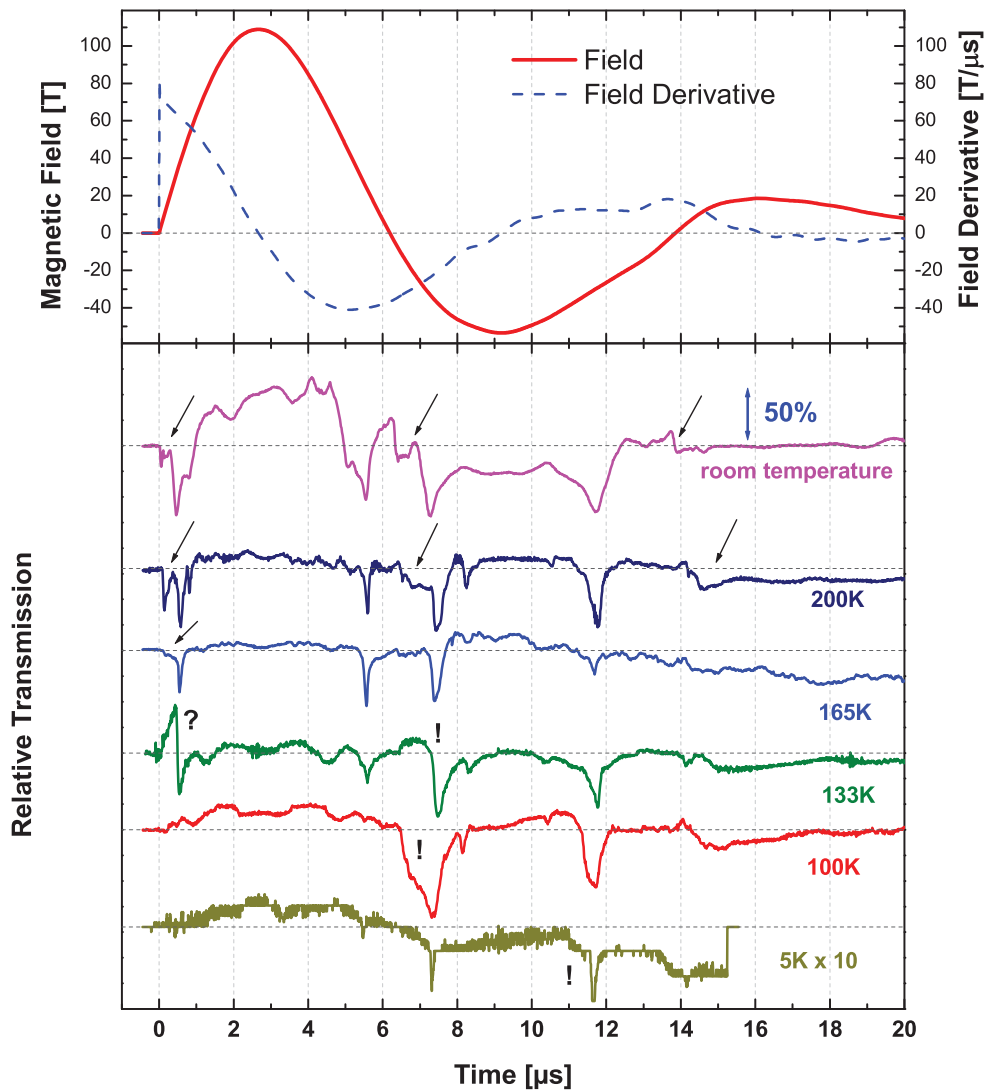


Figure 5.24: Temperature dependence of CR spectra for  $\lambda = 9.64 \mu\text{m}$  and a medium field. The arrows indicate the transmission drop if occurring as previously reported, "!" denotes the observation of a transmission drop after the  $6 \mu\text{s}$  when it is not observed at the beginning of field at  $T=100 \text{ K}$ ,  $133 \text{ K}$  and an increase in cyclotron resonance after the first zero crossing at  $5 \text{ K}$ . "?" indicates a strange behavior in the trace at  $133 \text{ K}$  that is not understood at all and probably related to a problem with the recording device (RTD).

the conduction band, during the magnetic field pulse. The mechanism *cannot* trivially be explained by the ambient electric fields and impact ionization or avalanche breakthroughs because of its absence in the beginning of the field pulse where the quantities depending on the field derivative are much larger due to the higher sweep rate.

In the curve of  $T=100 \text{ K}$  we can observe a signature of the transmission drop after the first zero crossing near the cyclotron resonance. This points toward the existence of

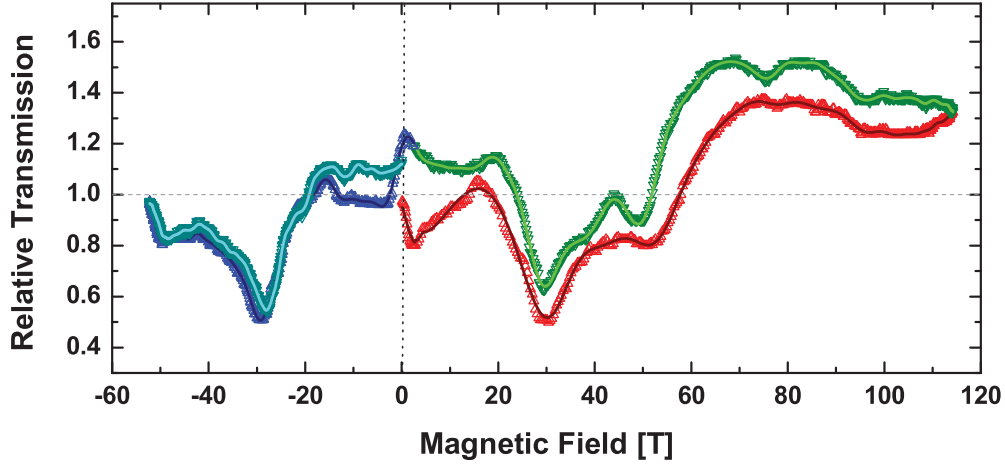


Figure 5.25: The infrared transmission of OK 123 at room temperature and  $\lambda = 9.64 \mu m$  in a medium field.

highly mobile charge carriers at this time.

The dependence of the infrared transmission on the magnetic field is depicted in fig. 5.25. The transmission drop occurs at  $(3.2 \pm 0.9) T$ . The spin split cyclotron resonance can be observed at  $(29.3 \pm 1.0) T$  and  $(49.5 \pm 1.0) T$  which is in good agreement with findings of [15,16].

The down sweep is shifted to higher transmission values compared to the up sweep at all times but shows similar resonant structures at the cyclotron resonance positions. However, there are two more resonant structures or, transmission drops at  $\approx 75 T$  and  $\approx 95 T$  that are not clearly observed in the up sweep. Also, the relative transmission does not return to the value of 1 at zero field.

The shift of the down sweep trace to higher transmission values compared to the up sweep was found unambiguously at all wavelengths for maximum fields larger than 50 T, that is with sweep rates higher than  $30 T/\mu s$  and the shift is increasing with sweep rate. The overall higher transmission in down sweeps indicates that the complex refraction index of the sample are not identical for up and down sweeps. It was only observed at room temperature, not at temperatures of  $T \approx 200 K$  as shown in fig. 5.24, where the transmission drop was still observable.

The shape of the transmission drop after the first zero crossing deviates from the shape at the beginning of field. This is attributed to the shifted down-sweep trace and the difficult referencing of the transmission drop to a transmission at zero field. However, the maximum at the first and properly referenced transmission drop occurs at  $(3.2 \pm 0.9) T$ . Within the experimental error, the position of the transmission drop is overlapping for all wavelengths of the  $CO_2$  Laser, whereas the cyclotron resonance position shifts clearly from  $26.2 T \rightarrow 27.5 T \rightarrow 29.3 T$  for  $\lambda = 10.59 \mu m \rightarrow 10.18 \mu m \rightarrow 9.64 \mu m$ .

Summarizing the observations on OK 123 we have found a transmission drop after each zero crossing of magnetic field at temperatures 200 K-295 K in infrared transmission experiments in non-destructive transient fields. Its intensity was found to be linearly dependent on the absolute value of the field derivative for temperatures higher than

250 K. It could be demonstrated that eddy current related effects can be determined by magnetization techniques in STCs. The conductivity was found to be independent of sweep rate within experimental error and to be of similar magnitude as in the DC case. An estimate for the temperature, pressure and avalanche ionization due to the azimuthal electric field, yielded that neither of these effects has a large enough magnitude to cause a detectable transmission drop. The position in magnetic field of the transmission drop was found to be independent of wavelength, suggesting a non-resonant phenomenon.

The generally higher transmission in down sweeps at high sweep rates indicates a modification of the refractive properties of InSb in the down sweep vs. the up sweep by the electric field. Intuitively this can be understood by assuming an accumulation or depletion of charge carriers in the respective sweeps. Another hint toward such a phenomenon is the CR FWHM which is smaller in down sweep than in up sweep for high sweep rates.

At room temperature it was found that the radial electric field can cause a transmission drop of qualitatively similar behavior as observed by the generation of hot carriers and free carrier absorption. Moreover, the radial electric field can move carriers into the sample center in up sweeps and out of it in down sweeps. This radial current provides a qualitative for the higher transmission in down sweeps as well as the absence of the transmission drop in down sweeps.

For other temperatures than 295 K the transmission drop could be observed in the intrinsic conductivity range. There are no data available in the literature for the effect of a high electric field at these temperatures onto the infrared transmission of InSb but there is likely a qualitatively similar dependence.

## 5.5 Undoped Indium Antimonide

The previously investigated sample, OK 123, showed the type III hysteresis as extensively discussed. Moreover, about 15 other samples from wafers designed for the same purpose have been investigated and showed nearly identical results. All of them were intentionally doped with Ge and oriented (211) or (111). The samples showed differences in the total transmission in dependence of the level of compensation, but all showed a similar type III hysteresis at elevated temperatures. However, the compensation was varied within less than one order of magnitude only.

For comparison with previously reported data it is useful to investigate samples of intrinsic InSb without compensation dopants. Such an investigation has been carried out with the CR equipment. The CZOCHRALSKI-grown plane samples available were oriented (001), had an intrinsic carrier concentration of  $n = 2 \times 10^{16} \text{ cm}^{-3}$ , a thickness of  $450 \mu\text{m}$  and were polished on one side.

A comparison of the infrared transmission obtained with OK 123 and an intrinsic sample is given in fig. 5.26. It can be seen that the transmission drop, indicated by arrows, occurs in the intrinsic sample as well but is far less pronounced. The cyclotron resonance is also smaller than it was for OK 123, but is increased after the zero crossing as was observed for OK 123 at lower temperatures. The spikes in the trace of the intrinsic sample are bit errors of the digitizers (RTD).

It should be pointed out that the overall transmission of the intrinsic samples was better by a factor of four compared to OK123. As can be seen on fig. 5.26 the transmission drop was very small at room temperature, about 9% at maximum. The maximum of the

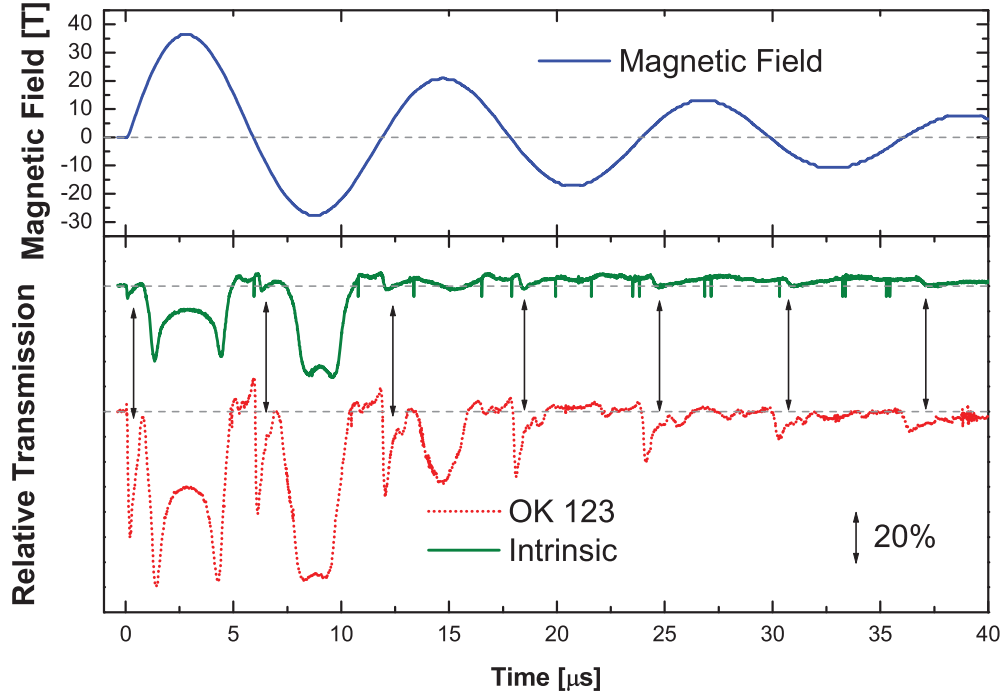


Figure 5.26: *Top: Magnetic field, bottom: Infrared transmission of OK 123 (dots) and intrinsic InSb (solid line) at room temperature and  $10.59 \mu\text{m}$ . Arrows indicate the transmission drop.*

transmission drop occurs independent of wavelength at  $B \approx 0.5 - 1.5 T$  though it cannot be exactly positioned due to the uncertainty of zero field. Nevertheless, the position was similarly found to be wavelength independent.

The important finding is that the transmission drop was observed in intrinsic InSb too. And correspondingly its magnitude showed a linear dependence on sweep rate.

### 5.5.1 Type I hysteresis?

There is a strong hint that for a specific maximum field magnitude of 46 T within few percent and a  $2 \times 2 \text{ mm}^2$  sample only we could observe a type I hysteresis in intrinsic InSb. The finding is shown in fig. 5.27. It can be seen that the spin-split cyclotron resonance is affected by a type I hysteresis. The higher field CR at  $\approx 42 T$  is decreased in intensity in the down sweep whereas the lower CR at  $\approx 26 T$  is increased vs. the up sweep. The integrated areas for up and down sweeps are *not* identical, the type I hysteresis can not be used to exactly deduce sample properties. This is most likely due to eddy current effects that cause an overlap of type II with the type I hysteresis. The type I and III hysteresis' could be observed independently of each other in one trace.

Moreover, the type I hysteresis could not be observed for any higher maximum field. For higher sweep rates the shift of the down sweep trace to higher transmission values obscures type I hysteresis' on the spin split cyclotron resonance.

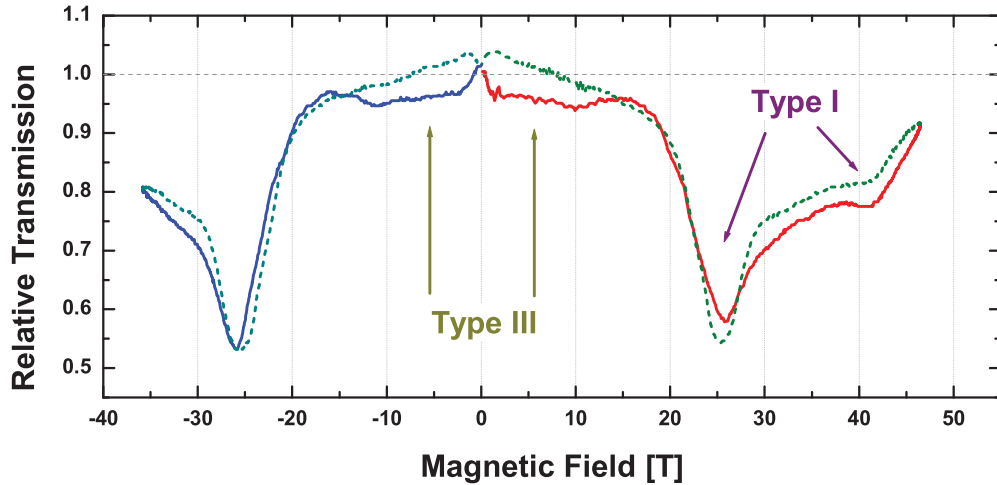


Figure 5.27: Relative transmission of intrinsic InSb at room temperature with  $\lambda = 10.59\mu\text{m}$ . Solid lines are up sweeps, dashed lines are down sweeps. The two hysteresis types I and III can be observed at the positions indicated by arrows.

### 5.5.2 CO-Laser Measurements

The good overall transmission of the intrinsic samples enabled investigation with the CO Laser, which allows a doubling of the radiation energy compared with the  $\text{CO}_2$  Laser. However, as the energy gap of InSb at room temperature is as small as 170 meV, the samples are opaque for CO-Laser radiation. Due to strong non-parabolicity of narrow gap semiconductor and therefore InSb energy bands the energy gap, the difference between highest valence and lowest conduction band at  $\Gamma$ ,  $\Delta_E$ , can be expected to increase with magnetic field. So with careful aligning spectra can be taken without signal at  $B = 0\text{ T}$ , the samples will show transmission when  $\Delta_E$  becomes larger than the Laser energy<sup>1</sup>. This is clearly observed in figure 5.28. The high magnetic field part of the spectrum shows the spin split cyclotron resonance marked with "CR" clearly resolved in the down sweep whereas in the up sweep the transmission is much lower (marked with arrows) and the cyclotron resonances at  $\approx 75\text{ T}$  are obscured. Again we find the down sweep transmission to be shifted to higher values compared with the up sweep.

The spin-split electron-cyclotron resonance is shifted from  $(75 \pm 5)\text{ T}$  and  $(120 \pm 5)\text{ T}$  at 216 meV to  $(85 \pm 5)\text{ T}$  and  $(135 \pm 5)\text{ T}$  at 230 meV to  $(88 \pm 8)\text{ T}$  and  $(142 \pm 10)\text{ T}$  at 235 meV. This is in good agreement with previously reported values [14].

In traces a) to c) of fig. 5.28 a sweep rate dependence of the relative transmission can be observed at one wavelength of  $\lambda = 5.74\mu\text{m}$ . The transmission was not very high in all experiments with the CO-Laser due to the alignment without sample and the sample mount following without further optimization. Therefore the data are more strongly affected by the ambient noise than the  $\text{CO}_2$  Laser measurements. The discrepancy between up- and down sweeps is increasing with increased sweep rate. Moreover, the onset of transmission, that is, the point where  $E_{\text{Laser}}$  exceeds  $\Delta_E(B)$ , is much less sharp in all

<sup>1</sup> $\Delta_E(B = 0) = E_g$

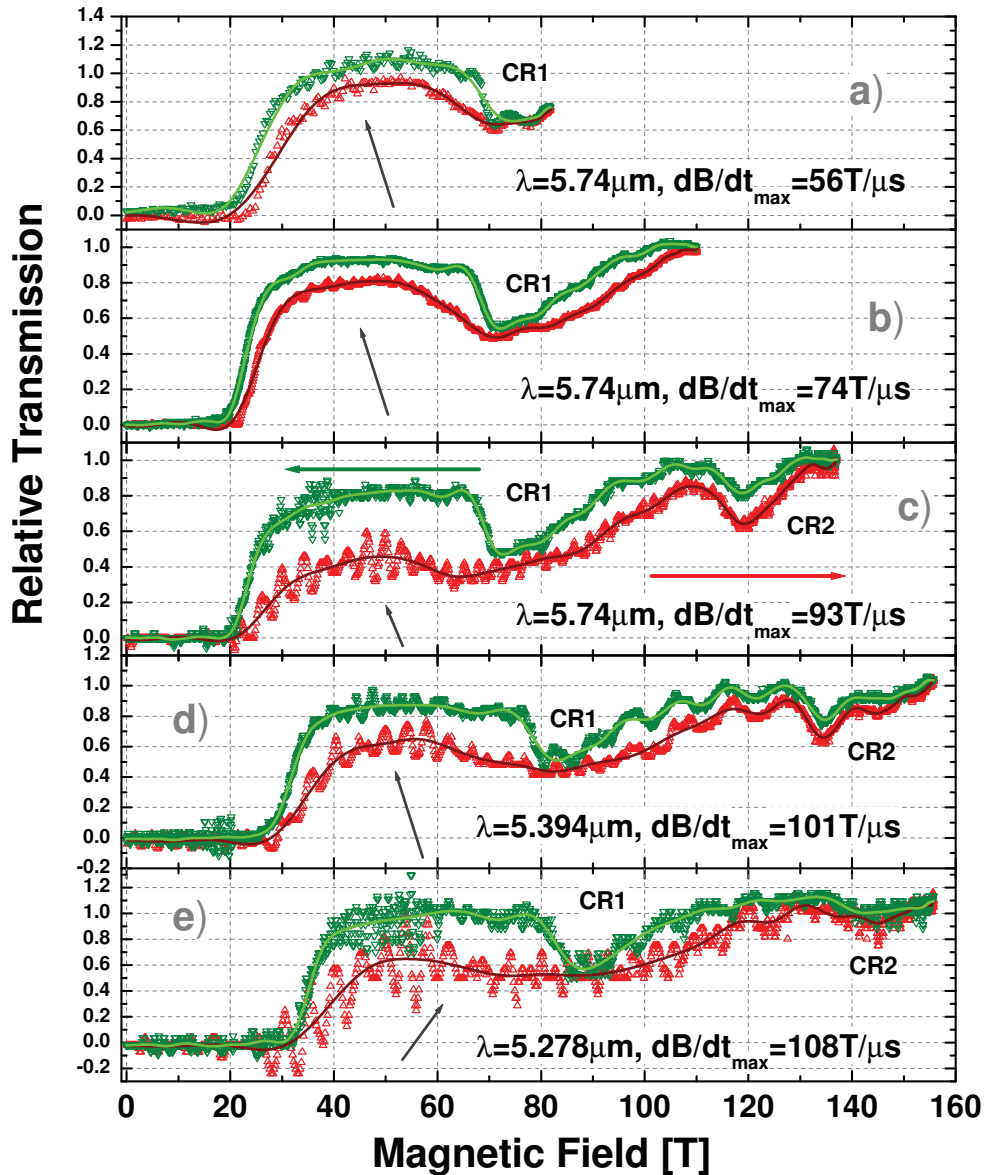


Figure 5.28: Relative Transmission of intrinsic InSb with CO Laser. a) - c): sweep rate dependence at 216 meV ( $\lambda = 5.74 \mu\text{m}$ ). c)- e): wavelength dependence at comparable sweep rate 216 meV, 230 meV ( $\lambda = 5.394 \mu\text{m}$ ) and 235 meV ( $\lambda = 5.277 \mu\text{m}$ ). Lower curves are the up sweep traces. The horizontal arrows indicate the sweep direction.

up sweeps than it is in the down sweeps. This phenomenon is observed at a magnitude that exceeds the noise level.

This may be an indication for the free carrier absorption in the up sweeps. The radial electric field cannot be estimated in this field range due to the lack of appropriate methods to determine the conductivity and mobility.

Table 5.1: *Previous CR Measurements on InSb in transient magnetic fields.*

	Chicago group (1974) [14]	Tokyo group (1976) [15, 16]
Method:	Reflectivity	Transmission
Magnet:	single turn coil	flux compression, STC
Material:	(111) n-type InSb	n-type InSb
Sample Size:	2 - 3 mm	2 mm disc
thickness:		?
Wavelengths:	10.6 $\mu\text{m}$ , 5.56 $\mu\text{m}$	9.4-11 $\mu\text{m}$
Remarks:	useless up sweep data only down sweep reported	STC and EMFC methods rise time 23 $\mu\text{s}$ @ 50T (STC)
	Both report (rough estimates of) eddy current heating or line broadening with increased sweep rate, respectively.	

### 5.5.3 Comparison With Previous Measurements

The observation can now be excellently compared to previous publications for intrinsic InSb investigated at room temperature in transient fields whose experimental conditions are summarized in table 5.1.

The authors of [14] give an estimate for eddy current heating using the conductivity at 77 K for a calculation. They also ignore the magnetic field dependence of  $\sigma_0$ . Hence their estimate for the temperature rise of more than 500 K is overrated by at least one order of magnitude. Moreover, they report an increase of CR line width with increasing sweep rate, which may have been caused by eddy current heating. This behavior could not be confirmed as e.g. seen in fig. 5.28, traces a) to c) for CR1. Yet a dependence of the overall transmission conditions on the sweep rate is clearly seen.

The authors of [15, 16] estimate the effect of eddy current heating to be less than 30 K. In their measurement a single turn coil has been used with a pulse duration of  $\approx 25 \mu\text{s}$  at a maximum field of  $\approx 50 T$  and the EMFC with a similar time constant and a maximum field of  $\approx 100 T$ . Based on the considerations in this thesis the eddy current heating should be much smaller than the stated value for a sweep rate that is comparable to later oscillations of a nondestructive fields. In [15, 16] eddy currents effects were estimated to judge the reliability of the obtained data, no dependence on sweep rate of the observed spectra was reported. This is most likely due to the much smaller sweep rate compared with [14] and this work.

The observed cyclotron resonance positions of this work are in excellent agreement with the previously published values. The observed spectra of this thesis are not contradictory to previous measurement, they have been obtained with a much better signal to noise ratio and a well adjusted sweep rate. The hints for sweep rate related phenomena in InSb of [14–16] could be confirmed and extended.



Summarizing the observations in InSb we find

- The type III hysteresis was observed in Ge-doped and intrinsic InSb at elevated temperatures. The magnitude of the transmission drop was proportional to the field derivative times the magnetic field.
- Comparing DC transport with eddy current spectroscopy it was determined that contributions of all conductivity dependent quantities are negligible and cannot cause the type III transmission drop.
- It was shown that the radial electric field and the transmission drop are correlated. The change of transmission due to a high electric field is in good qualitative agreement with available references.
- In intrinsic InSb a hint for a type I hysteresis was observed that interferes with the generally higher transmission in down sweeps that is similarly caused the radial electric field.

## Chapter 6

# Mercury Based Compounds

In this chapter we would like to present data obtained with infrared transmission experiments on other materials than InSb. Hysteresis effects of all three types have been observable in various samples. An extensive study of the origin of the hysteresis effects was made impossible by the unavailability of appropriate amounts of samples or the lack of bulk, macroscopically sufficiently large dimensioned material for eddy current spectroscopy. However, within experimental resolution, hysteretic phenomena seem to be rather the typical situation than the exception.

The discussion on these materials will not be as extensive as it was for InSb due to the availability of only limited amounts of each sample or its structure. The purpose of this chapter is the investigation on the influence of the sweep rate onto cyclotron resonance measurements. Moreover, most hysteretic phenomena reported here do not occur in low fields but in field magnitudes that are hardly accessible with non-destructive STC experiments or even steady magnets. This makes a clear indication very difficult. When non-destructive STC fields can not be used sweep rate dependent measurements involve a sample dismounting and mounting. This was carried out very carefully but the overall conditions (e.g. Laser incidence) are not as reproducible as with a series of non-destructive experiments. Large effort has been applied to provide reproducible conditions, all conditions were multiply checked.

The mercury based binary compounds HgSe and HgTe as well as the ternary compound  $Hg_{1-x}Cd_xTe$  for  $x < 0.4$  are zero and narrow gap semiconductors, respectively [26]. The resulting strong non-parabolicity manifests in well distinguishable spin split cyclotron resonances. Hence these materials are well suited for the observation of a type I hysteresis as was shown for HgSe in chapter 1. On the other hand the small or vanishing energy gap makes these materials susceptible to very small changes in temperature.

### 6.1 Mercury Selenide

The HgSe sample Q 472 showing a hysteresis of type I was grown by molecular beam epitaxy. The sample had a layer of  $1 \mu m$  HgSe on (100) GaAs substrate with a buffer of  $\approx 0.5 \mu m$  ZnTe. The electron concentration at room temperature was determined to be of order  $n = 6 \times 10^{17} cm^{-3}$  at a mobility of  $\mu = 1 \times 10^4 cm^2/Vs$  [4]. This sample was not available for further investigation due to a failure in an experiment [12].

The type I hysteresis could be observed at room temperature and 207 K. For similar sample structure (samples B) with a conductivity that is larger by at least a factor of

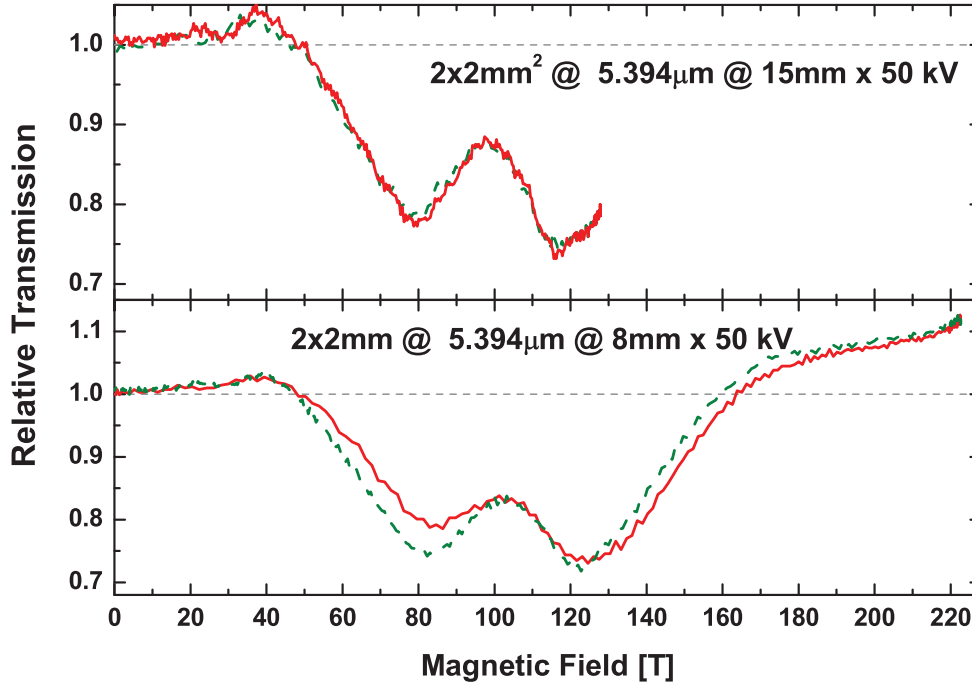


Figure 6.1: Relative infrared transmission of HgSe at  $\lambda = 5.394 \mu\text{m}$  and room temperature for two field different semi-destructive field shapes. The sample used was a  $2 \times 2 \text{ mm}^2$  square. The down sweeps are indicated by dashed lines.

four, no hysteresis was observed at all at the similar conditions as for Q472 [12]. That is, room temperature and  $\lambda = 10.59 \mu\text{m}$  at a field of 140 T. The dependence on conductivity points to eddy current effects such as a temperature rise to obscure the type I hysteresis.

Sweep rate dependent studies as well as wavelength dependent studies have not been carried out by the authors of [4,5] due to sample destruction at an early stage [12]. For the B samples this behavior can be studied.

A square sample of HgSe (B,  $2 \times 2 \text{ mm}^2$ ) was tested at a wavelength of  $\lambda = 5.394 \mu\text{m}$  at room temperature with two field shapes of 50 kV discharges in a 15 mm and 8 mm coil respectively. The field traces are given in fig. 2.10. The resulting traces are depicted in fig. 6.1. It can be seen that there are two resonant structures in both traces. The lower field resonance can be identified as the spin down electron cyclotron resonance, the higher field resonance as an interband transition [103,104]. Both resonances are broader in the higher sweep rate experiment while the resonance position is preserved compared with the lower sweep rate experiment. Moreover, the electron cyclotron resonance is unchanged for up and down sweep in the lower sweep rate experiment while it is increased in the down sweep for the higher sweep rate experiment. With this data it is unclear whether this is due to a type I or II hysteresis. The trace shows a similar behavior as type II hysteresis as well as the type I hysteresis observed for Q 472 at 207 K.

Unfortunately the large piece of the sample was destroyed in the high sweep rate experiment after the magnetic field pulse by an accident, so that further investigations

must be carried out on smaller samples. This reduces the effects of eddy currents by a factor of 2-4. The resulting traces for a 1 mm diameter sample at  $10.59 \mu\text{m}$  are shown in fig. 6.2.

A sweep rate dependence was found for the 1 mm sample. The traces for three different sweep rates are given in fig. 6.2. The traces have been obtained at room temperature with  $\lambda = 10.59 \mu\text{m}$  in a 15 mm coil at discharging voltages of 30, 40 and 45 kV. The electron CR positions are in good agreement with previously published data for Q472 [4,5] and recent theoretical models [103,104]. The band structure of HgSe is disputed, there are two competing models for the fundamental energy gap [26,105,106]. The identification of transitions has been carried out with a tight binding - zero gap model [104].

It can be clearly seen that at 30 kV there is no hysteresis to be observed. Moreover, there is a much smaller absorption intensity than for the two others. The electron cyclotron resonance is very small, approximately 2%. This results even in a deviating position of the transmission minimum as compared to the other two traces. A wrong positioning of the sample in the coil that would cause a similar behavior can explicitly be ruled out. The spin down CR transmission change is 14% for the 40kV experiment, and 12% for the 45 kV one in the up sweeps. The down sweeps show 17% and 14% respectively. The spin up CR is not affected by a hysteresis. A clear identification of the type of hysteresis (I or II) is not possible without further measurements.

However, these findings show another, very important conclusion on the experimental conditions. The observability of CR is increased with increased sweep rate while the resonance condition  $\omega = \omega_c\tau$  was left unchanged for all experiments. The CR can only be observed unambiguously at high sweep rates.

In fig. 6.3 the relative transmission traces are given for a wavelength of  $\lambda = 9.62 \mu\text{m}$ . It is clearly seen that the spin down CR is affected by a hysteresis and is increased in the down sweep. The higher field resonance may be a combination of an interband transition and the electron spin up resonance [103,104]. Nevertheless this and the previous findings show, that the observation of the hysteresis effect is independent of wavelength but strongly dependent on the sweep rate.

For a clear distinction of the hysteresis types I and II the sample size must be further reduced to diminish the influence of eddy current related phenomena. A mechanical reduction of sample dimensions was not possible, a chemical reduction would require an opaque material surrounding the active area to avoid transmission through the substrate which results in a very high transmission and small effects of the active layer. This must be introduced at the growth stage of sample preparation and provides a challenge for future.

## 6.2 Mercury Telluride

It was shown in chapter 1 that this sample of HgTe exhibits a type II hysteresis. The mechanism of the increase of absorption in the down sweep was not conclusive. Based on the considerations of this thesis eddy current related phenomena are likely to cause such a behavior. Although the actual physical process cannot be worked out at this point due to the lack of sufficient sample material for transport and eddy current spectroscopy, it is possible to determine whether or not the infrared transmission trace depends on the diameter of the sample and the sweep rate.

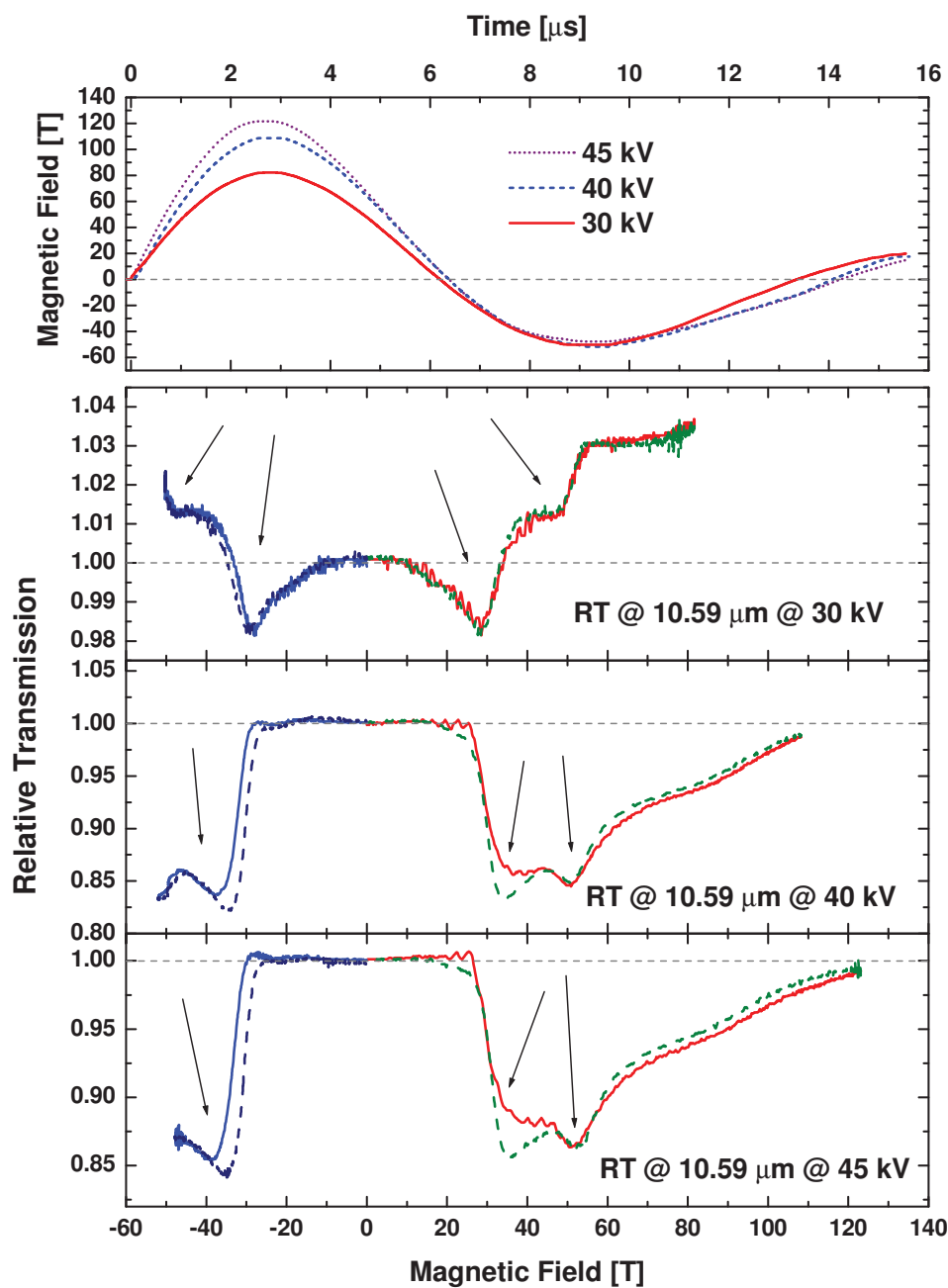


Figure 6.2: Infrared transmission traces for HgSe (B) at a sample diameter of 1 mm. Top to bottom: Magnetic Fields, relative transmission for 30 kV, 40 kV, 45 kV charging voltages. All traces taken at room temperature and  $10.59 \mu\text{m}$ . The down sweeps are indicated by dashed lines.

The investigated sample Q 1510 was epitaxially grown on  $0.9 \text{ mm } \text{Cd}_{0.96}\text{Zn}_{0.04}\text{Te}$  with a  $100 \text{ nm}$  buffer of CdTe. The thickness of the conductive layer of HgTe was  $(2.0 \pm 0.2) \mu\text{m}$ . This value is much larger than the lattice constant and the relaxation depth,

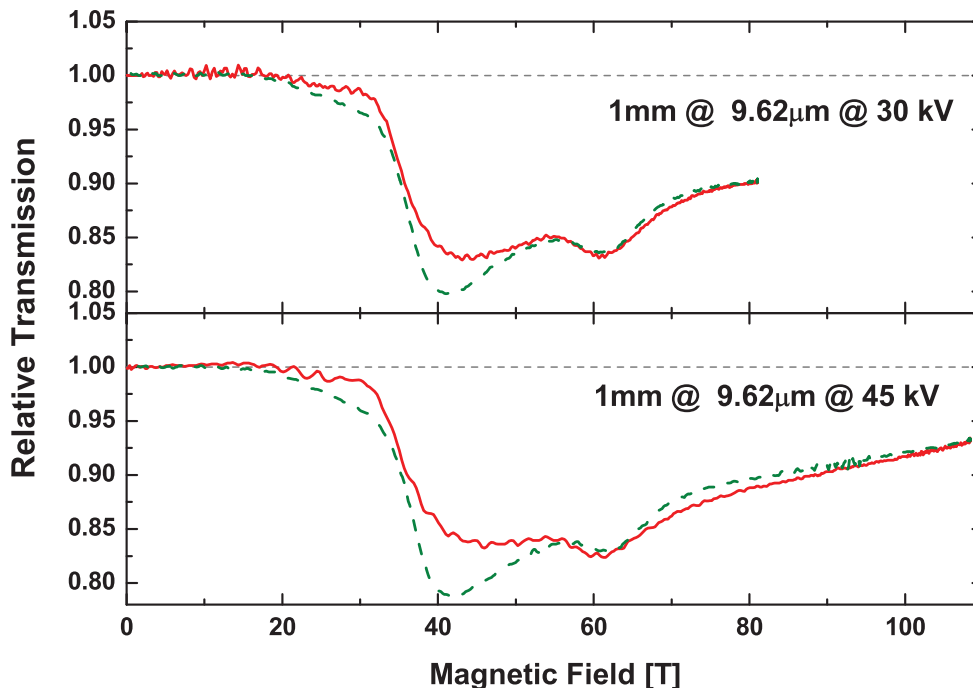


Figure 6.3: Relative infrared transmission of HgSe at  $\lambda = 9.62 \mu\text{m}$  and room temperature for two field different semi-destructive field shapes. The sample was cylindrical with diameter 1 mm. The down sweeps are indicated by dashed lines.

we can consider the sample as quasi-bulk HgTe [107]. The room temperature carrier concentration was  $n \approx 5 \times 10^{17} \text{ cm}^{-3}$  at a mobility of order  $\mu \approx 3 \times 10^4 \text{ cm}^2/\text{Vs}$ .

Figure 6.4 shows infrared transmission traces of HgTe Q1510 at room temperature and a field obtained with a 45 kV discharge at 15 mm coil diameter. The magnetic field trace corresponds to the dotted trace of the top layer of fig. 6.2. The magnetic fields used for the two measurements have been identical within one bit of the ADC. The sample sizes were a square of  $2 \times 2 \text{ mm}^2$  and 1mm diameter cylindrical shape. It is clearly seen that the 1 mm sample is much stronger affected by hysteresis than the  $2 \times 2 \text{ mm}^2$  sample.

It is important to note that the absorption in the up sweep shows is approximately equal for both sample sizes, the down sweep trace is depending on sweep rate. The spin down electron cyclotron resonance [6, 7] has the transmission drop of 81% in both up sweeps but 78% for the  $2 \times 2 \text{ mm}^2$  and 73% for the 1 mm sample in the down sweep respectively. The FWHM is nearly identical for both traces (14 T). At the peak field the transmission is larger than at  $B=0$ . For the larger sample this increase of transmission is twice a high as for the smaller one.

These infrared transmission experiments clearly show a dependence on sample diameter. Sweep rate dependent measurements had been carried out by [6, 7] showing a similar behavior as HgSe in fig. 6.2. There was no hysteresis at low maximum fields and a very pronounced type II hysteresis at large sweep rates. The increase in absorption for the spin split CR was similarly observed after the zero crossing of B as shown for example

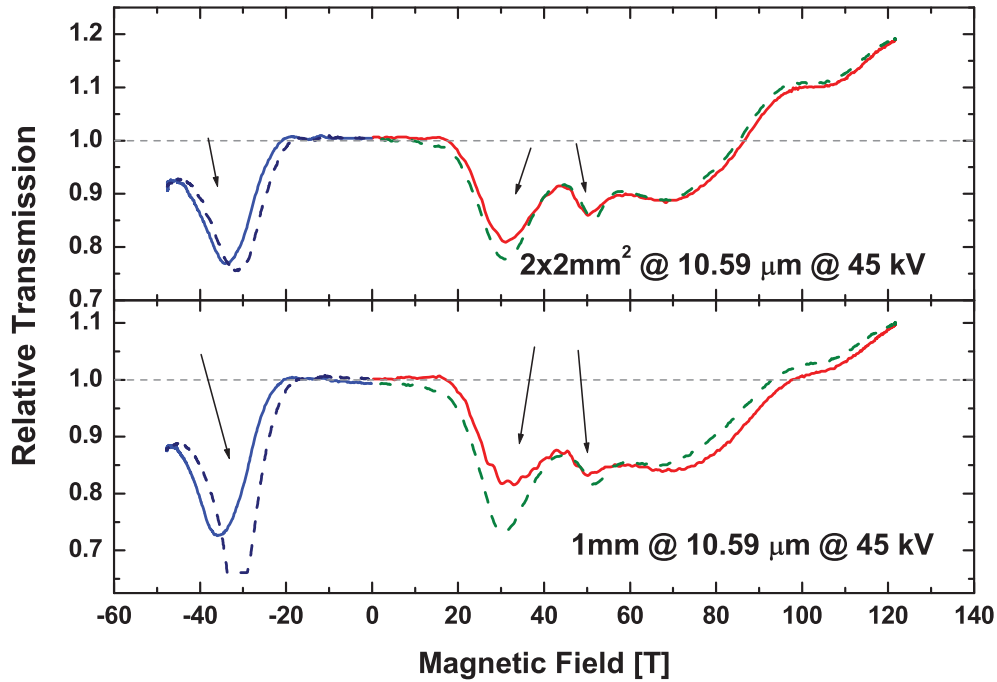


Figure 6.4: Infrared transmission traces of HgTe Q1510 at room temperature,  $10.59 \mu\text{m}$ ,  $45 \text{ kV}$  discharge voltage and sample sizes:  $2 \times 2 \text{ mm}^2$  (top) and  $1 \text{ mm}$  diameter (bottom). Down sweeps are indicated by dashed lines.

in chapter 1 [6, 7].

It can be concluded that eddy current related phenomena are relevant to the observation of the type II hysteresis in this material. A conclusion on the cause for this behavior is highly speculative. Intuitively the temperature rise is a possible explanation, but requires further measurements.

It should be noted that experiments with the CO Laser showed no difference between the sample sizes and the sweep rates. Even the relative transmission change was of similar magnitude, the traces are not distinguishable from each other for up and down sweeps. The resonance position was shifted to  $\approx 100 \text{ T}$ . At higher wavelength the CR is not affected by a hysteresis. This may point to a temperature difference as the cause of the hysteresis.

### 6.3 Mercury Cadmium Telluride (MCT)

MCT is a material widely used in infrared elements such as the detector used in the CR equipment in this thesis. Its main advantage is the tunability of its fundamental band gap from  $\approx 300 \text{ meV}$  to  $\approx 1.65 \text{ eV}$  by varying the composition parameter  $x$  from 0 to 1. The values are given for  $T=4 \text{ K}$ .

For composition parameters  $x \approx 0.25 \pm 0.1$  the electronic properties of MCT are very similar to InSb. However, a fundamental difference is found in this composition range as

the energy gap does not decrease with increasing temperature as InSb does but increases linearly. The energy gap of MCT at a temperature  $T$  is depending on the composition parameter and can be described by [108]

$$E_g(x, T)[eV] = -0.302 + 1.93x + 5.35 \times 10^{-4}T(1 - 2x) - 0.810x^2 + .832x^3 \quad . \quad (6.1)$$

### 6.3.1 Epitaxial MCT

The epitaxially grown sample of  $Hg_{1-x}Cd_xTe$  had the layer sequence, GaAs substrate, p-type MCT, n-type MCT and a CdTe cap. The thickness of the p-type layer was  $7.97 \text{ nm}$ , the n-type thickness  $3.38 \text{ nm}$ . At low temperatures the material is p-type with  $p \approx 4.66 \times 10^{15} \text{ cm}^{-3}$  at a mobility of  $\mu \approx 600 \text{ cm}^2/\text{Vs}$ . The composition parameter  $x=0.2927$  [109]. We obtain  $E_g(295 \text{ K}) = 277 \text{ meV}$  with (6.1).

The given sample was found to be extremely susceptible to the sweep rate. An illustration is given in fig. 6.5. The experiments have been carried out at room temperature with a wavelength of  $10.59 \mu\text{m}$  on a sample with radius  $1.44 \text{ mm}$ . It can be clearly seen that the transmission depends on the sweep rate in a non-trivial way. For field 1 of fig. 6.5 we find the down sweep resonance to be substantially increased vs. the up sweep whereas we cannot observe that for the other two fields.

For field 2 the up and down sweeps are nearly coincidental, the down sweep shows less pronounced structures than the up sweep does. This may be due to a similar phenomenon as discussed for InSb. However, at field 3 there is even an indication for a type I hysteresis, where the lower field resonance is increased in down sweep at the expense of the upper field structure. This behavior could not be found at higher sweep rates that showed traces similar to the field 2 trace.

It must be pointed out that the magnetic fields used for fig. 6.5 are different from each other by only very few T. The maximum field values for the lowest and the highest field differ by only 15 T, the time difference between resonance positions for up and down sweeps is nearly unchanged for all three fields. This illustrates, how critical hysteretic phenomena depend on the sweep rate.

At a significantly different wavelength of  $\lambda = 5.394 \mu\text{m}$  sweep rate dependent infrared transmission experiments have been performed. The results are reproduced in fig. 6.6. It can be clearly seen that the traces obtained on a square  $2 \times 2 \text{ mm}^2$  sample show a significantly different behavior depending on the sweep rate or maximum field. At the smallest maximum field value a nearly identical trace was obtained for up and down sweeps with a transmission change of  $\approx 30\%$ . For the medium maximum field the down sweep trace shows a larger FWHM than the up sweep indicating a larger number of carriers in the down sweep. The overall absorption is much smaller than with the smallest maximum field, approximately 6%. At the highest maximum field the down sweep resonance is not only much larger in FWHM than in the up sweep but the transmission change is also much stronger,  $\approx 8\% \rightarrow \approx 14\%$ . The resonance position is preserved for all three fields.

The stronger absorption at the smallest sweep rate is not caused by a cutoff of the detector response function in the faster swept traces. The FWHM in time was larger than 300 ns for all observations.

The determination of the involved energy level has not been carried out, the given traces are chosen to illuminate the occurring and vanishing of hysteretic phenomena with sweep rate.



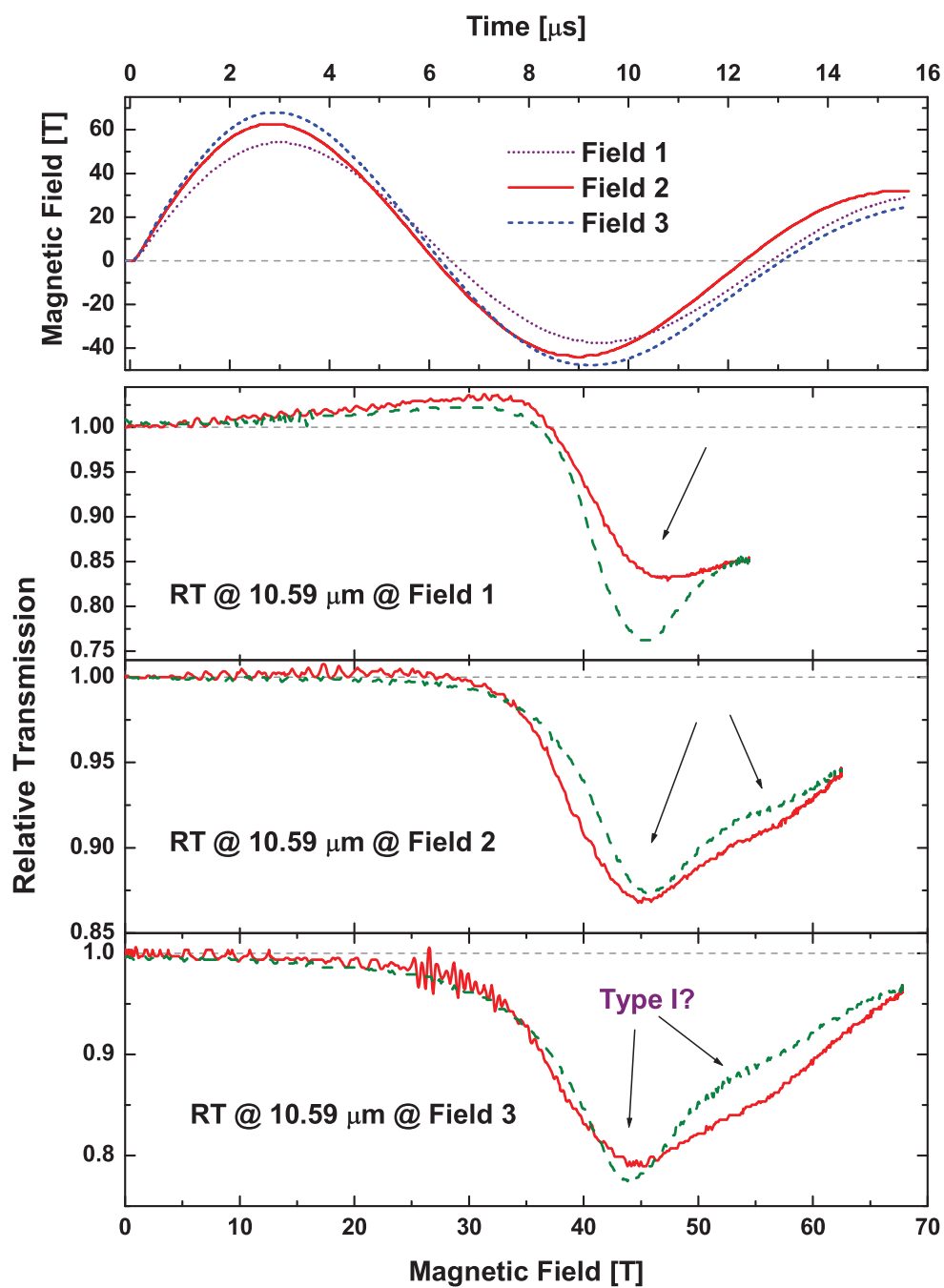


Figure 6.5: Sweep rate dependence of MCT relative transmission spectra at room temperature and  $10.59\ \mu\text{m}$ . Arrows indicate the phenomena affected by hysteresis. Down sweeps are indicated by dashed lines.

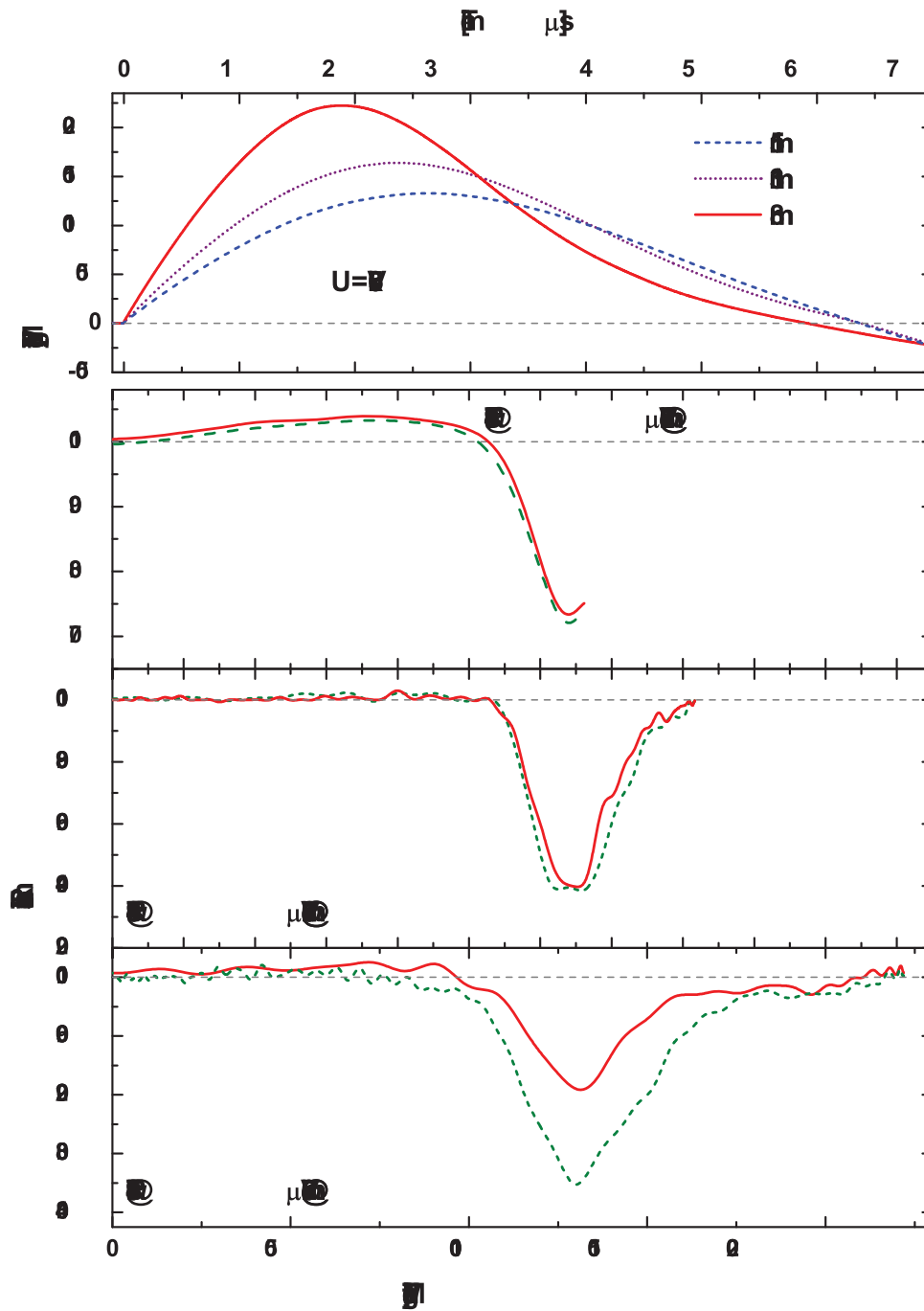


Figure 6.6: Infrared transmission traces of MCT at different sweep rates obtained at  $\lambda = 5.394 \mu\text{m}$  and room temperature. The sweep rate was varied by changing the coil diameter from 15 to 8 mm while the charging voltage was left unchanged. Down sweeps are indicated by dashed lines. The respective magnetic fields are given in the top layer.

### 6.3.2 Bulk MCT

The sample L-90-9-13-2-1 is n-type bulk MCT and was grown with a composition parameter  $x = 0.215 \pm 0.003$  to provide an energy gap that is infrared. The material was designed to be used as an infrared detector. The sample has macroscopic dimensions of  $2 \times 2 \times 0.9 \text{ mm}^3$  and is CZOCHRALSKI grown material. MCT with this composition is very similar in its electronic properties to InSb. The energy gap at room temperature is found as  $E_g = 175 \text{ meV}$  by (6.1). The electron concentration at 77 K was determined to be  $n \approx 1.5 \times 10^{14} \text{ cm}^{-3}$ , the mobility  $\mu \approx 2.24 \times 10^5 \text{ cm}^2/\text{Vs}$  [89]. At these parameters we can expect a strong influence of the radial electric field.

There is a type III phenomenon observable in this sample. Infrared transmission spectra at  $\lambda = 10.59 \mu\text{m}$  and various temperatures are depicted in fig. 6.7. At room temperature we can observe the electron cyclotron resonance and a very small type III transmission drop as indicated by the arrows. This type III phenomenon becomes much more pronounced as the temperature is decreased to 150 K (indicated by arrows). Although MCT is comparable to InSb in many properties, its energy gap dependence on temperature is significantly different. With decreasing temperature the band gap of MCT is decreasing. At temperatures lower than 150 K no transmission could be observed at all, indicating a band gap below the laser energy. At 150 K the energy gap is expected to be  $E_g \approx 129 \text{ meV}$  using (6.1).

Moreover, there is a clear dependence of its magnitude on the direction of the magnetic field at low temperatures. This can be most clearly seen on the trace of T=156 K. The traces are given vs. magnetic field in fig. 6.8 for the first two up and down sweeps. The arrows indicate the type III hysteresis. There is a clear asymmetry at 156 K for positive and negative magnetic field. This behavior could be similarly observed at a wavelength of  $10.24 \mu\text{m}$ . This transmission drop depends on the magnitude of the field derivative as well, but not linearly. However, if only the drops in one magnetic field direction are considered, there is a linear dependence, similarly for the opposite field orientation. Both have opposite signs but similar slopes and coincide at long times of  $\approx 50 \mu\text{s}$  when the magnetic field changes only by a few T as shown in fig. 4.10.

The origin of this phenomenon remains to be investigated in the future. Reported dependences of conductivity on high electric fields for low temperatures suggest a similar origin as in InSb [110]. Eddy current spectroscopy as well as CR in slowly varying fields will provide insights.

Summarizing the experimental findings on mercury based compounds we can state

- All investigated samples showed hysteretic phenomena depending on the sweep rate. For HgTe it was shown that the hysteresis is also dependent on sample dimensions indicating an eddy current related effect.
- Epitaxial samples of HgSe, HgTe and MCT showed hysteretic phenomena of type II independently of the wavelength used.
- In epitaxial MCT a hint for a type I hysteresis was observed.
- Bulk MCT samples showed a type III hysteresis that is more pronounced at low temperatures of  $\approx 180 \text{ K}$ .

As a closing remark it must be pointed out that hysteretic phenomena are affecting nearly all semi-conducting materials investigated in one way or another. During my

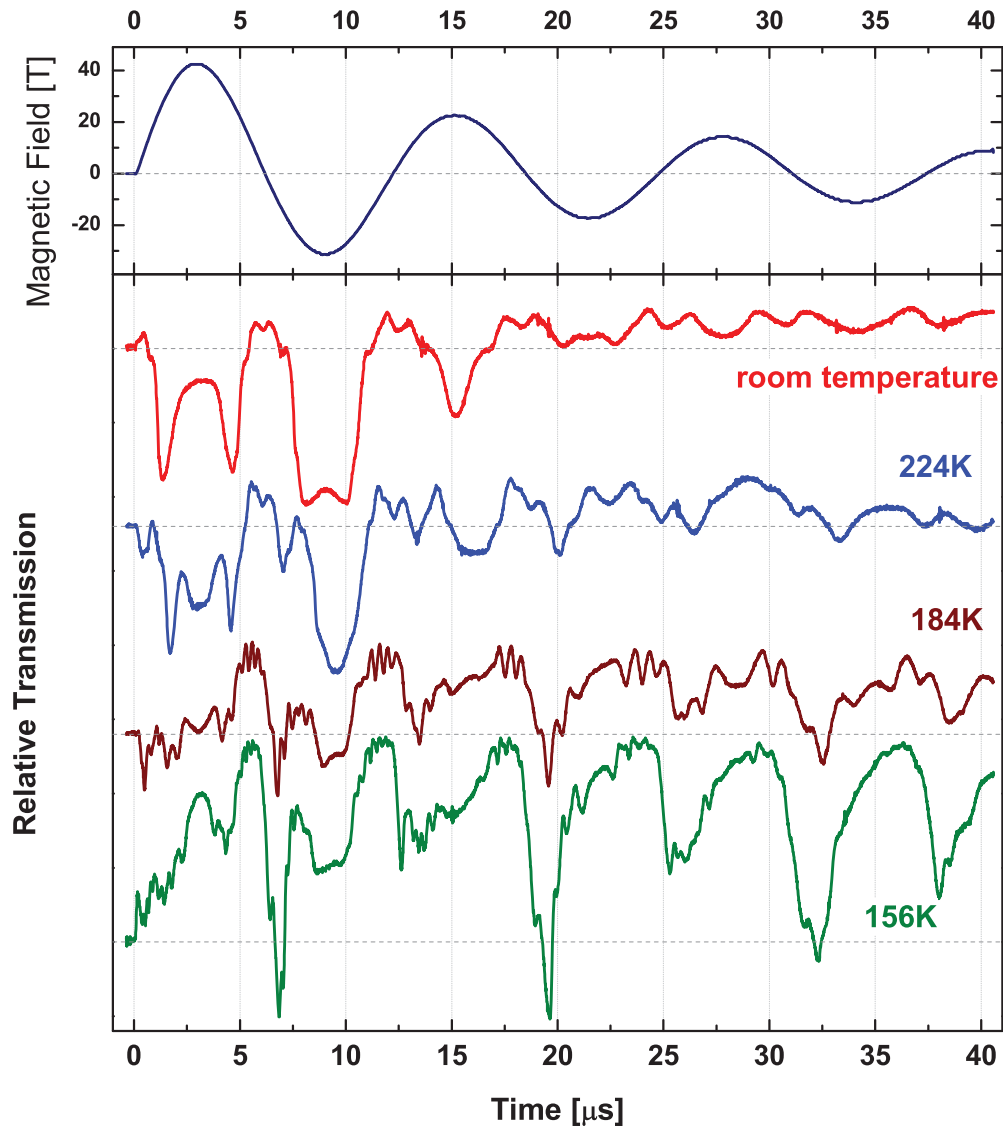


Figure 6.7: Traces of MCT sample L-90-9-13-2-1 at various temperatures. A type III hysteretic phenomenon is observed. The magnitude is dramatically increased for decreasing temperature.

work at the HUMBOLDT-Universität various collaborations have investigated materials showing type I, II and III hysteresis' such as thin layers of PbTe, InSb and 2D structures of GaAs as well as GaAs/GaAlAs. The detailed analysis of these materials and the involved energy levels is in progress by the respective collaborators [111].

It is also important to note, that eddy current effects will not be specific to infrared transmission experiments only, but have to be considered in every kind of experiment on semi-conductors exposed to transient magnetic fields.

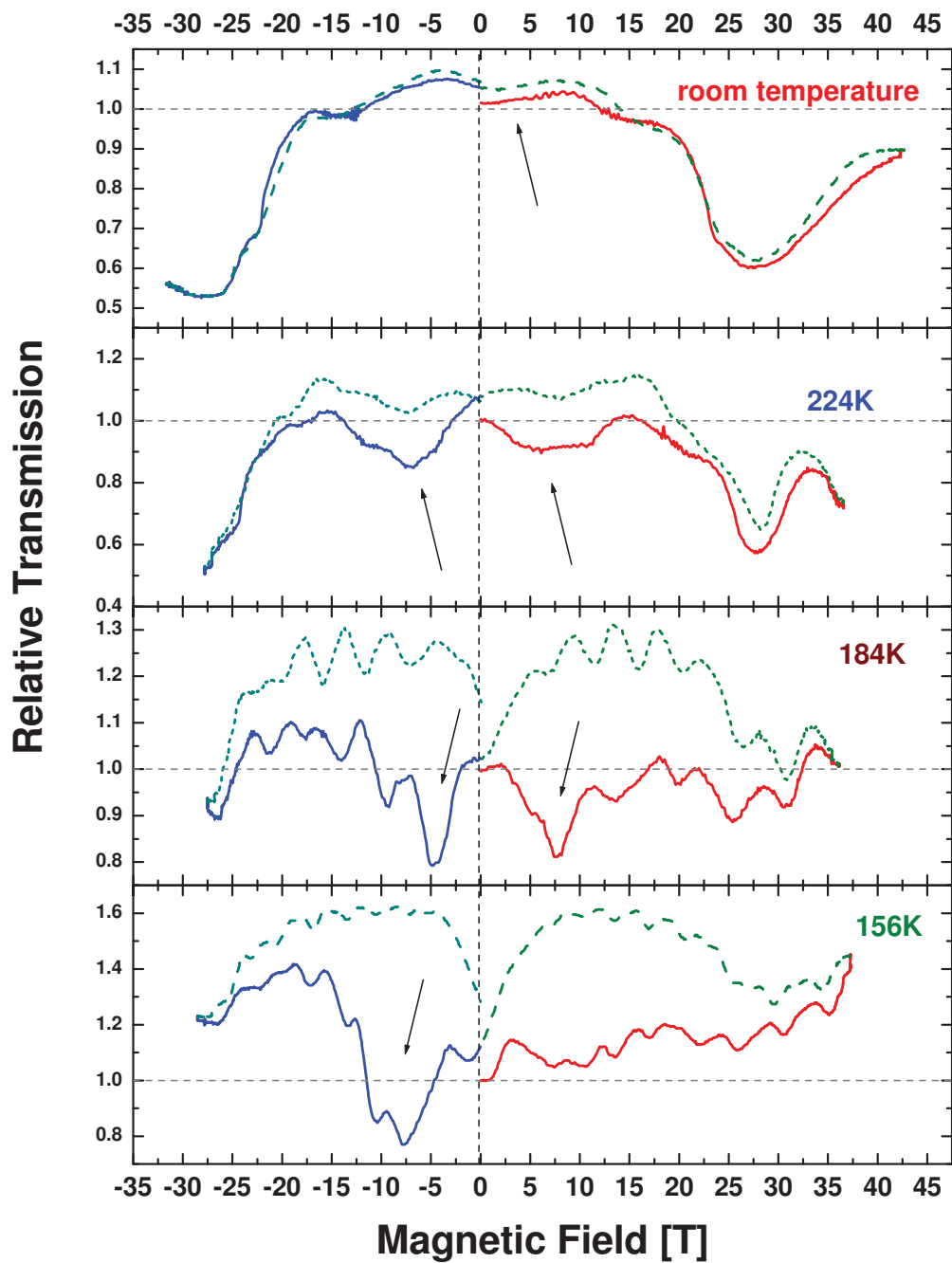


Figure 6.8: Traces of MCT sample L-90-9-13-2-1 at various temperatures. The down sweeps are indicated by dashed lines. Arrows point to the type III hysteresis.

# Summary

In this thesis hysteretic phenomena of semi-conductors in infrared transmission experiments in transient magnetic fields have been investigated. Besides a well known spin relaxation hysteresis phenomenon, two more effects could be reported for the first time that are directly connected with the magnetic field generation process.

A theoretical analysis with unprecedented complexity has been carried out for the behavior of conducting samples exposed to a transient magnetic field. Starting from MAXWELL's equations it was demonstrated that the transition from slowly varying or DC fields to transient magnetic field generation is accompanied by numerous phenomena connected with the induced electric field and eddy currents. The magnitude of which was found to be negligible in slowly varying fields but of major influence on the experimental situation in transient magnetic fields.

A quantitative determination of primarily the eddy current density and azimuthal electric field was carried out. Secondary effects such as the temperature rise due to the finite resistance of the current carrying conductor, the pressure distribution caused by the LORENTZ force, a radial HALL-like electric field given by the finite extension of the sample and the screening of the magnetic field during a transient pulse have been deduced. It was shown in theory and experiment that it is not possible to analyze a magnetic field dependence of a quantity in transient magnetic fields without considering the effects of eddy current related phenomena.

The eddy current related phenomena in a sample exposed to a transient magnetic field were found in complete analogy to well known problems limiting the generation of high magnetic fields, scaled by the conductivity and the macroscopic sample dimensions. It was shown that the infrared transmission of various semiconductors is affected by eddy current related phenomena. Due to the macroscopic dependence of the latter on the sample diameter, the influence on the resulting spectra can be reduced by decreasing the sample radius.

A prerequisite to the reliable detection of discrepancies in the infrared transmission traces in rising and falling field is an excellent signal to noise ratio of the respective experiment. An unprecedented data quality was achieved by carefully eliminating all sources of noise using a solid high-frequency-proof-FARADAY cage and well shielded cables for data transfer. The resolution of the optical data was improved by a factor of three to 0.2%. The data obtained at rising field that have been largely obscured by trigger noise in previous works show no significant noise anymore and can be used for data evaluation.

The data processing routines have been analyzed. Systematic sources of deviations in timing between optical and magnetic field data have been identified, their influence estimated and corrected.

A solid steel reinforcement has been developed for the existing magnetic field generator. This enables the application of nondestructive fields with small damping constants

and relatively small magnitude, but many oscillations of magnetic field. The benefit for investigations of hysteretic phenomena is a transient magnetic field with a magnitude comparable to fields that can be obtained with steady or slowly pulsed magnets.

The equipment was used to investigate a new hysteretic phenomenon in InSb in infrared transmission experiments. It was shown that a transmission drop which is asymmetric to the zero field position of a pulse occurs after each zero crossing of the magnetic field with a magnitude that is proportional to the absolute field derivative. The intuitive association with eddy currents was investigated by means of steady field transport and eddy current spectroscopy. The latter technique investigates semi-conducting samples with magnetization equipment in single turn coils, employing the exact same experimental parameters of the magnetic field as the optical experiments.

As a novelty the conductivity of semiconductors in transient fields could be quantitatively determined on the example of InSb. It was found to be independent of sweep rate and equal to the DC case. With this information, the conductivity dependent magnitudes of the temperature rise during a magnetic field pulse, the pressure as well as the screening of magnetic field could be determined and were found negligible. The transmission drop in InSb could be qualitatively explained by an increase of absorption coefficient due to an applied electric field. It was shown that the radial electric field can cause the shape and magnitude of the transmission drop as well as its asymmetric behavior.

For mercury based compounds sweep rate dependent measurements have been carried out. It was demonstrated that the infrared transmission of all investigated samples is subject to hysteresis effects that depend strongly on sweep rate. Measurements on samples with reduced dimensions have shown a clear dependence on sample radius. This indicates that eddy current related phenomena are effective in the infrared transmission experiments in transient magnetic fields.

It must be pointed out that experiments in transient magnetic fields can not be analyzed with the help of the magnetic field magnitude only. One has to consider effects accompanying the magnetic field generation process that are capable of substantially changing the sample properties under investigation. This has been demonstrated for infrared transmission experiments but applies to all experiments on highly conductive samples in transient magnetic fields.

# Zusammenfassung

In der vorliegenden Arbeit wurden Hysterese-Phänomene von Halbleitern bei Infrarot-Transmissionsexperimenten in transienten Magnetfeldern studiert. Neben einem gut untersuchten Spin-Relaxations-Phänomen, konnten zum ersten Mal zwei weitere Effekte beobachtet werden, die direkt mit der Art der Magnetfelderzeugung zusammenhängen.

Eine theoretische Analyse von nie da gewesener Komplexität wurde durchgeführt, um das Verhalten von leitenden Proben in einem transienten Magnetfeld zu untersuchen. Ausgehend von den Maxwell-Gleichungen wurde gezeigt, daß der Übergang von langsam-veränderlichen bzw. permanenten zu schnell-veränderlichen Magnetfeldern mit einer Vielzahl von Phänomenen einhergeht, die mit dem induzierten elektrischen Feld und Wirbelströmen zusammenhängen. Deren Größenordnung konnte für langsam veränderliche Felder als vernachlässigbar eingestuft werden, hat jedoch großen Einfluß in transienten Magnetfeldern.

Eine quantitative Bestimmung von primär der Wirbelstromdichte und dem azimuthalen elektrischen Feld wurde durchgeführt. Sekundäre Effekte wie die Temperaturerhöhung eines stromführenden Leiters mit nicht-verschwindendem Widerstand, die Druckverteilung die durch die Lorentzkraft wirkt, ein Hall-artiges radiales elektrisches Feld, das durch die räumliche Begrenzung der Probe entsteht, sowie die Abschirmung des äußeren Magnetfeldes im Inneren der Probe wurden hergeleitet. In Theorie und Experiment konnte gezeigt werden, daß es nicht möglich ist, ohne die Berücksichtigung dieser Effekte Abhängigkeiten von Größen vom Magnetfeld in einem schnell veränderlichen Feld zu analysieren.

Die damit zusammenhängenden Phänomene sind in vollständiger qualitativer Entsprechung zu Betrachtungen, die bei der Erzeugung von hohen Magnetfeldern relevant sind, skaliert mit der Probenleitfähigkeit und den Probendimensionen. Es konnte gezeigt werden, daß die infraroten Transmissionsspektren einer Vielzahl von Halbleitern durch Wirbelströme und verwandte Phänomene beeinflusst werden. Durch deren Abhängigkeit von den makroskopischen Probendimensionen, kann man ihren Einfluss reduzieren durch Verkleinerung der Probenradii.

Als Voraussetzung für die zuverlässige Detektion von Unterschieden in der Transmission für steigendes und fallendes Feld wurde das Signal-Rausch-Verhältnis des Messaufbaus entscheidend verbessert. Eine bislang unerreichte Datenqualität konnte erzielt werden durch die konsequente Abschirmung der Datenaufnahmegerate von Störquellen. Dies wurde realisiert durch einen Hochfrequenz-sicheren Faraday Käfig in massiver Bauart. Die Auflösung der relativen Transmission liegt nun einen Faktor drei besser als bei vorausgegangenen Untersuchungen bei 0.2%. Zum ersten Mal konnten auch die Daten im steigenden Feld vollständig zu Auswertung verwendet werden, da zuvor vorhandene elektromagnetische Störungen durch den Einschaltvorgang in ihrer Wirkung eliminiert werden konnten.



Die Methoden der Datenverarbeitung wurden sorgfältig analysiert. Systematische Fehlerquellen wurden identifiziert, ihr Einfluss abgeschätzt und, wenn möglich, korrigiert.

Durch die Verwendung einer massiven Verstärkung aus Stahl konnten vorhandene Spulen benutzt werden, um ein nicht-destruktives Verhalten des transienten Magnetfeldes zu erzeugen. Durch die kleine Abschwächungskoeffizienten und die Vielzahl von Oszillationen konnten erstmalig Hysterese-Phänomene in transienten Magnetfeldern von gleichem Betrag wie langsam veränderliche Felder ausgezeichnet untersucht und verglichen werden.

Diese Ausrüstung wurde verwendet, um ein vollkommen neues Hysterese-Phänomen in InSb zu untersuchen. Es wurde gezeigt, daß ein Abfall der Transmission vorliegt, welcher asymmetrisch zur Nullposition des Magnetfeldes ist, dessen Ausprägung jedoch linear vom Betrag der Feldableitung abhängt. Der intuitiv vermutete Zusammenhang mit Wirbelströmen wurde mit Hilfe von Transportuntersuchungen in supraleitenden Magneten und Wirbelstrom-Spektroskopie untersucht. Letztere Technik nutzt die exakt gleichen Magnetfeldverhältnisse wie die Transmissionsexperimente in transienten Feldern durch Verwendung von vorhandenen Magnetisierungstechniken an halbleitenden Proben.

Erstmalig konnte dabei diese Technik am Beispiel von InSb für eine quantitative Bestimmung der Leitfähigkeit von Halbleitern in transienten Feldern genutzt werden. Sie konnte als unabhängig von der Feldableitung und gleich der im langsam veränderlichen Feld bestimmt werden. Damit liessen sich die Temperaturerhöhung, der Druck sowie das Abschirmen des äußeren Feldes im Inneren der Probe als vernachlässigbar abschätzen. Der Transmissionsabfall in InSb konnte qualitativ mit einem Anstieg des Absorptionskoeffizienten durch das vorhandene elektrische Feld erklärt werden. Weiterhin wurde gezeigt, daß das radiale elektrische Feld sowohl die Form und Größe des Transmissionsabfall als auch dessen Asymmetrie bezüglich der Nullposition des Feldes erzeugen kann.

Für Quecksilberverbindungen wurden Transmissionsexperimente in Abhängigkeit der Feldableitung durchgeführt. Dabei konnte eine Hysterese festgestellt werden, die stark von der Feldänderungsgeschwindigkeit abhängt. Durchmesserabhängige Messungen zeigten eine klare Abhängigkeit der Hysterese-ausprägung vom Probenradius. Dies weist darauf hin, daß Wirbelstromphänomene in den Infrarot-Transmissionsexperimenten in schnell veränderlichen Magnetfeldern wirksam sind.

Es muss betont werden, daß die Auswertung von Experimenten in transienten Magnetfeldern nicht allein auf deren Betrag beschränkt werden darf. Effekte, die den Magnetfelderzeugungsprozess begleiten und die zu untersuchenden Probeneigenschaften massiv beeinflussen können, müssen berücksichtigt werden. Dies wurde für Infrarot-Transmissionsexperimente gezeigt, gilt jedoch für alle Experimente an hochleitfähigen Proben in schnell veränderlichen Magnetfeldern.

# Bibliography

- [1] H. Arimoto, N. Miura and R. A. Stradling, “Hysteretic Phenomena in Spin-Split Cyclotron Resonance Spectra of InAs/AlSb Single Quantum Well under Short Pulse of High Magnetic Fields up to 150 T”, in “Proc. 9th Intl. Conf. on Narrow Gap Semiconductors”, , edited by N. Puhlmann, H. Müller and M. von Ortenberg, Magnetotransport, Humboldt-Universität zu Berlin, Berlin, Germany, 1999 pp. 10–15
- [2] K. Sugihara, H. Arimoto and N. Miura, “Cyclotron resonance of InAs/AlSb single quantum well in high magnetic fields and spin relaxation process”, *Physica B*, **298** (2001) 195–198
- [3] H. Arimoto, N. Miura and R. A. Stradling, “Effects of nonequilibrium electron distribution and electron-electron interaction observed in spin-split cyclotron resonance of InAs/AlSb single quantum wells at high magnetic fields”, *Phys. Rev. B*, **67** (2003) 155319
- [4] I. Stolpe, O. Portugall, N. Puhlmann, H.-U. Mueller, M. von Ortenberg, M. von Truchseß, C. Becker, A. Pfeuffer-Jeschke and G. Landwehr, “Intra- and inter-band transitions in HgSe in megagauss fields”, *Physica B*, **294-295** (2001) 459–462
- [5] M. von Ortenberg, I. Stolpe, O. Portugall, N. Puhlmann, H.-U. Müller, M. von Truchseß, C. Becker, A. Pfeuffer-Jeschke and G. Landwehr, “Spin effects in HgSe in Megagauss fields”, in “Proc. 25th Intl. Conf. Phys. Semicond.”, , edited by N. Miura and Ando, volume 1, Springer, Osaka, Japan, 2000 pp. 51–52
- [6] S. Hansel, I. Stolpe, A. Kirste, H.-U. Müller and M. von Ortenberg, “Megagauss-Magnetspectroscopy on II-VI Compounds”, in “Proceedings 26th International Conference on Infrared and Millimeter Waves”, , edited by O. Portugall and J. Leotin, Toulouse, France, 2001 pp. 4–74
- [7] S. Hansel, *Infrarotspektroskopie an Narrow-Gap Halbleitermaterialien der Quecksilbertelluridfamilie in Megagaussfeldern*, Diplomarbeit, Humboldt-Universität zu Berlin (September 2001)
- [8] “Webster’s Online Dictionary”, <http://www.webster-dictionary.org/>
- [9] A. Kirste, *Magnetization Measurements in Ultrahigh Magnetic Fields*, Ph.D. thesis, Humboldt-Universität zu Berlin (2003)
- [10] R. J. Elliot, “Theory of the Effect of Spin-Orbit Coupling on Magnetic Resonance in Some Semiconductors”, *Phys. Rev.*, **96** (1954) 266–279

- [11] J. Kono and N. Miura, “Cyclotron resonance in high magnetic fields”, in “High Magnetic Fields: Science and Technology”, , edited by F. Herlach and N. Miura, volume III, World Scientific, Singapore, 2005, manuscript from Dr. Kono’s website
- [12] M. v. Ortenberg, private communication
- [13] S. Hansel, C. Puhle, M. von Ortenberg and E. Huseynov, “Magneto-optical Detection of Carrier-Dynamics in p-type Indiumantimonide”, *Physica B*, **346-347** (2004) 479–482
- [14] F. Herlach, J. Davis, R. Schmidt and H. Spector, “Cyclotron Resonance in InSb and GaAs with magnetic fields up to 140 T”, *Phys. Rev. B*, **10** (1974) 682–688
- [15] N. Miura, G. Kido and S. Chikazumi, “Infrared Cyclotron Resonance in InSb, GaAs and Ge in very high magnetic fields”, *Solid State Communications*, **18** (1976) 885–888
- [16] G. Kido, N. Miura, K. Kawauchi, I. Oguro and S. Chikazumi, “Technique for measuring infrared cyclotron resonance in ultrahigh magnetic fields”, *J. Phys. E: Sci. Instr.*, **9** (1976) 587–592
- [17] O. Drachenko, B. Bansal, V. V. Rylkov, J. Galibert, V. K. Dixit and J. Leotin, “Application of quantum cascade lasers for cyclotron resonance measurements in InAs<sub>x</sub>Sb<sub>1-x</sub> alloys”, in “Proc. 12th. Intl. Conf. on Narrow Gap Semiconductors”, , edited by J. Kono, LNCMP Toulouse, Toulouse, France, 2005 pp. 10–15
- [18] E. D. Palik and J. K. Furdyna, “Infrared and microwave magnetoplasma effects in semiconductors”, *Rep. Prog. Phys.*, **33** (1970) 1193–1322
- [19] C. Hamaguchi, *Basic Semiconductor Physics*, Springer, Berlin, Heidelberg, New York, 2001
- [20] J. Kono, “Cyclotron resonance”, in “Methods in Materials Research”, , edited by E. Kaufman, R. Abbaschian, A. Bocarsly, C.-L. Chien, D. Dollimore, B. Doyle, A. Goldman, R. Gronsky, S. Pearton and J. Sanchez, John Wiley & Sons, New York, 1999
- [21] R. Kubo, “Statistical-Mechanical theory of irreversible processes i: general theory and simple applications to magnetic and conduction problems”, *J. Phys. Soc. Japan*, **12** (1957) 570–586
- [22] M. Barczewski, *The Single-Turn Coil Technique: Installation and Application to IR Magnetospectroscopy on HgSe:Fe Layer Structures*, Ph.D. thesis, Humboldt-Universität zu Berlin (1998)
- [23] R. Kubo, H. Hasegawa and N. Hashitsume, “Quantum theory of galvanomagnetic effect. i. basic considerations”, *J. Phys. Soc. Japan*, **14** (1959) 56–74
- [24] O. Portugall, “Cyclotron resonance of PbSe layers on BaF<sub>2</sub>”, lecture at Kobe University (2003)
- [25] I. Vurgaftman, J. R. Meyer and L. R. Ram-Mohan, “Band parameters for III-V compound semiconductors and their alloys”, *J. Appl. Phys.*, **89** (2001) 5815–5875

- [26] P. Y. Yu and M. Cardona, *Fundamentals of Semiconductors - Physics and Materials Properties*, Springer, Berlin, Heidelberg, New York, 2001, 3rd edition
- [27] H. Knoepfel, *Magnetic Fields: A Comprehensive Theoretical Treatise for Practical Use*, John Wiley & Sons, Inc., New York, 2000
- [28] K. Seeger, *Semiconductor Physics - An Introduction*, Springer, Berlin, Heidelberg, New York, 1991, 5th edition
- [29] H. Knoepfel, *Pulsed High Magnetic Fields: Physical Effects and Generation Methods Concerning Pulsed Fields up to the MegaOersted Level*, North Holland Publishing Co., New York, 1970
- [30] M. Abramowitz and I. A. Stegun, *Handbook of Mathematical Functions with Formulas, Graphs, and Mathematical Tables*, New York, 1972
- [31] E.W.Weisstein, "Kelvin functions", Mathworld - A Wolfram Web Resource
- [32] O. Portugall, N. Puhlmann, H.-U. Müller, M. Barczewski, I. Stolpe and M. von Ortenberg, "Megagauss magnetic field generation in single-turn coil: new frontiers for scientific experiments", *J. Phys. D: Appl. Phys.*, **32** (1999) 2354–2366
- [33] M. Roux, Master's thesis, Illinois Institute of technology (1972)
- [34] N. Miura and K. Nakao, "Computer Analysis of Megagauss Field Generation by Condenser Bank Discharge", *Jap. J. Appl. Phys.*, **29** (1990) 1580–1599
- [35] N. Miura, private communication
- [36] O. Portugall, *Linear Response Phenomena in the Mixed Valence Compound  $Hg_{1-x}Fe_xSe$* , Ph.D. thesis, Technische Universität Carolo-Wilhelmina zu Braunschweig (1991)
- [37] M. Motokawa, "Physics in high magnetic fields", *Rep. Prog. Phys.*, **67** (2004) 1995–2052
- [38] F. Herlach, "Pulsed magnets", *Rep. Prog. Phys.*, **62** (1999) 859–920, and references therein
- [39] H. Jones, P. H. Frings, M. von Ortenberg, A. Lagutin, L. van Bockstal, O. Portugall and F. Herlach, "First experiments in fields above 75T in the European "coilin-coilex" magnet", *Physica B*, **346-347** (2004) 553–560
- [40] K. Kindo, "100 T magnet developed in Osaka", *Physica B*, **294-295** (2001) 585–590
- [41] L. J. Campbell, H. J. Boenig, D. G. Rickel, J. B. Schillig, J. R. Sims and H. J. Schneider-Muntau, "Status of the NHMFL 60 tesla quasi-continuous magnet", *IEEE Trans. Magn.*, **32** (1996) 2454–2457
- [42] Y. H. Matsuda, F. Herlach, S. Ikeda and N. Miura, "Generation of 600T by electromagnetic flux compression with improved implosion symmetry", *Rev. Sci. Instr.*, **73** (2002) 4288–4294

- [43] A. I. Bykov, M. I. Dolotenko, N. P. Kolokol'chikov, V. D. Selemir and O. M. Tatsenko, "VNIIEF achievements on ultra-high magnetic fields generation", *Physica B*, **294-295** (2001) 574–578
- [44] F. Herlach, "Magnets for the 21st century", *Physica B*, **246-247** (1998) 152–157
- [45] R. F. Service, "Los Alamos Magnet Leads the Field", *Science*, **281** (1998) 1262–1264
- [46] M. von Ortenberg (Ed.), *Proceedings of the Xth International Conference on Megagauss Magnetic Field Generation and Related Topics*, VNIIEF, 2005
- [47] C. A. Swenson, W. S. Marshall, A. V. Gavrilin, K. Han, J. Schillig, J. R. Sims, Jr. and H. J. Schneider-Muntau, "Progress of the insert coil for the US-NHMFL 100 T multi-shot pulse magnet", *Physica B*, **346-347** (2004) 561–565
- [48] N. Miura, "Solid-state physics in megagauss fields generated by electromagnetic flux compression and single-turn coils", *Physica B*, **201** (1994) 40–48
- [49] B. Novac, I. R. Smith, D. F. Rankin and M. Hubbard, "A fast and compact  $\theta$ -pinch electromagnetic flux compression generator", *J. Phys. D: Appl. Phys.*, **37** (2004) 3041–3055
- [50] N. Miura, Y. H. Matsuda, K. Uchida, S. Todo, T. Goto, H. Mitamura, T. Osada and E. Ohmichi, "New Megagauss Laboratory of ISSP at Kashiwa", *Physica B*, **294-295** (2001) 562–567
- [51] H. P. Furth, M. A. Levine and R. W. Waniek, "Production and Use of High Transient Magnetic Fields. II", *Rev. Sci. Instr.*, **28** (1957) 949–958
- [52] H. Knoepfel and R. Luppi, "Very high magnetic fields generated in single-turn solenoids", *J. Phys. E: Sci. Instr.*, **5** (1972) 1133–1141
- [53] G. A. Shneerson, *Field and Transients in Super High Pulse Current Devices*, Nova Science Publishers, New York, 1997
- [54] G. A. Shneerson, "Получение Сильного Импульсного Магнитного Поля в Сплошных Одновитковых Соленоидах Малого Объема", *Журнал Технической Физики*, **32** (1962) 1153–1156, "A Strong Pulse Magnetic Field in a Small Solid One-Coil Solenoid", *Sov. Phys. - Tech. Phys.* **7** (1963) pp. 848-850
- [55] J. W. Shearer, "Interaction of Capacitor-Bank-Produced Megagauss Magnetic Field with Small Single-Turn Coil", *J. Appl. Phys.*, **40** (1969) 4490–4497
- [56] D. W. Forster and J. C. Martin, "2.5 Megagauss from a Capacitor Discharge", in "Proc. Int. Conf. Les champs magnétiques intenses, leur production et leurs applications", , edited by R. Pauthenet, CNRS, Grenoble, France, 1967 pp. 361–370
- [57] F. Herlach and R. McBroom, "Megagauss fields in single turn coils", *J. Phys. E: Sci. Instr.*, **6** (1973) 652–654
- [58] F. Herlach, R. McBroom, T. Erber, J. Murray and R. Gearhart, "Experiments with Megagauss Targets at SLAC", *IEEE Trans. Nucl. Science*, **NS-18** (1971) 809–813

- [59] S. Takeyama, T. Osada and N. Miura, “Solid-state physics towards pulsed ultra-high magnetic fields at *ISSP*”, *Physica B*, **346-347** (2004) 576–581
- [60] K. Nakao, F. Herlach, T. Goto, S. Takeyama, T. Sakakibara and N. Miura, “A laboratory instrument for generating magnetic fields over 200 T with single turn coils”, *J. Phys. E: Sci. Instrum.*, **18** (1985) 1018–1026
- [61] F. Herlach and M. von Ortenberg, “pulsed Magnets for Strong and Ultrastrong Fields”, *IEEE Trans. Magn.*, **32** (1996) 2438–2443
- [62] F. Herlach and N. Miura, “Generation of megagauss fields”, in “High Magnetic Fields: Science and Technology”, , edited by F. Herlach and N. Miura, volume 1, pp. 235–284, World Scientific, Singapore, 2003
- [63] G. Shneerson and S. I. Krivosheev, private communication (2001)
- [64] J. Singleton, C. H. Mielke, A. Migliori, G. S. Boebinger and A. H. Lacerda, “The National High Magnetic Field Laboratory Pulsed-Field Facility at Los Alamos National Laboratory”, *Physica B*, **346-347** (2004) 614–617
- [65] O. Portugall, N. Puhmann, H.-U. Müller, M. Barczewski, I. Stolpe and M. von Ortenberg, “The generation and application of megagauss fields at the Humboldt High Magnetic Field Center”, *Physica B*, **246-247** (1998) 54–60
- [66] I. Stolpe, *IR-Spektroskopie in extrem hohen Magnetfeldern bis 700 T*, Ph.D. thesis, Humboldt-Universität zu Berlin (2000)
- [67] Maxwell, Inc., USA, *US patent specification*
- [68] Farbwerke Hoechst AG, *Hostaphan*® (Germany) aka *Mylar*® (UK, US)
- [69] DuPont, France, *Kapton*® (Polyimide)
- [70] I. Thomas, “Schlußmappe”, Technical report, I. Thomas GmbH, Stade, Germany (March 2003), email communication, Megagauß-Labor, Bodenaufbau, May 2004
- [71] T. Ikaida, Laboratory Message, ISSP, University of Tokyo (November 2001)
- [72] H. Nojiri and M. v. Ortenberg, private communication (2002/2003)
- [73] R. Chodziesner-Bonne, “Non-destructive magnet at 60 Teslas”, Technical report, Humboldt-Universität zu Berlin (March 2003)
- [74] C. Mielke, private communication & napkin drawing (March 2005)
- [75] C. W. Wegst, *Stahlschlüssel*, volume 19, Verlag Stahlschlüssel Wegst, Marbach, Germany, 2001
- [76] A. Kirste, private communication (2005)
- [77] P. D. Thang, P. H. Frings and E. Brück, “A 20 T pulse magnet with 80% field reversal for fast hysteresis measurements”, *Physica B*, **294-295** (2001) 653–656

- [78] H.-U. Müller, H. Scholz, N. Puhlmann, O. Portugall, M. Barczewski, I. Stolpe and M. von Ortenberg, “High sensitivity data acquisition during strong transient electromagnetic fields”, *Physica B*, **246-247** (1998) 356–359
- [79] M. von Ortenberg, N. Puhlmann, I. Stolpe, H.-U. Müller, A. Kirste and O. Portugall, “The Humboldt high magnetic field center at Berlin”, *Physica B*, **294-295** (2001) 568–573
- [80] V. Druzhinin, O. M. Tatsenko, A. I. Bykov, M. I. Dolotenko, N. P. Kolokol’chikov, Y. B. Kudasov, V. M. Platonov, C. M. Fowler, B. L. Freeman, J. D. Goettee, J. C. King, W. Lewis, B. R. Marshall, B. J. Papatheofanis, P. J. Rodriguez, L. R. Veeseer and W. D. Zerwekh, “Nonlinear Faraday effect in CdS semiconductor in an ultrahigh magnetic field”, *Physica B*, **211** (1995) 392–395
- [81] Apollo Lasers, Inc., *Model 550A Tunable CO<sub>2</sub> Laser*
- [82] Edinburgh Instruments, Edinburgh, *PL 3 Invar stabilised CW CO/CO<sub>2</sub> laser* (2004)
- [83] Electro Optical Systems, Inc., 1000 Nutt Road, Phoenixville, PA, 19640, USA, *Final Data Sheet, MCT-Series HgCdTe Detector* (April 1994)
- [84] Hewlett Packard, Inc., USA, *Digitizing Oscilloscope 54512 B*
- [85] Sony Texttronix, Inc., Japan, *Digitizer RTD 710 A*
- [86] O. M. Tatsenko, V. V. Platonov and S. Hansel (2006), to be published
- [87] Emerson & Cummings, *Stycast 1266*
- [88] Lake Shore, Inc., USA, *US patent specification*
- [89] E. Hüseyinov, private communication (2003)
- [90] “National semiconductor materials archive”, <http://www.ioffe.ru/SVA/NSM/Semicond/Insb/> (June 2003)
- [91] in “Semiconductors: group IV elements and III-V compounds”, , edited by O. Madelung, Landolt Börnstein, pp. 141–150, Springer Verlag, Berlin, Heidelberg, 1991
- [92] M. von Ortenberg and S. Artjushenko, “Fiber Technologies for 30 THz-Magneto spectroscopy”, in “Digest Terahertz 2003”, Sendai, Japan, 2003 p. 16
- [93] L. Vorob’ev, V. Stafeev, V. Shalygin and A. Shturbin, “Light-modulation investigation of impact ionization in intrinsic InSb”, *Sov. Phys. Semicond.*, **17** (1983) 81–84, *Физ. Тех. Полупроводн.* **17** (1983) pp. 129-133
- [94] H. Bruhns and K. Hübner, “Impact Ionization by Electric Fields in Intrinsic Indium-Antimonide”, *Zeit. f. Physik B*, **26** (1976) 227–232
- [95] A. Krotkus and A. Plitnikas, “Ударная Ионизация в Антимониде Индия при Комнатной Температуре”, *Физ. Тех. Полупроводн.*, (1979) 1230–1233

- [96] M. von Ortenberg, “High-Field Investigations on Semimagnetic Semiconductors”, in “High Magnetic Fields in Semiconductor Physics II - Transport and Optics”, , edited by G. Landwehr, *Springer Series in Solid-State Science*, volume 87, Springer, Würzburg, Germany, 1988 pp. 486–495
- [97] D. Matz, “Effects of Nonparabolicity on Non-Ohmic Transport in InSb and InAs”, *Phys. Rev.*, **168** (1968) 843–849
- [98] E. W. S. Caetano, E. A. Mendes, V. N. Freire, J. A. P. da Costa and X. L. Lei, “High-magnetic-field effects on the terahertz mobility of hot electrons in n-type InSb”, *Phys. Rev. B*, **57** (1998) 11872–11874
- [99] H. Fujisada, S. Kataoka and A. C. Beer, “Electric Field Dependence of Galvanomagnetic Properties in n-Type InSb at 77°K”, *Phys. Rev. B*, **3** (1971) 3249–3257
- [100] X. M. Weng and X. L. Lei, “Hot-Electron Magneto-Transport in Narrow Gap Semiconductors in Quantum Magnetic Field”, *phys. stat. sol. (b)*, **191** (1995) 183–188
- [101] T. Yao, K. Inagaki and S. Maekawa, “Energy Relaxation Process in n-type InSb under Strong Longitudinal Magnetic Fields”, *J. Phys. Soc. Japan*, **38** (1975) 1394–1399
- [102] D. K. Ferry and H. Heinrich, “Effect of Magnetic Fields on Impact Ionization Rates and Instabilities in InSb”, *Phys. Rev.*, **169** (1968) 670–673
- [103] M. von Ortenberg, C. Puhle and S. Hansel, “HgSe and HgSe:Fe in extreme magnetic fields”, in “Proc. 27th Int. Conf. Phys. Semicond.”, , edited by L. van de Walle and J. Menendez, American Institute of Physics, Flagstaff, Arizona, USA, 2004 p. 357
- [104] C. Puhle, *Quecksilberselenid in Megagauss-Feldern: Das tight binding-Modell*, Diplomarbeit, Humboldt-Universität zu Berlin (January 2004)
- [105] K.-U. Gawlik, L. Kipp, M. Skibowski, N. Orlowski and R. Manzke, “HgSe: Metal or Semiconductor?”, *Phys. Rev. Lett.*, **78** (1997) 3165–3168
- [106] T. Dietl, W. Dobrowolski, J. Kossut, B. J. Kowalski, W. Szuszkiewicz, Z. Wilamowski and A. M. Witowski, “Comment on: HgSe: Metal or Semiconductor?”, *Phys. Rev. Lett.*, **81** (1997) 1535
- [107] C. Becker, private communication (2005)
- [108] G. L. Hansen, J. L. Schmit and T. N. Casselman, “Energy Gap versus Alloy Composition and Temperature in  $Hg_{1-x}Cd_xTe$ ”, *J. Appl. Phys.*, **53** (1982) 7099
- [109] L. Wei, private communication (2004)
- [110] S. Bhaumik and C. Sarkar, “Electrical Conductivity of Hot Electrons in Narrow-Gap Semiconductors in the Extreme Quantum Limit at Low Temperatures”, *phys. stat. sol. (b)*, **175** (1993) 403–407
- [111] EUROMAGTechNet Collaboration, to be published (2006)





# List of Publications

- [1] **Dynamic Magnetic Alignment of Single-Walled Carbon Nanotubes in Megagauss Fields**  
J. Shaver, J. Kono, S. HANSEL, A. Kirste, M. von Ortenberg, C. H. Mielke, O. Portugall, R. H. Hauge and R. E. Smalley, in *Proceedings 12th International Conference on the Physics of Narrow Gap Semiconductors*, edited by J. Kono, Toulouse, France and Houston, TX, US, 2005
- [2] **The HUMBOLDT High Magnetic Field Center**  
S. HANSEL, A. Kirste, H.-U. Mueller, T. T. Anh and M. von Ortenberg, in *Digest Physical Phenomena at High Magnetic Fields - V*, Tallahassee, FL, USA, 2005 p. 73
- [3] **High field magneto-spectroscopy in HgSe and HgTe up to 225 T**  
S. HANSEL, B. Richter, T. Tran-Anh, M. von Ortenberg and C. R. Becker, in *Digest 30th International Conference on Infrared and Millimeter Waves - Terahertz 2005*, IEEE, Williamsburg, VA, USA, 2005 p. 56
- [4] **IR-Magneto-Optics on HgSe:Fe in Fields up to 1000 T**  
A. Kirste, S. HANSEL, M. von Ortenberg, O. Tatsenko, I. Markevtsev, A. Moiseenko, V. Platonov and V. Selemir, , in *Digest Joint 29th International Conference on Infrared and Millimeter Waves and 12th International Conference on Terahertz Electronics*, edited by M. Thumm, W. Wiesbeck and S. Illy, IEEE, Karlsruhe, Germany, 2004 pp. 129–130
- [5] **Characterization of II-VI Narrow Gap Semiconductors by Megagauss Infrared Spectroscopy**  
A. Kirste, S. HANSEL, , I. Stolpe, H.-U. Müller and M. v. Ortenberg, *J. All. Comp.*, **371** (2004) 133–137
- [6] **Growth and Characterization of HgSe:Fe Quantum Dots**  
T. Tran-Anh, S. HANSEL, A. Kirste, H.-U. Müller, M. v. Ortenberg, J. Barner and J. Rabe, *J. All. Comp.*, **371** (2004) 198–201
- [7] **Rare-earth zircons and intermetallic compounds in megagauss-fields: investigation of new magnetic phenomena**  
A. Kirste, N. Kolmakova, S. HANSEL, H.-U. Müller and M. von Ortenberg, *Physica B*, **346-347** (2004) 191–195

- [8] **The Humboldt High Magnetic Field Center**,  
S. HANSEL, A. Kirste, C. Puhle, M. Bayir, H.-U. Müller and M. von Ortenberg, *Physica B*, **346-347** (2004) 623–626
- [9] **Magneto-optical Detection of Carrier-Dynamics in p-type Indiumantimonide** S. HANSEL, C. Puhle, M. von Ortenberg and E. Huseynov, *Physica B*, **346-347** (2004) 479–482
- [10] **Investigation of magnetic properties in strong and ultrastrong magnetic fields using the single-turn coil technique: new phenomena in intermetallic compounds and rare-earth circons**  
A. Kirste, Z. Kazei, N. Kolmakova, S. HANSEL, H. Müller and M. von Ortenberg, *Journal of Magnetism and Magnetic Materials*, **272-276** (2004) e1677–e1678
- [11] **HgSe:Fe quantum dots: growth and characterization**  
T. Tran-Anh, S. HANSEL, A. Kirste, H.-U. Müller and M. v. Ortenberg, *Physica E*, **20** (2004) 444–448
- [12] **Magneto-optical Experiments using the explosive driven Flux Compression up to 1000 T**  
S. HANSEL, T. Tran-Anh, A. Kirste, N. Puhlmann, M. von Ortenberg, O. Tatsenko, V. Platonov, A. N. Moisseenko and V. Selemir, in *Proc. Int. Conf. Physics Semiconductors in High Magnetic Fields*, edited by Y.-J. Wang, Natnl. High Magn. Field Lab., Tallahassee, FL, USA, 2004 p. 333
- [13] **HgSe and HgSe:Fe in extreme magnetic fields**  
M. von Ortenberg, C. Puhle and S.Hansel, in *Proc. 27th Int. Conf. Phys. Semicond.*, edited by L. van de Walle and J. Menendez, American Institute of Physics, Flagstaff, Arizona, USA, 2004 p. 357
- [14] **Magnetotransport in HgSe:Fe quantum-dot systems**  
M. Bayir, A. Kirste, T. Tran-Anh, S. HANSEL and M. von Ortenberg, in *Proc. 27th Int. Conf. Phys. Semicond.*, edited by L. van de Walle and J. Menendez, American Institute of Physics, Flagstaff, Arizona, USA, 2004 p. 795
- [15] **Megagauss-Investigation of the magneto-optical Transition between the bound Fe-donor and quasi-free Electrons in HgSe:Fe**  
S. HANSEL, A. Kirste, T. Tran-Anh, H.-U. Müller and M. von Ortenberg, in *Proceedings of the Tenth International Conference on Megagauss Magnetic Field Generation and Related Topics*, edited by M. von Ortenberg, VNIIEF, Berlin, Germany and Sarov, Russia, 2005 pp. 291–294
- [16] **Magnetization of  $LaMnO_3$  in strong magnetic fields**  
A. Kirste, H. Nojiri, S. HANSEL, H.-U. Müller and M. von Ortenberg, in *Proceedings of the Tenth International Conference on Megagauss Magnetic Field Generation and Related Topics*, edited by M. von Ortenberg, VNIIEF, Berlin, Germany and Sarov, Russia, 2005 pp. 295–299

- [17] **Magnetization Measurements in  $Rb_2CoF_4$  in Megagauss Fields**  
M. Motokawa, S. Itoh, S. HANSEL, A. Kirste and M. von Ortenberg, in *Proceedings of the Tenth International Conference on Megagauss Magnetic Field Generation and Related Topics*, edited by M. von Ortenberg, VNIIEF, Berlin, Germany and Sarov, Russia, 2005 pp. 272–275
- [18] **Peculiarities of the Cyclotron Resonance Recording in Semiconductor Materials in Magnetic Fields up to 1000T**  
P. Duday, I. Markevtsev, A. Moiseenko, O. Tatsenko, A. Filippov, M. von Ortenberg, N. Puhlmann, I. Stolpe, A. Kirste and S. HANSEL, in *Proceedings of the Tenth International Conference on Megagauss Magnetic Field Generation and Related Topics*, edited by M. von Ortenberg, VNIIEF, Berlin, Germany and Sarov, Russia, 2005 pp. 248–251
- [19] **Infrared Spectroscopy in Transient Magnetic Fields**  
S. HANSEL, C. Puhle, A. Kirste, H.-U. Müller, M. v. Ortenberg and E. Huseynov, in *Digest 28th International Conference on Infrared and Millimeter Waves*, edited by Hiromoto, IEEE, Ohtsu, Shiga Ken, Japan, 2003 pp. 109–110
- [20] **MCT based PEM detector for middle range of IR spectrum**  
F. Gaziyeu, E. Huseynov, I. Nasibov and S. HANSEL, in *Digest 28th International Conference on Infrared and Millimeter Waves*, edited by Hiromoto, IEEE, Ohtsu, Shiga Ken, Japan, 2003 pp. 427–428
- [21] **Magnetospectroscopy at the L-Point in GaAs in Magnetic Fields up to 1000T**  
M. von Ortenberg, N. Puhlmann, I. Stolpe, A. Kirste, H.-U. Müller, S. HANSEL, O. Tatsenko, I. Markevtsev, A. N. Moiseenko, V. Platonov, A. Bykov and V. Selemir, in *Proc. Int. Conf. Phys. Semicond. in Magn. Fields, SemiMag 15*, edited by A. Long and J. Davies, volume 171, Institute of Physics, Edinburgh, U.K., 2002 p. F1.2
- [22] **Growth and Characterization of HgSe:Fe Quantum Dots**  
T. T. Anh, S. HANSEL, A. Kirste, H. U. Müller, M. von Ortenberg, T. Spangenberg and H. Niehus, in *Proc. 26th Int. Conf. Phys. Semicond.*, edited by A. Long and J. Davies, volume 171, Institute of Physics, Edinburgh, U.K., 2002 p. D161
- [23] **Frontiers in Physics: Infrared Magnetospectroscopy at the L-Point in GaAs in Magnetic Fields up to 1000T**  
M. von Ortenberg, N. Puhlmann, I. Stolpe, A. Kirste, H.-U. Müller, S. HANSEL, O. M. Tatsenko, I. M. Markevtsev, N. A. Moiseenko, V. V. Platonov, A. I. Bykov, and V. D. Selemir, in *Proc. 9th International Conference on Megagauss Magnetic Field Generation and Related Topics*, edited by V. Selemir and L. Plyashkevich, VNIIEF, Sarov, Russia, 2004 pp. 454–462
- [24] **HgSe:Fe Quantum Dots in Megagauss Magnetic Fields**  
T. Tran-Anh, S. HANSEL, A. Kirste, H.-U. Müller, M. v.Ortenberg, J. Barner and J. Rabe, in *Proc. 9th International Conference on Megagauss Magnetic Field*

*Generation and Related Topics*, edited by V. Selemir and L. Plyashkevich, VNIIEF, Sarov, Russia, 2004 pp. 463–468

- [25] **High Sensitivity Magnetization Measurements in Megagauss Fields**  
A. Kirste, H.-U. Müller, S. HANSEL and M. v.Ortenberg, in *Proc. 9th International Conference on Megagauss Magnetic Field Generation and Related Topics*, edited by V. Selemir and L. Plyashkevich, VNIIEF, Sarov, Russia, 2004 pp. 475–479
- [26] **Infrared Detection of Carrier Dynamics in Indiumantimonide in Megagauss Fields**  
S. HANSEL, A. Kirste, H.-U. Müller, M. von Ortenberg and E. Huseynov, in *Digest 27th International Conference on Infrared and Millimeter Waves*, edited by R. J. Temkin, San Diego, California, USA, 2002 pp. 171–172
- [27] **The Effect of Quantum Dots on the Infrared Cyclotron Resonance in HgSe:Fe**  
T. T. Anh, S. HANSEL, A. Kirste, H.-U. Müller and M. von Ortenberg, in *Digest 27th International Conference on Infrared and Millimeter Waves*, edited by R. J. Temkin, IEEE, San Diego, California, USA, 2002 pp. 317–318
- [28] **Megagauss-Magneto spectroscopy on II-VI Compounds**  
S. HANSEL, I. Stolpe, A. Kirste, H.-U. Müller and M. von Ortenberg, in *Digest 26th International Conference on Infrared and Millimeter Waves*, edited by O. Portugall and J. Leotin, Toulouse, France, 2001 pp. 4–74
- [29] **Infrarotspektroskopie an Narrow-Gap Halbleitermaterialien der Quecksilbertelluridfamilie in Megagaussfeldern,**  
S. HANSEL, Diplomarbeit, Humboldt-Universität zu Berlin (September 2001)

# Acknowledgments

First of all I would like to thank Prof. Dr. M. von Ortenberg for the opportunity to do my PhD in his supervision. His enthusiasm and profound physical knowledge encouraged me to produce this work. His hearty contact with the international community that he transferred generously onto his students will certainly support any of my future activities as well as it did with this work.

Furthermore, I would like to thank all the people who have provided samples to be investigated in this study, Prof. Dr. E. Hüseyinov, Dr. Wei Lu, Dr. C. R. Becker and J. Sölle. I do also appreciate the basic data and invaluable hints and experiences so frankly shared by these people.

I thank the Magnetotransport group, especially Dr. A. Kirste and Dr. H.-U. Müller for scientific support during the performance of measurements and analysis as well as intense discussion. Mr. C. Puhle, Mr. H. Roßmann supported a part of the measurements significantly.

I owe great gratitude to the people that made this work possible by their technical support to the successful operation of laboratory and performing the measurements. Among many others, I want to acknowledge the contributions of the mechanics of the Magnetotransport group, Mrs. D. Fahnauer & Mr. S. Schultz as well as Mr. W. Stock, the mechanical workshop of the Department of Physics headed by Mr. T. Rausche & Mr. S. Fahnauer as well as the ones of Mr. S. Schmidt and Mr. J. Sölle.

I would like to express appreciation to the liquid Helium department, Dr. U. Preppernau and Mr. V. Misch, that kept my measurements possible as well as the crew of the glass manufacturing workshop, led by Mr. F. Leinung and Mrs. A. Kottke.

For introducing me to FTIR measurements I would like to thank Dr. U. Müller and Dr. M. Sentsiv as well as Prof. Dr. Masselink for the chance of using the equipment and support of his group.

Moreover, I like to thank all the stimulating discussion partners that I met on many occasions. I appreciate Prof. Dr. F. Herlach's support to me with his wide knowledge and access to hard-to-get literature.

Last but not least, I thank my family and friends for making the time spent besides pure physics enjoyable.







